

***f*-ELEMENTS IN IONIC LIQUIDS: A SYNTHETIC, SPECTROSCOPIC AND ELECTROCHEMICAL STUDY**

Anand Indravadan Bhatt

A thesis submitted to the University of Manchester

for the degree of Ph.D. in the Faculty of Science and Engineering

Department of Chemistry, 2004

ProQuest Number: 10757225

All rights reserved

INFORMATION TO ALL USERS

The quality of this reproduction is dependent upon the quality of the copy submitted.

In the unlikely event that the author did not send a complete manuscript and there are missing pages, these will be noted. Also, if material had to be removed, a note will indicate the deletion.



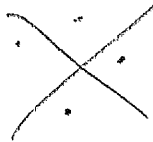
ProQuest 10757225

Published by ProQuest LLC (2018). Copyright of the Dissertation is held by the Author.

All rights reserved.

This work is protected against unauthorized copying under Title 17, United States Code
Microform Edition © ProQuest LLC.

ProQuest LLC.
789 East Eisenhower Parkway
P.O. Box 1346
Ann Arbor, MI 48106 – 1346



Th 24083

THE
JOHN F. LANDS
UNIVERSITY
LIBRARY

CONTENTS

List of Figures	page 11
List of Tables	page 17
Abstract	page 21
Declaration	page 22
Notes on copyright	page 22
Dedication	page 23
Acknowledgements	page 24
Preface	page 26
List of abbreviations	page 27

Chapter 1: Introduction

1.1	General introduction to <i>f</i> -element chemistry	page 30
1.2	Actinide radiochemistry, nuclear power and the Purex process	page 38
1.3	High temperature molten salts reprocessing	page 44
1.4	Low temperature ionic liquids (LTILs)	page 46
1.5	British Nuclear Fuels Limited (BNFL) ionic liquids research programme	page 54
1.6	Aims and objectives	page 57
1.7	References	page 58

Chapter 2: Experimental techniques

2.1	Introduction	page 65
2.2	Elemental analysis	page 65
2.3	Thermogravimetric analysis	page 65
2.4	NMR spectroscopy	page 66
2.5	UV/vis/nIR spectroscopy	page 66
2.6	Vibrational spectroscopy	page 67
2.7	Single crystal X-ray diffraction	page 68
2.8	Electrochemistry	page 68
2.9	X-ray absorption spectroscopy	page 69
2.9.1	<i>XAS – Experimental method</i>	page 69
2.9.2	<i>XAS – Theory</i>	page 70
2.9.3	<i>X-ray Absorption Near Edge Structure (XANES)</i>	page 72
2.9.4	<i>Extended X-ray Absorption Fine Structure (EXAFS)</i>	page 73
2.10	References	page 75

Chapter 3: Synthesis and spectroscopic, structural and electrochemical characterisation of low temperature ionic liquids of bis(trifluoromethanesulfonyl)amide with Group 15 quaternary cations

3.1	Introduction	page 76
3.2	Synthesis of bis(trifluoromethanesulfonyl)amide-based low temperature ionic liquids with Group 15 quaternary cations	page 79
3.2.1	<i>General considerations</i>	page 79

3.2.2	<i>Synthesis of tetramethylammonium bis(trifluoromethanesulfonyl)amide – [Me₄N][TFSI]</i>	page 80
3.2.3	<i>Synthesis of tetramethylphosphonium bis(trifluoromethanesulfonyl)amide – [Me₄P][TFSI]</i>	page 80
3.2.4	<i>Synthesis of tetramethylarsonium bis(trifluoromethanesulfonyl)amide ([Me₄As][TFSI]) and tetramethylstibonium bis(trifluoromethanesulfonyl)amide ([Me₄Sb][TFSI])</i>	page 81
3.2.5	<i>Synthesis of N,N-trimethylethylammonium bis(trifluoromethanesulfonyl)amide – [Me₃NEt][TFSI]</i>	page 81
3.2.6	<i>Synthesis of N,N-trimethyl-n-butylammonium bis(trifluoromethanesulfonyl)amide – [Me₃NⁿBu][TFSI]</i>	page 81
3.2.7	<i>Synthesis of N,N-trimethyl-n-hexylammonium bis(trifluoromethanesulfonyl)amide – [Me₃NⁿHex][TFSI]</i>	page 82
3.2.8	<i>Synthesis of P,P-dimethyldiphenylphosphonium bis(trifluoromethanesulfonyl)amide ([Me₂PPh₂][TFSI], P,P- methyltriphenylphosphonium bis(trifluoromethanesulfonyl)amide ([MePPh₃][TFSI]) and tetraphenylphosphonium bis(trifluoromethanesulfonyl)amide ([Ph₄P][TFSI])</i>	page 83

3.2.9	<i>Preparation of single crystals of tetramethylphosphonium bis(trifluoromethanesulfonyl)amide ([Me₄P][TFSI]) and tetramethylstibonium bis(trifluoromethanesulfonyl)amide ([Me₄Sb][TFSI]) suitable for X-ray diffraction</i>	page 83
3.3	Physical characterisation of Group 15 cation and TFSI anion based LTILs	page 84
3.3.1	<i>Elemental analysis and melting points</i>	page 84
3.3.2	<i>Thermogravimetric analysis</i>	page 85
3.4	Spectroscopic characterisation of TFSI-based LTILs	page 86
3.4.1	<i>Vibrational spectroscopy</i>	page 86
3.4.2	<i>NMR spectroscopy</i>	page 88
3.5	Single crystal X-ray diffraction studies of [Me ₄ P][TFSI] and [Me ₄ Sb][TFSI]	page 90
3.5.1	<i>X-ray diffraction study of [Me₄P][TFSI]</i>	page 90
3.5.2	<i>X-ray diffraction study of [Me₄Sb][TFSI]</i>	page 94
3.6	Electrochemical windows of TFSI-based melts	page 98
3.6.1	<i>Electrochemical window of LTILs in MeCN using TFSI-based LTILs as supporting electrolyte – experimental method</i>	page 98
3.6.2	<i>Electrochemical windows of molten TFSI-based LTILs – experimental method</i>	page 99

3.6.3	<i>Voltammetry of Li[TFSI] in MeCN using [Me₄P][TFSI] as supporting electrolyte and in molten [Me₄P][TFSI] at 190 °C – experimental method</i>	page 105
3.6.4	<i>Electrochemical window measurements of TFSI based melts – results and discussion</i>	page 105
3.6.5	<i>Voltammetry of Li[TFSI] in MeCN using [Me₄P][TFSI] as supporting electrolyte and in molten [Me₄P][TFSI] at 190 °C – results and discussion</i>	page 108
3.7	Density functional theory calculations of electrochemical windows of TFSI based LTILs in MeCN	page 112
3.7.1	<i>Introduction</i>	page 112
3.7.2	<i>Experimental</i>	page 113
3.7.3	<i>Discussion</i>	page 114
3.8	Radiation stability of LTILs	page 116
3.9	Summary	page 119
3.10	References	page 121

Chapter 4: Syntheses, structure and electrochemistry of lanthanide

bis(trifluoromethanesulfonyl)amides

4.1	Introduction	page 127
4.2	Synthesis of lanthanide bis(trifluoromethanesulfonyl)amides	page 129
4.2.1	<i>General considerations</i>	page 129

4.2.2	<i>Triaqua tris{bis(trifluoromethanesulfonyl)amide} lanthanum(III) – [La(TFSI)₃(H₂O)₃]</i>	page 130
4.2.3	<i>Triaqua tris{bis(trifluoromethanesulfonyl)amide} europium(III) – [Eu(TFSI)₃(H₂O)₃]</i>	page 130
4.2.4	<i>Triaqua tris{bis(trifluoromethanesulfonyl)amide} samarium(III) – [Sm(TFSI)₃(H₂O)₃]</i>	page 131
4.2.5	<i>Crystallisation of [La(TFSI)₃(H₂O)₃] suitable for X-ray diffraction</i>	page 131
4.3	Single crystal X-ray diffraction of [La(TFSI) ₃ (H ₂ O) ₃]	page 131
4.4	Vibrational spectroscopy	page 139
4.5	Electrochemical behaviour of [Ln(TFSI) ₃ (H ₂ O) ₃] (Ln = La, Sm and Eu) in LTILs	page 144
4.5.1	<i>Experimental method</i>	page 144
4.5.2	<i>Cyclic voltammetry of [La(TFSI)₃(H₂O)₃] in TFSI based LTILs and MeCN</i>	page 146
4.5.3	<i>Cyclic voltammetry of [Eu(TFSI)₃(H₂O)₃] in TFSI based LTILs and MeCN</i>	page 147
4.5.4	<i>Cyclic voltammetry of [Sm(TFSI)₃(H₂O)₃] in TFSI based LTILs and MeCN</i>	page 149
4.5.5	<i>Diffusion coefficients of [Ln(TFSI)₃(H₂O)₃] (Ln = La, Sm and Eu) in [Me₃NⁿBu][TFSI] and MeCN using [Me₃NⁿBu][TFSI] as supporting electrolyte</i>	page 154
4.6	Summary	page 157

4.7	References	page 158
-----	------------	----------

Chapter 5: Synthesis and electrochemistry of a thorium(IV) TFSI complex in [Me₃NⁿBu][TFSI]

5.1	Introduction	page 162
5.2	Synthesis of hydrogen pentakis-bis(trifluoromethanesulfonyl)amidethorium(IV) dihydrate – H[Th(TFSI) ₅].2H ₂ O	page 164
5.3	Thermogravimetric analysis of H[Th(TFSI) ₅].2H ₂ O	page 164
5.4	Vibrational spectroscopy	page 167
5.5	Electrochemistry	page 171
5.6	Summary	page 174
5.7	References	page 175

Chapter 6: Uranium Speciation in TFSI-based ionic liquids and Electrochemistry in [Me₃NⁿBu][TFSI]

6.1	Introduction	page 178
6.2	Synthesis of uranium TFSI and chloride complexes	page 180
6.2.1	<i>General considerations</i>	page 180
6.2.2	<i>Uranium bis(trifluoromethanesulphonyl)amide – U(TFSI)₄.xH₂O</i>	page 181
6.2.3	<i>Uranyl bis(trifluoromethanesulphonyl)amide hydrate – UO₂(TFSI)₂.H₂O</i>	page 181

6.3	UV/vis/nIR spectroscopy of uranium compounds in the solid state and dissolved in LTILs	page 182
6.4	Vibrational spectroscopy	page 186
6.5	X-ray absorption spectroscopy	page 192
6.5.1	<i>Experimental method</i>	page 192
6.5.2	<i>XANES spectroscopy</i>	page 194
6.5.3	<i>EXAFS of uranium compounds in BN</i>	page 200
6.5.4	<i>EXAFS of uranium TFSI and chloride complexes in [Me₃NⁿBu][TFSI]</i>	page 205
6.6	Electrochemical behaviour of uranium(IV) compounds in [Me ₃ N ⁿ Bu][TFSI]	page 211
6.6.1	<i>Experimental method</i>	page 211
6.6.2	<i>Results and discussion</i>	page 211
6.7	Summary	page 221
6.8	References	page 223

Chapter 7: Synthesis and electrochemistry of a neptunium

bis(trifluoromethanesulfonyl)amide complex

7.1	Introduction	page 228
7.2	Synthesis of a lower oxidation state neptunium bis(trifluoromethanesulfonyl)amide complex	page 230
7.3	Vibrational spectroscopy of Np-TFSI complexes	page 232
7.4	UV/vis/nIR spectroscopy of Np-TFSI complexes in solution	page 237
7.4.1	<i>UV/vis/nIR studies of Np-TFSI complexes in aqueous solution</i>	page 237

7.4.2	<i>UV/vis/nIR studies of Np-TFSI complexes in [Me₃NⁿBu][TFSI] solution</i>	page 239
-------	--	----------

7.5	Electrochemistry of a {NpO ₂ } ⁺ -TFSI complex in [Me ₃ N ⁿ Bu][TFSI]	page 244
7.6	Summary	page 254
7.7	References	page 255

Chapter 8: Conclusions

8.1	Conclusions	page 257
-----	-------------	----------

Appendix 1: Single crystal X-ray diffraction of penta-aquadioxouranium(VI)

bis{bis(trifluoromethanesulfonyl)amide} - [UO₂(H₂O)₅][TFSI]₂

A1.1	Single crystal X-ray diffraction of [UO ₂ (H ₂ O) ₅][TFSI] ₂	page 263
A1.2	References	page 269

Appendix 2: Additional X-ray absorption spectroscopy measurements

A2.1	U L _{III} edge EXAFS of uranium TFSI and chloride complexes dissolved in [Me ₄ N][TFSI]	page 272
A2.2	U L _{III} edge EXAFS of uranium TFSI and chloride complexes dissolved in [nHex ₃ Pdec][NCNCN]	page 274
A2.3	U L _{III} edge EXAFS of uranium TFSI and chloride complexes dissolved in [tBu ₃ P ⁿ Hex][Ots] (where OTs = <i>p</i> -toluenesulfonate)	page 276
A2.4	Zr K edge EXAFS of ZrCl ₄ dissolved in quaternary alkyl group 15 cation and TFSI anion based LTILs	page 278

LIST OF FIGURES

Chapter 1

- Figure 1.2.1 Simplified schematic of the PUREX process page 43
- Figure 1.3.1 Schematic representation of ANL irradiated nuclear fuel molten
salt electrochemical refiner page 45
- Figure 1.5.1 Electrochemical windows of various LTILs measured using cyclic
voltammetry page 56

Chapter 2

- Figure 2.9.1 Schematic of Perspex XAS cells; solution and solid page 70
- Figure 2.9.2 A typical U L_{III} edge XAS spectrum showing the characteristic
regions page 71
- Figure 2.9.3 Schematic representaion of X-ray scattering page 72

Chapter 3

- Figure 3.5.1 Crystal structure of $[Me_4P][TFSI]$ showing one ordered cation and
one disordered anion page 93
- Figure 3.5.2 Crystal structure of $[Me_4Sb][TFSI]$ showing one ordered cation
and one ordered anion page 96
- Figure 3.6.1 Electrochemical windows of tetramethyl Group 15-based LTILs in
the molten state at 160 °C and as supporting electrolytes in MeCN
at 25 °C page 101

Figure 3.6.2	Electrochemical windows of alkyl/aryl phosphonium-based LTILs in the molten state at 160 °C and as supporting electrolyte at 25 °C	page 102
Figure 3.6.3	Electrochemical windows of trimethyl alkyl ammonium-based LTILs in the molten state at 160 °C and as supporting electrolytes in MeCN at 25 °C	page 103
Figure 3.6.4	Electrochemical windows of [Me ₃ N ⁿ Bu][TFSI] and [Me ₃ N ⁿ Hex][TFSI] LTILs in the molten state at 25 °C	page 104
Figure 3.6.5	CVs of Li[TFSI] in molten [Me ₄ P][TFSI] and in MeCN using [Me ₄ P][TFSI] as supporting electrolyte	page 110
Figure 3.6.6	Plots of I _p vs. v ^{1/2} for the reduction and oxidation processes of Li[TFSI] in molten [Me ₄ P][TFSI] at 190 °C	page 111
Figure 3.7.1	Comparison of experimentally measured and calculated cathodics using the B3LYP and MP3 methods	page 116
Figure 3.8.1	Mass spectra of pre- and post-irradiated [Me ₃ N ⁿ Bu][TFSI]	page 118

Chapter 4

Figure 4.3.1	Λ absolute configuration of [La(TFSI) ₃ (H ₂ O) ₃]	page 139
Figure 4.3.2	Δ absolute configuration of [La(TFSI) ₃ (H ₂ O) ₃]	page 135
Figure 4.4.1	Solid state ATR IR and Raman spectra of [Ln(TFSI) ₃ (H ₂ O) ₃] (Ln = La, Sm and Eu). The ATR IR and Raman spectra of Li[TFSI] are also shown for comparison	page 143
Figure 4.5.1	CV of [Ln(TFSI) ₃ (H ₂ O) ₃] in LTIL at 160 °C (Ln = La, Sm and Eu)	page 151

Figure 4.5.2	CV of $[\text{Ln}(\text{TFSI})_3(\text{H}_2\text{O})_3]$ in $[\text{Me}_3\text{N}^n\text{Bu}][\text{TFSI}]$ at 25 °C (Ln = La, Sm and Eu)	page 152
Figure 4.5.3	CV of $[\text{Ln}(\text{TFSI})_3(\text{H}_2\text{O})_3]$ in MeCN with $[\text{Me}_3\text{N}^n\text{Bu}][\text{TFSI}]$ as supporting electrolyte at 25 °C (Ln = La, Sm and Eu)	page 153
Figure 4.5.4	Plot of peak current as a function of scan rate for the La(III)/La(0) and Ln(II)/Ln(0) (Ln = Eu and Sm) reduction processes in $[\text{Me}_3\text{N}^n\text{Bu}][\text{TFSI}]$ at 25 °C	page 156
Figure 4.5.5	Plot of peak current as a function of scan rate for the Eu(II)/Eu(0) and Ln(III)/Ln(0) (Ln = La and Sm) reduction processes in MeCN using $[\text{Me}_3\text{N}^n\text{Bu}][\text{TFSI}]$ as supporting electrolyte at 25 °C	page 156

Chapter 5

Figure 5.3.1	Thermogravimetric analysis of $\text{H}[\text{Th}(\text{TFSI})_5] \cdot 2\text{H}_2\text{O}$	page 166
Figure 5.3.2	Proposed thermal decomposition route for $\text{H}[\text{Th}(\text{TFSI})_5] \cdot 2\text{H}_2\text{O}$	page 167
Figure 5.4.1	Solid state ATR mid-IR and Raman spectra of $\text{H}[\text{Th}(\text{TFSI})_5] \cdot 2\text{H}_2\text{O}$	page 170
Figure 5.5.1	Cyclic voltammograms of $\text{H}[\text{Th}(\text{TFSI})_5] \cdot 2\text{H}_2\text{O}$ in $[\text{Me}_3\text{N}^n\text{Bu}][\text{TFSI}]$ at 25 °C	page 173
Figure 5.5.2	Effect of multiple cycles around the Th(IV)/Th(0) reduction peak	page 174

Chapter 6

Figure 6.3.1	UV/vis/nIR spectra of $\text{U}(\text{TFSI})_4 \cdot x\text{H}_2\text{O}$ dissolved in $[\text{Me}_3\text{N}^n\text{Bu}][\text{TFSI}]$	page 184
--------------	--	----------

Figure 6.4.1	Solid state ATR IR spectra of $\text{U}(\text{TFSI})_4 \cdot x(\text{H}_2\text{O})$	page 189
Figure 6.4.2	Solid state ATR mid-IR and Raman spectra of $\text{UO}_2(\text{TFSI})_2 \cdot \text{H}_2\text{O}$	page 190
Figure 6.4.3	Solid state ATR IR and Raman spectrum of $[\text{UO}_2(\text{H}_2\text{O})_5][\text{TFSI}]_2$	page 191
Figure 6.5.1	XANES spectra of U(VI) compounds in LTILs	page 196
Figure 6.5.2	XANES spectra of U(IV) compounds in LTILs	page 197
Figure 6.5.3	XANES spectra of U(III) compounds in LTILs and BN	page 198
Figure 6.5.4	EXAFS and FT spectra of UCl_3 , $\text{U}(\text{TFSI})_4 \cdot x\text{H}_2\text{O}$ and $\text{UO}_2(\text{TFSI})_2 \cdot \text{H}_2\text{O}$ in BN	page 204
Figure 6.5.5	Proposed structure of multinuclear U species formed upon dissolution of UCl_4 in $[\text{Me}_3\text{N}^n\text{Bu}][\text{TFSI}]$	page 207
Figure 6.5.6	EXAFS and FT spectra of uranium TFSI and chloride complexes in $[\text{Me}_3\text{N}^n\text{Bu}][\text{TFSI}]$	page 210
Figure 6.6.1	CV of $\text{U}(\text{TFSI})_4 \cdot x\text{H}_2\text{O}$ in $[\text{Me}_3\text{N}^n\text{Bu}][\text{TFSI}]$ at 25 °C	page 216
Figure 6.6.2	CV of $\text{U}(\text{TFSI})_4 \cdot x\text{H}_2\text{O}$ with added $[\text{Eu}(\text{TFSI})_3(\text{H}_2\text{O})_3]$ in $[\text{Me}_3\text{N}^n\text{Bu}][\text{TFSI}]$ at 25 °C	page 217
Figure 6.6.3	CV of UCl_4 in $[\text{Me}_3\text{N}^n\text{Bu}][\text{TFSI}]$ at 25 °C	page 218
Figure 6.6.4	Arrhenius plot of $\ln D$ as a function of inverse temperature for U(III)/U(0) reduction in $[\text{Me}_3\text{N}^n\text{Bu}][\text{TFSI}]$	page 221

Chapter 7

Figure 7.3.1	Solid state ATR IR and Raman spectra of Np(IV)-TFSI complex	page 235
Figure 7.3.2	Comparison of the IR spectra of Np, Li, La, U(IV) and $\{\text{UO}_2\}^{2+}$ TFSI complexes	page 236

Figure 7.4.1	Reduction of Np(V) using HI monitored using solution UV/vis/nIR spectroscopy	page 238
Figure 7.4.2	Oxidation of Np(IV) in $[\text{Me}_3\text{N}^n\text{Bu}][\text{TFSI}]$	page 240
Figure 7.5.1	CV of $\{\text{NpO}_2\}^+$ in $[\text{Me}_3\text{N}^n\text{Bu}][\text{TFSI}]$ at 25 °C	page 245
Figure 7.5.2	LSV of $\{\text{NpO}_2\}^+$ in $[\text{Me}_3\text{N}^n\text{Bu}][\text{TFSI}]$ at 25 °C	page 246
Figure 7.5.3	Shain and Nicholson treatment of the Np(V)/Np(IV) reduction observed at 0.40 V in the CV experiment shown in Figure 7.5.1	page 250
Figure 7.5.4	Randles-Sevcik plot for the oxidation of Np(V) to Np(VI) observed at 1.75 V in the CV experiment shown in Figure 7.5.1	page 251
Figure 7.5.5	Randles-Sevcik plot for the reduction of Np(IV) to Np(III) observed at -0.50 V in the CV experiment shown in Figure 7.5.1	page 252
Figure 7.5.6	Randles-Sevcik plot for the reduction of Np(III) to Np(0) observed at -2.69 V in the CV experiment shown in Figure 7.5.1	page 253

Appendix 1

Figure A1.1	Single crystal X-ray diffraction structure of $[\text{UO}_2(\text{H}_2\text{O})_5][\text{TFSI}]_2$	page 268
Figure A1.2	Structure of $[\text{UO}_2(\text{H}_2\text{O})_5]^{2+}-1$ and $[\text{UO}_2(\text{H}_2\text{O})_5]^{2+}-1$ cations showing the out of plane coordinated water observed for $[\text{UO}_2(\text{H}_2\text{O})_5]^{2+}-2$	page 269

Appendix 2

Figure A2.1	EXAFS and FT spectra of uranium TFSI and chloride complexes in $[\text{Me}_4\text{N}][\text{TFSI}]$	page 273
-------------	--	----------

Figure A2.2	EXAFS and FT spectra of uranium TFSI and chloride complexes in [ⁿ Hex ₃ Pdec][NCNCN]	page 275
Figure A2.3	EXAFS and FT spectra of uranium TFSI and chloride complexes in [ⁱ Bu ₃ P ⁿ Hex][Ots]	page 277
Figure A2.4	EXAFS and FT spectra of ZrCl ₄ dissolved in quaternary alkyl group 15 cations and TFSI anion based LTILs	page 280

LIST OF TABLES

Chapter 1

Table 1.1.1	Electronic configurations and discovery dates of the <i>f</i> -elements	page 31
Table 1.1.2	Standard reduction potentials of the lanthanides	page 34
Table 1.1.3	Common oxidation states and standard reduction potentials of the actinides	page 37
Table 1.2.1	Half-lives and radiation energies of selected actinides	page 40
Table 1.4.1	Generic examples of LTILs reported in the literature and their applications	page 48
Table 1.4.2	Selected literature reports of LTIL electrochemical windows	page 50

Chapter 3

Table 3.3.1	Elemental analysis of Group 15 cation and TFSI anion-based LTILs	page 84
Table 3.3.2	Thermal stability of Group 15 cation and TFSI anion-based LTILs	page 85
Table 3.4.1	Solid state ATR mid-IR bands of TFSI-based LTILs synthesised (except [Me ₃ N ⁿ Bu][TFSI] and Me ₃ N ⁿ Hex][TFSI] which were recorded as liquids	page 87
Table 3.4.2	Multi nuclear NMR data for Group 15 cation and TFSI anion-based LTILs measured in CD ₃ CN	page 89
Table 3.5.1	Crystallographic data for [Me ₄ P][TFSI] and [Me ₄ Sb][TFSI]	page 91

Table 3.5.2	Selected bond lengths and angles for one of the two non-disordered TFSI anions and both cations in the structure of [Me ₄ P][TFSI]	page 92
Table 3.5.3	Selected bond lengths and angles for the two non-disordered TFSI anions and two cations in the structure of [Me ₄ Sb][TFSI]	page 97
Table 3.6.1	Electrochemical windows of TFSI-based LTILs in MeCN as supporting electrolytes and in the molten state at 160 °C	page 100
Table 3.7.1	Calculated electron affinities, free energy half-cell reduction potentials and cell potential, with experimental values given for reference	page 115
Table 3.8.1	Characterisation of [Me ₃ N ⁿ Bu][TFSI] after 4 h irradiation with a ⁶⁰ Co source (10 kGy h ⁻¹ dose rate)	page 117

Chapter 4

Table 4.3.1	Crystallographic data for [La(TFSI) ₃ (H ₂ O) ₃]	page 133
Table 4.3.2	Selected bond lengths and angles for the two crystallographically unique molecules in [La(TFSI) ₃ (H ₂ O) ₃]	page 138
Table 4.4.1	Solid state ATR IR and Raman bands of TFSI salt and complexes	page 142
Table 4.5.1	Experimental conditions for cyclic voltammetry measurements of [Ln(TFSI) ₃ (H ₂ O) ₃] complexes (Ln = La, Sm and Eu) in LTILs or MeCN using [Me ₃ N ⁿ Bu][TFSI] as supporting electrolyte	page 145
Table 4.5.2	Diffusion coefficients of Ln species in MeCN with [Me ₃ N ⁿ Bu][TFSI] as supporting electrolyte at 25 °C and in pure [Me ₃ N ⁿ Bu][TFSI] at 25 °C	page 155

Chapter 5

Table 5.4.1	Solid state ATR mid-IR bands of $\text{H}[\text{Th}(\text{TFSI})_5] \cdot 2\text{H}_2\text{O}$. IR/Raman bands of $\text{Li}[\text{TFSI}]$, HTFSI and $[\text{La}(\text{TFSI})_3(\text{H}_2\text{O})_3]$ crystals shown for comparison	page 169
-------------	---	----------

Chapter 6

Table 6.3.1	Major bands in the solid state diffuse reflectance UV/vis/nIR spectra for uranium TFSI and chloride complexes	page 184
Table 6.3.2	UV/vis/nIR bands for uranium complexes dissolved in $[\text{Me}_4\text{N}][\text{TFSI}]$ at 160 °C (room temperature solid state diffuse reflectance spectra of quenched melt), $[\text{Me}_3\text{N}^n\text{Bu}][\text{TFSI}]$, $[\text{Hex}_3\text{PDec}][\text{NCNCN}]$ and $[\text{Bu}_3\text{P}^n\text{Hex}][\text{OTs}]$ (solution UV/vis/nIR spectra)	page 185
Table 6.4.1	Solid state IR and Raman bands of uranium, lanthanum and lithium TFSI salts	page 188
Table 6.5.1	Experimental conditions for XAS measurements	page 193
Table 6.5.2	Absorption edge positions of various uranium compounds reported in the literature	page 199
Table 6.5.3	Calculated coordination modes of TFSI to $\{\text{UO}_2^{2+}\}$	page 202
Table 6.5.4	Best fit parameters to EXAFS data for solid state uranium compounds in BN	page 203
Table 6.5.5	Best fit parameters to EXAFS data for uranium TFSI and chloride complexes in $[\text{Me}_3\text{N}^n\text{Bu}][\text{TFSI}]$	page 209

Table 6.6.1	Diffusion coefficients for the U(III)/U(0) reduction in [Me ₃ N ⁿ Bu][TFSI] measured at varying temperatures using CA	page 220
-------------	--	----------

Chapter 7

Table 7.3.1	Solid state ATR mid-IR and Raman bands of synthesised Np(IV)-TFSI compound	page 234
Table 7.4.1	Assignments for major bands observed in the UV/vis/nIR spectra of Np(V) in [Me ₃ N ⁿ Bu][TFSI]	page 243

Appendix 1

Table A1.1	Crystallographic data for [UO ₂ (H ₂ O) ₅][TFSI] ₂	page 266
Table A1.2	Selected bond lengths and angles for [UO ₂ (H ₂ O) ₅][TFSI] ₂	page 267

Appendix 2

Table A2.1	Best fit parameters to EXAFS data for uranium TFSI and chloride complexes in [Me ₄ N][TFSI]	page 272
Table A2.2	Best fit parameters to EXAFS data for uranium TFSI and chloride complexes in [ⁿ Hex ₃ PDec][NCNCN]	page 274
Table A2.3	Best fit parameters to EXAFS data for uranium TFSI and chloride complexes in [^t Bu ₃ P ⁿ Hex][OTs]	page 276
Table A2.4	Best fit parameters to EXAFS data for ZrCl ₄ dissolved in quaternary alkyl group 15 cation and TFSI anion based LTILs	page 279

ABSTRACT

This thesis reports on chemical research directed towards the utilisation of low temperature ionic liquids (LTILs) for the electrorefining of uranium and plutonium from spent nuclear fuel. Initial studies focus on evaluating the relevant physical and electrochemical properties of LTILs. One room temperature ionic liquid, $[(\text{CH}_3)_3\text{N}(n\text{-C}_4\text{H}_9)][\text{N}(\text{SO}_2\text{CF}_3)_2]$, was identified as the most suitable candidate for further study.

A series of lanthanide bis(trifluoromethanesulfonyl)amide complexes of the general formula $[\text{Ln}(\text{N}(\text{SO}_2\text{CF}_3)_2)_3(\text{H}_2\text{O})_3]$ have been synthesised (where Ln = La, Sm or Eu). $[\text{La}(\text{N}(\text{SO}_2\text{CF}_3)_2)_3(\text{H}_2\text{O})_3]$ has been crystallographically characterised, revealing direct coordination of $[\text{N}(\text{SO}_2\text{CF}_3)_2]^-$ to La^{3+} through the sulfonyl oxygens. The electrochemistry of these complexes have been studied in $[(\text{CH}_3)_3\text{N}(n\text{-C}_4\text{H}_9)][\text{N}(\text{SO}_2\text{CF}_3)_2]$ with the La(III)/La(0), Sm(III)/Sm(II), Sm(II)/Sm(0), Eu(III)/Eu(II) and Eu(II)/Eu(0) couples all observed. As part of a more general study Ln electrochemistry was also studied in $[(\text{CH}_3)_4\text{N}][\text{N}(\text{SO}_2\text{CF}_3)_2]$ and $[(\text{CH}_3)_4\text{P}][\text{N}(\text{SO}_2\text{CF}_3)_2]$ high temperature melts and in MeCN, with $[(\text{CH}_3)_3\text{N}(n\text{-C}_4\text{H}_9)][\text{N}(\text{SO}_2\text{CF}_3)_2]$ acting as supporting electrolyte. Electroplating of the lanthanides appears to be inhibited by oxide formation.

The study of *f*-element electrochemistry in $[(\text{CH}_3)_3\text{N}(n\text{-C}_4\text{H}_9)][\text{N}(\text{SO}_2\text{CF}_3)_2]$ has been extended to selected actinides, Th, U and Np. The synthesis of pure $[\text{N}(\text{SO}_2\text{CF}_3)_2]^-$ complexes has proved challenging due to the instability of U(IV) and Np(IV) in the presence of $[\text{N}(\text{SO}_2\text{CF}_3)_2]^-$ and the moisture sensitive nature of these compounds. Nevertheless direct coordination of $[\text{N}(\text{SO}_2\text{CF}_3)_2]^-$ to actinide cation centres has been observed in $\text{H}[\text{Th}(\text{TFSI})_5] \cdot 2\text{H}_2\text{O}$, $\text{U}(\text{TFSI})_4 \cdot x\text{H}_2\text{O}$, $\text{UO}_2(\text{TFSI})_2 \cdot \text{H}_2\text{O}$ and $\text{NpO}_2(\text{TFSI}) \cdot x\text{H}_2\text{O}$, preliminarily through vibrational spectroscopy, and also XAS for the U complexes. The electrochemical properties of these compounds in $[(\text{CH}_3)_3\text{N}(n\text{-C}_4\text{H}_9)][\text{N}(\text{SO}_2\text{CF}_3)_2]$ have been investigated and the Th(IV)/Th(0), U(III)/U(0) and Np(III)/Np(0) reductions have been observed. For U and Np the expected additional redox processes were also studied and characterised. Although oxide formation was observed after $\text{An}^{(0)}$ electrochemical generation for the actinides investigated, cyclic voltammetry results suggest that U metal (and probably also Np metal) can be electroplated from $[(\text{CH}_3)_3\text{N}(n\text{-C}_4\text{H}_9)][\text{N}(\text{SO}_2\text{CF}_3)_2]$.

DECLARATION

No portion of the work referred to in this thesis has been submitted in support of an application for another degree or qualification of this or any other institute of learning.

NOTES ON COPYRIGHT

Copyright in text of this thesis rests with the Author. Copies (by any process) either in full, or of extracts, may be made only in accordance with instructions given by the Author and lodged in the John Rylands University Library of Manchester. Details may be obtained from the Librarian. This page must form part of any such copies made. Further copies (by any process) of copies made in accordance with such instructions may not be made without the permission (in writing) of the Author.

The ownership of any intellectual property rights which may be described in this thesis is vested in BNFL, subject to any prior agreement to the contrary, and may not be made available for use by third parties without the written permission of BNFL, which will prescribe the terms and conditions of any such agreement.

Further information on the conditions under which disclosures and exploitation may take place is available from the Head of Department of the Department of Chemistry. Any such disclosure or exploitation shall be discussed and agreed beforehand with BNFL

DEDICATION

For Mum and Dad

ACKNOWLEDGEMENTS

The Author would like to thank the following people without whom this thesis could not have been written:

I would like to thank my supervisors, Dr David Collison and Dr Iain May, for all their help and support during this project. Thank you for making (and/or finding) time for all the useful discussions and for all the help and advice when things were not going well.

Dr Vladimir Volkovich for all the invaluable help, advice and support with this project and especially for knowing just about everything and saving me from having to spend time in the library. Thank you for also for teaching me good laboratory practice *e.g.* whenever unsure as to whether a chemical is flammable just set fire to a small sample (in a fumehood for safety of course).

Dr. Madeleine Helliwell, Dr Jim Raftery, Dr Andy Gaunt and Dr Clint Sharrad for the crystallography and Dr Helen Steele for all the theoretical calculations. Thanks also to Martin Jennings and colleagues for the microanalysis results

Dr John Charnock for the useful discussions regarding X-ray absorption spectroscopy.

To all those people at BNFL involved with this project and including BNFL for providing funding for this work.

Professor Francis Livens for all the useful discussions, advice and support over the past few years. A big thank you for stopping me doing a PhD in quantum dot chemistry (what was I thinking?) with the magic phrase: 'do you want to play with radioactive stuff?'. Thanks also to Dr Nick 'people are only nice to me when they want something' Bryan and Dr Steve 'scary but nice' Faulkner for advice and useful discussions.

Dr Mark 'don't ever touch my vac line' Sarsfield and Dr Simon Pope for their expertise in the labs and general help.

All the past and present members of the radiochemistry group for making the past few years seem like fun rather than work. A big thank you to all the radiochemistry/inorganic chemistry football players for keeping me healthy (who will stop you losing to the organic chemists once I leave?).

Special thanks to Andrew Heydon, Laura Butchins, Rebeca Alvarez, Clint Sharrad and Nick Bryan for proof reading thesis chapters at short notice.

A big thank you to my Family for all their love, support and encouragement. Without you I could not have done this.

Thanks to all my friends for making the past few years fun, especially Mark, Sarah, Andy S., Dom, Liv, Gordon, Andy G., Alison, Rose, Ben B-P, Ben D., Rebecca A, Steve, Leigh, Mandy, Anna, Anne, Ranjit, Roy, Manue, Jo, Haji, and Brice for generally being there and making the past few years a laugh.

Thanks also to Professor Ken Seddon, Dr Will Pitner and Dr Tona Bradley for all the useful discussions and for showing me and Vlad the sights and sounds of Belfast

Last but not least, a big thank you to God for allowing me to have this opportunity in life.

PREFACE

The Author graduated from The University of Leicester with a 2.1 Honours degree in Chemistry in July 1999.

Between September 2000 to September 2003 he has been working on *f*-elements in ionic liquids: a synthetic, spectroscopic and electrochemical study towards a Ph.D.

These studies have been undertaken under the joint supervision of Dr Iain May and Dr David Collison, at the Department of Chemistry, The University of Manchester.

LIST OF ABBREVIATIONS

Ln	Lanthanide
An	Actinide
FP	Fission products
LTIL	Low Temperature Ionic Liquid
RTIL	Room Temperature Ionic Liquid
Purex	Plutonium Uranium Extraction Process
THORP	Thermal Oxide Reprocessing Plant
TBP	Tri- <i>n</i> -butylphosphate
OK	Odourless kerosene
TFSI	bis(trifluoromethanesulfonyl)amide, $[N(SO_2CF_3)_2]^+$
Me	Methyl
Et	Ethyl
ⁿBu	<i>n</i> -Butyl
ⁿHex	<i>n</i> -Hexyl
Ph	Phenyl
MeCN	Acetonitrile
Fc	Ferrocene,
DMSO	dimethylsulfoxide
OTs	<i>p</i> -toluenesulfonate
RIAR	Russian Institute of Atomic Reactors
ANL	Argonne National Laboratory
LANL	Los Alamos National Laboratory
BNFL	British Nuclear Fuels Ltd

QUILL	Queens University Ionic Liquids Laboratories
CRR	Centre for Radiochemistry Research
ESRF	European Synchrotron Radiation Facility
SRS	Synchrotron Radiation Source
XAS	X-Ray Absorption Spectroscopy
XANES	X-ray Absorption Near Edge Structure
EXAFS	Extended X-Ray Absorption Fine Structure
ATR	Attenuated Total Reflectance
IR	Infra Red
TGA	Thermogravimetric Analysis
DFT	Density Functional Theory
CV	Cyclic Voltammetry
LSV	Linear Scan Voltammetry
CA	Chronoamperometry
QRE	Quasi-Reference Electrode
GC	Glassy Carbon
SHE	Standard Hydrogen Electrode
SCE	Saturated Calomel Electrode
D	Diffusion Coefficient
m	Minute
h	Hour
d	Day
y	Year

CHAPTER 1

INTRODUCTION

1.1 General introduction to *f*-element chemistry

The *f*-block elements are split into 14 lanthanide elements (and La) and 14 actinide elements (and Ac). The lanthanides comprise the series Ce-Lu ($z = 58 - 71$) and correspond to the filling of the $4f$ electronic orbitals. The lanthanides were first identified from the minerals Yttria and Ceria. Yttria was first isolated by J. Gadolin in 1794 while Ceria was first isolated by M. H. Klaproth in 1803, and independently by J. J. Berzelius and W. Hisinger at the same time. Both Klaproth and Berzelius and Hisinger discovered Ceria from the heavy mineral first described by A. F. Cronstedt in 1751.^{1,2} Initially Yttria was thought to be an oxide of a single new element. However, subsequent work showed it to consist of 10 new elements – Y, Sc, Gd, Tb, Dy, Ho, Er, Tm, Yb and Lu. Similarly Ceria was shown to consist of the oxides of La, Ce, Pr, Nd, Sm and Eu (see Table 1.1.1). The final lanthanide, radioactive Pm, was discovered in 1947 by J. A. Marinsky, L. E. Glendenin and C. D. Coryell from ^{235}U fission products.^{1,2}

The actinides are the series of elements from Th-Lr ($z = 90-103$) formally corresponding to the filling of the $5f$ orbitals. U was first isolated from the mineral pitchblende in 1789 by M. H. Klaproth.¹⁻³ In 1828 J. J. Berzelius identified Th from thorite, whilst in 1913, Pa was identified from the ^{238}U decay products by K. Fajans and O. Gohring.¹⁻³ The rest of the actinides were synthesised from 1940 onwards (see Table 1.1). All of the actinides elements exhibit radioactive decay because of their nuclear instabilities.^{2,3}

Lanthanide	Electronic configuration	Discovery	Actinide	Electronic configuration	Discovery
La	$[\text{Xe}]5d^1 6s^2$	1839	Ac	$[\text{Rn}]6d^1 7s^2$	1899
Ce	$[\text{Xe}]4f^1 5d^1 6s^2$	1839	Th	$[\text{Rn}]6d^2 7s^2$	1828
Pr	$[\text{Xe}]4f^3 6s^2$	1885	Pa	$[\text{Rn}]5f^2 6d^1 7s^2$	1913
Nd	$[\text{Xe}]4f^4 6s^2$	1885	U	$[\text{Rn}]5f^3 6d^1 7s^2$	1789
Pm	$[\text{Xe}]4f^5 6s^2$	1947	Np	$[\text{Rn}]5f^4 6d^1 7s^2$	1940
Sm	$[\text{Xe}]4f^6 6s^2$	1879	Pu	$[\text{Rn}]5f^6 7s^2$	1940
Eu	$[\text{Xe}]4f^7 6s^2$	1901	Am	$[\text{Rn}]5f^7 7s^2$	1944
Gd	$[\text{Xe}]4f^7 5d^1 6s^2$	1880	Cm	$[\text{Rn}]5f^7 6d^1 7s^2$	1944
Tb	$[\text{Xe}]4f^9 6s^2$	1843	Bk	$[\text{Rn}]5f^9 7s^2$	1949
Dy	$[\text{Xe}]4f^{10} 6s^2$	1886	Cf	$[\text{Rn}]5f^{10} 7s^2$	1950
Ho	$[\text{Xe}]4f^{11} 6s^2$	1879	Es	$[\text{Rn}]5f^{11} 7s^2$	1952
Er	$[\text{Xe}]4f^{12} 6s^2$	1843	Fm	$[\text{Rn}]5f^{12} 7s^2$	1952
Tm	$[\text{Xe}]4f^{13} 6s^2$	1879	Md	$[\text{Rn}]5f^{13} 7s^2$	1955
Yb	$[\text{Xe}]4f^{14} 6s^2$	1878	No	$[\text{Rn}]5f^{14} 7s^2$	1965
Lu	$[\text{Xe}]4f^{14} 5d^1 6s^2$	1907	Lr	$[\text{Rn}]5f^{14} 6d^1 7s^2$	1961-1971

Table 1.1.1: Electronic configurations and discovery dates of the *f*-elements

The physical and chemical properties of the lanthanides are determined largely by the $4f$ orbitals. In general, the electrons in the f -orbitals are poorly shielding and pulled in closer to the nucleus compared to the electrons in the $6s$ and $5d$ orbitals. As a result overlap between f -orbitals and ligand orbitals is not great and lanthanides exhibit hard Lewis acid properties, generally forming compounds with hard bases such as F^- , OH^- and H_2O .^{1,2} Thus bonding is dominated by electrostatic interactions. Although soft ligands such as P, S can bond to the lanthanides, this is usually only accomplished in the absence of water or other hard ligands.^{1,2}

Going across the series (Ce-Lu) the ionic radii of the lanthanides display a gradual reduction with increasing atomic number.^{1,2} Although increase in protons is balanced by the addition of an f -electron, the poorly shielding nature of the orbitals means that the effective nuclear charge increases causing a contraction of the atom/ion across the series *i.e.* 'lanthanide contraction'.

The chemistry of the lanthanides is largely dominated by the trivalent oxidation state. However, compounds of the tetravalent and divalent state are also known.^{1,2} Compounds of Nd, Dy, Tb and Pr in the tetravalent state are generally limited to the solid state.^{1,2} The most extensive chemistry in the tetravalent state is that of Ce(IV) and a number of compounds are known. Nd, Sm, Eu, Dy, Tm and Yb can form compounds in the divalent state, although these are again generally confined to the solid state. In aqueous solution both Ce(IV) and Eu(II) are stable, but are very strong oxidising and reducing agents, respectively. Sm(II) is known to be stable in organic solvents. It should be noted that

although compounds of the divalent and tetravalent oxidation states are known, the trivalent oxidation state is still the most common oxidation state for lanthanides.

The large ionic radii and largely electrostatic bonding interactions of the lanthanides mean that they generally form complexes/compounds with high coordination numbers, usually between 6-12 (*e.g.* 7 coordinate $[\text{Dy}(\text{Me}_3\text{CC}(\text{O})\text{CHC}(\text{O}^-)\text{CMe}_3)_3(\text{H}_2\text{O})]$, 8 coordinate SmF_3 and 9 coordinate $[\text{Ln}(\text{H}_2\text{O})_9]^{3+}$).¹ As the radius drops across the series due to the lanthanide contraction, there is often a concomitant drop in coordination number. In water the $[\text{Ln}(\text{H}_2\text{O})_9]^{3+}$ ion is usually formed^{1,4} for the early lanthanides, however, due to lanthanide contraction the late lanthanides usually form the $[\text{Ln}(\text{H}_2\text{O})_{7-8}]^{3+}$ ion.⁴ All of the lanthanides are very electropositive and this is reflected in their electrochemical behaviour and in general the reduction of the lanthanide ions to the zerovalent state is difficult as observed from the standard reduction potentials (Table 1.1.2)

Standard reduction potentials / V (vs. SHE)				
	Ln(III)/Ln(0)	Ln(II)/Ln(0)	Ln(III)/Ln(II)	Ln(IV)/Ln(III)
La	-2.379	-	-	-
Ce	-2.336	-	-	1.72
Pr	-2.353	-	-3.1	3.2
Nd	-2.323	-2.1	-2.7	-
Pm	-2.30	-2.2	-2.6	-
Sm	-2.304	-2.68	-1.55	-
Eu	-1.991	-2.812	-0.36	-
Gd	-2.279	-	-	-
Tb	-2.28	-	-	3.1
Dy	-2.295	-2.2	-2.6	-
Ho	-2.33	-2.1	-2.8	-
Er	-2.331	-2.0	-3.0	-
Tm	-2.319	-2.4	-2.2	-
Yb	-2.19	-2.76	-1.05	-
Lu	-1.96	-	-	-

Table 1.1.2: Standard reduction potentials of the lanthanides⁵

The chemistry of the actinides is more complex than that observed for the lanthanides due to the higher number of accessible oxidation states (see Table 1.1.3). The chemistry of the early actinides (Th, Pa) is dominated by the f^0 configuration and although for both Th and Pa other oxidation states are known,^{1,3} the bulk of the chemistry is restricted to the tetravalent (Th) and pentavalent (Pa) oxidation states corresponding to removal of all the f -electrons. The mid actinides (U, Np, Pu and Am) show a range of accessible oxidation states, both in solution and in the solid state, whilst for the late actinides (Cm-Lr) the trivalent state is predominantly most stable and the chemistry is similar to that observed for the lanthanides. In general the greater radial extension of the $5f$ compared to the $4f$ orbitals results in higher orbital energies and greater availability of $5f$ orbitals for covalent bonding. However, the actinides still generally act as hard Lewis acids preferentially coordinating to hard anions *via* electrostatic interactions.¹⁻³ Only Th and U have long enough lived radioisotopes to undertake synthetic chemistry in standard chemical laboratories, although it is possible to undertake Np and Pu chemistry at specialist facilities. The short half lives of the isotopes of the other actinides restrict the chemistry that can be undertaken with these elements.

Like the lanthanides, high coordination numbers are often observed for the actinide cations, typically between 6-12 (*e.g.* 6 coordinate $[\text{UCl}_6]^{2-}$ and 12 coordinate $[\text{Pu}(\text{NO}_3)_6]^{2-}$).^{1,3} The coordination and redox chemistry of the mid actinides is further complicated by the formation of linear, dioxo, actinyl ions, $\{\text{AnO}_2\}^{x+}$ (where An = U, Np, Pu or Am and $x = 1$ or 2) in the +V and +VI oxidation states. The short, multiple, $\text{An}=\text{O}$ actinyl bonds are formed from overlap of the $5f$ and $6d$ orbitals on the actinide and

the $2p$ orbitals on oxygen.⁶ For U and Np the most stable species in aqueous solution are the uranyl, $\{U^{(VI)}O_2\}^{2+}$, and neptunyl $\{Np^{(V)}O_2\}^+$ ions, respectively.¹⁻³ As a result of the axial orientation of the oxygens for both these ions (and indeed other actinyl ions) additional ligand coordination is usually restricted to the equatorial plane with coordination numbers ranging between 4 and 6 within the plane.¹⁻³

In contrast to the electrochemical behaviour of the lanthanides, the electrochemistry of the actinides can be further complicated for the series U-Am due to the reductions of the actinyl ions introducing oxygen into the system as the O^{2-} ion. This can be problematic in inert atmosphere systems where the generation of low oxidation states is required. However, the formal reduction potential for the $An(III)/An(0)$ reductions⁵ are generally comparable to those observed for the lanthanides (see Table 1.1.3).

Common		Standard reduction potentials / V		
Oxidation states		(vs. SHE)		
		An(II)/An(0)	An(III)/An(0)	An(IV)/An(0)
Ac	III	-	-2.20	-
Th	III, IV	-	-	-1.899
Pa	III, IV, V	-	-1.34	-1.49
U	III, IV, V, VI	-	-1.789	-
Np	III, IV, V , VI, VII	-	-1.856	-
Pu	III, IV , V, VI, VII	-	-2.031	-
Am	II, III , IV, V, VI,	-1.9	-2.048	-
Cm	III , IV	-	-2.04	-
Bk	III , IV	-1.6	-	-
Cf	II, III , IV	-2.12	-1.94	-
Es	II, III	-2.23	-1.91	-
Fm	II, III	-2.30	-1.89	-
Md	II, III	-2.40	-1.65	-
No	II , III	-2.50	-1.20	-
Lr	III	-	-1.96	-

Table 1.1.3: Common oxidation states and standard reduction potentials of the actinides.⁵ Oxidation states shown in bold indicate most stable states

1.2 Actinide radiochemistry, nuclear power and the Purex process

As stated previously, one of the most important properties of the actinides is that they all exhibit radioactive decay. Although hazardous to human health this property has useful advantages. The hazards due to radioactivity are dependent on the type of radiation. Both α and β emitters present serious hazards if ingested or inhaled, whilst γ -radiation presents a serious external hazard. The energies of emitted radiation for the actinides investigated in this thesis (^{232}Th , Chapter 5, ^{238}U , Chapter 6 and ^{237}Np , Chapter 7) are given in Table 1.2.1 with the radiation energies of selected common Pu isotopes also given for comparison.^{2,3} For ^{232}Th and ^{238}U , the principle radiation is low energy α , whereas for ^{237}Np the energy of the α radiation is higher. For all three isotopes daughter product decay also results in significant γ -radiation release. This is particularly important for ^{237}Np which decays to give ^{233}Pa , a very short half-life β and γ emitter.

One of the most significant non-military uses of this radioactive decay is in energy production. During nuclear fission, the process of an unstable nucleus splitting into two smaller nuclei with greater stability compared to the parent nucleus, neutrons can be released as well as large quantities of energy in the form of heat.⁷ The released neutrons can then induce fission in further nuclei and with the correct amount of fissile material present the reaction can be self-sustaining.⁷ Both ^{235}U and ^{239}Pu are capable of spontaneous nuclear fission.

The heat energy released during the nuclear fission process can be converted to electrical energy in a power plant,⁸ and the first commercial nuclear reactor for power generation was commissioned in 1956 at Calder Hall, Sellafield, UK.^{2,3} Since then a number of different reactors have been designed and constructed in several countries and in 2002, 31 countries worldwide were operating over 440 nuclear reactors for the purposes of energy production totalling 16 % of the world electricity supply.⁹ Although nuclear power generation has advantages compared to fossil fuel burning the major disadvantage is the highly radioactive waste that is generated.

Different types of nuclear reactors use different types of fuel *e.g.* natural U metal, ^{235}U enriched UO_2 pellets or depleted UO_2 and $^{239}\text{PuO}_2$ mixed oxide (MOX).^{7,8} During the nuclear reaction, fission products (FP) from radioactive decay of ^{235}U and ^{239}Pu accumulate within the fuel. As many of these FP can absorb neutrons they can stop the chain reaction before all the ^{235}U and ^{239}Pu has been consumed. The irradiated fuel elements must therefore be periodically removed.^{7,8} For U based fuels there are still significant quantities of fissile ^{235}U and/or ^{239}Pu remaining and these materials can potentially be recycled in a procedure known as nuclear fuel reprocessing. This is usually accomplished by moving the highly radioactive fuel elements (by remote control) from the reactor and storing in large 'cooling ponds' under water to allow the short lived radioisotopes (*e.g.* ^{131}I , $t_{1/2} = 8 \text{ d.}$) to decay.^{7,8}

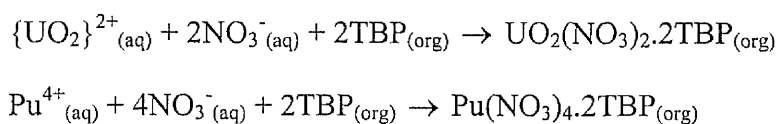
Actinide	Half-life	Radiation type and energy (MeV)
^{232}Th	$1.40 \times 10^{10} \text{ y}$	α , 4.016 α , 3.957
^{235}U	$7.037 \times 10^8 \text{ y}$	α , 4.397 α , 4.367 γ , 0.186
^{238}U	$4.468 \times 10^9 \text{ y}$	α , 4.196 α , 4.149
^{237}Np	$2.14 \times 10^6 \text{ y}$	α , 4.788 α , 4.770 γ , 0.086
^{239}Pu	$2.41 \times 10^4 \text{ y}$	α , 5.155 α , 5.143 γ , 0.129
^{240}Pu	$6.56 \times 10^3 \text{ y}$	α , 5.168 α , 5.123

Table 1.2.1: Half-lives and radiation energies of selected actinides

In the UK, nuclear fuel reprocessing is accomplished using a solvent extraction process generically known as the Purex process (Plutonium URanium EXtraction process). Two plants currently operate this process in the UK at the BNFL Sellafield site in Cumbria, these are B205 Magnox plant and THORP (Thermal Oxide Reprocessing Plant).⁸

Although the two plants operate slightly different processes because of the types of fuel that are reprocessed in each plant (U metal at B205 and oxide fuel at THORP), the main extraction process is the same for both plants.

A schematic of the Purex process is given in Figure 1.2.1.^{7,8} Initial processes are required to get the nuclear fuel into a state where it can be dissolved into nitric acid. For metallic fuel, this requires the magnesium casing to be mechanically removed, whilst the oxide fuel must be chopped into pieces prior to dissolution. In the Purex process the aqueous nitric acid phase containing the dissolved U, Pu and FP is mixed with an organic phase containing the extractant tri-*n*-butylphosphate in odourless kerosene (30 % TBP/OK). TBP is a neutral donor ligand which extracts metal ions in the presence of anions (*i.e.* NO₃⁻). Both U and Pu extract well with TBP to form the following neutral complexes:



The distribution of the U and Pu between the two phases is dependent on the nitrate and TBP concentrations, as well as temperature and phase volumes. Conditions can be controlled largely to exclude FP and transplutonium actinide extraction. Reduction of Pu(IV) to inextractable Pu(III) facilitates U/Pu separation.

Although the Purex process seems ideal as a reprocessing method, it does have a number of significant problems. Firstly during the nitric acid dissolution stage a number of volatile fission products are formed including ³H₂, ¹⁴CO, ¹⁴CO₂, ⁸⁵Kr, ¹²⁹I₂.⁸ Additionally, insoluble complexes of Ru, Rh, Tc, Pa and Mo can also be formed.⁸ Procedures to remove/collect these solid/gaseous compounds from a solution based process must be in place. Thermal, chemical and radiolytic degradation products of TBP (dibutylphosphoric

acid and monobutylphosphoric acid),^{7,8} can form unwanted complexes with U and Pu or insoluble precipitates. In addition to this, TBP can also co-extract Np and Tc,¹⁰⁻¹⁶ which can interfere with the Pu reduction step as well as the subsequent formation of pure UO_2 fuel.⁸ Finally, a large quantity of aqueous and organic radioactive waste is produced from the several washing/extraction steps. Therefore, there are good reasons to consider alternative fuel processing technologies.

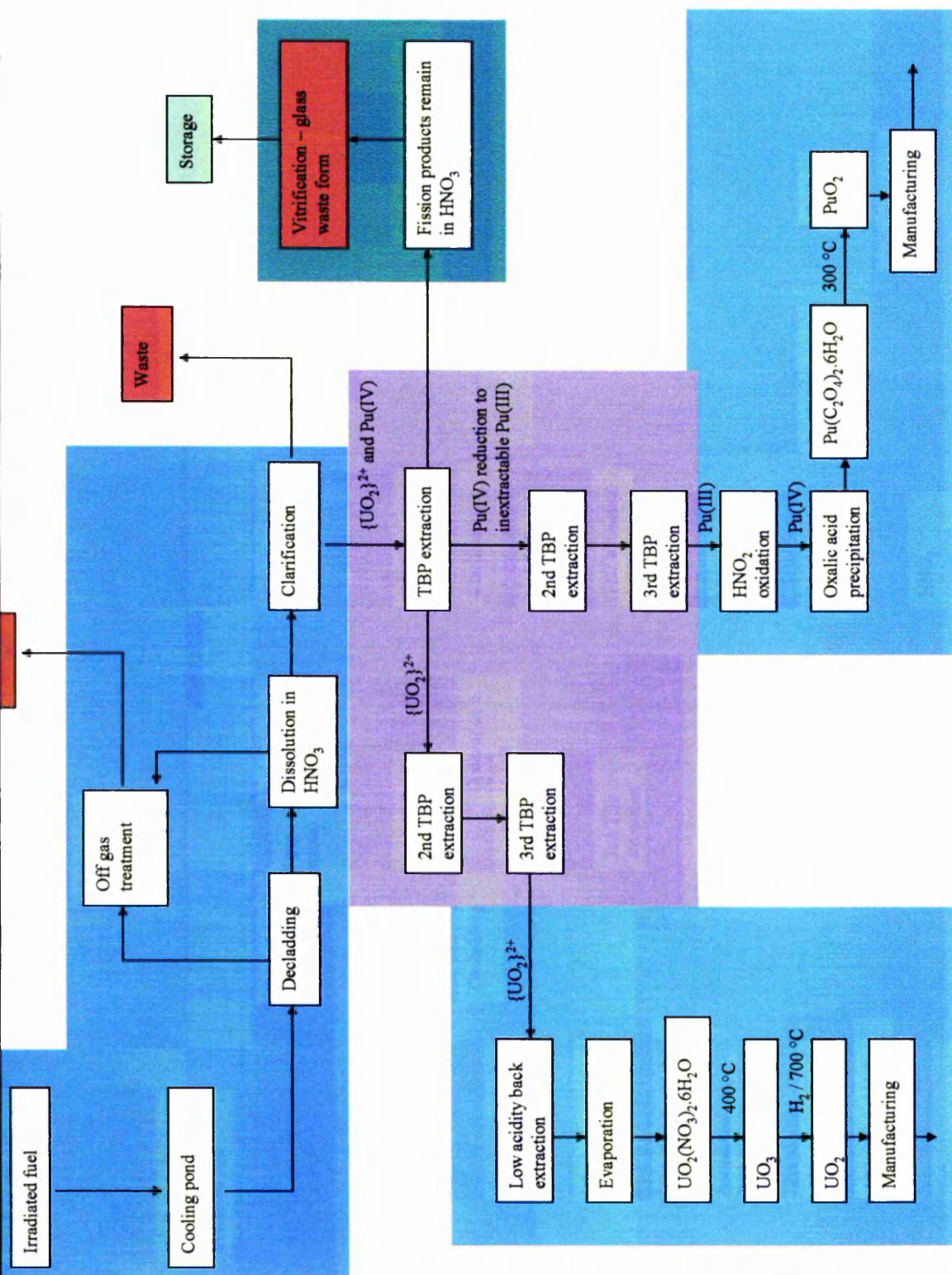


Figure 1.2.1: Simplified schematic of the Purex process. TBP = tri-*n*-butyl phosphate

1.3 High temperature molten salts reprocessing

There are several reasons why it may be advantageous to develop alternative technologies to reprocess irradiated nuclear fuel (see Section 1.2). One such method involves moving away from a solvent extraction process to one based on electrochemistry with the generation of pure actinide metals by electrolysis. This can be accomplished in high temperature molten salts¹⁷⁻²¹ (e.g. equimolar NaCl:KCl, 650 °C) due to the wide electrochemical windows available, and such a process has been previously demonstrated on a near industrial scale at RIAR (Russian Institute of Atomic Reactors)²² and at Argonne National Laboratory (ANL).^{23,24}

In the irradiated nuclear fuel molten salt electrochemical refiner developed at RIAR, the decladded fuel is reacted with Cl₂ gas to form soluble species (U(VI) oxychlorides and Pu(IV) chlorides), with the U(VI) oxychlorides electrochemically reduced to UO₂ and removed. By then reacting the solution with O₂ gas Pu(IV) can be precipitated as PuO₂. In the ANL process (see Figure 1.3.1) the irradiated fuel is chopped into small pieces which are then placed into a perforated steel basket (anode) and lowered into the molten salt, LiCl-KCl eutectic at 500 °C. The fuel elements are then dissolved electrochemically and U is transported through the electrolyte solution to a steel cathode where it is reduced to U metal. Pu, Am, Np, Cm and small traces of U are then electrochemically transported to a molten Cd cathode suspended in a ceramic basket in the electrolyte solution where they are reduced to the zerovalent state. The rest of the fission products are collected at a Cd pool on the bottom of the refiner by the chemical formation of intermetallic alloys.

Although molten salt nuclear fuel processing has some advantages over the Purex process, overcoming a number of co-extraction problems with reduced waste volumes generated, it is not without its drawbacks. The high temperatures of operation introduce significant problems in terms of plant design. Additionally, the use of highly reactive chemicals (Cl_2 , O_2) introduces significant corrosion problems to the plant machinery.²⁵ Clearly a switch to lower temperatures of operation would remove some of these problems. Previously Osteryoung *et al.*^{26,27} have shown that AlX_3/MX mixtures (where X = halide anion and M = alkali metal cation) have similar electrochemical properties to molten salts, though with lower working temperatures in the range of 150 – 200 °C (e.g. equimolar $\text{AlCl}_3/\text{NaCl}$ mixture has a melting point of 175 °C).

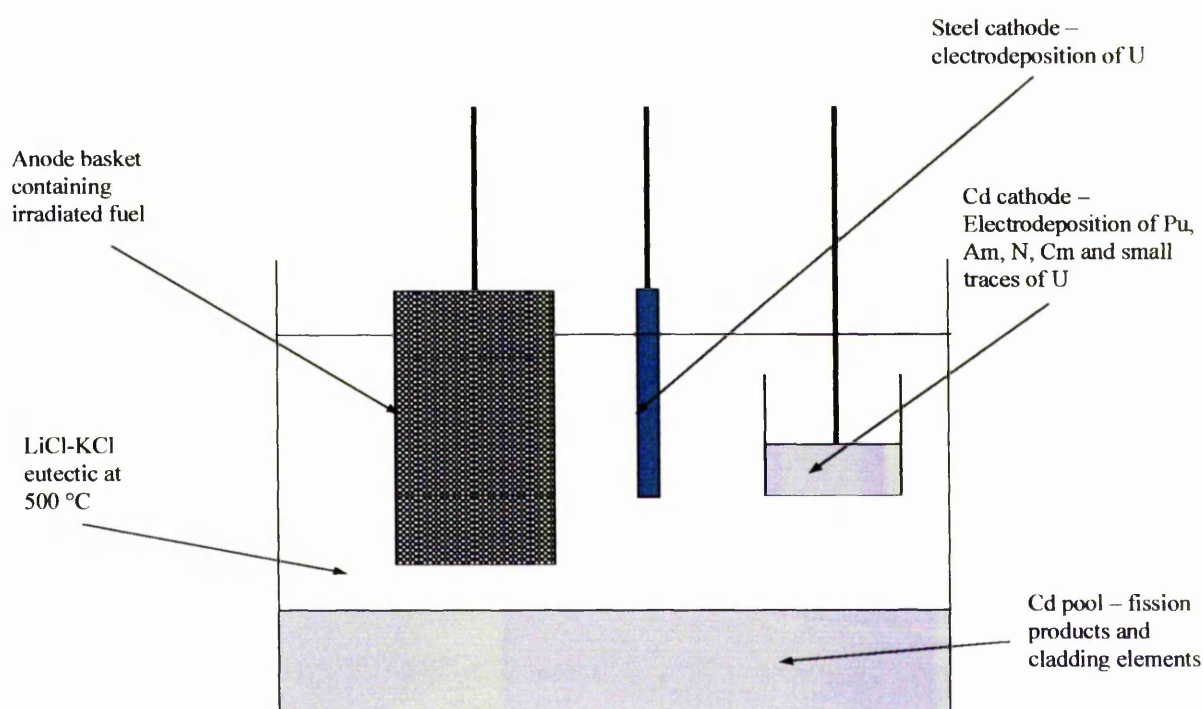


Figure 1.3.1: Schematic representation of ANL irradiated nuclear fuel molten salt electrochemical refiner

1.4 Low temperature ionic liquids (LTILs)

Low temperature ionic liquids (LTILs)* are liquids composed solely of anions and cations with much lower melting points and liquidus ranges than conventional high temperature molten salts. The first known examples of LTILs were reported by Walden in 1914 and were room temperature melts of tetraalkylammonium nitrate salts²⁸ for example $[\text{H}_3\text{NET}][\text{NO}_3]$ (m. pt. 12 °C). However, it was not until the mid 20th century that LTILs were first investigated for their potential as replacements for molten salts²⁶ and traditional organic solvents.

LTILs have a number of physical properties that make them attractive replacements for traditional organic solvents, many are non-flammable and form LTILs with low or negligible vapour pressures.²⁶ The physical and chemical properties of the LTIL can be controlled by the choice of cation and anion. Properties such as melting point, viscosity and conductivity^{26,29-31} can be changed by changing the cation and/or anion, with the choice of weakly interacting and low symmetry cation/anions leading to lower melting points and viscosities. The ionic nature of these solvents means that they can also act as electrolytes and thus have potential uses in electrochemical applications. From an electrochemical perspective the choice of the cation and anion are crucial as the potential window is related to the electrochemical oxidation and reduction of the cation/anion.³²

* Although no universally accepted definition of an ionic liquid exists, room temperature ionic liquids are assumed to have a melting point below 100 °C. Within this thesis, low temperature ionic liquids are defined as salts with a melting point below 200 °C.

LTILs have a number of possible applications ranging from organic/inorganic synthesis, metal deposition, battery electrolytes, phase transfer and separations *etc.* Recent reviews by K. R. Seddon,³³ T. Welton,²⁹ P. Wasserchied,³⁰ R. D. Rogers³⁴ and J. F. Brennecke³⁵ discuss the applications and properties of LTILs in more depth. Examples of LTILs currently being studied for potential industrial applications are shown in Table 1.4.1.

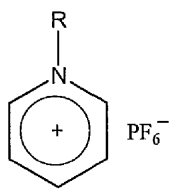
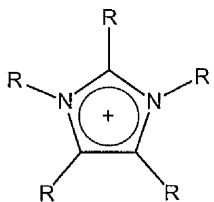
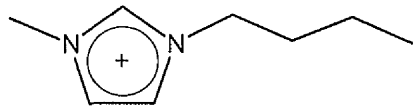
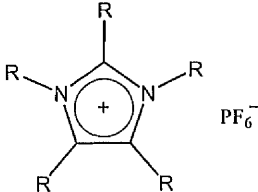
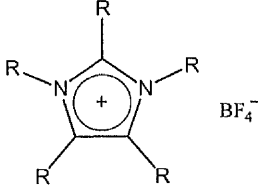
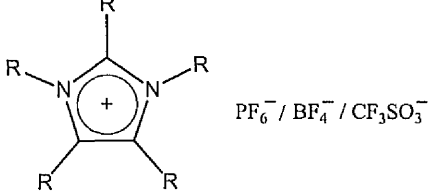
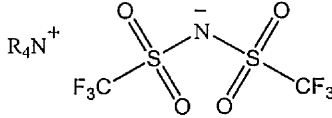
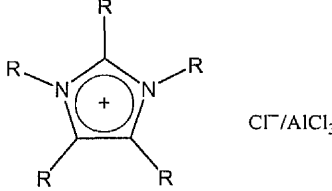
LTIL	Application	Reference
  PF_6^- $\text{Cl}^-/\text{AlCl}_3$ $[\text{R}_4\text{N}][\text{BF}_4]$	Organic synthesis	29, 36
 BF_4^-	Transition metal catalysis	30
 PF_6^-	Liquid-liquid extractions	31
 BF_4^-	CO_2 capture	37-39
 $\text{PF}_6^- / \text{BF}_4^- / \text{CF}_3\text{SO}_3^-$	Battery electrolytes	40
 R_4N^+	Cu deposition	41
 $\text{Cl}^-/\text{AlCl}_3$	Metal and semiconductor deposition	42

Table 1.4.1: Generic examples of LTILs reported in the literature and their applications

From an electrochemical perspective, initially LTIL research focussed on imidazolium chloroaluminate based LTILs as a replacement solvent for LiCl/KCl eutectics used as electrolytes in thermal batteries.²⁶ The observation of the Li(I)/Li(0) reduction in these melts²⁶ suggests the possibility of their use in the nuclear fuels industry as the Li(I)/Li(0) reduction is known to have a more negative standard reduction potential than the Pu(III)/Pu(0) and U(III)/U(0) reduction potentials (-3.04 V for Li(I)/Li(0) vs. -2.031 V for Pu(III)/Pu(0) and -1.789 V for U(III)/U(0) all vs. SHE).⁵

Although the imidazolium chloroaluminate systems are extremely hygroscopic and must be handled under an inert atmosphere,^{29,30} a number of air and moisture stable LTILs have been synthesised with comparable electrochemical windows to the chloroaluminate systems^{41,43-50} (see Table 1.4.2 for selected examples). It should be noted that direct comparison of electrochemical windows between LTILs reported by different research groups is extremely difficult due to the use of quasi reference electrodes making comparison of absolute potentials difficult. Recently, Bond *et al.* have investigated the problems associated with the quasi reference electrode and have suggested that transition metal cyclopentadienyl complexes be used to standardise potentials⁴⁷ as often used in traditional non-aqueous solvent electrochemistry, however, this is not yet standard laboratory practice.

LTIL	Electrochemical window / V	reference
1-ethyl-3-methylimidazolium chloride/ AlCl_3	4	42
1-ethyl-3-methylimidazolium ethylsulfate	4.25	43
1-butyl-3-methylimidazolium tetrafluoroborate	4 – 6.1 (dependent on electrode material)	45
1-butyl-3-methylimidazolium hexafluorophosphate	3.1 – 7.1 (dependent on electrode material)	42, 45-47
triethylhexylammonium bis(trifluoromethanesulfonyl)amide	4.5 – 5	48, 49
triethyloctylammonium bis(trifluoromethanesulfonyl)amide	5	48
trimethylbutylammonium bis(trifluoromethanesulfonyl)amide	5	46, 49
trimethylhexylammonium bis(trifluoromethanesulfonyl)amide	5.6	41

Table 1.4.2: Selected literature reports of LTIL electrochemical windows

The electrochemistry and chemistry of lanthanides has been investigated in a range of LTILs, *e.g.* Eu^{51} and La^{52} in 1-ethyl-3-methylimidazolium Cl/AlCl_3 , Eu in 1-butyl-3-methylimidazolium hexafluorophosphate,⁵³ Yb and Sm in *N*-butylpyridinium chloride,⁵⁴ and Yb in 1-ethyl-3-methylimidazolium Cl/AlCl_3 .⁵⁵

In Lewis basic *N*-butylpyridinium chloride, Gau and Sun's investigations using UV/vis/nIR spectroscopy and electrochemistry found that the Yb^{3+} cation exists as the $[\text{YbCl}_6]^{3-}$ species.⁵⁴ However upon electrochemical reduction, a new species, $[\text{YbCl}_5]^{3-}$, is formed. Similar studies in Lewis basic 1-ethyl-3-methylimidazolium Cl/AlCl_3 , found that Eu exists in solution as the $[\text{EuCl}_6]^{3-}$ ion.⁵¹ Their bulk electrolysis results indicated that Eu(II) is not stable in this system and spontaneously oxidises to Eu(III) presumably through reaction with oxygen or protons dissolved in the melt.⁵¹ In acidic solution, they found that the speciation of Eu changes and that Eu(II) was stable. However, the authors did not report on the reduction of the Eu ion to the zerovalent state in this LTIL. Billard *et al.* investigated Eu chemistry in 1-butyl-3-methylimidazolium hexafluorophosphate and showed that Eu(II) was stable in this system.⁵³ These results show that the coordination chemistry and electrochemistry of Eu (and Yb) is strongly dependent on the LTIL.

Perhaps the most interesting electrochemical study of a lanthanide was conducted by Ito *et al.* who observed the electrodeposition of La metal from 1-ethyl-3-methylimidazolium Cl/AlCl_3 .⁵² From this result it would appear that a similar La deposition reaction could presumably be observed in less air/moisture sensitive RTILs although an inert atmosphere regime would have to be maintained to prevent re-oxidation of La metal.

The possible application of lower temperature melts to supersede molten salt electrochemical actinide processing means that it is not surprising that actinide electrochemistry and speciation has also been studied in LTILs. Schoebrechts and Gilbert

have investigated the electrochemical conversion of Np(IV) to Np(III) using UV/vis/nIR and Raman spectroscopy in 1-butyl-3-methylimidazolium Cl/AlCl₃ melts.⁵⁶ Their results showed that in the basic melt, Np exists as the [NpCl₆]^{x-} species (where x = 2 and 3 for Np(IV) and Np(III), respectively), whilst in the acidic systems, the speciation and solubility of Np is dependent on the acidity of the melt as well as the stability of the Np(III) or Np(IV) species. However, the authors did not report on the reduction of Np to the zerovalent state in this LTIL.

Similarly the speciation and electrochemical behaviour of U in LTILs has also been studied. Choppin *et al.*⁵⁷ have studied the electrochemical reduction of U(IV) to U(III) in 1-ethyl-3-methylimidazolium Cl/AlCl₃ melts using EAS to show that [UCl₆]^{x-} (x = 2 or 3) species exist in the melt. Despite using exhaustive electrolysis the authors observed that the reduction of U(IV) to U(III) did not go to completion and proposed that this was due to the presence of oxide or protons in the melt.⁵⁷ However, the authors did not report on the electrochemical reduction of U to the zerovalent state in this melt. The speciation of U(V) in the same melt was investigated by Dai *et al.*⁵⁸ and UV/vis/nIR used to confirm the presence of [UCl₆]⁻. Finally, on dissolution of U(VI) as the {UO₂}²⁺ moiety, in 1-ethyl-3-methylimidazolium Cl/AlCl₃^{59,60} and 2,3-dimethyl-1-propylimidazolium Cl/AlCl₃⁶⁰ systems, spectroscopic evidence for the existence of [UO₂Cl₄]²⁻ has been obtained.^{59,60}

Researchers at Los Alamos National Laboratory (LANL) have been investigating the possible use of LTILs within the nuclear fuels industry, focussing on the application of

LTILs as replacement solvents for high temperature molten salts electrochemical processing.⁶¹⁻⁶⁴ Initially their research focussed on 1,2-dialkylimidazolium chloroaluminate based LTILs, and they have observed the electrochemical reduction of both Pu and U to the zerovalent state in such melts.^{61-63,64} However, the extremely hygroscopic nature of this melt means that an industrial scale up of any electrochemical process may be unfeasible due to the high costs of manufacturing plants to work under a very strictly controlled inert atmosphere. In addition, the high cost of manufacturing and transportation of this LTIL means industrially a process based on this LTIL may be unsuitable. More recently research has concentrated on quaternary alkylammonium and N-heterocycle based LTILs, which are air and moisture stable.^{63,64} These melts have wide electrochemical windows that are comparable to those observed for chloroaluminate systems, and the reduction of K(I) to the zerovalent state in $[\text{NMe}_2(i\text{-Pr})(n\text{-Pr})][\text{TFSI}]$ (where TFSI = bis(trifluoromethanesulfonyl)amide, $[\text{N}(\text{SO}_2\text{CF}_3)_2]^-$) suggests that these LTILs may be suitable for an electrochemical reprocessing of irradiated fuel.⁶⁴

In addition to the electrochemical separation of *f*-elements in LTILs, solvent extraction of *f*-elements into LTILs from aqueous solutions has also been investigated. Rogers and Visser have studied the extraction of Am^{3+} , Pu^{3+} , Th^{4+} and $\{\text{UO}_2\}^{2+}$ from nitric acid solution into 1-methyl-3-butylimidazolium hexafluorophosphate using TBP and octyl(phenyl)-*N,N*-diisobutylcarbamoylmethyl phosphine oxide (CMPO).⁶⁶ They showed that $\{\text{UO}_2\}^{2+}$ is the most strongly extracted with distribution ratios in the range of 10^2 , whilst both Pu^{3+} and Th^{4+} are less extractable (distribution ratios in the order of 10) and Am^{3+} is not extracted.⁶⁶ EXAFS and UV/vis/nIR studies of the $\{\text{UO}_2\}^{2+}$ complex formed

in this LTIL and in [1-methyl-3-butylimidazolium][TFSI] were inconclusive as to the speciation of the actinide cation in the LTIL phase.⁶⁷ Jensen *et al.* have also investigated the extraction of Eu^{3+} and Nd^{3+} from an aqueous $\text{HClO}_4/\text{NaClO}_4$ phase into 1-methyl-3-butylimidazolium TFSI with 1-(2-thienyl)-4,4,4-trifluoro-1,3-butanedione (Htta).⁶⁸ Using UV/vis and luminescence spectroscopies and EXAFS their results indicate that the Ln ion extracts into the LTIL phase as the $[\text{Ln}(\text{tta})_4]^-$ complex.⁶⁸ The solvent extraction of two FPs, Cs^+ and Sr^{2+} , from aqueous solution into LTILs using crown ethers has also been investigated by the research groups of Dia⁶⁹⁻⁷¹ and Jensen.^{72,73} Their results indicate that both these cations can be extracted into LTILs and that the structure of the LTIL cation and anion has an effect on the extraction process.⁶⁹⁻⁷³

1.5 British Nuclear Fuels Limited (BNFL) ionic liquids research programme

The ionic liquids research program at BNFL actively explored the possibility of using LTILs as a replacement for molten salts for an electrochemical separation process. Initial research, in collaboration with Prof K. R. Seddon, Queens University Ionic Liquids Laboratory (QUILL), Queens University of Belfast and The Centre for Radiochemistry Research (CRR), The University of Manchester, was focussed on the use of two LTILs, 1-ethyl-3-methylimidazolium chloride and 1-hexyl-3-methylimidazolium chloride. The electrochemical behaviour of U has been investigated within 1-hexyl-3-methylimidazolium chloride and the voltammetric reduction of U to the zerovalent state has been previously observed.⁷⁴⁻⁷⁶ However, the imidazolium based LTILs are problematic due to the U reduction occurring near the cathodic limit of the

electrochemical window. It is known from high temperature molten salts electrochemistry that the Pu(III)/Pu(0) reduction is more negative than that observed for U(III)/U(0),³² thus the electrochemical window of the LTIL needs to have a much more negative cathodic limit. Coupled to this problem is the extremely poor solubility of U and Lns within these melts (*ca.* 5 mol %)⁷⁵ indicating that imidazolium based LTILs are not suitable for application in a nuclear fuel electrochemical reprocessing technology.

Preliminary research conducted by the author and Dr V. A. Volkovich (CRR) collaborating with Prof. K. R. Seddon (QUILL) and Dr. W. Pitner (QUILL), identified a number of possible replacement LTILs. The electrochemical windows of the LTILs investigated are shown in Figure 1.5.1.

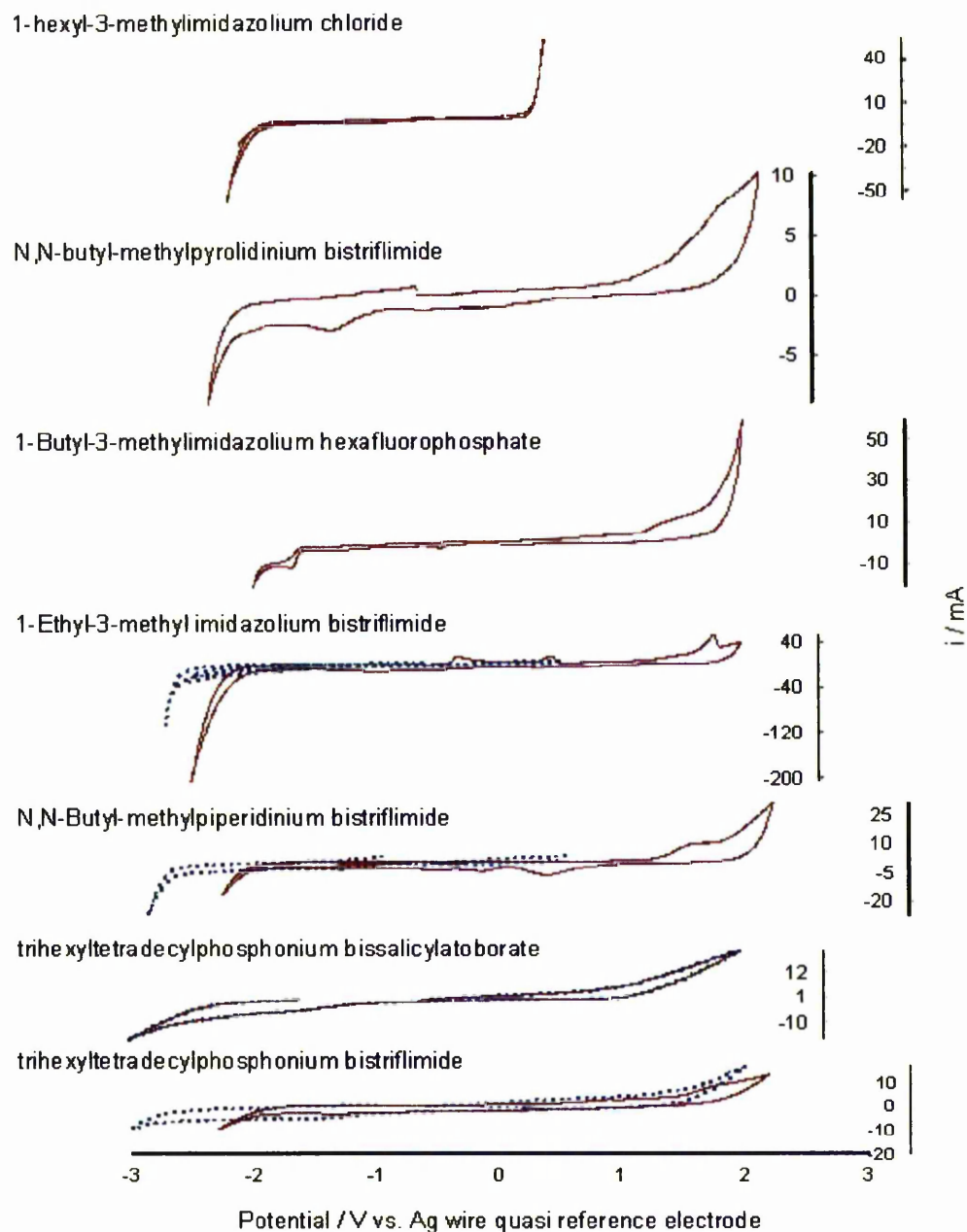


Figure 1.5.1: Electrochemical windows of various LTILs measured using cyclic voltammetry. Red trace = Pt working electrode, blue trace = glassy carbon working electrode. Peaks in the voltammograms within the working range are due to trace impurities in the bulk LTIL. Bistriflimide = TFSI anion

1.6 Aims and objectives

As shown in Figure 1.5.1, the electrochemical windows of trihexyltetradecylphosphonium bissalicylatoborate ($[\text{Hex}_3\text{P}(\text{C}_{14}\text{H}_{29})][\text{BOB}]$) and trihexyltetradecylphosphonium bis(trifluoromethanesulfonyl)amide ($[\text{Hex}_3\text{P}(\text{C}_{14}\text{H}_{29})][\text{TFSI}]$) would appear to have cathodic limits wide enough to observe the electrochemical reduction of U(III) and Pu(III) to the zerovalent state. However, although $[\text{Hex}_3\text{P}(\text{C}_{14}\text{H}_{29})][\text{TFSI}]$ is commercially available it is very viscous at room temperature whilst the use of $[\text{Hex}_3\text{P}(\text{C}_{14}\text{H}_{29})][\text{BOB}]$ is restricted by 3M-Corporation who hold the patent rights. Interestingly, LTILs such as $[\text{Me}_3\text{N}^n\text{Bu}][\text{TFSI}]$ ^{46,49} and $[\text{Me}_3\text{N}^n\text{Hex}][\text{TFSI}]$ ⁴¹ would also appear to have wide enough electrochemical windows and merit further investigation.

The overall objective of this PhD research is to assess the viability of ionic liquids as solvent systems for the electrochemical processing of spent nuclear fuel. In an attempt to meet this objective the following research is required:

1. Identification of an LTIL with a wide enough electrochemical window to observe the electrochemical reduction of U(III) and Pu(III) to the zerovalent state. Due to the negative $\text{An(III)}/\text{An(0)}$ potentials, the cathodic limit of the electrochemical window needs to be large. As quaternary group 15 cations appear to have the required cathodic limit RTILs based on these cations would be synthesised. Due to its weakly coordinating

properties, and hence ability to form low melting point salts, TFSI would be chosen as the anion.

2. After a suitable candidate RTIL has been identified the next step would be to determine whether U and Pu reduction to the metallic state can be achieved in the chosen melt. An incremental approach will be required, firstly studying non-radioactive electrochemistry in simple straightforward Ln systems before moving up in electrochemical complexity and radiological hazards through Th, U and finally Np (the latter as a Pu analogue). As very few studies have been undertaken on the behaviour of TFSI as ligand, relevant *f*-element-TFSI complexes will also have to be synthesised and characterised as part of the programme.

1.7 References

1. N. N. Greenwood, A. Earnshaw, *Chemistry of the Elements*, Butterworth-Heinemann, Oxford, 1984.
2. P. Scott, N. Kaltsoyanis, *The F Elements*, Oxford University Press, Oxford, 1999.
3. J. J. Katz, G. T. Seaborg, L. R. Morss, *The Chemistry of the Actinide Elements*, Chapman and Hall, New York, 1986.
4. H. C. Aspinall, *Chemistry of the F-Block Elements*, Gordon and Breach Science Publishers, The Netherlands, 2001.
5. *CRC Handbook of Chemistry and Physics*, Ed. D. R. Lide, CRC Press, Inc., USA, 1995.

6. R. G. Denning, *Struct. Bonding*, 1992, **79**, 215.
7. G. Choppin, J-O Liljenzin, J. Rydberg, *Radiochemistry and Nuclear Chemistry*, Butterworth-Heinmann, Oxford, 2002.
8. P. D. Wilson, *The Nuclear Fuel Cycle From Ore to Waste*, Oxford University Press, UK, 1996.
9. *International Atomic Energy Authority Report: Nuclear Technology Review - 2004*, GC(48)/INF/4, 2004.
10. K-W Kim, S-H Kim, K-C Song, E-H Lee, J-H Yoo, *J. Radioanal. Nucl. Chem.*, 2002, **253**, 3.
11. A. N. Mashkin, K. K. Korchenkin, N. A. Svetlakova, *Radiochemistry*, 2002, **44**, 34.
12. M. I. Konarev, V. S. Il'yashenko, S. M. Baranov, M. Ya. Zel'venskii, A. M. Rozen, *Radiokhimiya*, 1975, **17**, 759.
13. Y. Wada, K. Morimoto, H. Tomiyasu, *Radiochim. Acta*, 1996, **72**, 195.
14. I. May, R. J. Taylor, G. C. Brown, N. J. Hill, *Radiochim. Acta*, 1998, **83**, 135.
15. Z. Kolarik, P. Dressler, *Solv. Ex. Ion Exch.*, 1989, **7**, 625.
16. Z. Kolarik, G. Petrich, H. J. Bleyl, *Proc. Met.*, 1992, **7A**, 561.
17. J. L. Willit, W. E. Miller, J. E. Battles, *J. Nucl. Mater.*, 1992, **195**, 229.
18. I. Johnson, *J. Nucl. Mater.*, 1988, **154**, 169.
19. M. B. Brodsky, B. G. F. Carleson, *J. Inorg. Nucl. Chem.*, 1962, **24**, 1675.
20. I. Johnson, *J. Nucl. Mater.*, 1974, **51**, 163.
21. T. Nishimura, T. Koyama, M. Iizuka, H. Tanaka, *Prog. Nucl. Energy*, 1998, **32**, 381.

22. A. V. Bychkov, O. V. Skiba, *Chemical Separation Technology and Related Methods of Nuclear Fuel Waste Management*, Kluwer Academic Publishers, The Netherlands, 1999.
23. C. C. McPheeters, R. D. Pierce, T. P. Mulcahey, *Prog. Nucl. Energy*, 1997, **31**, 175.
24. J. J. Laidler, J. E. Battles, W. E. Miller, J. P. Ackerman, E. L. Carls, *Prog. Nucl. Energy*, 1997, **31**, 131.
25. Y-J Park, H-R Pyo, D-Y Kim, K-Y Jee, W-H Kim, *J. Kor. Nucl. Soc.*, 2000, **32**, 514.
26. *Ionic Liquids in Synthesis*, Eds. P. Wasserscheid, T. Welton, Wiley-VCH, Germany, 2003.
27. *Ionic Liquids*, Eds. D. Inman, D. G. Lovering, Plenum Press, New York, 1981.
28. P. Walden, *Bull. Acad. Imper. Sci.*, 1914, 1800.
29. T. Welton, *Chem. Rev.*, 1999, **99**, 2071.
30. P. Wasserscheid, W. Kiem, *Angew. Chem. Int. Ed.*, 2000, **39**, 3772.
31. A. E. Visser, R. P. Swatloski, W. M. Reichert, R. Mayton, S. Sheff, A. Wierzbicki, J. H. Davis, R. D. Rogers, *Chem. Commun.*, 2001, 135.
32. R. T. Carlin, J. Fuller, *Molten Salts From Fundamentals to Applications*, Ed. M. Guane-Escard, Kluwer Academic Publishers, The Netherlands, 2002.
33. M. J. Earle, K. R. Seddon, *Pure Appl. Chem.*, 2000, **72**, 1391.
34. A. E. Visser, R. P. Swatloski, M. W. Reichert, H. D. Willauer, J. G. Huddleston, R. D. Rogers, *NATO ASI Ser., Ser. 2*, 2003, **92** (Green Industrial Applications of Ionic Liquids), 137.

35. J. F. Brennecke, E. J. Maginn, *AIChE J.*, 2001, **47**, 2384.
36. C. J. Mathews, P. J. Smith, T. Welton, A. J. P. White, D. J. Williams, *Organometallics*, 2001, **20**, 3848.
37. L. A. Blanchard, D. Hancu, E. J. Beckman, J. F. Brenneke, *Nature*, 1999, **399**, 28.
38. L. A. Blanchard, Z. Gu, J. F. Brenneke, *J. Phys. Chem. B*, 2001, **105**, 2437.
39. E. D. Bates, R. D. Mayton, I. Ntai, J. H. Davis, *J. Am. Chem. Soc.*, 2002, **124**, 926.
40. J. Fuller, A. C. Breda, R. T. Carlin, *J. Electroanal. Chem.*, 1998, **459**, 29.
41. K. Murase, K. Nitta, T. Hirato, Y. Awakura, *J. Appl. Electrochem.*, 2001, **31**, 1089.
42. F. Endres, *ChemPhysChem*, 2002, **3**, 144.
43. J. D. Holbrey, W. M. Reichert, R. P. Swatloski, G. A. Broker, W. R. Pitner, K. R. Seddon, R. D. Rogers, *Green Chem.*, 2002, **4**, 407.
44. S. A. Forsyth, S. R. Batten, Q. Dai, D. R. MacFarlane, *Aust. J. Chem.*, 2004, **57**, 121.
45. P. A. Z. Suarez, V. M. Selbach, J. E. L. Dullius, S. Einloft, C. M. S. Piatnicki, D. S. Azambuja, R. F. de Souza, J. Dupont, *Electrochim. Acta*, 1997, **42**, 2533.
46. B. M. Quinn, Z. Ding, R. Moulton, A. J. Bard, *Langmuir*, 2002, **18**, 1734.
47. V. M. Hultgren, A. W. A. Mariotti, A. M. Bond, A. G. Wedd, *Anal. Chem.*, 2002, **74**, 3151.
48. J. Sun, M. Forsyth, D. R. MacFarlane, *J. Phys. Chem. B*, 1998, **102**, 8858.
49. D. R. MacFarlane, J. Sun, J. Golding, P. Meakin, M. Forsyth, *Electrochim. Acta*, 2000, **45**, 1271.

50. M. C. Buzzeo, R. G. Evans, R. G. Compton, *ChemPhysChem*, 2004, **5**, 1106.
51. W-J Gau, I-W Sun, *J. Electrochem. Soc.*, 1996, **143**, 170.
52. T. Tsuda, Y. Ito, T. Nohira, *Electrochim. Acta*, 2001, **46**, 1891.
53. I. Billard, G. Moutiers, A. Labet, A. E Azzi, C. Gaillard, C. Mariet, K. Lutzenkirchen, *Inorg. Chem.*, 2003, **42**, 1726.
54. J. P. Schoebrechts, B. P. Gilbert, G. Duyckaerts, *J. Electroanal. Chem.*, 1983, **145**, 127.
55. W-J Gau, I-W Sun, *J. Electrochem. Soc.*, 1996, **143**, 914.
56. J. P. Schoebrechts, B. P. Gilbert, *Inorg. Chem.*, 1985, **24**, 2105.
57. C. J. Anderson, M. R. Deakin, G. R. Choppin, W. D'Olieslger, L. Heerman, D. J. Pruett, *Inorg. Chem.*, 1991, **30**, 4013.
58. S. Dai, L. M. Toth, G. R. Hayes, J. R. Peterson, *Inorg. Chim. Acta*, 1997, **256**, 143.
59. T. A. Hopkins, J. M. Berg, D. A. Costa, W. H. Smith, H. J. Dewey, *Inorg. Chem.*, 2001, **40**, 1820.
60. S. Dai, Y. S. Shin, L. M. Toth, C. E. Barnes, *Inorg. Chem.*, 1997, **36**, 4900.
61. D. A Costa, W. H. Smith, *Los Alamos yearly report*, LA-UR-99-5521, 1999.
62. W. H. Smith, D. A. Costa, *Los Alamos yearly report*, LA-UR 98-3669, 1998.
63. K. D. Abney, E. Bluhm, E. Garcia, W. H. Smith, M. Barr, W. Oldham, D. A. Costa, D. Morris, D. Tait, *Los Alamos yearly report*, LA-UR-00-5043, 2000.
64. D. A Costa, W. H. Smith, W. J. Oldham, *Los Alamos yearly report*, 2001.
65. D. A. Costa, W. H. Smith, K. D. Abney, W. J. Oldham, *Plutonium Futures – The Science*, American Institute of Physics, 2000.

66. A. E. Visser, R. D. Rogers, *J. Solid State Chem.*, 2003, **171**, 109.
67. A. E. Visser, M. P. Jensen, I. Laszak, K. L. Nash, G. R. Choppin, R. D. Rogers, *Inorg. Chem.*, 2003, **42**, 2197.
68. M. P. Jensen, J. Neuefeind, J. V. Beitz, S. Skanthakumar, L. Soderholm, *J. Am. Chem. Soc.*, 2003, **125**, 15466.
69. S. Dai, Y. H. Ju, C. E. Barnes, *J. Chem. Soc., Dalton Trans.*, 1999, 1201.
70. H. Luo, S. Dai, P. V. Bonnesen, *Anal. Chem.*, 2004, **76**, 2773.
71. H. Luo, S. Dai, P. V. Bonnesen, A. C. Buchanan, III, J. D. Holbrey, N. J. Bridges, R. D. Rogers, *Anal. Chem.*, 2004, **76**, 3078.
72. M. P. Jensen, J. A. Dzielawa, P. Rickert, M. L. Dietz, *J. Am. Chem. Soc.*, 2002, **124**, 10664.
73. M. P. Jensen, J. A. Dzielawa, M. L. Dietz, I. Laszak, B. A. Young, *Green Chem.*, 2003, **5**, 682.
74. A. E. Bradley, A. Haile, J. E. Hatter, W. R. Pitner, D. W. Sanders, K. R. Seddon, R. C. Thied, *BNFL Internal Report – Progress and Current Status of Ionic Liquids Project*, SAP No: 10/00342.03.02.
75. A. E. Bradley, *BNFL Internal Report – Processing of Spent Nuclear Fuel Using Ionic Liquids*.
76. W. R. Pitner, A. E. Bradley, D. W. Sanders, K. R. Seddon, R. C. Thied, J. E. Hatter, *NATO ASI Ser., Ser. 2*, 2003, **92** (Green Industrial Applications of Ionic Liquids), 209.

CHAPTER 2

EXPERIMENTAL TECHNIQUES

2.1 Introduction

The chemistry of synthesised LTILs and *f*-element complexes has been investigated using a number of spectroscopic, structural and electrochemical techniques. Experimental details for the techniques employed are given below with more specific details given in the subsequent chapters. For X-ray absorption spectroscopy a brief introduction into the theory is also provided.

2.2 Elemental analysis

Elemental analysis was performed by Mr M. Jennings (Department of Chemistry, The University of Manchester) using a CHNS-O EA1108 elemental analyser and a Fisons Horizon elemental analyser ICP-OES spectrometer. The hygroscopic lanthanide and uranium samples were prepared by placing *ca.* 1-10 mg of sample into alumina sample holders inside an Ar drybox prior to measurements in air (see Chapters 4 and 6).

2.3 Thermogravimetric analysis

Thermogravimetric analysis (TGA) was undertaken using a Mettler Toledo TGA/SDTA 851° analyser. Initial sample weights were recorded in air and samples were heated in alumina crucibles from 25 to 900 °C at a rate of 5 °C m.⁻¹ in air. Decomposition points (T_{dec}) were obtained from the minimum of the first derivative of the curves.

2.4 NMR spectroscopy

NMR spectra were recorded using a Bruker Avance 400 MHz spectrometer using automated X-WIN NMR software. Samples were prepared by dissolving *ca.* 5-10 mg of solid/liquid in *ca.* 1 mL of CD₃CN. ⁷⁵As and ¹²¹Sb/¹²³Sb spectra were referenced to KAsF₆ and KSbF₆, respectively. ¹H and ¹³C spectra were referenced to the external standards tetramethylsilane (TMS), whilst ³¹P spectra were referenced to 85 % phosphoric acid.

2.5 UV/vis/nIR spectroscopy

Solid state diffuse reflectance UV/vis/nIR spectra of uranium compounds (Chapter 6) were recorded inside an Ar-filled drybox using an Ocean Optics SD2000 spectrometer fitted with a fibre optic probe and a Deuterium-Halogen DH-200 light source. Calibration of the instrument and background spectra for solid samples were recorded using BaSO₄ placed onto a white filter paper as a reference, whilst samples were recorded by placing *ca.* 10-15 mg of powdered sample onto the filter paper.

Solution UV/vis/nIR spectra of U compounds dissolved in LTILs (Chapter 6) were recorded using an Ocean Optics SD2000 spectrometer fitted with a fibre optic probe and a Deuterium-Halogen DH-200 light source. Calibration of the instrument and background spectra were performed using LTILs samples in an XAS solution cell (Section 2.9.1), whilst samples were recorded by dissolving *ca.* 40 mg of U into an LTIL before placing

into the XAS cell. All uranium spectra were recorded inside an Ar-filled atmosphere drybox. Solution UV/vis/nIR spectra of Np complexes (Chapter 7) were recorded using a Cary-Varian 500 scan UV/vis/nIR spectrometer. Calibration of the instrument and background spectra were performed on samples of distilled water or pure $[\text{Me}_3\text{N}^n\text{Bu}][\text{TFSI}]$ prior to measurements of Np dissolved in these solvents.

2.6 Vibrational spectroscopy

All attenuated total reflectance (ATR) IR spectra were recorded using a Bruker Equinox 55/ Bruker FRA 106/5 FTIR/Raman spectrometer with a coherent 500 mW Laser. ATR-IR spectra were recorded in the solid (using crushed samples) or liquid state by placing *ca.* 10 mg of sample onto a detachable 'Golden Gate' attachment with 4 cm^{-1} resolution. For the hygroscopic lanthanide and uranium compounds (see Chapters 4 and 6), the samples were placed onto the ATR attachment inside an Ar-filled drybox and sealed using Sellotape[®] prior to measurements. ATR-IR spectra of the Np-TFSI complex (see Chapter 7) were recorded by placing *ca.* 10 mg of sample onto the ATR attachment in air and sealing with Sellotape[®]. Raman spectra were measured using the same instrument fitted with a 633 nm laser. The spectra were measured by placing *ca.* 10 mg of sample into a stainless steel sample holder and covered with Sellotape[®]. For the lanthanide and uranium compounds (see Chapters 4 and 6), samples were prepared inside an Ar-filled drybox. For the Np-TFSI complex (Chapter 7), the sample was prepared in air inside an active fumehood. All Raman spectra were recorded by scanning the samples for at least 30 m.

2.7 Single crystal X-ray diffraction

All single crystal X-ray diffraction measurements were performed using a Bruker platform CCD area detector diffractometer using a Mo K- α X-ray source, with a wavelength of 0.71073 Å. All data analyses were performed by either Dr M. Helliwell or Dr J. Raftery of the Department of Chemistry, The University of Manchester, or Dr. A. J. Gaunt or Dr. C. A. Sharrad of the Centre for Radiochemistry Research, The University of Manchester. Crystal structure refinement was performed using SHELXL or SHELXTL programs and the structures solved by direct methods followed by Fourier synthesis, and refined on F^2 .

2.8 Electrochemistry

Electrochemical measurements were performed using a PAR EG&G 263A potentiostat operated by model 250 Research Electrochemistry Software (M270), ver. 4.41. In all experiments a conventional 3-electrode cell was used comprising of a large surface area Pt gauze counter electrode (0.063 cm²), a working electrode (see pertinent Chapters for further details) and either a Ag wire quasi reference electrode or a Ag/AgNO₃ reference electrode. Solution resistance (iR compensation) was determined using the iR compensation option in the model 250 Research Electrochemistry Software (M270) program and all voltammograms were corrected by this value using the IR compensation option in the voltammetry software. All measurements were recorded under an Ar

atmosphere either in an inert atmosphere drybox or in a Faraday cage where the solution was purged with Ar for 30 m. prior to scans and 30 s. in between scans.

2.9 X-ray absorption spectroscopy

2.9.1 XAS – Experimental method

XAS measurements were performed at either beamline BM20 at the European Synchrotron Radiation Facility in Grenoble, France (ESRF) or at Station 16.5 at the Synchrotron Radiation Source in Daresbury, Warrington, UK (SRS).

All samples were prepared and handled in an inert atmosphere drybox. Solutions of U (*ca.* 40 mg) or Zr (*ca.* 10 mg) compounds dissolved in LTILs were sealed in Perspex[®] cells containing Mylar windows, sealed with Kapton[®] tape and then contained in two layers of Polythene (see Figure 2.9.1). Solid samples (*ca.* 40 mg U or *ca.* 10 mg Zr) were mixed using a mortar and pestle with BN prior to sealing in Perspex[®] cells containing Mylar windows, sealed with Kapton[®] tape and again contained in two layers of Polythene (Figure 2.9.1).

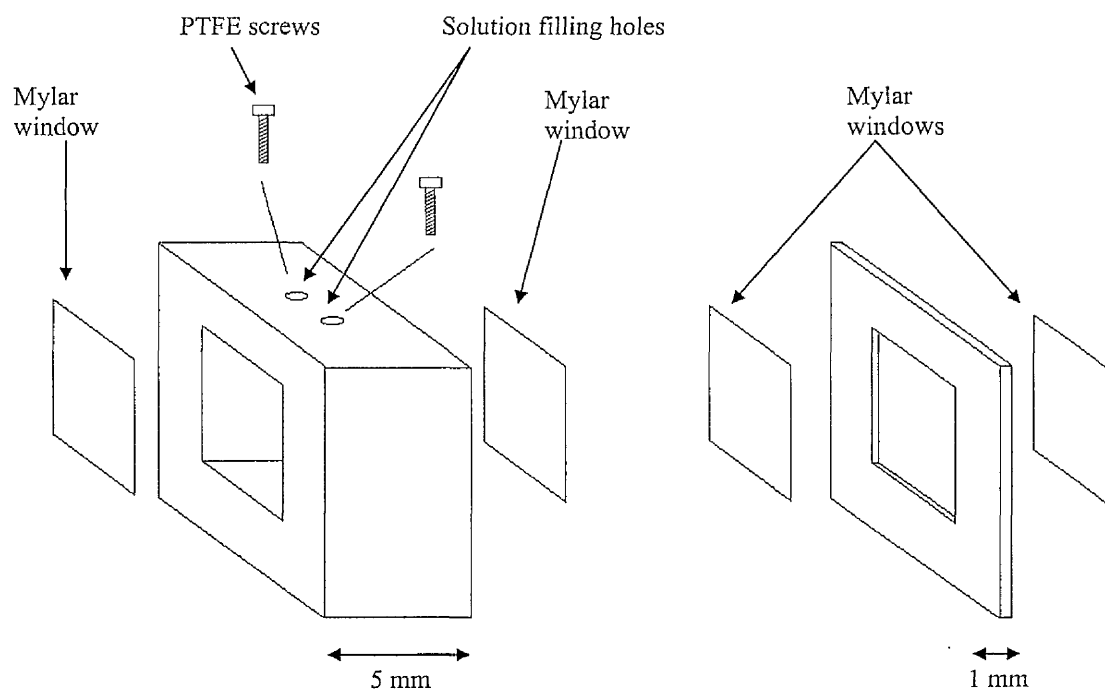


Figure 2.9.1 Schematic of Perspex XAS cells; solution (left) and solid (right)

2.9.2 XAS – Theory

In an XAS experiment, the sample is bombarded with monochromatic X-rays, where the precise energy of the X-rays can be varied. Some of these X-rays will be absorbed by the sample, and the transmitted X-rays can be described by the following equation¹:

$$I = I_0 e^{-\mu x} \quad \text{Equation 2.1}$$

where I = intensity of transmitted X-ray, I_0 = intensity of incident X-ray, μ = absorption coefficient and x = thickness of absorber.

An XAS spectrum can be recorded by selectively tuning the X-ray beam energies to values before and after the absorption energy of a selected element (Figure 2.9.2). At certain wavelengths X-rays can be absorbed by an element, and a core electron can be

emitted in a spherical wave¹. This electron wave can be scattered by the surrounding atoms and can either constructively or destructively interfere with the outgoing electron wave (see Figure 2.9.3). This interference pattern gives rise to the EXAFS oscillations.

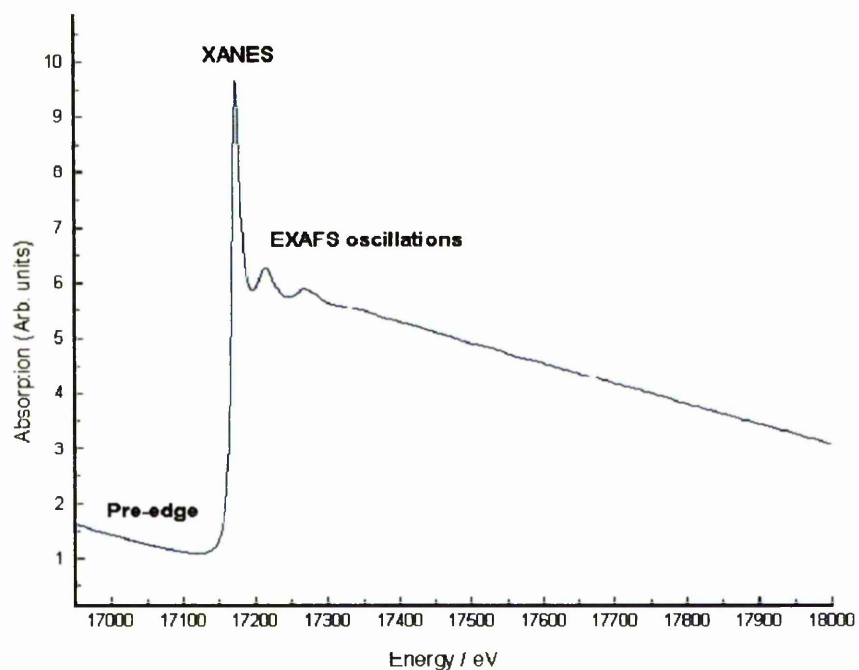


Figure 2.9.2: A typical U L_{III} edge XAS spectrum showing the characteristic regions

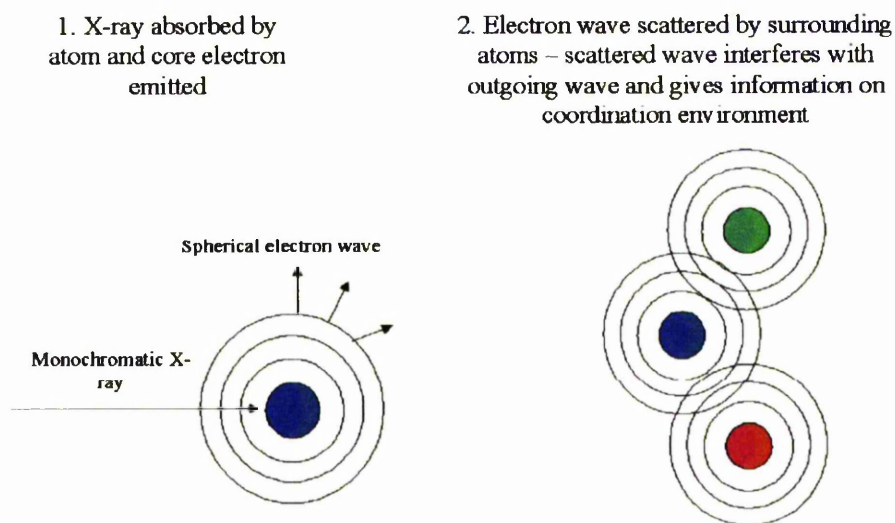


Figure 2.9.3: Schematic representation of X-ray scattering¹

2.9.3 X-ray Absorption Near Edge Structure (XANES)

The XAS spectrum can be split into 3 areas, the pre-edge, the X-ray Absorption Near Edge Structure (XANES) and the Extended X-ray Absorption Fine Structure (EXAFS) oscillations (Figure 2.9.2).

At a fixed energy, X-ray photons are absorbed by the sample and a core electron is emitted (17.166 keV for zero-valent U L_{III} electron) and absorption of X-rays is observed. The region around this absorption is known as the XANES region and the structure of this region can give information on the chemical environment at the absorber. The energy of absorption is related to the energy of the electronic orbital. An increase in valency

results in the atomic orbitals contracting, thus the orbital energy increases causing a positive shift in the absorption edge position. Coordination and bonding around the centre will also have an effect on the energy of the orbital and hence an effect on the edge position and XANES. Thus, by comparing absorption edge positions of characterised samples with known oxidation states with similar coordination environments the XANES edge position can be used to determine the oxidation state of less well characterised samples.

2.9.4 Extended X-ray Absorption Fine Structure (EXAFS)

The spherical electron wave emitted after initial absorption of the X-ray photons can interact with the electronic orbitals of the surrounding atoms. This interaction causes scattering of the electron wave. This scattered electron wave can interfere with the emitted electron wave constructively or destructively. In the EXAFS experiment the oscillations caused by the interference are recorded and the amplitude is plotted as a function of path length. It is known that the oscillation amplitude has a dependency on the scattering amplitude of elements around the central atom. As each different element has a different scattering amplitude (due to the differences in electronic environment), this can be used as a basis for modelling of the experimental EXAFS data obtained. This is done using a program called EXCURV98 written by Binsted *et al.*,² which theoretically fits the EXAFS data by calculating the oscillations that arise for a model involving the number, type and distance of atoms from the central absorber. However, it should be noted that the scattering by atoms of similar size (*e.g.* N and O) will be similar

and a reasonable fit may be achieved for either. Therefore, fits in this case should be made with atoms that may be present as indicated by other spectroscopic techniques, or from known chemical connectivity.

To judge the 'goodness' of a fit there are several formulae that can be used. The results presented in this thesis are all best fits obtained with the lowest value of the R_{EXAFS} parameter. R_{EXAFS} gives an indication of the quality of a fit, and is represented in Equation 2.1:³

$$R_{\text{EXAFS}} = \sum_i^N \frac{1}{\sigma_i} \left(\left| \chi_i^{\text{exp}}(k) - \chi_i^{\text{theory}}(k) \right| \right) \times 100\% \quad \text{Equation 2.1}$$

where σ_i is defined as $\frac{1}{\sigma_i} = \frac{k_i^n}{\sum_j^N k_j^n \left| \chi_j^{\text{exp}}(k_j) \right|}$

where $\chi_i^{\text{exp}}(k)$ and $\chi_i^{\text{theory}}(k)$ are the experimental and theoretical EXAFS and k is the magnitude of the photoelectron wavevector.

The number of data points that can be justifiably fitted in an EXAFS experiment (N_{ind}) can be calculated using Equation 2.2:³

$$N_{\text{ind}} = \frac{2\Delta k \Delta R}{\pi} + 1 \quad \text{Equation 2.2}$$

where ΔR is the path length range and Δk is the data range

All the results presented in this thesis will have the maximum number of parameters fitted less than or equal to N_{ind} and all shells fitted result in an R_{EXAFS} parameter decrease of 5 % or more.

2.10 References

1. *X-ray absorption : principles, applications, techniques of EXAFS, SEXAFS, and XANES*, Eds. D.C. Koningsberger and R. Prins, John Wiley & Sons, New York, 1988.
2. N. Binsted (1998), EXCURV98: CCLRC Daresbury Laboratory computer program; N. Binsted, R. W. Strange, S. S. Hasnain, *Biochemistry*, 1992, **31**, 12117.
3. S. J. Gurman, *J. Synchrotron Rad.*, 1995, **2**, 56.

CHAPTER 3

SYNTHESIS AND ELECTROCHEMICAL

CHARACTERISATION OF

BIS(TRIFLUOROMETHANESULFONYL)

AMIDE SALTS WITH GROUP 15

QUATERNARY CATIONS

3.1 Introduction

The 1,3-dialkylimidazolium-based LTILs initially investigated by BNFL are not suitable solvent media for LTIL based nuclear fuel reprocessing technology (see Chapter 1).

Primarily this is because the cathodic limits of the electrochemical windows are not negative enough to encompass the Pu(III)/Pu(0) reduction potential. In addition, although it has been shown that the U(III)/U(0) reduction can be observed in these LTILs it is only just within the limits of the window¹⁻³ and thus unsuitable for the overpotentials required for bulk electrodeposition.⁴

It is known that the electrochemical windows limits are controlled by the electrochemical destruction of the LTIL cation and anion.⁵ Fuller *et al.* have shown that, as expected, the cathodic limit is due to reduction of the cation and the anodic limit due to oxidation of the anion.⁵ Recently Awakura *et al.* have shown that quaternary alkylammonium-based LTILs may have sufficiently wide enough electrochemical windows to observe the Pu(III)/Pu(0) reduction.⁶ An internal LANL report appears to back up this evidence with a study which also encompassed pyrrolidinium-based LTILs.⁷ Investigations have also shown that quaternary alkylphosphonium-based LTILs may also be suitable (Chapter 1).

It would appear that the quaternary alkyl phosphonium-based LTILs (Chapter 1) have a more negative cathodic limit than the quaternary alkyl ammonium LTILs investigated by Awakura *et al.*,⁶ presumably because of the differences in central atom, N vs. P.

However, direct comparison between the two LTILs is difficult to make because the effect of the alkyl chains cannot be ignored.

It is hypothesised that by changing the central atom in quaternary Group 15 based LTILs, variations in the cathodic limits of the electrochemical window should be observed arising from the variable stability of the radical species formed upon reduction. Until now, there have been no systematic studies on the effects that the central atom of these LTILs have on the electrochemical window. It was decided to synthesis a number of model LTILs based on quaternary alkyl Group 15 salts to investigate whether the central atom has an effect on the electrochemical properties. In addition, more detailed studies would be made on quaternary ammonium salts due to the relatively inexpensive starting reagents and potentially lower chemical toxicities. Previously Rogers *et al.*⁸ and Costa *et al.*⁹ have shown that for imidazolium and quaternary alkylammonium-based LTILs, changes in the alkyl groups in the LTIL cation has an effect on the melting points and viscosities of the LTIL. Therefore, it is also desirable to investigate the effect that increases of alkyl group chain length would have on the electrochemical window of the quaternary ammonium salts. Finally, the effect of alkyl vs. aryl substituents on the cation was also investigated in relation to the electrochemical stability. This was undertaken for phosphonium based melts because of the ease of synthesis and availability of cheap starting reagents.

Recently the TFSI anion has been used in the synthesis of LTILs due to the low coordinating properties of the anion, which leads to lower viscosities in the LTIL¹⁰ and

lower melting points.¹¹ Another advantage of the TFSI anion, is the relatively large anodic stability,¹² although this is of less relevance to this project. In order to have meaningful comparisons TFSI was chosen as the counter ion for all the LTILs.

Any LTIL that will be used industrially in a nuclear fuel reprocessing technology will have to be stable to large doses of γ -radiation, and for one of the LTILs synthesised, [Me₃NBu][TFSI], the radiation stability was also investigated. Previous research by Seddon *et al.* using 1,3-dialkylimidazolium-based cation and either Cl⁻ or NO₃⁻ anion-based RTILs have shown that allyl rings have high radiation stability.¹³

3.2 Synthesis of bis(trifluoromethanesulfonyl)amide based low temperature ionic liquids with Group 15 quaternary cations

3.2.1 General considerations

All the LTILs were synthesised by a metathesis reaction between Group 15 based alkyl/aryl cation halide salts and Li[TFSI] in water using standard Shlenck line techniques. The LTILs were characterised using elemental analysis, NMR spectroscopy and vibrational spectroscopy. Thermogravimetric analysis was used to find the thermal decomposition point of each LTIL synthesised. Elemental analysis results and melting points are given in Table 3.2.1. It should be noted that both [Me₃NⁿBu][TFSI] and [Me₃NⁿHex][TFSI] have been previously prepared by other workers.^{6,14,15}

3.2.2 Synthesis of tetramethylammonium bis(trifluoromethanesulfonyl)amide – [Me₄N][TFSI]

An aqueous solution of Me₄NCl (15.4 g, 0.141 mol, 90 mL H₂O) was reacted with an aqueous solution of Li[TFSI] (40.4 g, 0.141 mol, 50 mL H₂O) with stirring to form a white coloured precipitate of [Me₄N][TFSI]. CH₂Cl₂ (100 mL) was added to the mixture with stirring to dissolve the solid. After 4 h, the CH₂Cl₂ layer was separated and solvent removed *in vacuo* to yield a white microcrystalline solid of [Me₄N][TFSI] (yield = 45.09 g, 90.1 %).

3.2.3 Synthesis of tetramethylphosphonium bis(trifluoromethanesulfonyl)amide – [Me₄P][TFSI]

An aqueous solution of Me₄PBr (5.25 g, 30.7 mmol, 30 mL H₂O) was reacted with an aqueous solution of Li[TFSI] (9.77 g, 34.0 mmol, 15 mL H₂O) with stirring to form a white coloured precipitate of [Me₄P][TFSI]. CH₂Cl₂ (100 mL) was added to the mixture with stirring to dissolve the solid. After 4 h, the CH₂Cl₂ layer was separated and solvent removed *in vacuo* to yield a white microcrystalline solid of [Me₄P][TFSI] (yield = 9.65 g, 84.7 %).

3.2.4 Synthesis of tetramethylarsonium bis(trifluoromethanesulfonyl)amide

([Me₄As][TFSI]) and tetramethylstibonium bis(trifluoromethanesulfonyl)amide

([Me₄Sb][TFSI])

[Me₄As][TFSI] and [Me₄Sb][TFSI] were synthesised by Dr. V. A. Volkovich (CRR, The University of Manchester) and used as supplied.

3.2.5 Synthesis of N,N-trimethylethylammonium bis(trifluoromethanesulfonyl)amide –

[Me₃NEt][TFSI]

[Me₃NEt][TFSI] was synthesised by Dr N. Ertok, from Izmir Yuksek Teknoloji Enstitusu, Turkey whilst visiting the CRR on a research fellowship and used as supplied.

3.2.6 Synthesis of N,N-trimethyl-n-butylammonium

bis(trifluoromethanesulfonyl)amide – [Me₃NⁿBu][TFSI]

Me₂NⁿBu (100 mL, 0.72 mol) was placed into an salt ice bath at -17 °C. After 15 m, MeI (45 mL, 0.72 mol) was added dropwise over 1 h to form a white precipitate of [Me₃NⁿBu]I. Et₂O (100 mL) was then added to this precipitate with stirring. To the resultant suspension, H₂O (100 mL) was added to dissolve the [Me₃NⁿBu]I with the aqueous layer then extracted and the H₂O removed *in vacuo* to form a white microcrystalline solid (yield of [Me₃NⁿBu]I = 127.79 g, 73.9 %).

Li[TFSI] (151.2 g, 0.53 mol) was dissolved in water (150 mL) and added to a solution of $[\text{Me}_3\text{N}^n\text{Bu}]\text{I}$ (127.79 g, 0.53 mol) in water (200 mL) with stirring. The resultant pale yellow coloured, water immiscible liquid was extracted and washed with an aqueous solution of $\text{Na}_2\text{S}_2\text{O}_3 \cdot 5\text{H}_2\text{O}$ (5 g, 10 mL). The liquid $[\text{Me}_3\text{N}^n\text{Bu}][\text{TFSI}]$ was then dried *in vacuo* at 110-130 °C to yield a colourless clear liquid (yield = 181.63 g, 87.1 %)

3.2.7 Synthesis of N,N-trimethyl-n-hexylammonium

bis(trifluoromethanesulfonyl)amide – $[\text{Me}_3\text{N}^n\text{Hex}][\text{TFSI}]$

$\text{Me}_2\text{N}^n\text{Hex}$ (3.0 mL, 0.017 mol) was dissolved in Et_2O (20.0 mL) and the solution placed into an ice bath at 0 °C. After 5 m, excess MeI (4.0 mL, 0.064 mol) was added dropwise over 1 h to form a white precipitate of $[\text{Me}_3\text{N}^n\text{Hex}]\text{I}$. Excess MeI was removed by passing N_2 over the reaction mixture for 30 m. The solid $[\text{Me}_3\text{N}^n\text{Hex}]\text{I}$ was collected by filtration and dried *in vacuo* for 1 h (yield of $[\text{Me}_3\text{N}^n\text{Hex}]\text{I}$ = 3.59 g, 76.5 %).

Li[TFSI] (3.80 g, 0.013 mol) was dissolved in water (20 mL) and added to a solution of $[\text{Me}_3\text{N}^n\text{Hex}]\text{I}$ (3.59 g, 0.013 mol) in water (100 mL) with stirring. The resultant pale yellow coloured, water immiscible liquid was extracted and washed with an aqueous solution of $\text{Na}_2\text{S}_2\text{O}_3 \cdot 5\text{H}_2\text{O}$ (5 g, 10 mL). The liquid $[\text{Me}_3\text{N}^n\text{Hex}][\text{TFSI}]$ was then dried *in vacuo* at 110-130 °C to yield a colourless clear liquid (yield = 4.61 g, 83.6 %)

3.2.8 Synthesis of P,P-dimethyldiphenylphosphonium

bis(trifluoromethanesulfonyl)amide ([Me₂PPh₂][TFSI],

P,P-methyltriphenylphosphonium bis(trifluoromethanesulfonyl)amide

([MePPh₃][TFSI] and tetraphenylphosphonium bis(trifluoromethanesulfonyl)amide

([Ph₄P][TFSI])

[Me₂PPh₂][TFSI], [MePPh₃][TFSI] and [PPh₄][TFSI] were synthesised by Dr V. A.

Volkovich (CRR, The University of Manchester) and were used as supplied.

3.2.9 Preparation of single crystals of tetramethylphosphonium

bis(trifluoromethanesulfonyl)amide ([Me₄P][TFSI]) and tetramethylstibonium

bis(trifluoromethanesulfonyl)amide ([Me₄Sb][TFSI]) suitable for X-ray diffraction

Single crystals of [Me₄P][TFSI] and [Me₄Sb][TFSI] suitable for X-ray diffraction were grown by dissolving the respective salts in *ca.* 5 mL of acetone and the solvent allowed to slowly evaporate in air over 24 h.

3.3 Physical characterisation of Group 15 cation and TFSI anion based

LTILs

3.3.1 Elemental analysis and melting points

Melting points and elemental analysis results are given in Table 3.3.1. All of the salts have a melting point above 100 °C apart from [Me₃NⁿBu][TFSI] and [Me₃NⁿHex][TFSI], which are liquid at room temperature.

LTIL	Elemental analysis		Melting point / °C
	Calc. %	Found %	
[Me ₄ N][TFSI]	C, 20.34; H, 3.42; N, 7.91; S, 18.10	C, 20.21; H, 3.40; N, 7.82; S, 17.95	133.5 – 137.1
[Me ₄ P][TFSI]	C, 19.41; H, 3.26; N, 3.77; S, 17.27; P, 8.34	C, 19.40; H, 3.24; N, 3.72; S, 17.56; P, 8.42	149.3 – 150.3
[Me ₄ As][TFSI]	C, 17.36; H, 2.91; N, 3.37; S, 15.44; As, 18.04	C, 17.17; H, 2.80; N, 3.31; S, 15.38; As, 18.09	138.7 – 142.1
[Me ₄ Sb][TFSI]	C, 15.59; H, 2.62; N, 3.03; S, 13.88; Sb, 26.35	C, 15.90; H, 2.67; N, 3.02; S, 13.89; Sb, 26.35	142.6 – 144.2
[Me ₃ NEt][TFSI]	C, 22.83; H, 3.80; N, 7.60; S, 17.40	C, 23.13; H, 3.68; N, 7.51; S, 17.27	103.6 – 106.1
[Me ₃ N ⁿ Bu][TFSI]	C, 27.27; H, 4.59; N, 7.07; S, 16.61	C, 27.21; H, 4.78; N, 6.98; S, 16.18	Liquid at RT
[Me ₃ N ⁿ Hex][TFSI]	C, 31.13; H, 5.22; N, 6.60; S, 15.11	C, 31.18; H, 5.61; N, 6.59; S, 15.27	Liquid at RT
[MePPh ₃][TFSI]	C, 45.25; H, 3.25; N, 2.51; S, 11.50; P, 5.56	C, 45.41; H, 3.17; N, 2.46; S, 11.59; P, 5.59	126.3 – 128.0
[Me ₂ PPh ₂][TFSI]	C, 38.79; H, 3.26; N, 2.83; S, 12.95; P, 6.25	C, 38.96; H, 3.22; N, 2.77; S, 13.11; P, 6.23	67.2 – 69.3
[PPh ₄][TFSI]	C, 50.40; H, 3.25; N, 2.26; S, 10.35; P, 5.00	C, 50.41; H, 3.24; N, 2.25; S, 10.35; P, 5.08	135.9 – 136.7

Table 3.3.1: Elemental analysis of Group 15 cation and TFSI anion based LTILs

3.3.2 Thermogravimetric analysis

Thermogravimetric analysis (TGA) of the synthesised TFSI-based LTILs was undertaken and the results summarised in Table 3.3.2. TGA analysis showed one decomposition step for all LTILs, corresponding to 100 % mass loss, the only exception being [Me₄Sb][TFSI], where a mass loss of 70.8 % was recorded. This is probably due to formation of an involatile Sb oxide phase. The synthesised TFSI-based LTILs are all thermally stable to at least 320 °C, thus showing a wide thermal stability range.

LTIL	Decomposition point / °C	Mass loss / %
[Me ₄ N][TFSI]	380	100
[Me ₄ P][TFSI]	420	100
[Me ₄ As][TFSI]	360	100
[Me ₄ Sb][TFSI]	320	70.8
[Me ₃ NEt][TFSI]	380	100
[Me ₃ N ⁿ Bu][TFSI]	440	100
[Me ₃ N ⁿ Hex][TFSI]	390	100
[MePPh ₃][TFSI]	415	100
[Me ₂ PPh ₂][TFSI]	400	100
[PPh ₄][TFSI]	420	100

Table 3.3.2: Thermal stability of Group 15 cation and TFSI anion-based LTILs

3.4 Spectroscopic characterisation of TFSI-based LTILs

3.4.1 Vibrational spectroscopy

ATR mid-IR spectra of Group 15 cation and TFSI anion-based LTILs have been measured in the solid state, apart from $[\text{Me}_3\text{N}^n\text{Bu}][\text{TFSI}]$ and $[\text{Me}_3\text{N}^n\text{Hex}][\text{TFSI}]$, which were measured as liquid samples. Results are summarised in Table 3.4.1. Previously Lassègues *et al.*^{16,17} have fully assigned the IR and Raman bands of TFSI for HTFSI and $\text{Li}[\text{TFSI}]$. Based on these studies, the IR bands observed for the LTILs have been assigned as shown in Table 3.4.1. The IR bands of the group 15 cations have also been assigned based on literature references.^{18,19}

Assignment	Li[TFSI]	[Me ₄ N]	[Me ₄ P]	[Me ₄ As]	[Me ₄ Sb]	[Me ₃ NEt]	[Me ₃ N ^u Bu]	[Me ₃ N ^u Hex]	[MePPh ₃]	[Me ₂ PPh ₂]	[PPh ₄]
$\delta(\text{CH})^a$	-	1466	1433	1440	1437	1421	1481	1481	1438	1431	1437
$\nu(\text{C}=\text{C})^a$	-	-	-	-	-	-	-	-	1438?	1438?	1438?
$\nu_a^{\text{i.p./o.p.}}(\text{SO}_2)$	1323 1307	1344 1330	1346 1329	1337 1319	1344 1332	1344 1330	1348 1329	1346 1327	1350	1344	1340 1319
$\nu_s(\text{CF}_3)$	1242	-	1222	1222	-	1222	1222	1224	1224	-	1226
$\nu_a(\text{CF}_3)$	1195	1176	1178	1184	1184	1180	1178	1176	1178	1182	1178
$\nu_s^{\text{o.p.}}(\text{SO}_2)$	1138	1139	1139	1143	1138	1136	1134	1134	1136	1135	1134
$\nu_a(\text{SNS})$	1062	1043	1049	1053	1047	1053	1051	1053	1049	1050	1057
$\nu(\text{C-Z})^b$	-	971?	980?	885?	864?	958?	972?	958?	997?	977?	995?
$\nu(\text{CS})$	810?	816	790	-	792	790	789	789	789	787	788
$\nu_s(\text{SNS})$	773?	793	763	-	763	763	762	761	760	-	752
$\delta_s(\text{CF}_3)$	746	758	739	741	741	741	739	740	738	-	740
$\delta^{\text{o.p./i.p.}}(\text{SO}_2)$	606	612	606	601	607	613	613	613	609	604	609
$\delta_a(\text{CF}_3)$	569 510	571 514	568 510	570 516	567 513	569 515	569 511	569 511	569 509	571 507	567 511

Table 3.4.1: Solid state ATR mid-IR bands of TFSI-based LTLs synthesised (except [Me₃N^uBu][TFSI] and

[Me₃N^uHex][TFSI] which were recorded as liquids). a, several overlapping bands; b, Z = N, P, As or Sb; ? = tentative

assignment

3.4.2 NMR spectroscopy

Samples of all the synthesised LTILs were dissolved in *ca.* 1 mL CD₃CN and ¹H, ¹³C and ¹⁹F NMR spectra measured. For [Me₄As][TFSI] and [Me₄Sb][TFSI], ⁷⁵As and ¹²¹Sb/¹²³Sb respectively, were also measured with results summarised in Table 3.4.2. ⁷⁵As spectra were referenced to KAsF₆²⁰ whereas ¹²¹Sb/¹²³Sb spectra were referenced to KSbF₆.²¹

DesMarteau and Foropoulos have previously synthesised and characterised TFSI salts and derivatives of the TFSI anion using ¹H and ¹⁹F NMR spectroscopy.²² They observed a single peak at -75.97 ppm in the ¹⁹F NMR spectrum for Li[TFSI], which they assigned to the TFSI anion. For Cs[TFSI] they observed that this peak shifted to -79.3 ppm.²³ For all the LTILs synthesised a single peak at -80.6 ppm was observed in the ¹⁹F NMR spectrum.

For the ¹H NMR spectra the peak positions and splitting patterns are as expected for each cation.¹⁸ In the ¹³C NMR spectrum, the quartet (due to ¹³C-¹⁹F coupling) observed at *ca.* 119 ppm has been assigned to the TFSI anion, all other peaks observed can be assigned to the organic cation. In the ¹³C NMR spectra, many of the α-C signals from the quaternary ammonium based cations are split into a 1:1:1 triplet as a result of coupling between ¹⁵N and ¹³C.²⁴⁻²⁶

L ⁺ TIL	¹ H / ppm (J / Hz)	¹³ C / ppm (J / Hz)	Multinuclear / ppm
[Me ₄ N][TFSI]	2.91 (s)	119.64 (q, <i>J</i> _{C,F} = 1272), 54.91 (1:1:1 t, <i>J</i> _{C,N} = 16)	-
[Me ₄ P][TFSI]	2.93 (s)	119.64 (q, <i>J</i> _{C,F} = 1276), 29.58 (s)	³¹ P, 25.20 (s)
[Me ₄ As][TFSI]	2.9 (s)	119.63, ^a 29.57 (s)	⁷⁵ As, 210.10 (s)
[Me ₄ Sb][TFSI]	2.9 (s)	119.65, ^a 29 ^a	¹²¹ Sb, 663.22 (s) ¹²³ Sb, 663.71 (s)
[Me ₃ NEt][TFSI]	3.54 (q, <i>J</i> _{H,H} = 7.2)	119.64 (q, <i>J</i> _{C,F} = 1276), 61.80 (1:1:1 t, <i>J</i> _{C,N} = 12), 52.00 (1:1:1 t, <i>J</i> _{C,N} = 16)	-
	3.23 (s), 1.56 (t of t, <i>J</i> _{H,H} = 7.2/2.2)	<i>J</i> _{C,N} = 16	
[Me ₃ N ⁿ Bu][TFSI]	3.23 (m), 3.03 (s), 1.73 (m), 1.39 (sext, <i>J</i> _{H,H} = 7.2), 0.98 (t, <i>J</i> _{H,H} = 7.2)	119.69 (q, <i>J</i> _{C,F} = 1272), 66.21 (1:1:1 t, <i>J</i> _{C,N} = 12), 52.58 (1:1:1 t, <i>J</i> _{C,N} = 16), 24.14 (s), 18.87 (1:1:1 t, <i>J</i> _{C,N} = 8), 12.45 (s)	-
[Me ₃ N ⁿ Hex][TFSI]	3.25 (m), 3.05 (s), 2.23 (s), 1.97 (quin, <i>J</i> _{H,H} = 7.2/2.5), 1.74 (m), 1.35 (m), 0.93 (m)	119.62 (q, <i>J</i> _{C,F} = 1276), 66.31 (1:1:1 t, <i>J</i> _{C,N} = 12), 52.53 (1:1:1 t, <i>J</i> _{C,N} = 20), 30.49 (s), 25.08 (s), 22.08 (s), 21.70 (s), 12.85 (s)	-
[MePPh ₃][TFSI]	7.65 (m), 7.41-7.52 (m), 1.91 (s)	134.83 (d, <i>J</i> _{C,N} = 16), 133.00 (s), 132.89 (s), 129.95 (s), 129.82 (s), 119.1, ^a 8.34 (s), 7.77 (s)	³¹ P, 22.8 (s)
[Me ₂ PPh ₂][TFSI]	7.60 (m), 2.84 (s)	134.78 (s), 134.44 (s), 131.67 (s), 131.56 (s), 129.73 (s), 129.60 (s), 118, ^a 29.56 (s)	³¹ P, 21.8 (s)
[PPh ₄][TFSI]	7.81 (m), 7.54-7.66 (m)	135.08 (d, <i>J</i> _{C,N} = 12), 135.45 (s), 134.35(s), 130.08 (s), 129.95 (s), 118 ^a	³¹ P, 24.1 (s)

Table 3.4.2: NMR data for Group 15 cation and TFSI anion-based LTILs measured in CD₃CN. a = poorly resolved multiplets

distorted by noise

3.5 Single crystal X-ray diffraction studies of [Me₄P][TFSI] and [Me₄Sb][TFSI]

A number of TFSI salts have been crystallographically characterised, including [Mg(H₂O)₆][TFSI]₂.2H₂O,²⁷ [Cu(CO)₂TFSI],²⁸ Li[TFSI],²⁹ K[TFSI],³⁰ HTFSI,³⁰ Li[TFSI].H₂O,²³ Na[TFSI].H₂O.MeOH,²³ Rb[TFSI].H₂O,²³ Cs[TFSI]²³ and 1-ethyl-2-methyl-3-benzyl imidazolium [TFSI],³¹ the last being an example of a crystallographically characterised TFSI based LTIL (melting point of *ca.* 50 °C). In general TFSI behaves only as a counter anion, however direct coordination is observed for [Cu(CO)₂TFSI] *via* the central N and HTFSI where the proton is believed to be bonded to the N.

3.5.1 X-ray diffraction study of [Me₄P][TFSI]

[Me₄P][TFSI] crystallises in the triclinic, space group *P*-1. The asymmetric unit contains two ordered [Me₄P]⁺ cations, with one whole and two half [TFSI]⁻ anions. The N atoms in the half [TFSI] anions are disordered over two sites each with 50 % occupancy while the N atom and adjacent S atom in the complete anion is disordered over two sites with 74 and 26 % occupancy. Finally, all but one of the CF₃ groups are disordered.

Crystallographic information and selected bond lengths and angles are given in Tables 3.5.1 and 3.5.2, respectively, and the structure of [Me₄P][TFSI] is represented in Figure 3.5.1.

	[Me₄P][TFSI]	[Me₄Sb][TFSI]
Empirical formula	C ₆ H ₁₂ F ₆ NO ₄ PS ₂	C ₆ H ₁₂ F ₆ NO ₄ SbS ₂
Formula weight	371.26	462.04
Space group	<i>P</i> -1	<i>P</i> -1
Crystal group	Triclinic	Triclinic
<i>a</i> (Å)	8.3272(14)	15.136(2)
<i>b</i> (Å)	12.475(2)	15.154(2)
<i>c</i> (Å)	14.289(2)	16.173(2)
α (deg)	91.554(3)	75.564(4)
β (deg)	91.636(3)	74.747(4)
γ (deg)	95.511(3)	61.702(3)
<i>V</i> (Å ³)	1476.3(4)	3117.1(8)
<i>Z</i>	4	8
<i>T</i> (K)	100(2)	150(2)
λ (Å)	0.71073	0.71073
<i>D</i> _{calcd} (mg M ⁻³)	1.670	1.969
μ (mm ⁻¹)	0.0544	0.2109
<i>R</i> ₁ , <i>Rw</i> ² indices [<i>I</i> > 2 σ^2 (<i>I</i>)]	0.0509, 0.1167	0.0476, 0.1060
<i>R</i> ₁ , <i>Rw</i> ² (all data)	0.0547, 0.1192	0.0902, 0.1262

Table 3.5.1: Crystallographic data for [Me₄P][TFSI] and [Me₄Sb][TFSI]

Bond lengths / Å			
N1A – S2A	1.571(4)	C1 – F1	1.313(6)
N1B – S2B	1.584(11)	C1 – F2	1.328(13)
S2A – C2	1.848(3)	C1 – F3	1.412(6)
S2B – C2	1.828(6)	C1 – F1B	1.34(4)
C2 – F4	1.315(4)	C1 – F3B	0.994(12)
C2 – F5	1.305(4)	C1 – F2B	1.797(10)
C2 – F6	1.308(4)	P1 – C5	1.776(4)
N1A – S1A	1.510(4)	P1 – C6	1.779(3)
N1B – S1A	1.623(11)	P1 – C7	1.782(4)
S1A – C1	1.808(4)	P1 – C8	1.782(3)
S1A – O1A	1.471(3)	P2 – C9	1.766(4)
S1A – O1B	1.300(8)	P2 – C10	1.773(4)
S2A – O4A	1.439(4)	P2 – C11	1.775(4)
S2A – O3A	1.425(4)	P2 – C12	1.788(4)
Bond angles / °			
S1A – C1 – F1	113.4(3)	S2B – C2 – F4	103.2(3)
S1A – C1 – F2	114.3(6)	S2B – C2 – F5	98.1(3)
S1A – C1 – F3	105.7(3)	S2B – C2 – F6	129.9(4)
S1A – C1 – F1B	104.2(13)	C5 – P1 – C6	109.94(19)
S1A – C1 – F2B	88.9(4)	C6 – P1 – C7	108.2(2)
S1A – C1 – F3B	135.5(10)	C7 – P1 – C8	109.12(18)
S1A – N1A – S2A	125.3(3)	C8 – P1 – C5	108.9(2)
S1A – N1B – S2B	136.3(7)	C5 – P1 – C7	111.0(3)
N1A – S2A – C2	100.96(19)	C9 – P2 – C10	108.0(2)
N1B – S2B – C2	102.2(5)	C10 – P2 – C11	110.79(18)
S2A – C2 – F4	113.3(2)	C11 – P2 – C12	109.01(19)
S2A – C2 – F5	111.3(2)	C12 – P2 – C9	110.3(2)
S2A – C2 – F6	107.7(3)	C9 – P2 – C11	110.3(2)

Table 3.5.2: Selected bond lengths and angles for one of the two non-disordered

TFSI anions and both cations in the structure of [Me₄P][TFSI]

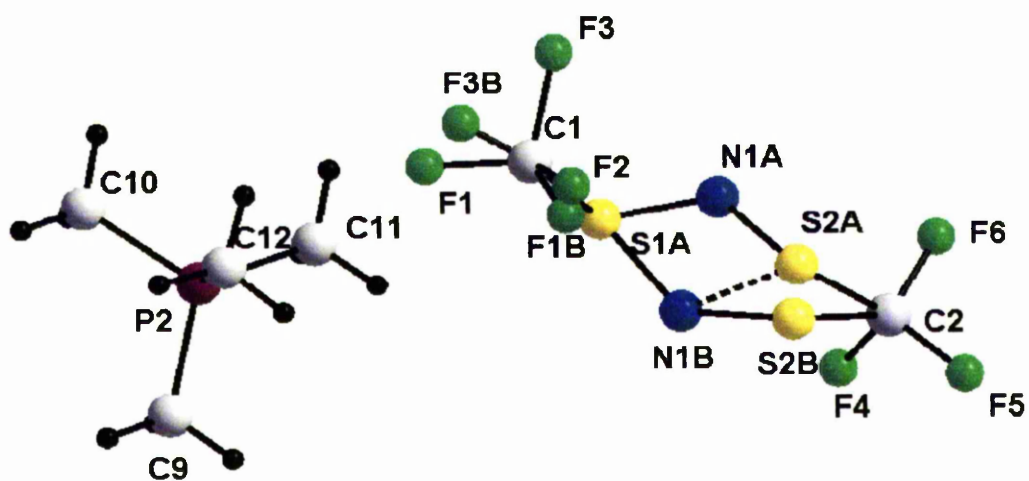


Figure 3.5.1: Crystal structure of $[\text{Me}_4\text{P}][\text{TFSI}]$ showing one ordered cation and one disordered anion (sulfonyl oxygen atoms removed for clarity)

3.5.2 X-ray diffraction study of [Me₄Sb][TFSI]

[Me₄Sb][TFSI] crystallises in the triclinic space group, *P*-1. The asymmetric unit contains 8 ions, comprising of four well ordered [Me₄Sb]⁺ cations, two ordered [TFSI]⁻ anions, and two disordered anions with most of the atoms disordered over 2 sites at 50 % occupancy. Crystallographic information and selected bond lengths and angles for the ordered TFSI anions and Me₄Sb cations are given in Tables 3.5.1 and 3.5.3, respectively. The structure of [Me₄Sb][TFSI], showing one [Me₄Sb]⁺ cation and one non-disordered [TFSI]⁻ anion is given in Figure 3.5.2.

The range in S–O, S–N and S–C bond lengths in the non-disordered crystallographically independent [TFSI]⁻ anions (1.414(5) to 1.446(5) Å, 1.567(5) to 1.579(5) Å and 1.818(8) to 1.831(7) Å, respectively) are comparable with those previously observed^{23,27-30} (for example, in the imidazolium TFSI salt,³¹ the S–O, S–N and S–C average bond lengths are 1.421(9), 1.569(6) and 1.82(10), respectively). The S–N–S bond angles in the non-disordered [TFSI]⁻ anions are similar (S1A–N1A–S2A is 124.6(3) ° *cf.* S2B–N1B–S1B is 126.0(3) °) and comparable to the S–N–S bond angles previously observed for the [TFSI]⁻ anion^{23,27-30} (again, for example, in the imidazolium TFSI salt,³¹ the S–N–S bond angle is 125 °). Each of the sulfonyl moieties has distorted tetrahedral geometry, which is comparable in both non-disordered anions (X–S–X angles in the ranges of 118.1(3) to 103.1(3) ° for S1A and 119.2(3) to 103.7(3) ° for S2A compared to 119.3 to 102.0(3) ° for S1B and 118.2(3) to 102.1(3) ° for S2B). There are some significant differences in the bond angles between atoms containing the same element

combinations (e.g. O1A–S1A–N1A is 108.2(3) ° compared with 116.4(3) ° in O2A–S1A–N1A) but again this has been observed previously (e.g. O–S–N angles range between 107.7(2) and 116.5(2) ° in $[\text{Mg}(\text{H}_2\text{O})_6][\text{TFSI}]_2 \cdot 2\text{H}_2\text{O}$ ²⁷).

The lack of any close cation–anion interactions in the imidazolium TFSI salt (the closest O, N and F interactions with H are *ca.* 2.6, 2.7 and 2.55 Å, respectively³¹) has been used to explain, at least in part, why TFSI salts have low melting points and have found useful application as LTILs. The closest cation-anion interactions found (from the two ordered anions) for $[\text{Me}_4\text{Sb}]\text{TFSI}$ are between O, N, F of the TFSI^- anion and H from the $[\text{Me}_4\text{Sb}]^+$ cation (*ca.* 2.4, 2.5 and 2.5 Å, respectively), and are slightly shorter than in the imidazolium salt. This is used to explain the higher melting point of the Sb salt (*ca.* 143 °C) compared to the imidazolium salt (50 °C).³¹

It has previously been shown that the CF_3 groups of TFSI can orientate in either a *cisoid* or *transoid* conformation with regards to the SNS plane.^{23,32} Computational studies by Pennington *et al.*²³ and Arnaud *et al.*³² have shown that the *transoid* conformation is more stable than the *cisoid* configuration. Pennington *et al.* have hypothesised that the *transoid* conformation is favoured when there are weak cation-anion interactions. In $[\text{Me}_4\text{Sb}][\text{TFSI}]$, the *transoid* conformation is observed with a C–S–S–C dihedral angle of 173.49(40) ° and thus is consistent with this hypothesis.

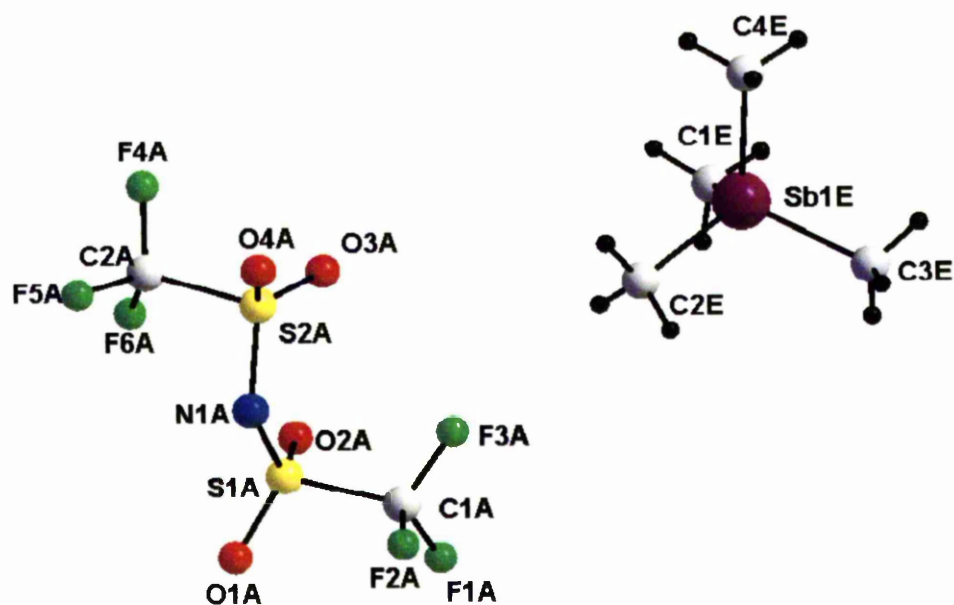


Figure 3.5.2: Crystal structure of [Me₄Sb][TFSI] showing one ordered cation and one ordered anion

Bond lengths / Å			
S1A – O1A	1.419(5)	S1B – O1B	1.414(5)
S1A – O2A	1.431(5)	S1B – O2B	1.427(5)
S1A – N1A	1.577(6)	S1B – N1B	1.572(5)
S1A – C1A	1.818(8)	S1B – C1B	1.831(7)
S2A – O4A	1.420(5)	S2B – O4B	1.429(5)
S2A – O3A	1.446(5)	S2B – O3B	1.436(4)
S2A – N1A	1.579(5)	S2B – N1B	1.567(5)
S2A – C2A	1.822(7)	S2B – C2B	1.825(8)
C1A – F1A	1.326(9)	C2B – F4B	1.295(9)
C1A – F2A	1.312(9)	C2B – F5B	1.307(8)
C1A – F3A	1.312(9)	C2B – F6B	1.349(9)
Sb1E – C1E	2.084(7)	Sb1H – C1H	2.105(6)
Sb1E – C2E	2.104(6)	Sb1H – C2H	2.103(6)
Sb1E – C3E	2.088(7)	Sb1H – C3H	2.076(6)
Sb1E – C4E	2.104(7)	Sb1H – C4H	2.099(6)
Bond angles / °			
O1A – S1A – O2A	118.1(3)	O1B – S1B – O2B	119.3(3)
O1A – S1A – N1A	108.7(3)	O1B – S1B – N1B	108.3(3)
O2A – S1A – N1A	116.4(3)	O2B – S1B – N1B	116.0(3)
O1A – S1A – C1A	104.7(3)	O1B – S1B – C1B	105.0(3)
O2A – S1A – C1A	103.9(4)	O2B – S1B – C1B	104.1(3)
N1A – S1A – C1A	103.1(3)	N1B – S1B – C1B	102.0(3)
O4A – S2A – O3A	119.2(3)	O4B – S2B – O3B	118.2(3)
O4A – S2A – N1A	109.1(3)	O4B – S2B – N1B	116.6(3)
O3A – S2A – N1A	115.2(3)	O3B – S2B – N1B	108.7(3)
O4A – S2A – C2A	104.6(3)	O4B – S2B – C2B	104.4(3)
O3A – S2A – C2A	103.7(3)	O3B – S2B – C2B	104.6(3)
N1A – S2A – C2A	102.9(3)	N1B – S2B – C2B	102.1(3)
S1A – N1A – S2A	124.6(3)	S2B – N1B – S1B	126.0(3)
C1E – Sb1E – C2E	110.4(3)	C1H – Sb1H – C2H	111.1(3)
C2E – Sb1E – C3E	110.0(0)	C2H – Sb1H – C3H	108.9(3)
C3E – Sb1E – C4E	110.8(3)	C3H – Sb1H – C4H	108.2(3)
C4E – Sb1E – C1E	107.3(4)	C4H – Sb1H – C1H	109.8(3)

Table 3.5.3: Selected bond lengths and angles for the two non-disordered TFSI anions and two cations in the structure of [Me₄Sb][TFSI]

3.6 Electrochemical windows of TFSI-based melts

3.6.1 Electrochemical window of LTILs in MeCN using TFSI-based LTILs as supporting electrolyte – experimental method

Cyclic voltammetric (CV) measurements were made using 0.2 mol L^{-1} of each salt as a supporting electrolyte in purified MeCN at 25°C using a glassy carbon working electrode ($6.3 \times 10^{-3} \text{ cm}^2$), Pt gauze counter electrode (0.063 cm^2) and a Ag/AgNO₃ reference electrode (0.01 mol L^{-1} in MeCN). The electrochemical measurements in MeCN were referenced to the Fc⁺/Fc couple, which was used as an internal standard.³³ Electrochemical windows observed are reported in Table 3.6.1 and selected voltammograms are presented in Figures 3.6.1 to 3.6.3.

MeCN used for electrochemical measurements was purified using a procedure provided by Dr L. J. Yellowlees, The University of Edinburgh, UK. HPLC grade MeCN was refluxed with AlCl₃ for 1 h and then distilled. The distilled MeCN was then refluxed with KMnO₄ / Li₂CO₃ for 1 h before distillation and then refluxed with KHSO₄ for 1 h. After distillation, this was followed by three reflux/distillation steps over CaH₂ and the purified MeCN stored under Ar. All purification and handling of MeCN was carried out under an Ar atmosphere in a specially modified Dean and Stark apparatus. All the LTILs were pre-dried by heating at 120°C under ambient pressure to remove any moisture prior to the electrochemical experiments.

3.6.2 Electrochemical windows of molten TFSI-based LTILs – experimental method

CV measurements were made on the LTILs at 160 °C using a glassy carbon working electrode (0.031 cm²) or platinum disc working electrode (0.031 cm²), Pt gauze counter electrode (0.063 cm²) and a Ag wire quasi-reference electrode (QRE). For [Me₃NⁿBu][TFSI] and [Me₃NⁿHex][TFSI], electrochemical measurements were also undertaken at 25 °C using the Fc⁺/Fc couple (0.0 V *vs.* Ag/AgNO₃) as an internal standard. Electrochemical windows measured are reported in Table 3.6.1 and Figures 3.6.1 to 3.6.4.

The use of Fc as an internal standard for the high temperature measurements was not possible as Fc sublimes above 120 °C. A Ag wire QRE had to be used instead as standard molten salt electrodes (Cl₂/Cl⁻ or NiF₂/Ni)³⁴ were also not suitable for use with these organic ion based melts. The Ag wire QRE has been used before in molten salts³⁵ and LTIL electrochemistry,³⁶ but it is known to have a fluctuating potential with respect to chemical composition and temperature³⁷ and this was also observed in these LTILs. To take account of this, the anodic limit (corresponding to the oxidation of TFSI) recorded in MeCN solutions, and those of [Me₃NⁿBu][TFSI] and [Me₃NⁿHex][TFSI] liquids recorded at 25 °C, were used as an additional standard for measurements of electrochemical windows in the melts at 160 °C and all measurements reported are calibrated to this anodic limit.

LTIL	Electrochemical window (V) of 0.2 M	Electrochemical window
	solution in MeCN (25 °C)	(V) of melt (160 °C)
[Me ₄ N][TFSI]	-3.0 to + 2.6	-1.8 to + 2.7
[Me ₄ P][TFSI]	-3.2 to +2.6	-2.0 to + 2.7
[Me ₄ As][TFSI]	-3.5 to +2.6	-2.1 to + 2.7
[Me ₄ Sb][TFSI]	-1.7 to + 2.7	-1.6 to + 2.7
[Me ₃ NEt][TFSI]	-2.7 to + 2.7	-2.1 to + 2.7
[Me ₃ N ⁿ Bu][TFSI]	-3.0 to + 2.7	-2.5 to + 2.7
[Me ₃ N ⁿ Hex][TFSI]	-3.2 to + 2.7	-2.3 to + 2.7
[Me ₂ Ph ₂ P][TFSI]	-2.3 to + 2.7	-1.2 to + 2.7
[MePh ₃ P][TFSI]	-2.2 to + 2.7	-1.5 to + 2.7
[Ph ₄ P][TFSI]	-2.1 to + 2.7	-1.4 to + 2.7

Table 3.6.1: Electrochemical windows of TFSI-based LTILs in MeCN as supporting electrolytes and in the molten state at 160 °C

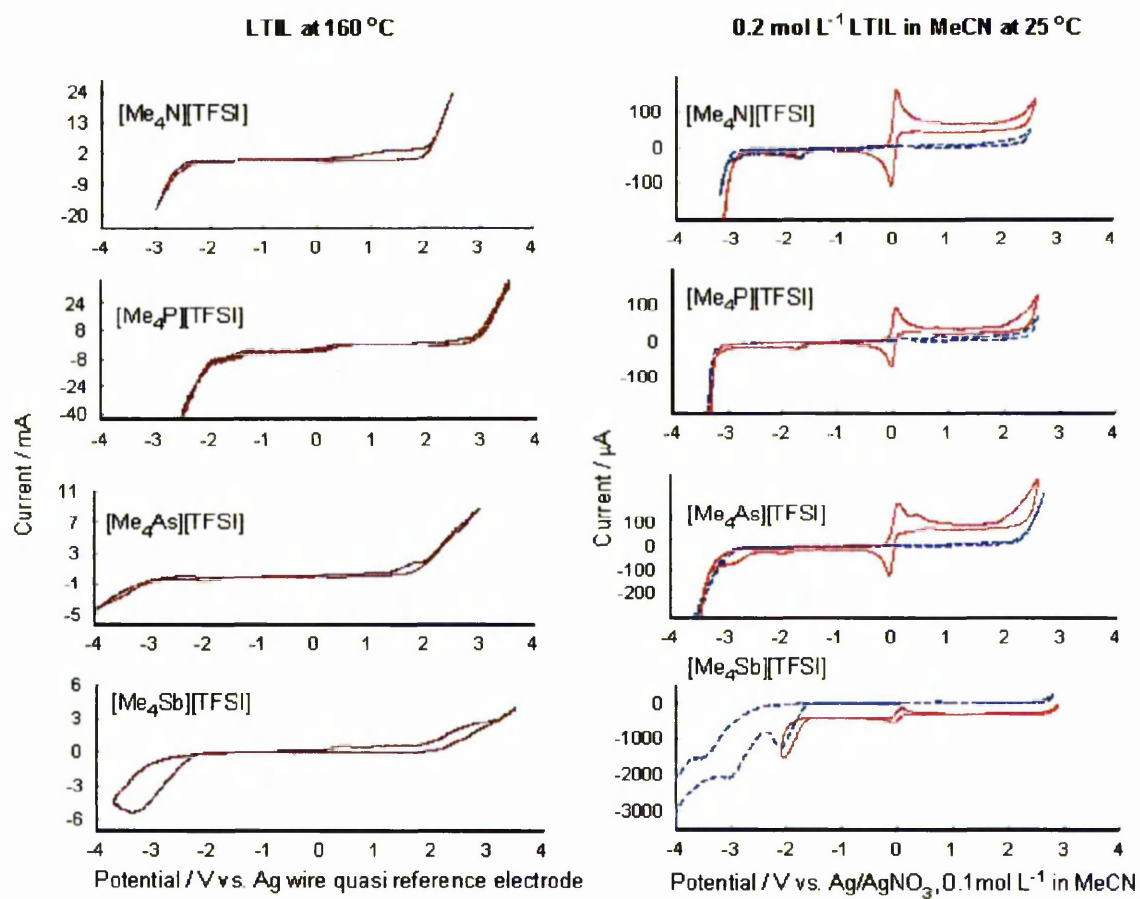


Figure 3.6.1: Electrochemical windows of tetramethyl Group 15-based LTILs in the molten state at 160 °C and as supporting electrolytes in MeCN at 25 °C in the absence (dashed line) and presence (solid line) of Fc

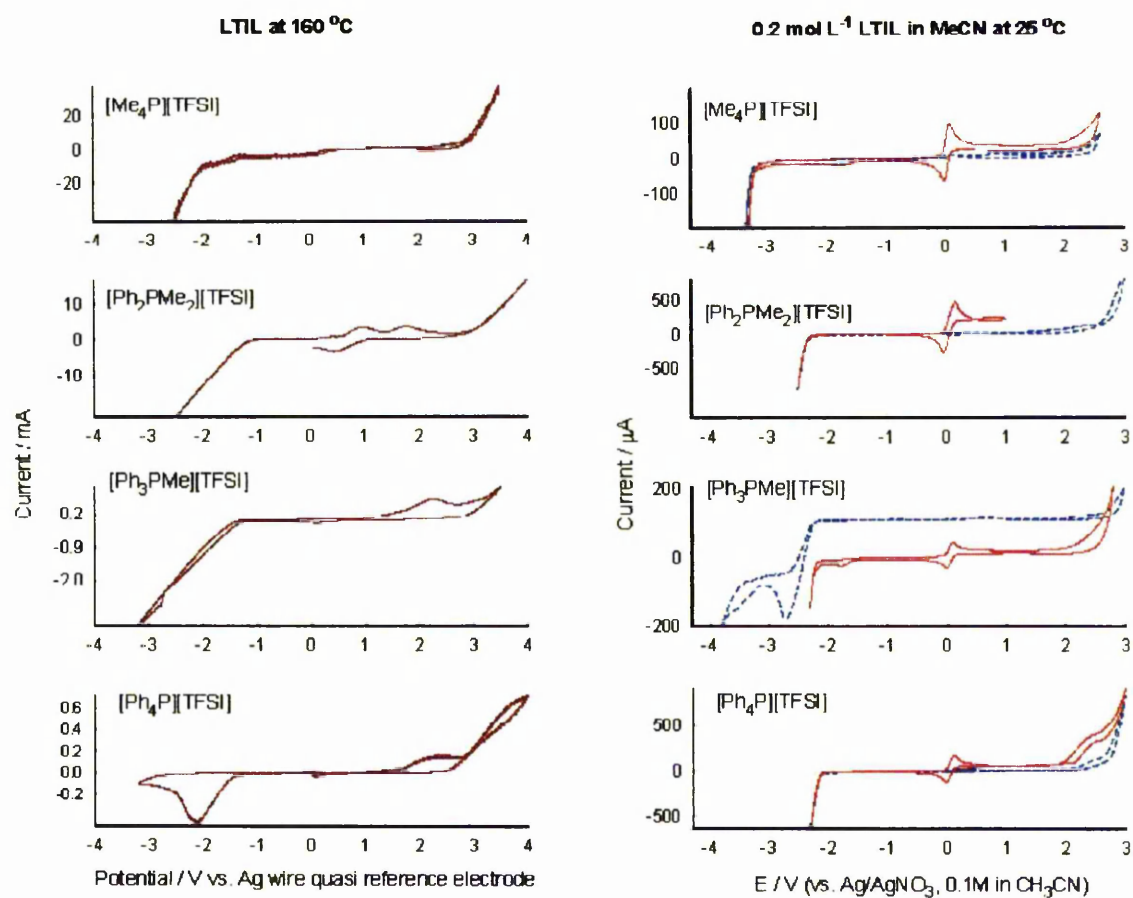


Figure 3.6.2: Electrochemical windows of alkyl/aryl phosphonium-based LTILs in the molten state at 160 °C and as supporting electrolytes in MeCN at 25 °C in the absence (dashed line) and presence (solid line) of Fc

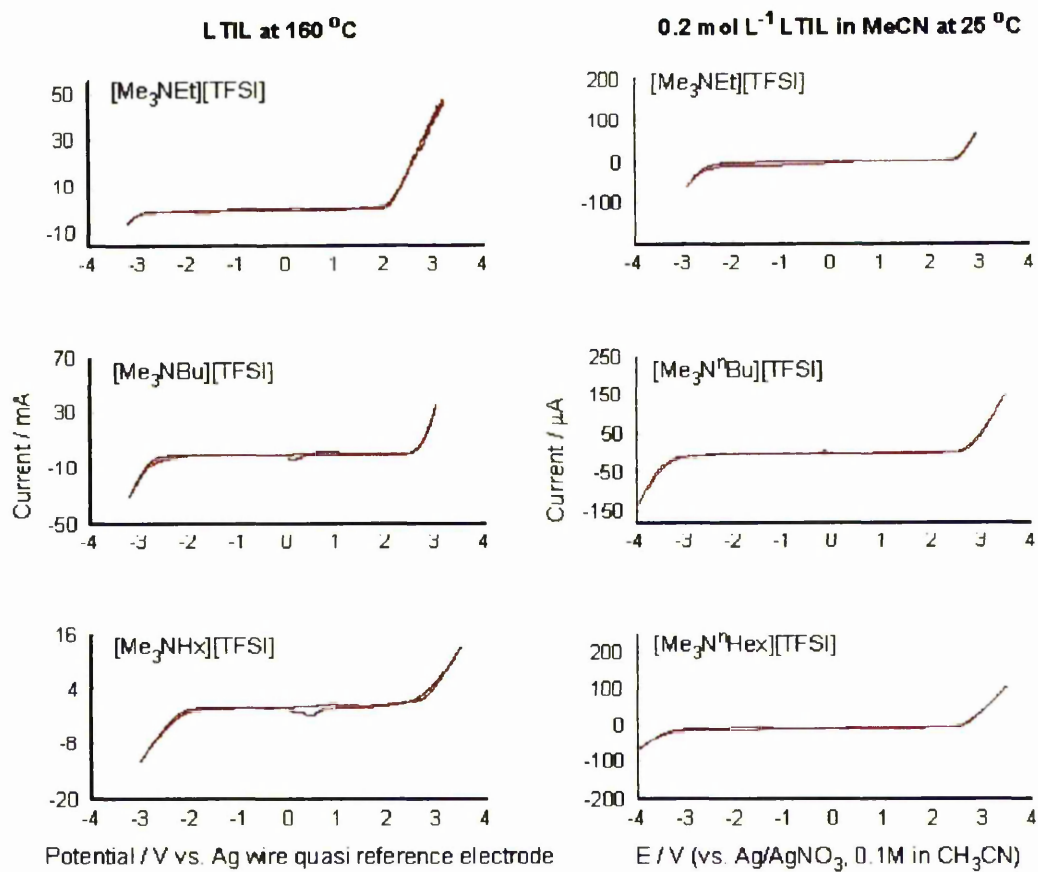


Figure 3.6.3: Electrochemical windows of trimethylalkylammonium-based LTILs in the molten state at 160 °C and as supporting electrolytes in MeCN at 25 °C

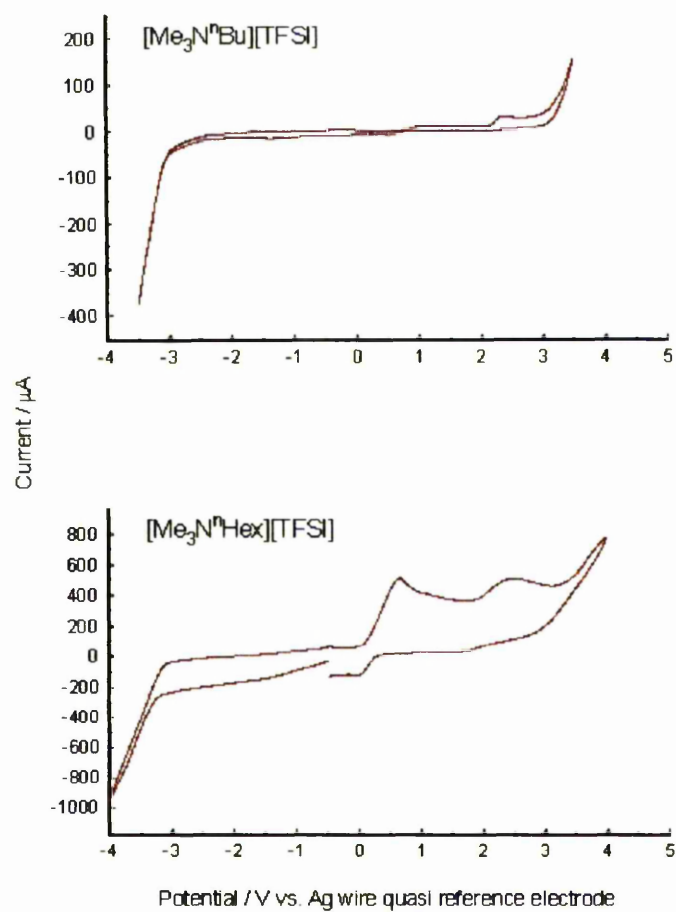


Figure 3.6.4: Electrochemical windows of $[\text{Me}_3\text{N}^n\text{Bu}][\text{TFSI}]$ and $[\text{Me}_3\text{N}^n\text{Hex}][\text{TFSI}]$

LTILs in the molten state at 25 °C

3.6.3 Voltammetry of Li[TFSI] in molten [Me₄P][TFSI] at 190 °C and in MeCN using [Me₄P][TFSI] as supporting electrolyte at 25 °C – experimental method

Li[TFSI] (0.145 g, 0.51 mmol) was dissolved in a solution of [Me₄P][TFSI] in MeCN (0.237 g, 0.64 mmol, 3 mL). A Pt disk working electrode (2 mm dia.), Pt gauze counter electrode and a Ag/AgNO₃ (0.1 mol L⁻¹ in MeCN) reference electrode were used. Prior to CV measurements, the solution was purged with Ar for 30 m. and again for 30 s. in between scans. CVs of Li[TFSI] were calibrated by dissolving Fc (0.090 g, 0.48 mmol) and using the Fc/Fc⁺ couple as an internal standard.

CVs of Li[TFSI] (0.835 g, 2.91 mmol) in molten [Me₄P][TFSI] (5.617 g, 15.1 mmol) were measured inside an inert atmosphere drybox at 190 °C. A Pt disk working electrode (2 mm dia.), Pt gauze counter electrode and a Ag wire QRE were used.

3.6.4 Electrochemical window measurements of TFSI based melts – results and discussion

Going down the Group 15 series from N to Sb, for the [Me₄Z][TFSI] salts (where Z = N, P, As and Sb), the trend in cathodic limits observed in MeCN is reflected in the molten state measurements (Table 3.6.1). The electrochemical window values obtained in the molten state are smaller than those observed for the salts dissolved in MeCN and this is assigned to the effect of increase in temperature and may also be in part due to the

decomposition of trace impurities within the melt decomposing at the working temperatures.

Comparison of cathodic limits of N, P, As and Sb salts shows an increase in cathodic limit going from N to As and a sharp decrease in limit for the Sb salt. The N-As increase is attributed to the decrease in electronegativity in the central Group 15 atom. The sharp decrease in the cathodic limit for Sb is most probably due to the increased metallic nature of the central atom and thus the weakening of the Sb-C bond.

Replacement of Me by Ph groups on the cation leads to a decrease in window size, presumably due to the relative stability of the phenyl radical compared with the methyl radical, formed on the electrochemical decomposition of the cation.³⁸⁻⁴⁰ Additionally, changing from MeCN solvent to a pure melt environment may allow interactions such as π -stacking between phenyl groups on adjacent cations to increase the stabilisation of the phenyl radicals formed. As can be observed from Figure 3.6.2 increasing the number of Ph groups on the cation does not dramatically change the cathodic limit of the LTIL, although a small decrease of *ca.* 100 mV per Ph group is observed.

Increasing the chain length from Me to Et shows an initial decrease in the cathodic limit before increasing as the chain length increases (Et *vs.* ⁿBu and ⁿHex). This is more difficult to explain as there appears to be no direct correlation between the chain lengths and Hammett parameters.^{41,42}

For both the room temperature melts $[\text{Me}_3\text{N}^n\text{Bu}][\text{TFSI}]$ and $[\text{Me}_3\text{N}^n\text{Hex}][\text{TFSI}]$, electrochemical windows were also recorded at room temperature and are shown in Figure 3.6.4. Windows of -3.2 V to +2.7 V for $[\text{Me}_3\text{N}^n\text{Bu}][\text{TFSI}]$ and -3.4 V to +2.7 V for $[\text{Me}_3\text{N}^n\text{Hex}][\text{TFSI}]$ vs. Ag wire QRE were measured. The waves observed in the voltammograms for $[\text{Me}_3\text{N}^n\text{Hex}][\text{TFSI}]$ are due to trace impurities in the melt. The window sizes are comparable to those measured for dialkylimidazolium chloroaluminates and quaternary Group 15 cation based LTILs investigated previously by Costa *et al.*,^{7,9} $[\text{Me}_3\text{N}^n\text{Bu}][\text{TFSI}]$ reported by Bard *et al.*¹⁵ and MacFarlane *et al.*¹⁴ (*ca.* -3.8 V to +1.7 V vs. Ag wire QRE and *ca.* -3.2 V to 2.8 V vs. Ag wire QRE, respectively) and $[\text{Me}_3\text{N}^n\text{Hex}][\text{TFSI}]$ previously reported by Awakura *et al.* (-3.0 to +2.6 V vs. I^-/I_3^-).⁶ Both $[\text{Me}_3\text{N}^n\text{Bu}][\text{TFSI}]$ and $[\text{Me}_3\text{N}^n\text{Hex}][\text{TFSI}]$ due to their high cathodic stabilities and being liquids at room temperature show the most promise for commercial application in electropositive metal deposition *e.g.* U, Pu.

3.6.5 Voltammetry of Li[TFSI] in MeCN using [Me₄P][TFSI] as supporting electrolyte and in molten [Me₄P][TFSI] at 190 °C – results and discussion

The electrochemical windows of the majority of the new Group 15 cation and TFSI anion based LTILs appear to have cathodic limits large enough to support the reduction of U(III) and Pu(III) to the zerovalent state. However, TFSI is a relatively novel anion and its chemical and electrochemical behaviour in comparison with other anions, *e.g.* Cl⁻, NO₃⁻ *etc.*, has thus far not been fully investigated. Ideally the electrochemistry of An and Ln (chemical and electrochemical analogues of the An) should firstly be investigated with TFSI-based complexes and salts in an attempt to simplify the electrochemistry.

The standard reduction potential for the Li(I)/Li(0) reaction is known to be more negative than those of U(III)/U(0) and Pu(III)/Pu(0), -3.0401 V (*vs.* SHE) compared with -1.798 V and -2.031 V (*vs.* SHE) for U and Pu, respectively.⁴³ Therefore, based on the availability of pure reagents (Li[TFSI]) it was decided to investigate the electrochemistry of Li in molten [Me₄P][TFSI] and in MeCN using [Me₄P][TFSI] as supporting electrolyte before attempting to synthesise TFSI complexes of Ln and An.

CVs of Li[TFSI] in MeCN with [Me₄P][TFSI] supporting electrolyte (Figure 3.6.5) show one broad reduction peak at -3.6 V assigned to the Li reduction, and one sharp oxidation peak at -2.9 V assigned to the Li oxidation. The shapes of the waves in the voltammograms are consistent with those expected for the plating/stripping behaviour at

an electrode surface.⁴⁴ The difference between the Li^+/Li reduction and the Fc^+/Fc couple (ca. 3.25 V, Figure 3.6.5) is comparable to the differences in standard potentials of 3.44 V,⁴³ thus suggesting that the proposed assignment is correct.

By comparison, in molten $[\text{Me}_4\text{P}][\text{TFSI}]$ at 190 °C, CVs of $\text{Li}[\text{TFSI}]$ show one reduction peak at -2.5 V assigned to the Li reduction and one oxidation peak at -2.0 V assigning to the Li oxidation (see Figure 3.6.5). The waveshapes are not consistent with those expected for plating of Li on the electrode surface as observed for CVs in MeCN.

Comparison of plots of peak current as a function of square root of scan rate (Randles-Sevcik plots) for both the reduction peak and the oxidation peak (see Figure 3.6.6), show that the Li reduction is diffusion controlled, whereas the oxidation is not. Li metal is also known to have a melting point of 180.5 °C,⁴³ thus based on the reaction temperature (190 °C) it is hypothesised that upon reduction to Li metal, liquid metal is formed at the electrode surface (presumably as small droplets). This would account for the diffusion controlled reduction process and the non-diffusion controlled oxidation as well as the waveshapes observed in the CV.

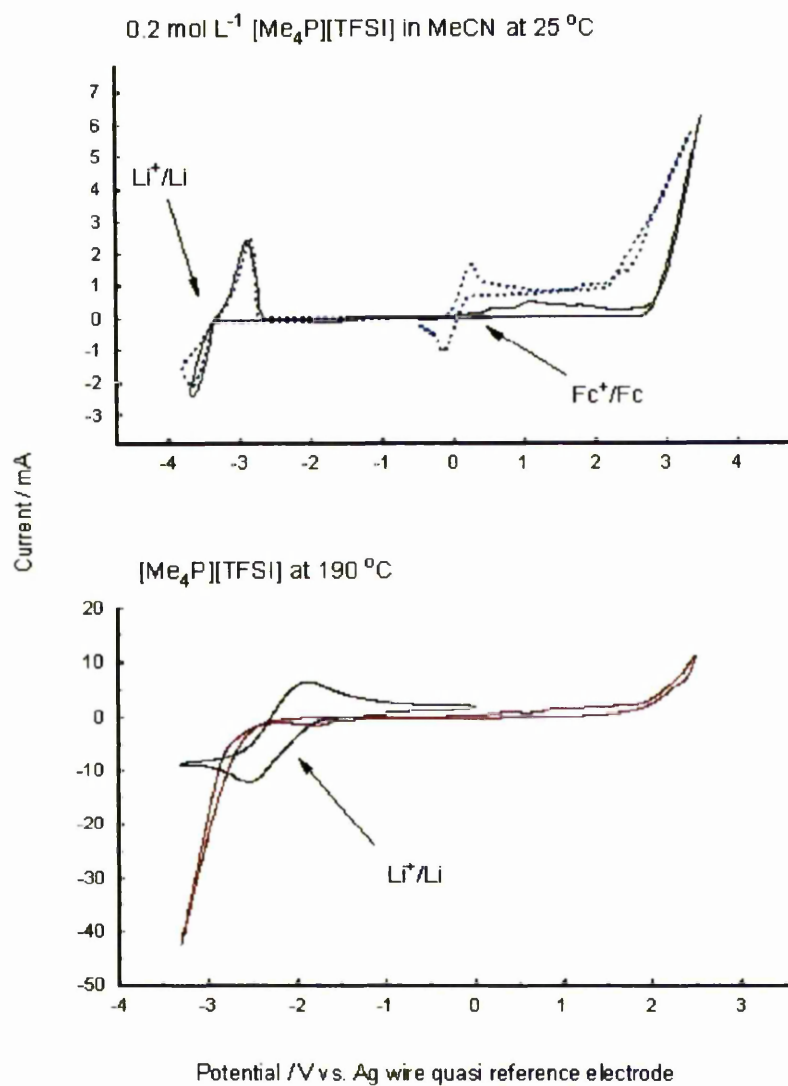


Figure 3.6.5: CVs of Li[TFSI] in molten [Me₄P][TFSI] (also shown [Me₄P][TFSI] without Li[TFSI] present, red line) and in MeCN using [Me₄P][TFSI] as supporting electrolyte in the presence (dashed line) and absence (solid line) of Fc

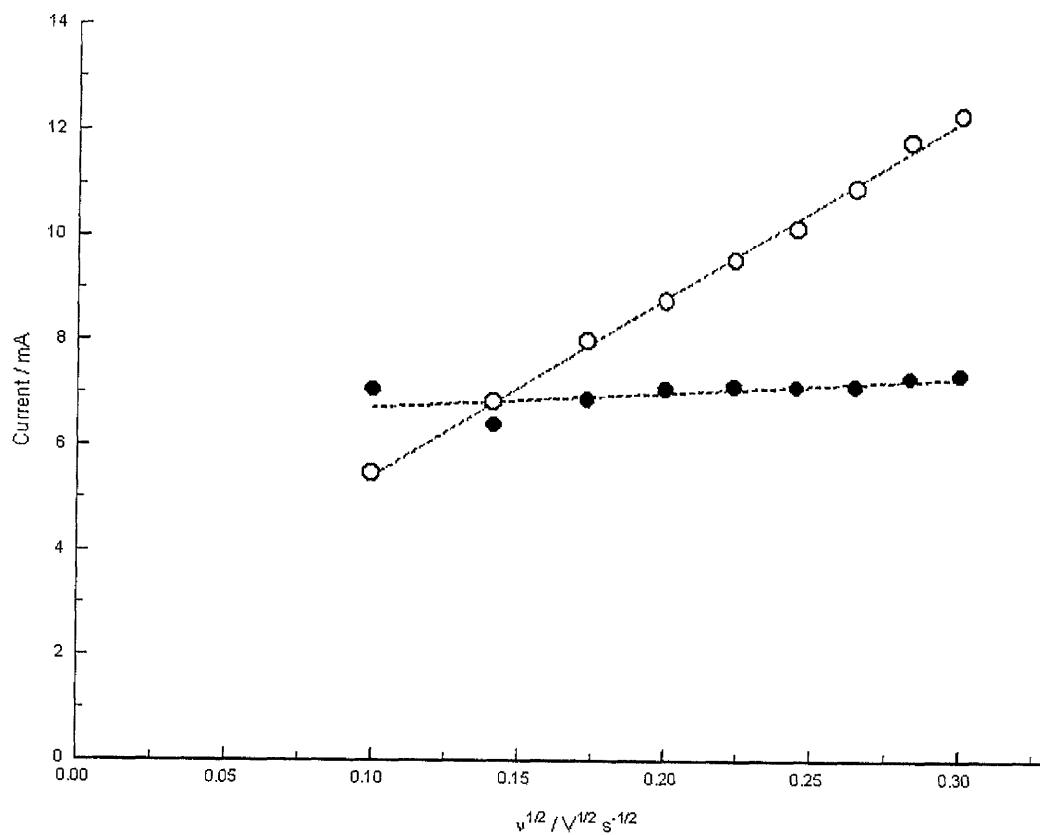


Figure 3.6.6: Plots of I_p vs. $v^{1/2}$ for the reduction (open circles) and oxidation (filled circles) processes for Li[TFSI] in molten $[Me_4P][TFSI]$ at 190 °C

3.7 Density functional theory calculations of electrochemical windows of TFSI based LTILs in MeCN

3.7.1 Introduction

The cathodic limit for the electrochemical windows of the TFSI-based LTILs in MeCN has been calculated using Density Functional Theory (DFT) and the results are presented in Table 3.7.1. All of these calculations were performed by Dr H. Steele of the Department of Chemistry, The University of Manchester. A more detailed description of this computational study is presented elsewhere.⁴⁵

Redox potentials can be calculated independently of experimental data using a free energy cycle, where the solvated reduction free energy is calculated using:⁴⁶

$$\Delta G_{\text{red}}^{\circ} = \text{EA}(X^{+}) + \Delta G_{\text{evr,gas}}(X^{+} + e^{-} \rightarrow X^{\bullet}) + \Delta G_{\text{s}}^{\circ}(X^{\bullet}) - \Delta G_{\text{s}}^{\circ}(X^{+})$$

where EA is the electron affinity; $\Delta G_{\text{evr,gas}}(X^{+} + e^{-} \rightarrow X^{\bullet})$ is the change in thermal contributions to the solute free energy arising from changes in the electronic, vibrational and rotational partition functions upon reduction; $\Delta G_{\text{s}}^{\circ}$ is the aqueous free energy of solvation; X^{+} and X^{\bullet} are the cation of interest and its reduced form; $\Delta G_{\text{red}}^{\circ}$ is the half-cell reduction free energy, which can be compared with the experimental potentials:

$$\Delta G_{\text{red}}^{\circ} = -nFE_{\text{red}}^{\circ}$$

$$\text{and } E_{\text{red}} = E_{\text{red}}^{\circ} + \frac{RT}{nF} \ln \frac{[\text{ox}]}{[\text{red}]}$$

3.7.2 Experimental

All calculations were performed using the standard Gaussian98 suite of programs.⁴⁶ Gas phase molecular geometries for the four tetramethyl cations were optimised at the DFT and MP2⁴⁷ levels of theory using both restricted and unrestricted formalisms. For the largest molecules, MP2 calculations were not performed. All DFT calculations made use of the hybrid Becke (B3)⁴⁸ exchange function and the correlation function of Lee, Yang and Parr (LYP).⁴⁹ For all DFT structures, expectation values of the square of the electron spin operator $\langle S^2 \rangle$ for the radical ions were all within the expected value of 0.75 by ± 0.02 , which indicates negligible spin contamination by incorrect spin multiplicities. The 6-31G, 6-31G* and 6-31++G* basis sets were used for all the light elements, whereas the much heavier Sb atoms were represented by a relativistic electron core pseudo-potential.⁵⁰

The experimental data were referenced to the Fc/Fc⁺ couple and all calculated values thermally corrected, but not referenced to any half-cell. Therefore, a constant must be subtracted from the calculated data to reference it to the Fc/Fc⁺ couple. For the standard hydrogen electrode (SHE) the absolute potential has been determined experimentally to be +4.43 eV,^{51,52} the more commonly used standard is the calomel electrode (SCE) that is 0.2412 V⁵³ more positive. The Fc⁺/Fc couple has been calculated to be 0.31 V⁵⁴ more

positive than the SCE, hence the final value required subtraction of 4.9812 V. The concentration of the ionic liquid is also non-standard but this can also be accounted for using the Nernst equation. In addition, there is a correction for non-standard concentration effects and a correction value of 0.04 V must be subtracted.

3.7.3 Discussion

A comparison between the calculated reduction potentials for the Group 15 cations and the experimentally observed values of the cathodic limit is shown in Figure 3.7.1. Overall the absolute calculated values are not directly comparable to the experimentally measured potentials, although the same trends as observed for the experimental data is reflected in the calculated potentials. In most cases there is a better agreement between the experimental and calculated values for the B3LYP level of theory than for the MP2 level. Interestingly, the trend of increased cation stability on increasing alkyl chain length ($[\text{Me}_3\text{N}^+\text{Hex}] > [\text{Me}_3\text{N}^+\text{Bu}] > [\text{Me}_3\text{NEt}]$) is not observed to the same extent computationally at either the B3LYP or MP2 levels, indicating that the differences may be due to experimental error (most probably due to trace impurities in the melts). Both levels of theory also greatly overestimate the electrochemical stability of the $[\text{Me}_4\text{Sb}]^+$ cation in comparison with the experimentally observed values (especially at the MP2 level). However, calculations do predict the experimental observation that the $[\text{Me}_4\text{Sb}]^+$ cation is less stable than the N, P and As analogues. Finally, the B3LYP level calculations predict the decrease in phosphonium cation stability on substitution of methyl groups by phenyl groups.

The most notable disagreement between the experimental reduction potentials and theoretical is for the antimony tetramethyl cation. No improvement was found using a different pseudopotential on the Sb centre. The MP2 correlation method predicted the reduction potential to be more negative than that from B3LYP. Two electron processes and quartet excited states were also considered, but no better agreement could be achieved.

Cation	EA /eV		$\Delta G_{\text{red}}^{\circ}$ /eV		E_{cell} /V		Experimental value
	B3LYP	MP2	B3LYP	MP2	B3LYP	MP2	
[Me ₄ N] ⁺	-3.16	-2.77	-1.21	-0.92	-3.67	-3.96	-3.0
[Me ₄ P] ⁺	-3.01	-2.67	-1.28	-1.18	-3.60	-3.70	-3.2
[Me ₄ As] ⁺	-2.99	-2.66	-1.19	-1.11	-3.69	-3.77	-3.5
[Me ₄ Sb] ⁺	-3.20	-2.71	-1.39	-1.27	-3.49	-3.61	-1.7
[Me ₃ NEt] ⁺	-2.99	-2.61	-1.12	-1.13	-3.76	-3.75	-2.7
[Me ₃ N ^{''} Bu] ⁺	-2.89	-2.51	-1.05	-1.04	-3.83	-3.84	-3.0
[Me ₃ N ^{''} Hex] ⁺	-2.86	-2.49	-1.04	-1.02	-3.84	-3.86	-3.2
[Me ₂ PPh ₂] ⁺	-3.31		-1.88		-3.00		-2.3
[MePPh ₃] ⁺	-3.27		-1.91		-2.97		-2.2
[PPh ₄] ⁺	-3.36		-2.10		-2.78		-2.1

Table 3.7.1: Calculated electron affinities (EA / eV), free energy half-cell reduction potentials ($\Delta G_{\text{red}}^{\circ}$ / eV) and cell potentials (E_{cell} / V), with experimental values given for reference.

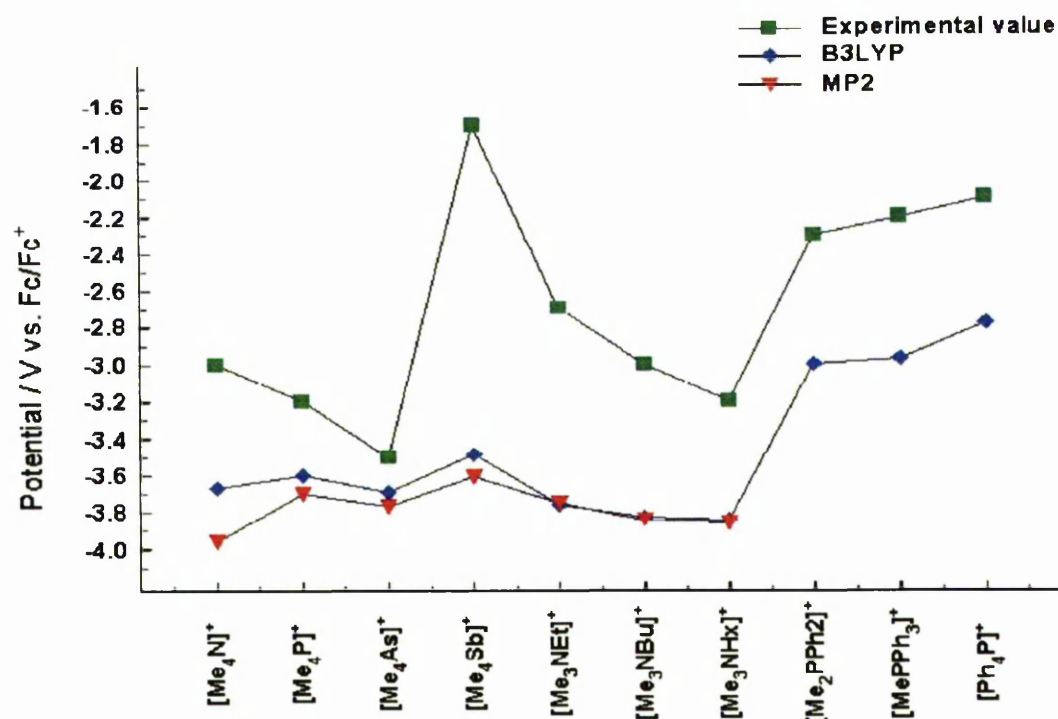


Figure 3.7.1: Comparison of experimentally measured and calculated cathodic limits using the B3LYP and MP3 methods

3.8 Radiation stability of LTILs

From the electrochemical measurements it would appear that the two room temperature melts, $[\text{Me}_3\text{N}^n\text{Bu}][\text{TFSI}]$ and $[\text{Me}_3\text{N}^n\text{Hex}][\text{TFSI}]$, have electrochemical windows large enough to support the electrochemical reduction of U(III) (see Chapter 5) and Pu(III) to the zerovalent state. These RTILs show promise for use with nuclear fuel's processing providing that they can withstand high radiation fields.

A sample of $[\text{Me}_3\text{N}^n\text{Bu}][\text{TFSI}]$ (3 mL), was sealed inside a glass tube *in vacuo* and irradiated with γ -radiation from a ^{60}Co source for 4 h (Raditech, Oxford, UK) with a total γ -dose of 40 kGy. After irradiation, the sample was analysed using TGA, IR, and electrospray ionisation mass spectroscopy (at the CRR, Department of Chemistry, University of Manchester and the Department of Chemistry, University of Manchester). The analysis results are summarised in Table 3.8.1 and the mass spectra are shown in Figure 3.8.1.

Technique	Pre-irradiation		Post-irradiation	
mass spectroscopy	$\text{E}^- = 280$ (100 %)	$[\text{TFSI}]^-$	$\text{E}^- = 280$ (100 %)	$[\text{TFSI}]^-$
	$\text{E}^+ = 116$ (100 %)	$[\text{Me}_3\text{N}^n\text{Bu}]^+$	$\text{E}^+ = 116$ (100 %)	$[\text{Me}_3\text{N}^n\text{Bu}]^+$
TGA	$T_{\text{dec}} = 420$ °C,		$T_{\text{dec}} = 420$ °C,	
	mass loss = 100 %		mass loss = 100 %	
IR	1346, 1176, 1134, 1051, 931,		1346, 1177, 1134, 1051, 931,	
	909, 789, 762, 740, 654, 613,		909, 789, 762, 740, 654, 613,	
	569, 511		569, 511	

Table 3.8.1: Characterisation of $[\text{Me}_3\text{N}^n\text{Bu}][\text{TFSI}]$ after 4 h irradiation with a ^{60}Co source (10 kGy h^{-1} dose rate)

As is shown in Table 3.8.1, there are no differences between the sample before irradiation and after irradiation, and any products formed due to decomposition of the LTIL during irradiation, were below the detection limits of the spectroscopic techniques used. Thus it is concluded that $[\text{Me}_3\text{N}^n\text{Bu}][\text{TFSI}]$ is stable to γ -radiation up to 10 kGy/h dose rates.

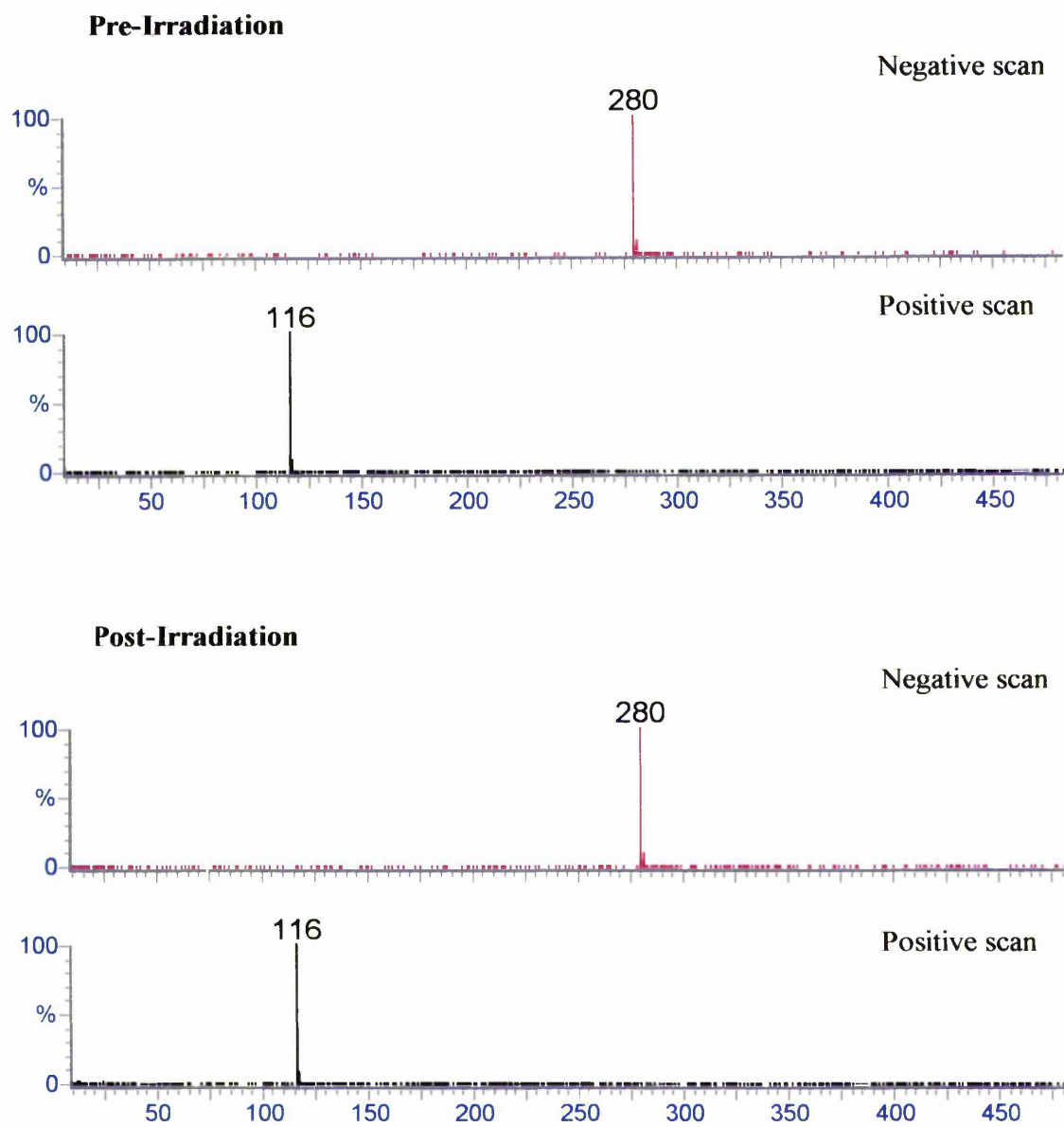


Figure 3.8.1 Mass spectra of pre- and post-irradiated $[\text{Me}_3\text{N}^n\text{Bu}][\text{TFSI}]$

3.9 Summary

A number of novel LTILs based on quaternary Group 15 cations and the TFSI anion have been synthesised and characterised using elemental and melting point analyses, TGA, mid-IR and NMR spectroscopies and in the case of [Me₄P][TFSI] and [Me₄Sb][TFSI] single crystal X-ray crystallography. TGA analysis shows all the LTILs synthesised to be stable to at least 320 °C. Vibrational spectroscopy has identified bands due to both the pnitcogen-based cation and TFSI.

X-ray diffraction studies show that for [Me₄Sb][TFSI], the bond lengths and angles of TFSI are comparable to those previously reported in the literature for [Mg(H₂O)₆][TFSI]₂.2H₂O,²⁷ [Cu(CO)₂TFSI],²⁸ Li[TFSI],²⁹ K[TFSI],³⁰ HTFSI,³⁰ Li[TFSI].H₂O,²³ Na[TFSI].H₂O.MeOH,²³ Rb[TFSI].H₂O,²³ Cs[TFSI]²³ and 1-ethyl-2-methyl-C-3-benzyl imidazolium [TFSI].³¹ The lack of any close interactions between the cation and anion results in the low melting points observed. For [Me₄Sb][TFSI], the cation/anion interactions are slightly shorter than those observed for 1-ethyl-2-methyl-C-3-benzyl imidazolium [TFSI] (O, N and F interactions with H are *ca.* 2.4 *vs.* 2.6 Å, 2.5 *vs.* 2.7 Å and 2.5 *vs.* 2.55 Å, respectively) and this may in part explain the higher melting point of [Me₄Sb][TFSI] (142.6 – 144.2 °C) compared to the imidazolium salt (*ca.* 50 °C). The CF₃ groups in TFSI have a *transoid* conformation with respect to the SNS plane, as previously observed by Pennington *et al.*²³ for Li[TFSI].H₂O, Na[TFSI].H₂O.MeOH, Rb[TFSI].H₂O and Cs[TFSI].

The electrochemical windows of these new LTILs have been measured in the molten state and as supporting electrolytes in MeCN and in most cases wide windows are observed (-2.1 to +2.7 V vs. Ag wire QRE and -3.5 to +2.6 V vs. Ag/AgNO₃ for [Me₄As][TFSI]). The effects of changing the central atom and alkyl/aryl substituents in the quaternary Group 15 cation has been investigated. The results show that an increase in cathodic limit is observed going from N-P-As before a sharp decrease at Sb.

Additionally, increases in chain length (Et to ⁿHex) also show an increase in cathodic limits (after an initial decreases from Me to Et). The results also show that addition of Ph groups to the cation, greatly reduce the size of the electrochemical window due to the lower cathodic stability of the Ph groups compared to alkyl groups. Both the room temperature melts, [Me₃NⁿBu][TFSI] and [Me₃NⁿHex][TFSI], have wide electrochemical windows at room temperature comparable to those measured for 1,3-dialkylimidazolium chloroaluminates. However, the two TFSI salts benefit from greater air and moisture stability and the Lewis acidity of anion does not affect the LTIL properties, as in the case of the chloroaluminate salts. The observation of Li reduction in [Me₄P][TFSI] suggests that these salts have cathodic limits wide enough to observe the reduction of U(III) and Pu(III) to the zerovalent state and are thus suitable for electrodeposition of these two metals.

The stability to γ -radiation of [Me₃NⁿBu][TFSI] has also been investigated. The results show that this molten salt is stable to radiation doses of a minimum of 10 kGy h⁻¹ dose rates. Thus suggesting that this LTIL is a suitable candidate for use in the nuclear fuels industry and further investigations of *f*-element electrochemistry in this melt.

3.10 References

1. A. E. Bradley, A. Haile, J. E. Hatter, W. R. Pitner, D. W. Sanders, K. R. Seddon, R. C. Thied, *BNFL Internal Report – Progress and Current Status of Ionic Liquids Project*, SAP No: 10/00342.03.02.
2. A. E. Bradley, *BNFL Internal Report – Processing of Spent Nuclear Fuel Using Ionic Liquids*.
3. W. R. Pitner, A. E. Bradley, D. W. Sanders, K. R. Seddon, R. C. Thied, J. E. Hatter, *NATO ASI Ser., Ser. 2*, 2003, **92** (Green Industrial Applications of Ionic Liquids), 209.
4. A. J. Bard, L. R. Faulkner, *Electrochemical Methods: Fundamentals and Applications*, John Wiley & Sons Inc., USA, 2001.
5. R. T. Carlin, J. Fuller, *Molten Salts From Fundamentals to Applications*, Ed. M. Guane-Escard, Kluwer Academic Publishers, The Netherlands, 2002.
6. K. Murase, K. Nitta, T. Hirato, Y. J. Awakura, *J. Applied Electrochem.*, 2001, **31**, 1089.
7. D. A Costa, W. H. Smith, *Los Alamos yearly report*, LA-UR-99-5521, 1999.
8. J. G. Huddleston, A. E. Visser, W. M. Riechert, H. D. Willauer, A. G. Broker, R. D. Rogers, *Green Chem.*, 2001, **3**, 156.
9. K. D. Abney, E. Bluhm, E. Garcia, W. H. Smith, M. Barr, W. Oldham, D. A. Costa, D. Morris, D. Tait, *Los Alamos yearly report*, LA-UR-00-5043, 2000.
10. P. Bonhote, A.-P. Dias, N. Papageorgiou, K. Kalyanasundaram, M. Graetzel, *Inorg. Chem.*, 1996, **35**, 1168.

11. (a) D. R. MacFarlane, J. Sun, J. Golding, P. Meakin, M. Forsyth, *Electrochim. Acta*, 2000, **45**, 1271.; (b) H. L. Ngo, K. LeCompte, L. Hargens, A. B. McEwen, *Thermochim. Acta*, 2000, **357**, 97.
12. B. M. Quinn, Z. Ding, R. Moulton, A. J. Bard, *Langmuir*, 2002, **18**, 1734.
13. D. Allen, G. Baston, A. E. Bradley, T. Gorman, A. Haile, I. Hamblett, J. E. Hatter, M. J. F. Healey, B. Hodgson, R. Lewin, K. V. Lovell, B. Newton, W. R. Pitner, D. W. Rooney, D. Sanders, K. R. Seddon, H. E. Sims, R. C. Thied, *Green Chem.*, 2002, **4**, 152.
14. D. R. MacFarlane, J. Sun, J. Golding, P. Meakin, M. Forsyth, *Electrochim. Acta*, 2000, **45**, 1271.
15. B. M. Quinn, Z. Ding, R. Moulton, A. J. Bard, *Langmuir*, 2002, **18**, 1734.
16. I. Rey, P. Johansson, J. Lindgren, J. C. Lassègues, J. Grondin, L. Servant, *J. Phys. Chem. A*, 1998, **102**, 3249.
17. I. Rey, J. C. Lassègues, J. Grondin, L. Servant, *Electrochim. Acta*, 1998, **43**, 1505.
18. R. M. Silverstein, G. C. Bassler, T. C. Morrill, *Spectrometric identification of organic compounds – 5th Ed.*, John Wiley & Sons Inc., USA, 1991.
19. A. Kornath, O. Blecher, F. Neumann, J. Ludwig, *J. Mol. Spec.*, 2003, **219**, 170.
20. M. Gerkin, P. Kolb, A. Wegner, H. P. A-. Mercier, H. Bormann, D. A. Dixon, G. J. Schrobilgen, *Inorg. Chem.*, 2000, **39**, 2813.
21. W. J. Casteel Jr., P. Kolb, N. LeBond, H. P. A-. Mercier, G. J. Schrobilgen, *Inorg. Chem.*, 1996, **35**, 929.
22. J. Foropoulos Jr., D. D. DesMarteau, *Inorg. Chem.*, 1984, **23**, 370.

23. L. Xue, C. W. Padgett, D. D. DesMarteau, W. T. Pennington, *Solid State Sciences*, 2002, **4**, 1535.
24. M. Wilczek, W. Komiski, K. Jackowski, *Chem. Phys. Lett.*, 2002, **358**, 263.
25. E. Kupě, E. Liepiņš, A. Lapsiņa, I. Urtāne, G. Zelāns, E. Lukevics, *J. Organomet. Chem.*, 1985, **279**, 343.
26. J. M. Schulman, T. Venanzi, *J. Am. Chem. Soc.*, 1976, **98**, 4701.
27. A. Haas, Ch. Klare, P. Betz, J. Bruckman, C. Krüger, Y. Tsay, F. Aubke, *Inorg. Chem.*, 1996, **35**, 1918.
28. O. G. Polyakov, S. M. Ivanova, C. M. Gaundinski, S. M. Miller, O. P. Anderson, S. H. Strauss, *Organomet.*, 1999, **18**, 3769.
29. J. L. Nowinski, P. Lightfoot, P. G. Bruce, *J. Mater. Chem.*, 1994, **4**, 1579.
30. Z. ák, A. Rika, Ch. Michot, *Z. Kristallogr.*, 1998, **213**, 217.
31. J. J. Golding, D. R. MacFarlane, L. Spiccia, M. Forsyth, B. W. Skelton, A. H. White, *Chem. Commun.*, 1998, 159.
32. R. Arnaud, D. Benrabah, J.- Y. Sanchez, *J. Phys. Chem.*, 1996, **100**, 10882.
33. R. R. Gagné, C. A. Koval, G. C. Lisensky, *Inorg. Chem.*, 1980, **19**, 2845.
34. Y. Castrillejo, M. R. Berjemo, R. Pardo, A. M. Martinez, *J. Electroanal. Chem.*, 2002, **522**, 124
35. D. L. Manning, J. M. Dale, G. Mamantov, *Nucl. Sci. Abstr.*, 1964, **18**, 5849.
36. A. M. Bond, V. M. Hultgren, A. W. A. Mariotti, A. G. Wedd, *Anal. Chem.*, 2002, **74**, 3151.
37. S. A. Kuznetsov, *Molten Salts From Fundamentals to Applications*, Ed. M. Guane-Escard, Kluwer Academic Publishers, The Netherlands, 2002.

38. R. T. Morrison, R. N. Boyd, *Organic Chemistry - 5th Ed.*, Allyn and Bacon, 1987
39. F. O. Rice, *J. Am. Chem. Soc.*, 1931, **53**, 1959.
40. J. A. Kerr, *Chem. Rev.*, 1966, **66**, 465.
41. Treichel, P. M.; Mueh, H. J. *Inorg. Chem.* 1977, **16**, 1167.
42. Chum, H. Li.; Dockal, E. R.; Rabockai, T. J. *Electroanal. Chem.* 1975, **63**, 197.
43. *CRC Handbook of Chemistry and Physics*, Ed. D. R. Lide, CRC Press, Inc., USA, 1995.
44. D. J. Schiffrin, *J. Electroanal. Chem.*, 1986, **201**, 199.
45. A. I. Bhatt, I. May, H. M. Steele, V. A. Volkovich, D. Collison, M. Helliwell, I. H. Hillier, N. E. Ertok, B. Lewin, *Submitted for publication to Dalton Trans.*
46. M. J. Frisch G. W. Trucks, H. B. Schlegel, G. E. Scuseria, M. A. Robb, J. R. Cheeseman, V. G. Zakrzewski, J. A. Montgomery, R. E. Stratmann, J. C. Burnant, S. Dapprich, J. M. Millam, A. D. Daniels, K. N. Kudin, M. C. Strain, O. Farakas, J. Tomasi, V. Barone, M. Cossi, R. Cammi, B. Mennucci, C. Pomelli, C. Adamo, S. Clifford, J. Ochterski, G. A. Petersson, P. Y. Ayala, Q. Cui, F. Morokuma, D. K. Malick, A. D. Rabuck, K. Raghavachari, J. B. Foresman, J. Cioslowski, J. V. Ortiz, B. B. Stefanov, G. Lui, A. Liashenko, P. Piskorz, I. Komaromia, R. Gomperts, R. L. Martin, R. D. J. Fox, T. Keith, M. A. Al-Laham, C. Y. Peng, A. Nanayakkara, C. Gonzalez, M. Challacombe, P. M. W. Gill, B. G. Johnson, W. Chen, M. W. Wong, J. L. Andres, M. Head-Gordon, E. S. Replogle, J. Pople, *Gaussian 98*, Gaussian, Inc., Pittsburgh PA.
47. W. J. Hehre, L. Radom, P. V. R. Schleyer, J. A. Pople, *Ab Initio Molecular Orbital Theory*, John Wiley & Sons, New York, 1986.

48. A. D. Becke, *J. Chem. Phys.*, 1996, **98**, 5648.
49. C. Lee, W. Yang, R. G. Parr, *Phys. Rev. B*, 1988, **37**, 785.
50. G. Igel-Mann, H. Stoll, H. Preuss, *Mol. Phys.*, 1988, **65**, 1321.
51. C. Lim, D. Bashford, M. Karplus, *J. Phys. Chem.*, 1991, **95**, 5610.
52. H. Reiss, A. Heller, *J. Phys. Chem.*, 1985, **89**, 4207.
53. P. H. Rieger, *Electrochemistry*, Prentice-Hall, Inc., New Jersey, 1987.
54. K. Daasbjerg, S. U. Pedersen H. Lund, *General Aspects of the Chemistry of Radicals*, Ed. Alfassi, Z.B., John Wiley & Sons, Chichester, 1999.

CHAPTER 4

SYNTHESES, STRUCTURE AND ELECTROCHEMISTRY OF LANTHANIDE BIS(TRIFLUOROMETHANESULFONYL) AMIDES

4.1 Introduction

LTILs based on group 15 tertiary alkyl ammonium cations and the TFSI anion (see Chapter 3) would appear to have electrochemical windows large enough to support the electrochemical reduction of U(III) and Pu(III) to the zerovalent state. The electrochemistry and synthetic methodology is best developed through non-radioactive analogues before moving on to U and Pu. In addition, both U and Pu have extensive and complicated redox chemistry (see Chapter 5), which has made previous studies of their electrochemistry in ionic liquids challenging.¹⁻⁵

The trivalent lanthanides are commonly used non-radioactive analogues to the trivalent actinides, both series comprising *f*-element cations of large ionic radius where electrostatic bonding dominates. The similar ionic radii and coordination number of the lanthanides and actinides also allows meaningful comparisons of information about electrochemical diffusion processes in the ionic liquid to be made. Finally, if the Ln(III)/Ln(0) reduction is observed in the LTIL media then in principle the An(III)/An(0) reduction should also be observed (An = U, Pu), as the standard reduction potentials for the Ln(III)/Ln(0) reduction are more negative than the corresponding An(III)/An(0) potentials (An = U, Pu, see Chapter 1).

There are reports of lanthanide electrochemistry in a range of solvent systems, including ionic melts. Gilbert *et al.* have studied the electrochemical behaviour of Ln(III)/Ln(II) reduction in NaCl/AlCl₃ melts (175 °C) and in 1-*n*-butylpyridinium chloride/AlCl₃

(40 °C) (Ln = Eu, Yb, Tm and Sm).⁶⁻⁸ After extensive study they found that the stability of the lanthanide(II) ion (with respect to the Ln(III) ion) depends on the Lewis acidity of the melt and that speciation is temperature dependent.

Peterson and Varlaskin have observed the reduction of trivalent lanthanides (Eu, Yb and Sm) to the divalent oxidation state at room temperature in dimethyl sulfoxide.⁹ Miles and Fletcher have observed the formation of lanthanide oxides at 180 °C in molten $\text{LiNO}_3/\text{KNO}_3$.¹⁰ In this system the lanthanides form metal-nitrato complexes and the metal oxide is formed *via* lanthanide oxide/nitrate complexes. This behaviour has been observed for a number of different trivalent lanthanides (La, Eu, Ce, Pr, Nd, Sm, Gd, Tb and Yb).¹⁰

In low temperature ionic liquids, Tsuda and Ito have investigated the electrochemical behaviour of lanthanum in 1-ethyl-3-methylimidazolium chloride ([emim]Cl)/ AlCl_3 melts.¹¹ They have demonstrated the electrodeposition of aluminium in a LaCl_3 saturated melt and the deposition of La-Al alloys. Gau and Sun have studied the electrochemistry and spectroscopy of Eu(III) and Eu(II) (electrochemically generated) in [emim]Cl/ AlCl_3 melts.¹² The authors explored the speciation of the Eu ion in the melt using electronic absorption spectroscopy and postulate Eu(III) exists as $[\text{EuCl}_6]^{3-}$. Although the speciation of the Eu(II) ion would appear to be dependant on the Lewis acidity of the melt.

The speciation of Eu has also been investigated in the LTIL, 1-butyl,3-methylimidazolium hexafluorophosphate by Billard and co-workers.¹³ Using electronic

absorption spectroscopy, they found that Eu(II) is stable in this melt. Attempts at chemically oxidising dissolved EuI₂ in this LTIL using K₂CrO₇, Ce(SO₄)₂ or O₂ showed no changes in the UV/vis spectrum. Indeed, the authors noted that after several months in air, solutions of EuI₂ in this LTIL showed no significant oxidation to the trivalent state and have rationalised this result by the low miscibility of water in this particular imidazolium based melt.

Finally, in 2003 Dormond *et al.* reported on the synthesis of Ln(TFSI)₃.xH₂O (where Ln = La, Nd and Yb).¹⁴ The authors explored the catalytic activity of these compounds using amongst other reactions, the Friedal-Crafts acetylation of anisole in acetic acid-acetic anhydride media. They found these new complexes to be efficient catalysts for the reaction tested with a yield of *ca.* 95%.¹⁴

4.2 Synthesis of lanthanide bis(trifluoromethanesulfonyl)amides

4.2.1 General considerations

Lanthanide bis(trifluoromethanesulfonyl)amides were synthesised using standard inert atmosphere Shlenck line techniques. The synthesised compounds readily absorbed water from the atmosphere and so were stored and manipulated under Ar in an inert atmosphere drybox. Samples for elemental analysis were prepared by sealing *ca.* 5-10 mg of sample in an aluminium capsule under Ar prior to measurements. However, due to a lack of inert atmosphere facilities, all elemental analysis measurements were performed in air.

4.2.2 *Triaqua tris{bis(trifluoromethanesulfonyl)amide} lanthanum(III) –*

[La(TFSI)₃(H₂O)₃]

A solution of HTFSI (8.75 g, 31.1 mmol) in H₂O (5 mL) was added to a suspension of La₂O₃ (1.71 g, 5.2 mmol) in H₂O (5 mL), with stirring. After 10 m excess H₂O was removed from the resultant clear solution by heating at 95 °C under reduced pressure using a rotary evaporator. The resultant wet colourless solid was transferred to a high vacuum line to remove the remaining water *in vacuo* by heating at 80 °C.

[La(TFSI)₃(H₂O)₃] was obtained as a hygroscopic, colourless, microcrystalline solid which was stored under Ar, (yield, 9.14 g, 88.9 %) (Found: C, 6.92 %; H, 0.71 %; N, 3.98 %; S, 19.50 %; La, 13.27 %; Calc. for [La(TFSI)₃(H₂O)₃]: C, 6.97 %; H, 0.59 %; N, 4.07 %; S, 18.62 %; La, 13.44 %; Calc. for [La(TFSI)₃(H₂O)₃].H₂O: C, 6.86 %; H, 0.77 %; N, 4.00 %; S, 18.30 %; La, 13.22 %)

4.2.3 *Triaqua tris{bis(trifluoromethanesulfonyl)amide} europium(III) –*

[Eu(TFSI)₃(H₂O)₃]

[Eu(TFSI)₃(H₂O)₃] was prepared as for the La analogue. A solution of HTFSI (4.71 g, 16.8 mmol) in H₂O (5 mL) was added to a suspension of Eu₂O₃ (0.98 g, 2.8 mmol) in H₂O (5 mL) with stirring. The clear solution formed was purified as for the La analogue and [Eu(TFSI)₃(H₂O)₃] was obtained as a hygroscopic, colourless, microcrystalline solid which was stored under Ar, (yield, 4.78 g, 86.7 %) (found: C, 7.17 %; H 0.72 %; N, 3.99 %; S, 17.34 %; Eu, 15.04 %; Calc. for [Eu(TFSI)₃(H₂O)₃]: C, 6.89 %; H, 0.58 %; N, 4.02 %; S, 18.39 %; Eu, 14.52 %; Calc. for [Eu(TFSI)₃(H₂O)₃].H₂O: C, 6.77 %; H, 0.76 %; N, 3.95 %; S, 18.08 %; Eu, 14.28 %)

4.2.4 Triqua tris{bis(trifluoromethanesulfonyl)amide} samarium(III) –

[Sm(TFSI)₃(H₂O)₃]

[Sm(TFSI)₃(H₂O)₃] was prepared as for the La analogue. A solution of HTFSI (1.14 g, 4.05 mmol) in H₂O (3 mL) was added to a suspension of Sm₂O₃ (0.24 g, 0.68 mmol) in H₂O (5 mL) with stirring. The resultant clear solution was purified as for the La analogue and [Sm(TFSI)₃(H₂O)₃] was obtained as a hygroscopic, colourless, microcrystalline solid which was stored under Ar, (yield, 1.31 g, 92.9 %) (found: C, 7.06 %; H 0.40 %; N, 4.05 %; S, 18.73 %; Sm, 15.40 %; Calc. for [Sm(TFSI)₃(H₂O)₃]: C, 6.90 %; H 0.58 %; N, 4.02 %; S, 18.41 %; Sm, 14.39 %)

4.2.5 Crystallisation of [La(TFSI)₃(H₂O)₃] suitable for X-ray diffraction

Single crystals of [La(TFSI)₃(H₂O)₃] suitable for X-ray diffraction were crystallised from aqueous solution under an Ar atmosphere over a period of several months. (found: C, 6.95 %; H, 0.70 %; N, 4.16 %; S, 18.26 %; La, 12.68 %; Calc. for [La(TFSI)₃(H₂O)₃]; C, 6.97 %; H, 0.59 %; N, 4.07 %; S, 18.62 %; La, 13.44 %)

4.3 Single crystal X-ray diffraction of [La(TFSI)₃(H₂O)₃]

In Chapter 3 the X-ray studies of [Me₄P][TFSI] and [Me₄Sb][TFSI] were described and related to other crystal structures of the TFSI anion. In both these compounds no coordination of the cation to TFSI was observed, rather TFSI acts as a counter ion. In HTFSI, the proton is believed to be coordinated to the TFSI anion *via* the central nitrogen.¹⁵ In [Cu(CO)₂TFSI] the Cu is coordinated to the central nitrogen,¹⁶ and

similarly in $[\text{Fe}(\text{CO})_2\text{CpTFSI}]$ (where $\text{Cp} = \text{C}_5\text{H}_5^-$) the Fe is coordinated to the central nitrogen.¹⁷ Previously Aubke *et al.* have reported the structure of $[\text{Mg}(\text{H}_2\text{O})_6][\text{TFSI}]_2 \cdot 2\text{H}_2\text{O}$ in which TFSI acts as a counter ion in the salt.¹⁵ and this is also observed for $[\text{Cu}(\text{acac})(\text{tmeda})][\text{TFSI}]$ (where $\text{acac} = \text{acetylacetonate}$ and $\text{tmeda} = \text{tetramethylethylenediamine}$) reported by Oldham and Williams.¹⁷ The same authors have also reported the structure of $[\text{Cp}_2\text{Ti}(\text{TFSI})_2]$, where they observed monodentate TFSI coordination *via* one of the sulfonyl oxygens.¹⁷

Single crystal X-ray diffraction was performed on a Bruker platform CCD area detector diffractometer with the structure solved by direct methods followed by Fourier synthesis, and refined on F^2 . The absolute configuration was determined by refinement of the Flack parameter.

$[\text{La}(\text{TFSI})_3(\text{H}_2\text{O})_3]$ crystallises in the cubic space group $P2_13$. The asymmetric unit contains two crystallographically distinct $\{\text{La}(\text{TFSI})(\text{H}_2\text{O})\}$ units, which can be grown into two crystallographically distinct $[\text{La}(\text{TFSI})_3(\text{H}_2\text{O})_3]$ molecules by a three-fold rotation axis passing through each of the two La centres. There are 8 molecules in the unit cell. Both crystallographically distinct molecules contain three TFSI anions coordinated through an oxygen of each sulfonyl unit, forming three six membered chelate rings bound to each La^{3+} cation. There are also three coordinated water molecules adjacent to each other in a piano-stool arrangement yielding 9-coordinate La in both cases. Crystallographic information and selected bond lengths and angles are given in Tables 4.3.1 and 4.3.2.

Each nine coordinate La centre has a distorted tricapped trigonal prismatic coordination geometry with respect to the coordinating oxygen atoms. The coordinating waters sit on one triangular face of the prism (bottom) and the TFSI anions chelate through the top face and the capping positions. The TFSI anions bond to the La centre in a propeller-type arrangement. One of the distinct La centres has an Λ absolute configuration (designated La1 in Figure 4.3.1), and the other has a Δ absolute configuration (designated La2 in Figure 4.3.2).

In the unit cell, the La complexes interact *via* intermolecular hydrogen bonding between the coordinated waters and the terminal oxygen atoms of the sulfonyl unit (O5 with O7 / O9 and O10 with O2 / O4), with H-O_{TFSI} distances between 1.94 and 2.16 Å. Hydrogen bonding is only observed between Λ and Δ molecules, and not between Λ/Λ or Δ/Δ pairs (shortest La-La distance between La(2) and La(1) is 8.07 Å).

Empirical formula	C ₆ H ₆ F ₁₈ LaN ₃ O ₁₅ S ₆
Formula weight	1033.41
Space group	<i>P</i> 2 ₁ 3
Crystal group	Cubic
<i>a</i> (Å)	18.5702(15)
α (deg)	90
<i>V</i> (Å ³)	6404.0(9)
<i>Z</i>	8
<i>T</i> (K)	100(2)
λ (Å)	0.71073
<i>D</i> _{calcd} (mg M ⁻³)	2.144
μ (mm ⁻¹)	0.1891
<i>R</i> ₁ , <i>Rw</i> ² indices [<i>I</i> > 2 σ ² (<i>I</i>)]	0.0394, 0.0865
<i>R</i> ₁ , <i>Rw</i> ² (all data)	0.0460, 0.0898

Table 4.3.1: Crystallographic data for [La(TFSI)₃(H₂O)₃]

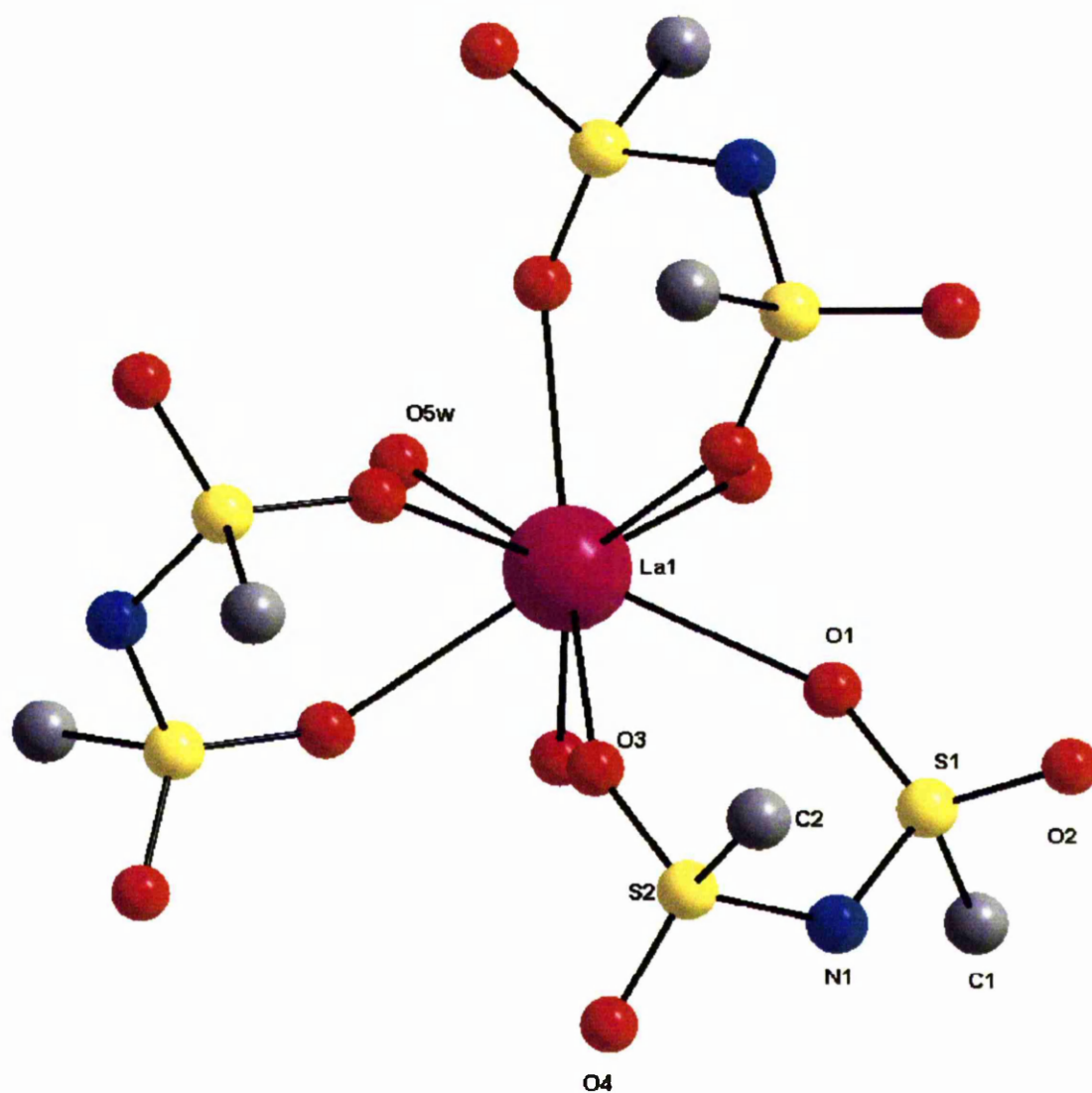


Figure 4.3.1: A absolute configuration of [La(TFSI)₃(H₂O)₃], H and F atoms omitted for clarity

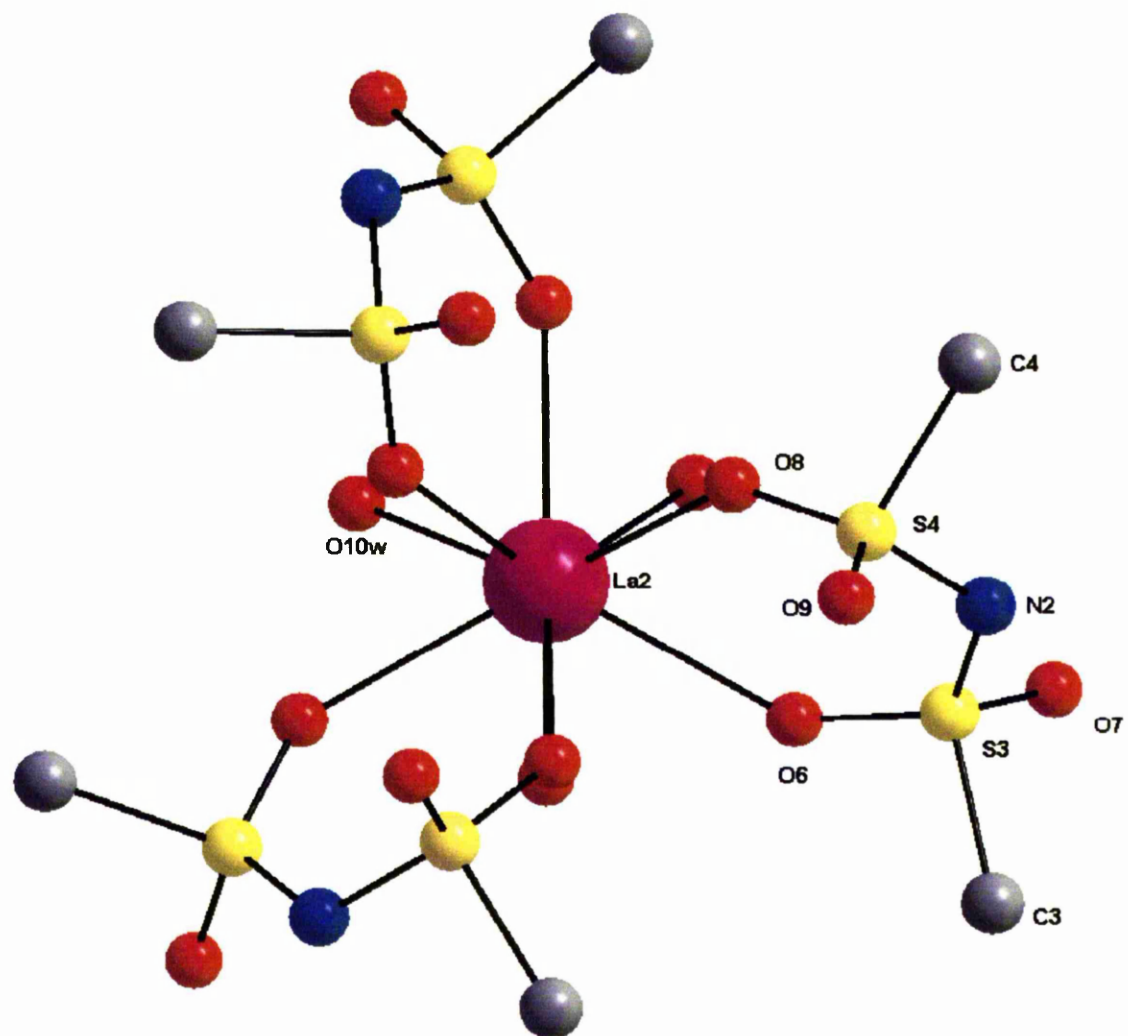


Figure 4.3.2: Δ absolute configuration of [La(TFSI)₃(H₂O)₃], H and F atoms omitted for clarity

In both the Λ and Δ configurations the TFSI ligand forms a 6-membered chelating ring in a distorted boat conformation. For the Δ conformer the dihedral angle between C-S-S-C is $122.87(55)^\circ$, whilst in the Λ configuration this dihedral angle is $148.00(32)^\circ$. The dihedral angles observed are different in the La complex than those in $[\text{Me}_4\text{Sb}][\text{TFSI}]$ salt (dihedral angle of $173.49(40)^\circ$), HTFSI (174.2°)¹⁵ and $\text{K}[\text{TFSI}]$ (17.12°)¹⁵. In $[\text{Me}_4\text{Sb}][\text{TFSI}]$ and HTFSI the dihedral angle is consistent for CF_3 groups with a *trans* orientation (with respect to the S-N-S plane), in the K salt the dihedral angle is consistent with a *cis* orientation. The distorted *trans* orientation of the CF_3 groups in both the Λ and Δ molecules of $[\text{La}(\text{TFSI})_3(\text{H}_2\text{O})_3]$, is a result of the formation of a 6-membered chelating ring.

Coordination of La to an oxygen of the sulfonyl unit, changes the achiral S centre in the TFSI anion to a chiral centre in the chelating ligand with both S centres in the TFSI ligand adopting an *R* configuration. This *R,R* configuration is observed for all TFSI ligands in each crystallographically distinct molecule. The *R,R* configuration of the TFSI anion is one of the possible orientations for the formation of a six membered chelating ring (the other being an *S,S* configuration). It seems unlikely that an *R,S* mode would form a 6-membered ring because of steric interferences because this configuration would have CF_3 groups *cis* with respect to the S-N-S plane, thus creating unfavourable steric interactions.

For coordinated water, the La-O bond length in each molecule (La1-O(5), $2.457(5) \text{ \AA}$ and La2 - O10, $2.489(4) \text{ \AA}$) is significantly shorter than the corresponding La-O_{TFSI} bond

lengths (La1–O(3), 2.543(5) Å, La1–O(1), 2.561(4) Å, La2–O(8), 2.539(4) Å and La2–O(6), 2.547(4) Å). They are also significantly shorter than the average La – water bond lengths in other 9 coordinate La(III) complexes with coordinated water (2.605 Å).¹⁸⁻²²

The shorter La–O_w bond length shows that the water molecules are more strongly bound to the La centre than the TFSI anion and so it can be concluded that the TFSI anion is a poorer ligand than water for La(III).

For the TFSI anion there is no significant lengthening of S–O, S–N or S–C bonds on coordination, nor change in the S–N–S bond angle (125.3 and 126.0 °) *cf.* the TFSI anion in [Me₄Sb][TFSI] (124.6 and 126.0 °). Although there is variation in X–S–X bond angles this has also been previously observed in uncoordinated TFSI (*e.g.* O–S–N angles range between 107.7(2) and 116.5(2) ° in [Mg(H₂O)₆][TFSI]₂·2H₂O¹⁵). Three of the four crystallographically distinct S–O–La bond angles are very similar, (S1–O1–La1, 146.8(2), S2–O3–La1, 146.3(2) and S3–O6–La2, 144.1(3)) with the fourth slightly smaller (S4–O8–La2, 139.9(3)).

Bond lengths / Å			
La1 – O5 _w	2.475(4)	La2 – O10 _w	2.489(4)
La1 – O3	2.543(4)	La2 – O8	2.539(4)
La1 – O1	2.561(4)	La2 – O6	2.547(4)
S1 – O2	1.421(4)	S3 – O7	1.413(7)
S1 – O1	1.439(4)	S3 – O6	1.421(5)
S1 – N1	1.561(5)	S3 – N2	1.544(8)
S1 – C1	1.839(7)	S3 – C3	1.860(12)
S2 – O4	1.425(4)	S4 – O9	1.395(6)
S2 – O3	1.452(4)	S4 – O8	1.444(4)
S2 – N1	1.564(5)	S4 – N2	1.573(7)
S2 – C2	1.836(7)	S4 – C4	1.818(10)
Bond angles / °			
O2 – S1 – O1	116.8(3)	O7 – S3 – O6	116.6(3)
O2 – S1 – N1	113.1(3)	O7 – S3 – N2	108.3(5)
O1 – S1 – N1	114.5(3)	O6 – S3 – N2	115.0(3)
O2 – S1 – C1	104.9(3)	O7 – S3 – C3	103.2(5)
O1 – S1 – C1	104.3(3)	O6 – S3 – C3	103.6(5)
N1 – S1 – C1	100.9(3)	N2 – S3 – C3	109.3(6)
O4 – S2 – O3	116.6(2)	O9 – S4 – O8	117.1(3)
O4 – S2 – N1	110.5(3)	O9 – S4 – N2	116.8(5)
O3 – S2 – N1	115.1(3)	O8 – S4 – N2	112.4(3)
O4 – S2 – C2	105.9(3)	O9 – S4 – C4	104.9(3)
O3 – S2 – C2	103.6(3)	O8 – S4 – C4	104.9(4)
N1 – S2 – C2	103.6(3)	N2 – S4 – C4	97.5(5)
S1 – N1 – S2	125.3(3)	S1 – N1 – S2	126.0(3)
S1 – O1 – La1	146.8(2)	S3 – O6 – La2	144.1(3)
S2 – O3 – La1	146.3(2)	S4 – O8 – La2	139.9(3)

Table 4.3.2: Selected bond lengths and angles for the two crystallographically unique molecules in [La(TFSI)₃(H₂O)₃]

4.4 Vibrational spectroscopy

The effect of coordination of TFSI to Ln(III) has been probed by vibrational spectroscopy. IR and Raman analysis of crystals of $[\text{La}(\text{TFSI})_3(\text{H}_2\text{O})_3]$ suggest that the TFSI ligand is coordinated in an analogous manner in both the crystalline sample used for X-ray diffraction, and the synthesised bulk microcrystalline products of $[\text{Ln}(\text{TFSI})_3(\text{H}_2\text{O})_3]$ (where Ln = La, Sm or Eu). Solid state Raman and ATR IR spectra of crystals of $[\text{La}(\text{TFSI})_3(\text{H}_2\text{O})_3]$ and $\text{Ln}(\text{TFSI})_3 \cdot \text{XH}_2\text{O}$ (Ln = La Sm and Eu) are shown in Figure 4.4.1.

The major IR and Raman bands for HTFSI and $\text{Li}[\text{TFSI}]$ have previously been fully assigned by Lassègues *et al.*,^{23,24} and based on this work the IR and Raman bands observed for $[\text{La}(\text{TFSI})_3(\text{H}_2\text{O})_3]$ crystals and the bulk $[\text{Ln}(\text{TFSI})_3(\text{H}_2\text{O})_3]$ products have been assigned as is shown in Table 4.4.1 (where Ln = La, Sm or Eu). Single crystal X-ray diffraction studies have shown for $\text{Li}[\text{TFSI}]$, that TFSI does not act as a coordinating ligand, but instead as an anion.¹⁵ IR and Raman spectra of the Ln complexes recorded have thus been compared with spectra of $\text{Li}[\text{TFSI}]$ to observe the effects of coordination.

There are several distinct shifts in band positions of TFSI upon coordination to Ln(III) cations. The Raman active $\nu_s^{\text{ip}}(\text{SO}_2)$ band shifts from 1131 cm^{-1} in $\text{Li}[\text{TFSI}]$ to 1146 cm^{-1} in $[\text{La}(\text{TFSI})_3(\text{H}_2\text{O})_3]$ crystals and 1148 cm^{-1} in bulk $[\text{Ln}(\text{TFSI})_3(\text{H}_2\text{O})_3]$ (where Ln = La, Sm and Eu).

In Li[TFSI] the $\nu_s^{\text{op}}(\text{SO}_2)$ IR band is observed at 1138 cm^{-1} , upon TFSI coordination three bands are observed in this region, the major band occurring lower in energy, 1105 cm^{-1} in $[\text{La}(\text{TFSI})_3(\text{H}_2\text{O})_3]$, 1105 cm^{-1} in $[\text{Sm}(\text{TFSI})_3(\text{H}_2\text{O})_3]$ and 1109 cm^{-1} in $[\text{Eu}(\text{TFSI})_3(\text{H}_2\text{O})_3]$.

It is known from crystallography that there are three coordinated water molecules in $[\text{La}(\text{TFSI})_3(\text{H}_2\text{O})_3]$, and in the IR and Raman spectra of the crystals, $\nu(\text{OH})$ (3458 cm^{-1}) and $\delta(\text{OH})$ bands (1631 cm^{-1}) bands for coordinated H_2O have been observed. These are comparable to those observed by Dormond *et al.* for $\text{Ln}(\text{TFSI})_3 \cdot x\text{H}_2\text{O}$ (where $\text{Ln} = \text{La}$, Nd and Yb) complexes (3450 cm^{-1} and 1630 cm^{-1}).¹⁴ The band position for $\delta(\text{OH})$ is comparable to those obtained for the fully hydrated $[\text{La}(\text{H}_2\text{O})_9][\text{OTf}]_3$ complex, where the $\delta(\text{OH})$ band is observed at 1638 cm^{-1} .²⁵ In this complex the $\nu(\text{OH})$ band appears at *ca.* 3600 cm^{-1} which is higher than that observed in $[\text{La}(\text{TFSI})_3(\text{H}_2\text{O})_3]$. The $\delta(\text{OH})$ vibration for coordinated water has been observed in the IR spectrum of the bulk $[\text{La}(\text{TFSI})_3(\text{H}_2\text{O})_3]$ and $[\text{Sm}(\text{TFSI})_3(\text{H}_2\text{O})_3]$ products (at 1632 cm^{-1} and 1630 cm^{-1} respectively), but not the less well resolved IR spectrum of $[\text{Eu}(\text{TFSI})_3(\text{H}_2\text{O})_3]$. Similarly the $\nu(\text{OH})$ band has also been observed at 3468 cm^{-1} for $[\text{La}(\text{TFSI})_3(\text{H}_2\text{O})_3]$ and $[\text{Sm}(\text{TFSI})_3(\text{H}_2\text{O})_3]$ and *ca.* 3460 cm^{-1} for $[\text{Eu}(\text{TFSI})_3(\text{H}_2\text{O})_3]$.

As previously stated, in 2003 Dormond *et al.* published a synthesis for lanthanide TFSI salts.¹⁴ Their vibrational spectroscopy showed water bands at 3450 and 1630 cm^{-1} which they assigned to coordinated water. The authors of this paper attempted to remove water by reaction of the $\text{Ln}(\text{TFSI})_3 \cdot x\text{H}_2\text{O}$ ($\text{Ln} = \text{La}$, Nd and Yb) complex with ethanol and

confirmed this by the absence of peaks due to water in the IR spectrum. Lack of coordinated ethanol was inferred from ^1H NMR spectroscopy. Additional changes in the vibrational spectra indicated a different coordination mode of TFSI, possibly bridging.

Assignment	Crystals											
	R	IR	R	IR	R	IR	R	IR	R	IR	R	IR
$\nu(\text{OH})$	-	-	-	3458	-	3468	-	3468	-	3468	-	ca. 3460
$\delta(\text{OH})$	-	-	-	1631	-	1632	-	1630	-	1630	-	-
$\nu_a^{\text{i.p./o.p.}}(\text{SO}_2)$	1318	1323	1316	1312	1316	1314	1314	1316	1316	1316	1316	1317
		1307										
$\nu_s(\text{CF}_3)$	1247	1242	1243	1235?	1243	1235	1247	1234	1247	1234	1247	1236
$\nu_a(\text{CF}_3)$	-	1195	-	1219	-	1221	-	1221	-	1221	-	1221
				1196		1198		1198		1198		1198
$\nu_s^{\text{o.p.}}(\text{SO}_2)$	-	1138	-	1138	-	1138	-	1138	-	1138	-	1139
				1126		1126		1130		1130		1132
				1105		1105		1105		1105		1109
$\nu_s^{\text{i.p.}}(\text{SO}_2)$	1131	-	1146	-	1148	-	1148	-	1148	-	1148	-
$\nu_a(\text{SNS})$	-	1062	-	1051	-	1051	-	1055	-	1055	-	1055
$\nu(\text{CS})$	-	810?	-	806?	-	806?	-	806?	-	806?	-	806?
$\nu_s(\text{SNS})$		773?	-	773	-	774	-	773	-	773	-	775
$\delta_s(\text{CF}_3)$	747	746	755	750	754	750	754	750	754	750	757	752
$\delta(\text{SNS})$	-	ca.	-	662	-	662	-	663	-	663	-	665
		665		650		650		650		650		649
$\delta^{\text{i.p./o.p.}}(\text{SO}_2)$	593?	606		597		601	-	600	-	600	-	592
$\delta_a(\text{CF}_3)$		569	575	573	573	570	575	572	-	572	-	567
		510										
$\delta_s(\text{SO}_2)$	552?	554?	554	-	554	-	557	-	556	-	556	-
$\rho(\text{SO}_2)$	330	-	332	-	332	-	-	-	332	-	332	-
	310		310		310				310		310	
$\rho(\text{CF}_3)$	276	-	-	-	-	-	-	-	-	-	-	-
$\nu(\text{LnO})^\dagger$			297?	-	297?	-	-	-	298	-	-	-

Table 4.4.1: Solid state ATR IR and Raman bands of TFSI salt and complexes. ν , stretching; δ , bending; ω , wagging; τ , torsion; ρ , rocking. ? = tentative assignment, [†] Assignments based on references 26 and 27

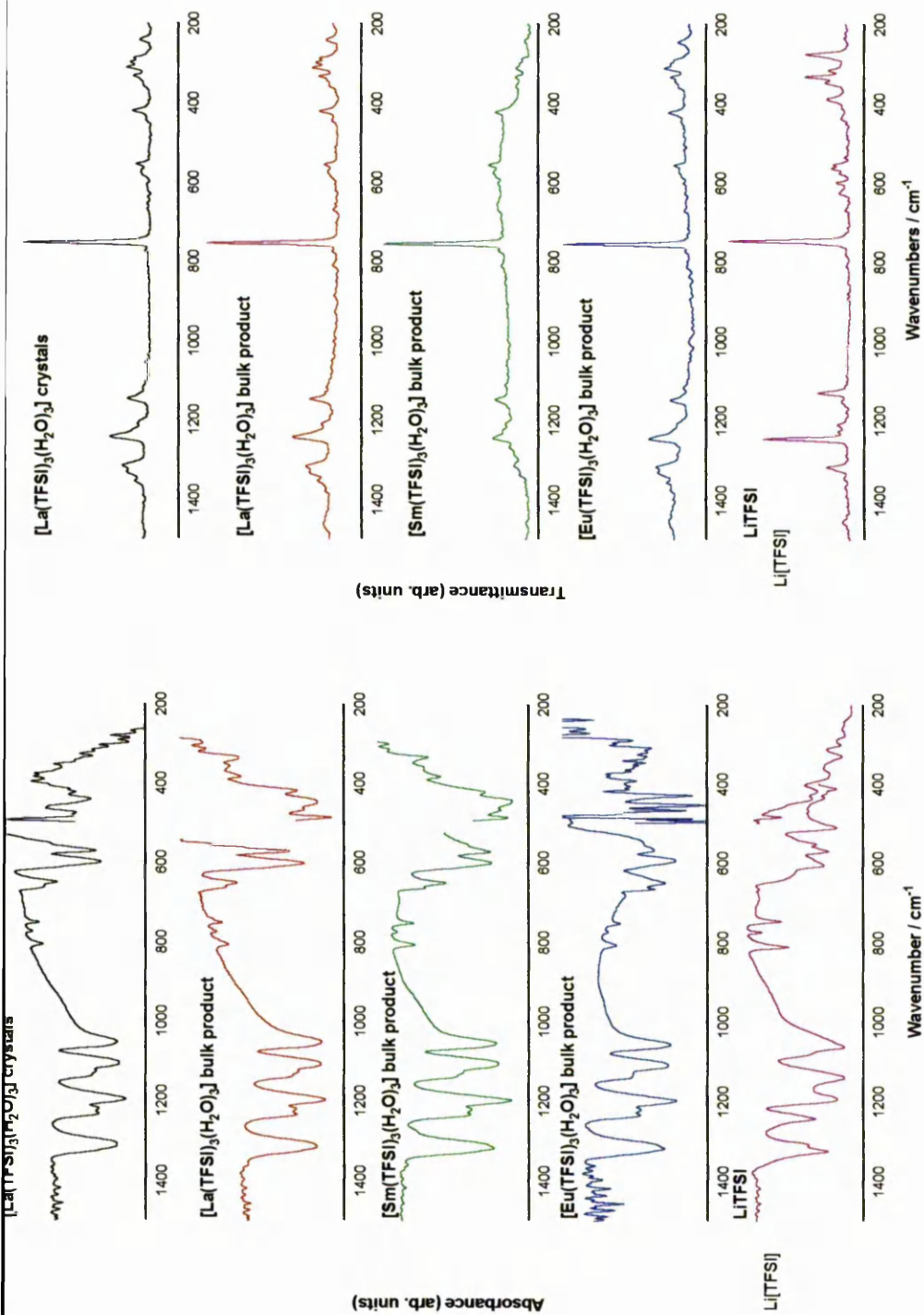


Figure 4.4.1: Solid state ATR IR and Raman spectra of $[Ln(TFSD)_3(H_2O)_3]$ ($Ln = La, Sm$ and Eu). The ATR IR and Raman spectra of Li[TFSI] are also shown for comparison

4.5 Electrochemical behaviour of $[\text{Ln}(\text{TFSI})_3(\text{H}_2\text{O})_3]$ ($\text{Ln} = \text{La}, \text{Sm}$ and Eu) in LTILs

4.5.1 Experimental method

The voltammetric behaviour of $[\text{Ln}(\text{TFSI})_3(\text{H}_2\text{O})_3]$ complexes ($\text{Ln} = \text{La}, \text{Sm}$ and Eu) has been investigated in selected TFSI based LTILs, $[\text{Me}_4\text{N}][\text{TFSI}]$, $[\text{Me}_4\text{P}][\text{TFSI}]$, $[\text{Me}_3\text{N}^n\text{Bu}][\text{TFSI}]$ and finally in MeCN with $[\text{Me}_3\text{N}^n\text{Bu}][\text{TFSI}]$ as a supporting electrolyte. The obtained cyclic voltammograms are shown in Figures 4.5.1 to 4.5.3 with experimental conditions summarised in Table 4.5.1.

A typical 3 electrode cell (see Chapter 2) was used for all cyclic voltammetry (CV) measurements, and comprised of a Pt or glassy carbon (GC) disk working electrode, a large surface area Pt gauze counter electrode and a Ag wire quasi-reference electrode (QRE) or a Ag/AgNO₃ (0.1 mol L⁻¹)/MeCN reference electrode. CVs in $[\text{Me}_4\text{N}][\text{TFSI}]$, $[\text{Me}_4\text{P}][\text{TFSI}]$ and $[\text{Me}_3\text{N}^n\text{Bu}][\text{TFSI}]$ were recorded inside an inert atmosphere drybox. CVs in MeCN were recorded inside a Faraday cage under an Ar atmosphere (to minimise electrical noise), with the solution purged for 30 min prior to measurements and 30 s between scans. The MeCN solution was kept under a blanket of Ar at all times.

Voltammograms of $[\text{Sm}(\text{TFSI})_3(\text{H}_2\text{O})_3]$ in $[\text{Me}_4\text{N}][\text{TFSI}]$ were recorded by Dr V. Volkovich (CRR, The University of Manchester) and are shown in Figure 4.5.1 with experimental conditions given in Table 4.5.1. CVs using Ag wire QRE were not standardised using the Fc^+/Fc couple due to either thermal decomposition of Fc (in

[Me₄N][TFSI] and [Me₄P][TFSI] at 160 °C) or chemical reaction of Fc with the Ln complexes in solution (an initial orange coloured solution quickly turns blue/purple in colour).

Solvent system	Dissolved lanthanide species	Temperature / °C	Working Electrode	Reference electrode
Me ₃ NBu][TFSI] (4 mL)	[La(TFSI) ₃ (H ₂ O) ₃] (0.094 mmol)	25	GC (2 mm dia.)	Ag wire QRE
Me ₃ NBu][TFSI] (1.2 mL)	[Sm(TFSI) ₃ (H ₂ O) ₃] (0.268 mmol)	25	Pt (2 mm dia.)	Ag wire QRE
Me ₃ NBu][TFSI] (0.8 mL)	[Eu(TFSI) ₃ (H ₂ O) ₃] (0.115 mmol)	25	Pt (2 mm dia.)	Ag wire QRE
CN (4 mL) and Me ₃ NBu][TFSI] (0.33 mmol)	[La(TFSI) ₃ (H ₂ O) ₃] (0.036 mmol)	25	Pt (1 mm dia.)	Ag/AgNO ₃ (0.1 mol L ⁻¹)
CN (4 mL) and Me ₃ NBu][TFSI] (0.33 mmol)	[Sm(TFSI) ₃ (H ₂ O) ₃] (0.040 mmol)	25	Pt (1 mm dia.)	Ag/AgNO ₃ (0.1 mol L ⁻¹)
CN (4 mL) and Me ₃ NBu][TFSI] (0.45 mmol)	[Eu(TFSI) ₃ (H ₂ O) ₃] (0.035 mmol)	25	Pt (1 mm dia.)	Ag/AgNO ₃ (0.1 mol L ⁻¹)
Me ₄ N][TFSI] 4 g, 8.57 mmol)	[La(TFSI) ₃ (H ₂ O) ₃] (0.157 mmol)	160	Pt (2 mm dia.)	Ag wire QRE
Me ₄ N][TFSI] 6 g, 7.27 mmol)	[Sm(TFSI) ₃ (H ₂ O) ₃] (0.29 mmol)	160	Pt (2 mm dia.)	Ag wire QRE
Me ₄ P][TFSI] 2 g, 5.43 mmol)	[Eu(TFSI) ₃ (H ₂ O) ₃] (0.659 mmol)	160	Pt (2 mm dia.)	Ag wire QRE

Table 4.5.1: Experimental conditions for cyclic voltammetry measurements of [Ln(TFSI)₃(H₂O)₃] complexes (Ln = La, Sm and Eu) in LTILs or in MeCN using [Me₃NⁿBu][TFSI] as supporting electrolyte . QRE = quasi-reference electrode, GC = glassy carbon

4.5.2 Cyclic voltammetry of $[La(TFSI)_3(H_2O)_3]$ in TFSI based LTILs and MeCN

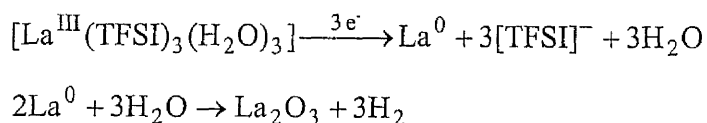
CVs of $[La(TFSI)_3(H_2O)_3]$ in $[Me_4N][TFSI]$ at 160 °C (using the La complex from the bulk synthesis) show one reduction and one oxidation peak, $E_p^c = -2.0$ V and $E_p^a = -1.8$ V vs. Ag wire QRE. The reduction has been assigned to the La(III)/La(0) process. In $[Me_3NBu][TFSI]$, this reduction is observed at -2.8 V vs. Ag wire QRE at 25 °C (corresponding oxidation at -2.2 V), and in MeCN the La(III)/La(0) reduction is observed at -2.7 V vs. Ag/Ag⁺ (corresponding oxidation at -2.3 V), again at 25 °C. The observation of the La(III)/La(0) reduction is not unexpected from the E^0 values which predict that this reduction would occur within the electrochemical window of the LTILs investigated.

If La metal was formed by this electrochemical reaction and had plated onto the surface of the metallic working electrode, a sharp oxidation peak in the CV would be observed. However a broad, shallow peak is observed in all cases. The waveform for this oxidation/reduction processes are consistent with that expected for the deposition of an insoluble product on the electrode surface.^{28,29}

Tsuda and Ito have explored the electrochemical behaviour of La in a $LaCl_3$ -saturated ionic liquid ($emimCl/AlCl_3$).⁶ Voltammograms of $LaCl_3$ (with added LiCl and $SOCl_2$) showed the oxidation of thionyl chloride and deposition and stripping of lithium. The authors also observed the reduction of the La^{3+} cation, although no corresponding oxidation wave was observed. The authors suggested this was a result of the formation of a lanthanum hydroxide, oxide or chloride layer (from small amounts of water in the melt

or from the added thionyl chloride) on the electrode, similar to what happens in lithium batteries.¹¹

Vibrational spectroscopy (Section 4.4) and single crystal X-ray diffraction (Section 4.3) has shown that there is water present in the Ln complexes formed. Based on this, these literature references, and the shape of the reduction/oxidation waves in the CV, it would appear that the same process may be occurring here *i.e.* reduction to La metal followed by oxidation of the metal on the electrode surface. Therefore, the following reaction mechanism is proposed for the reduction of the La³⁺ cation in the LTILs:



4.5.3 Cyclic voltammetry of [Eu(TFSI)₃(H₂O)₃] in TFSI based LTILs and MeCN

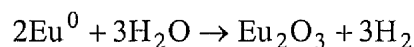
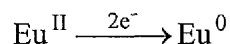
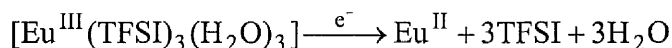
In [Me₄P][TFSI] at 160 °C two reductions are observed at +0.7 V and -2.1 V with corresponding oxidations at +1.3 V and -2.6 V vs. Ag wire QRE. The reductions have been assigned to the Eu(III)/Eu(II) and Eu(II)/Eu(0) processes (at 0.70 V and -2.1 V respectively). The differences between the two peaks is *ca.* 2.8 V, which is slightly larger than the separation between standard potentials of 2.45 V.³⁰

In [Me₃NⁿBu][TFSI], the redox couple at -0.13 V ($E_p^c = -0.16$ V, $E_p^a = -0.11$ V vs. Ag wire QRE, at 0.10 V s⁻¹ scan rate) is assigned to the Eu(III)/Eu(II) process. The reduction

at -3.27 V (corresponding oxidation at -2.56 V *vs.* Ag wire QRE, $E_{1/2} = -2.92$ V) is assigned to the Eu(II)/Eu(0) process. The peak separation between the Eu(II)/Eu(0) 'couple' and the Eu(III)/Eu(II) process is 2.78 V and comparable to 2.45 V for standard electrode potentials.³⁰

In MeCN similar behaviour is observed with reductions at -0.7 V (assigned to Eu(III)/Eu(II) process) and -3.0 V (assigned to Eu(II)/Eu(0) process) *vs.* Ag/Ag⁺. The separation between the reduction peaks (2.30 V) is again reasonably consistent with the separation between the standard potentials of 2.45 V.³⁰ Only one oxidation peak is observed in the CV at *ca.* -2.6 V. Further investigations into the absence of a corresponding oxidation peak for the Eu(III)/Eu(II) reduction were unfortunately not conducted.

Looking at the reduction to the zerovalent state, the peak shapes are similar to those obtained for [La(TFSI)₃(H₂O)₃], and constant with those expected for the formation of an insoluble product. It is thus hypothesised that a similar reduction reaction is occurring *i.e.* reduction of Eu(II) to Eu(0) then the subsequent oxidation of the Eu metal formed:



4.5.4 Cyclic voltammetry of $[Sm(TFSI)_3(H_2O)_3]$ in TFSI based LTILs and MeCN

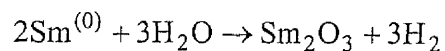
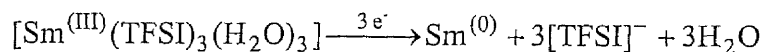
The voltammetric behaviour of Sm is slightly different again from that observed for La and Eu. In $[Me_4N][TFSI]$ at 160 °C, one reduction peak is observed at -2.8 V (assigned to the Sm(III)/Sm(0) process) and a corresponding oxidation at -2.5 V *vs.* Ag wire QRE.

In MeCN with $[Me_3N^rBu][TFSI]$ as supporting electrolyte, one reduction peak is observed at *ca.* -2.9 V (corresponding oxidation at *ca.* -2.5 V) *vs.* Ag/Ag⁺. This reduction potential is comparable to the difference between the Ag/Ag⁺ and Sm(III)/Sm(0) standard reduction potentials of 3.10 V and thus has been assigned to the Sm(III)/Sm(0) process.³⁰

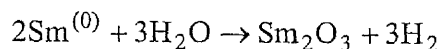
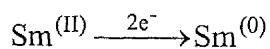
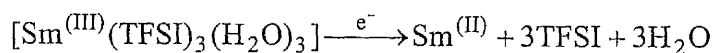
In $[Me_3N^rBu][TFSI]$, two reductions are observed at -1.27 V (corresponding oxidation at -1.04 V, $E_{1/2} = -1.16$ V) and at -3.0 V (corresponding oxidation at -2.75 V, $E_{1/2} = -2.88$ V) *vs.* Ag wire QRE. The first reduction/oxidation couple has been assigned to the Sm(III)/Sm(II) process and the reduction at -3.0 V assigned to the Sm(II)/Sm(0) process. The difference between the Sm(III)/Sm(II) couple and the Sm(III)/Sm(0) couple of 1.46 V is reasonably consistent to the differences in standard reduction potentials of 1.13 V,³⁰ thus indicating that the proposed assignment may be correct.

In all three solvent media the reduction to the zerovalent state shows similar peak shapes as previously observed for La and Eu. It is hypothesised that a similar reduction reaction is progressing at the electrode surface, i.e. reduction to metal followed by subsequent chemical oxidation to form the oxide. The following reaction mechanisms are proposed:

In MeCN with [Me₃NⁿBu][TFSI] supporting electrolyte, and [Me₄N][TFSI]:



and in [Me₃NⁿBu][TFSI]:



The reason for the differences in electrochemical behaviour between MeCN with [Me₃NⁿBu][TFSI] supporting electrolyte, [Me₄N][TFSI] and [Me₃NⁿBu][TFSI] is not immediately clear. Weakly coordinating solvents are known to be able to stabilise Ln(II) cations,⁶⁻⁸ however, this does not appear to be the case for Sm(II) in MeCN with [Me₃NⁿBu][TFSI] supporting electrolyte and in molten [Me₄N][TFSI] at 160 °C.

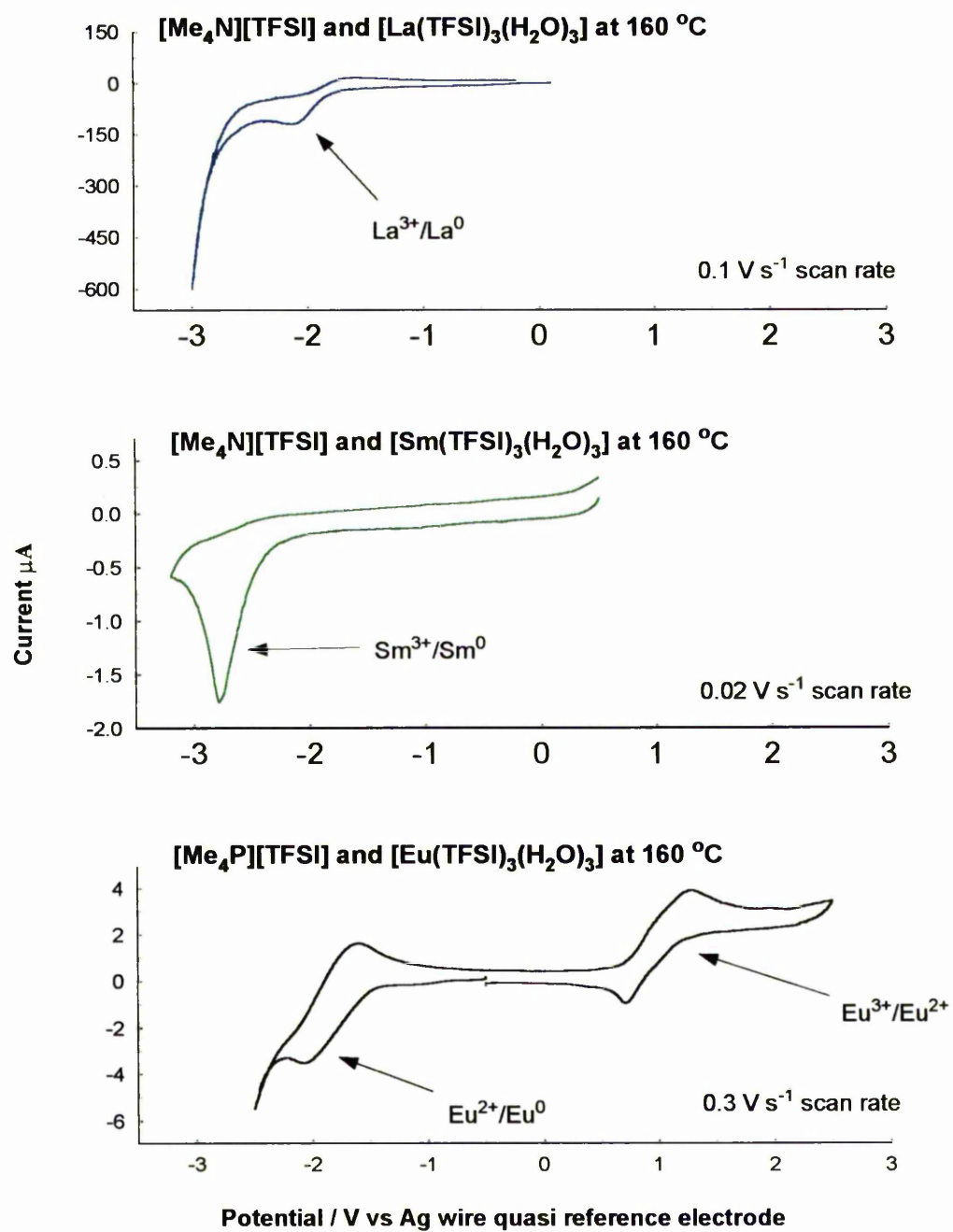


Figure 4.5.1: CV of [Ln(TFSI)₃(H₂O)₃] in LTIL at 160 °C (Ln = La, Sm and Eu)

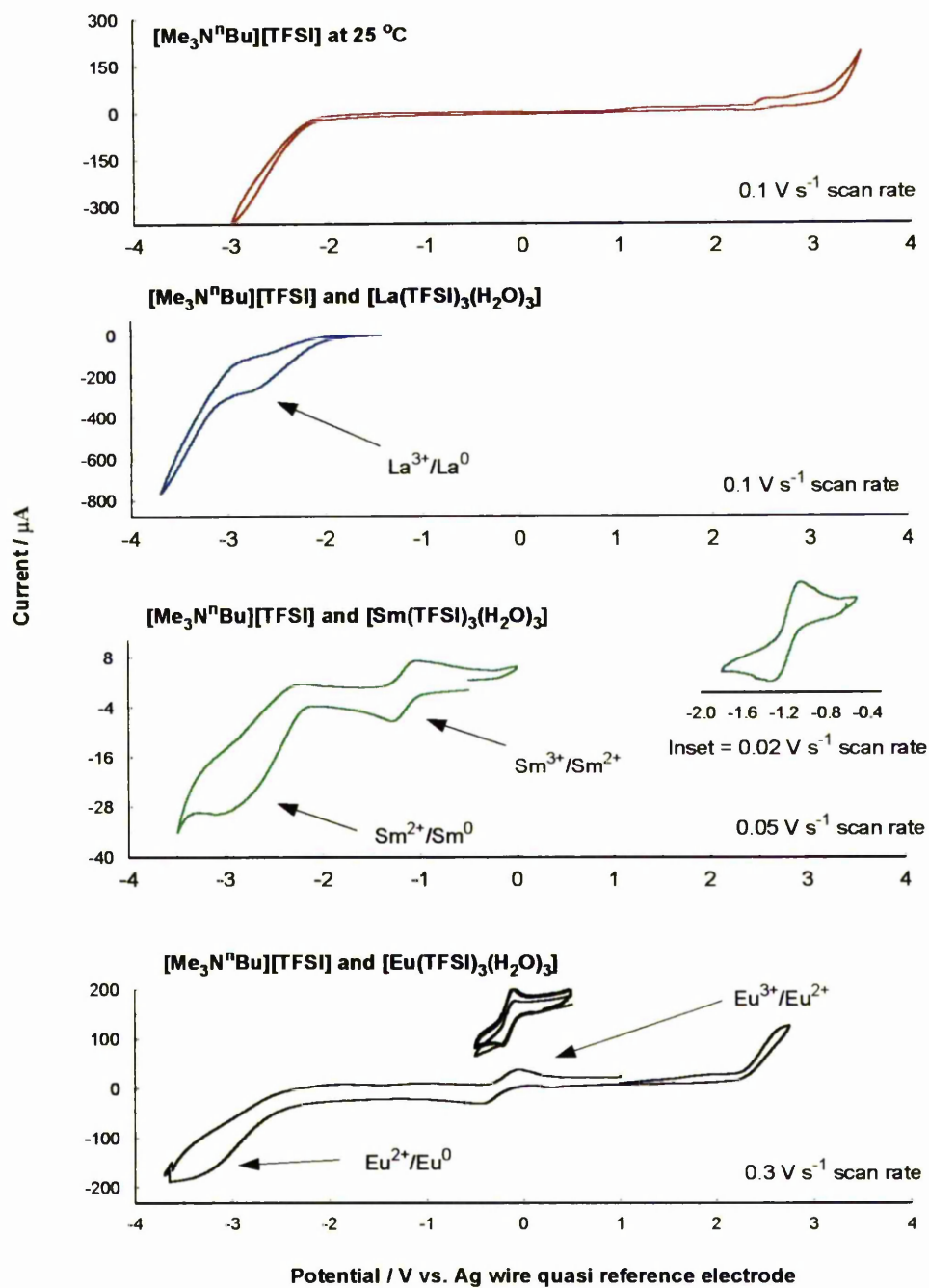


Figure 4.5.2: CV of [Ln(TFSI)₃(H₂O)₃] in [Me₃NⁿBu][TFSI] (Ln = La, Sm and Eu)

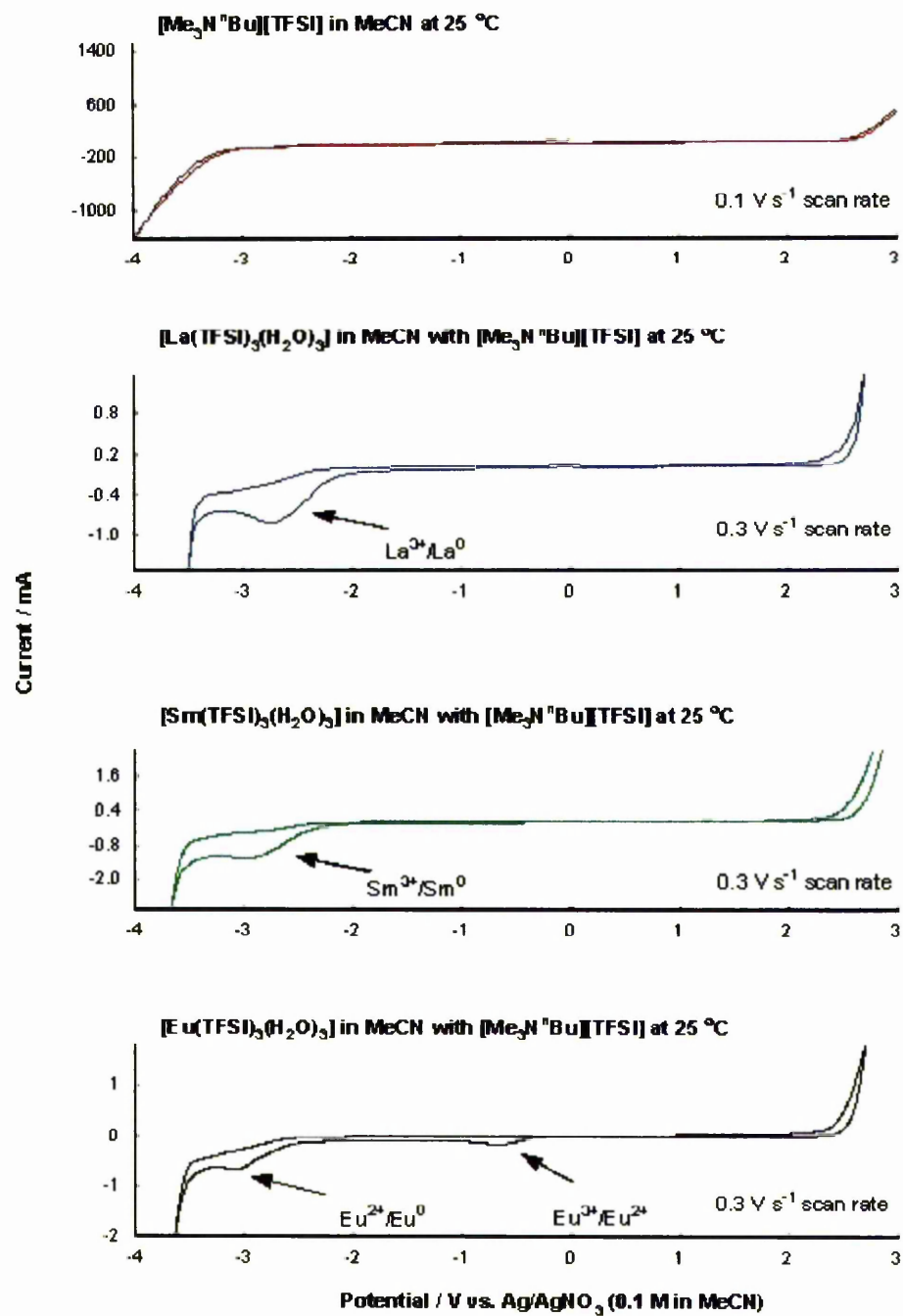


Figure 4.5.3: CV of [Ln(TFSI)₃(H₂O)₃] in MeCN with [Me₃N^tBu][TFSI] as supporting electrolyte (Ln = La, Sm and Eu)

4.5.5 Diffusion coefficients of $[Ln(TFSI)_3(H_2O)_3]$ ($Ln = La, Sm$ and Eu) in

$[Me_3N^nBu][TFSI]$ and $MeCN$ using $[Me_3N^nBu][TFSI]$ as supporting electrolyte

It is known for a diffusion controlled process (*i.e.* transport of ions from the bulk solution to the electrode surface is through diffusion) the observed current proportionally increases with square root of increasing scan rate. This relationship has previously been described by Randles³¹ and Sevcik³² and is shown in Equation 4:

$$i_p = 0.4463 \sqrt{\frac{z^3 F^3}{RT}} A C_{Bulk} D^{1/2} v^{1/2}$$

(Equation 4)

Where i_p = peak current, z = charge of the ion, F = Faraday constant, R = gas constant, T = temperature, A = area of the electrode surface, C_{Bulk} = concentration, D = diffusion coefficient and v = scan rate).

Plots of i_p vs. $v^{1/2}$ for the $La(III)/La(0)$, $Sm(III)/Sm(0)$ and $Eu(II)/Eu(0)$ reduction processes in $[Me_3N^nBu][TFSI]$ and in $MeCN$ with $[Me_3N^nBu][TFSI]$ as supporting electrolyte are shown in Figures 4.5.4 and 4.5.5. Using Equation 4, diffusion coefficients have been calculated and are presented in Table 4.5.2.

In $[Me_3N^nBu][TFSI]$, the diffusion coefficients obtained for Eu and Sm are comparable to those observed for $LnCl_3$ in $AlCl_3$ - $NaCl$ melts at $175\text{ }^\circ\text{C}$ (in the order of $10^{-6}\text{ cm}^2\text{ s}^{-1}$)⁶ and $LaCl_3$ in 1-*n*-butylpyridinium chloride/ $AlCl_3$ at $40\text{ }^\circ\text{C}$ (in the range of $10^{-7}\text{ cm}^2\text{ s}^{-1}$)⁷.

The value obtained for $[\text{La}(\text{TFSI})_3(\text{H}_2\text{O})_3]$ in $[\text{Me}_3\text{N}^n\text{Bu}][\text{TFSI}]$ is significantly higher than that observed for Eu and Sm, perhaps due to changes in speciation for the Ln(II) (Sm and Eu) and La(III) oxidation states, the low oxidation state Ln may be expected to have higher coordination numbers.

The diffusion coefficients obtained for $[\text{Ln}(\text{TFSI})_3(\text{H}_2\text{O})_3]$ complexes (where Ln = La, Sm and Eu) in MeCN with $[\text{Me}_3\text{N}^n\text{Bu}][\text{TFSI}]$ as supporting electrolyte are very low (in the order of $10^{-11} \text{ cm}^2 \text{ s}^{-1}$) and the reason for this is not immediately clear.

Compound	$D_{\text{MeCN}} / \text{cm}^2 \text{ s}^{-1}$	$D_{[\text{Me}_3\text{N}^n\text{Bu}][\text{TFSI}]} / \text{cm}^2 \text{ s}^{-1}$
$[\text{La}(\text{TFSI})_3(\text{H}_2\text{O})_3]$	2.69×10^{-11}	3.39×10^{-5}
$[\text{Sm}(\text{TFSI})_3(\text{H}_2\text{O})_3]$	1.18×10^{-11}	1.02×10^{-7}
$[\text{Eu}(\text{TFSI})_3(\text{H}_2\text{O})_3]$	1.79×10^{-11}	4.24×10^{-7}

Table 4.5.2: Diffusion coefficients of Ln species in MeCN with $[\text{Me}_3\text{N}^n\text{Bu}][\text{TFSI}]$ as supporting electrolyte at 25 °C and in pure $[\text{Me}_3\text{N}^n\text{Bu}][\text{TFSI}]$ at 25 °C

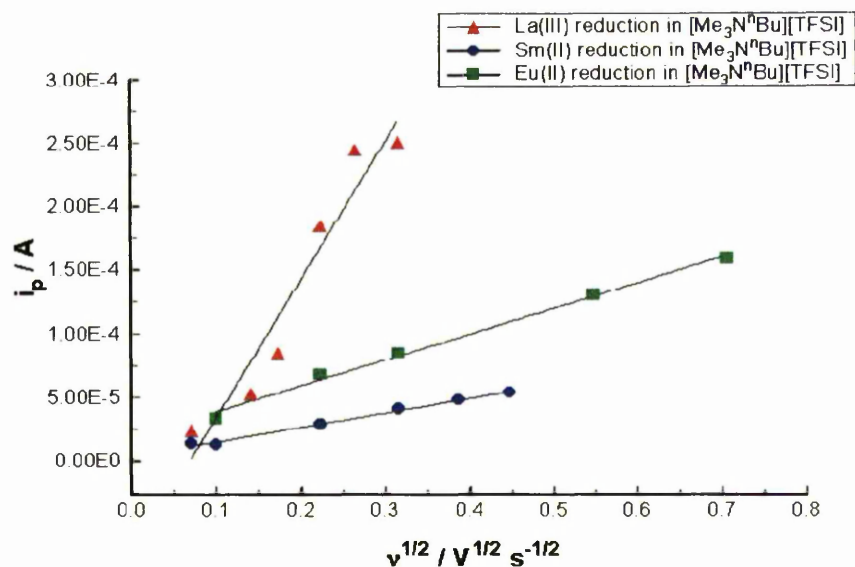


Figure 4.5.4: Plot of peak current as function of scan rate for the La(III)/La(0) and Ln(II)/Ln(0) (Ln = Eu and Sm) reduction processes in [Me₃N⁺Bu][TFSI] at 25 °C

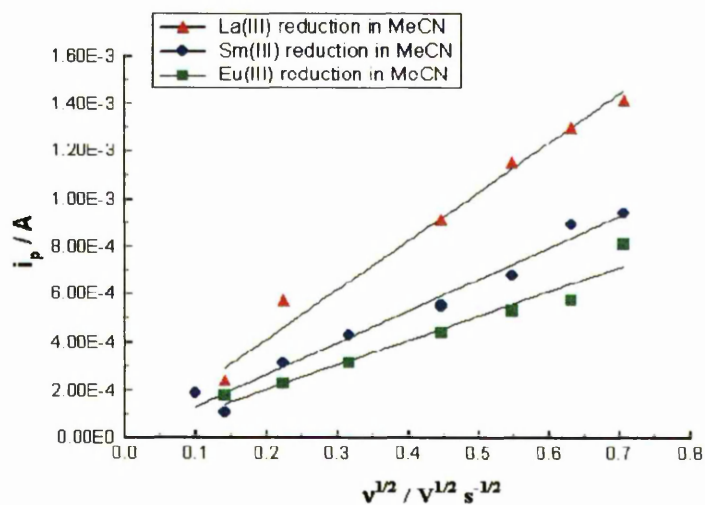


Figure 4.5.5: Plot of peak current as function of scan rate for the Eu(II)/Eu(0) and Ln(III)/Ln(0) (Ln = La and Sm) reduction processes in MeCN using [Me₃N⁺Bu][TFSI] as supporting electrolyte at 25 °C

4.6 Summary

Three novel lanthanide TFSI complexes ($[\text{Ln}(\text{TFSI})_3(\text{H}_2\text{O})_3]$, where $\text{Ln} = \text{La}, \text{Sm}$ and Eu) have been synthesised and characterised using elemental analysis, vibrational spectroscopy and, in the case of $[\text{La}(\text{TFSI})_3(\text{H}_2\text{O})_3]$ single crystal X-ray diffraction.

Single crystal X-ray diffraction studies of $[\text{La}(\text{TFSI})_3(\text{H}_2\text{O})_3]$ has shown a new TFSI coordination mode *via* the sulfonyl oxygens in a 6 membered chelate bonding arrangement. The structure of $[\text{La}(\text{TFSI})_3(\text{H}_2\text{O})_3]$ is the first reported crystal structure of an *f*-element TFSI complex, and shows that the TFSI anion is a poorer ligand for La than water based on bond lengths.

Based on previous studies by Lassègues *et al.*,^{17,18} the bands observed in the mid-IR and Raman spectra have been assigned. The vibrational spectroscopy study suggests that the bulk crystalline sample is the same as the single crystal used for X-ray diffraction. The presence of water in the Ln complexes has been inferred from the vibrational spectra for all the Ln complexes synthesised.

It was hypothesised in Chapter 3 that the TFSI based LTILs synthesised should have an electrochemical window with a cathodic limit wide enough to reduce lanthanides to the zerovalent state (based on standard reduction potentials). Observation of the $\text{Ln}(\text{III})/\text{Ln}(0)$ and $\text{Ln}(\text{II})/\text{Ln}(0)$ reductions in the LTILs investigated supports this hypothesis. The voltammetric behaviour of the Ln in the LTILs suggests that the

reduction to the zerovalent state is complicated by secondary chemical reactions *i.e.*

formation of lanthanide oxides by reaction with water.

Based on differences between the standard reduction potentials of the Ln(III)/Ln(0) / Ln(II)/Ln(0) and An(III)/An(0) processes it is hypothesised that the An of interest, U, Np and Pu, should also be reduceable to the zerovalent state in the LTILs investigated thus far. This leads to a natural progression to the low specific activity actinides, starting with the simplest case, Th, where the high stability of Th(IV) should ensure simple Th(IV)/Th(0) redox chemistry.

4.7 References

1. C. J. Anderson, G. R. Choppin, D. J. Prett, D. A. Costa, W. Smith, *Radiochim. Acta*, 1999, **84**, 31.
2. D. A Costa, W. H. Smith, *Los Alamos yearly report*, LA-UR-99-5521, 1999.
3. K. Abney, E. Bluhm, E. Garcia, W. Smith, M. Barr, W. Oldham, D. Costa, D. Morris, D. Tait, *Los Alamos yearly report*, LA-UR-00-5043, 2000.
4. W. H. Smith, D. A. Costa, *Los Alamos yearly report*, LA-UR 98-3669, 1998.
5. D. A. Costa, W. H. Smith, K. D. Abney, W. J. Oldham, *Plutonium Futures – The Science*, American Institute of Physics, 2000.
6. B. Gilbert, V. Demarteau, G. Duyckaerts, *J. Electroanal. Chem.*, 1978, **89**, 123.
7. J. P. Schoebrechts, B. P. Gilbert, G. Duyckaerts, *J. Electroanal. Chem.*, 1983, **145**, 139.

8. J. P. Schoebrechts, B. P. Gilbert, G. Duyckaerts, *J. Electroanal. Chem.*, 1983, **145**, 127.
9. P. G. Varlashkin, J. R. Peterson, *J. Less-Common Met.*, 1983, **94**, 333.
10. M. H. Miles, A. N. Fletcher, *J. Electroanal. Chem.*, 1987, **221**, 115.
11. T. Tsuda, Y. Ito, *Proc. Electrochem. Soc.*, 2000, **99-41** (Molten Salts XII), 100.
12. W. J. Gau, I. W. Sun, *J. Electrochem. Soc.*, 1996, **143**, 914.
13. I. Billard, G. Moutiers, A. Labet, A. El Azzi, C. Gaillard, C. Mariet, K. Lützenkirchen, *Inorg. Chem.*, 2003, **42**, 1726.
14. D. B. Baudry, A. Dormond, F. Duris, J. M. Bernard, J. R. Desmurs, *J. Fluorine Chem.*, 2003, **121**, 233.
15. A. Haas, C. Klare, P. Betz, J. Bruckmann, C. Kruger, Y. H. Tsay, F. Aubke, *Inorg. Chem.*, 1996, **35**, 1918.
16. O. G. Polyakov, S. M. Ivanova, C. M. Gaudinski, S. M. Miller, O. P. Anderson, S. H. Strauss, *Organometallics*, 1999, **18**, 3769.
17. W. J. Oldham, D. B. Williams, *Proc. Electrochem. Soc.*, 2002, **19**, 983.
18. E. M. Aricó, L. B. Zinner, B. Kanellakopoulous, E. Dornberger, J. Rebizante, C. J. Apostolodis, *J. Alloys Compd.*, 2001, **39**, 323.
19. R. Baggio, M. T. Garland, M. Perec, D. Vega, *Inorg. Chem.*, 1996, **35**, 2396.
20. M. S. Wickleder, *Z. Anorg. Allg. Chem.*, 1999, **625**, 1794.
21. B. Benmerad, A. Guebria-Laidoudi, F. Balegrouie, H. Birkedal, G. Chapuis, *Acta Cryst. C*, 2000, **C36**, 789.
22. T. Bataille, D. J. Louer, *J. Mater Chem.*, 2002, **12**, 3487.

23. I. Rey, P. Johansson, J. Lindgren, J. C. Lassègues, J. Grondin, L. Servant, *J. Phys. Chem. A*, 1998, **102**, 3249.
24. I. Rey, J. C. Lassègues, J. Grondin, L. Servant, *Electrochim. Acta*, 1998, **43**, 1505.
25. P. A. Bergström, J. Lindgren, *J. Mol. Struct.*, 1990, **239**, 103.
26. M. Hamidi, J. L. Pascal, *Polyhedron*, 1999, **13**, 1787.
27. M. Hamidi, M. Hnach, H. Zineddine, *J. Fluorine Chem.*, 1999, **99**, 109.
28. K. Aoki, N. Kato, *J. Electroanal. Chem.*, 1988, **245**, 51.
29. D. J. Schiffrin, *J. Electroanal. Chem.*, 1986, **201**, 199.
30. *CRC Handbook of Chemistry and Physics*, Ed. D. R. Lide, CRC Press, Inc., USA, 1995.
31. J. E. B. Randles, *Trans. Faraday Soc.*, 1948, **44**, 327.
32. A. Sevcik, *Collection Czech. Chem. Commun.*, 1948, **13**, 349.

CHAPTER 5

SYNTHESIS AND ELECTROCHEMISTRY OF A THORIUM(IV) TFSI COMPLEX IN $[\text{Me}_3\text{N}^n\text{Bu}][\text{TFSI}]$

5.1 Introduction

It has previously been shown that quaternary alkyl ammonium based LTILs have large electrochemical windows (up to +2.7 to -3.2 V for $[\text{Me}_3\text{N}^+\text{Bu}][\text{TFSI}]$) and the electrochemistry of selected Ln(III) TFSI compounds ($[\text{Ln}(\text{TFSI})_3(\text{H}_2\text{O})_3]$, where Ln = La, Sm and Eu) have previously been explored in $[\text{Me}_3\text{N}^+\text{Bu}][\text{TFSI}]$ (see Chapters 3 and 4) with both Ln(III)/Ln(0) and Ln(II)/Ln(0) reduction processes observed. The trivalent lanthanides are good chemical and electrochemical analogues for both U(III) and Pu(III), however both U and Pu can also exist in the tetravalent state.

The chemistry of Th is restricted to Th(IV)/Th(0) species and the standard reduction potential for the Th(IV)/Th(0) couple should be within the electrochemical window for the LTILs previously studied ($E^0(\text{Th(IV)/Th(0)}) = -1.899 \text{ V}$).¹ Although the choice of ^{232}Th presents some radiological hazards (^{232}Th has a half life of $1.40 \times 10^{10} \text{ y}$, see Chapter 1), Th(IV) can be used as a chemical and electrochemical analogue for U(IV) and Pu(IV). In addition, Th(IV) is by far the most stable oxidation state for Th, with higher oxidation states not possible, greatly simplifying observable electrochemical processes (e.g. U and Pu have four commonly encountered oxidation states which include actinyl and non-actinyl species). The chemistry and electrochemistry of U, Np and Pu, is complicated by more than one accessible oxidation state in solution, hence it is a logical step to investigate the electrochemical and chemical behaviour of Th(IV) before moving to the later actinides of more relevance to irradiated fuel processing.

The electrochemistry of Th has been studied in a variety of media including molten salts, organic solvents and aqueous solutions, the first two being most relevant to these studies. In high temperature molten salts Martinot studied the electrochemical behaviour of Th in LiCl-KCl eutectic at 400 °C, and also investigated the electrochemical response during the conversion of ThO₂ to Th in the same melt during the addition of HCl gas. In both cases the reduction followed a one step, four electron process.^{2,3}

At lower temperatures Martinot *et al.*⁴ and Duyckaerts and Degueldre⁵ studied the reduction of Th(IV) to Th(0) in molten dimethylsulfoxide (DMSO). Both groups found that Th(IV) was reduced in one step. Neither found any evidence for thorium reduction *via* a transient Th(II) species as observed by Astheimer and Schwochau in the same solvent system.⁶

The speciation and coordination of Th has been studied for a variety of compounds and complexes. In general this hard metal cation tends to form complexes/compounds with hard donor ligands, *e.g.* nitrate,^{7,8} chlorate,⁸ carbonate,⁸ and phosphate.^{8,9} The most common coordination number for Th(IV) is eight,¹⁰⁻¹³ however this can vary from six to twelve dependent on the ligands it forms complexes with.⁸

5.2 Synthesis of hydrogen

pentakis-bis(trifluoromethanesulfonyl)amidethorium(IV) dihydrate – $\text{H}[\text{Th}(\text{TFSI})_5] \cdot 2\text{H}_2\text{O}$

$\text{Th}(\text{NO}_3)_4 \cdot 6\text{H}_2\text{O}$ (1.27 g, 2.16 mmol) was dissolved in HNO_3 (5 mL, 1 mol L⁻¹) to yield a 0.43 mol L⁻¹ Th(IV) stock solution. 1 mL (0.43 mmol Th) of this stock solution was reacted with 2 mL of NaOH solution (0.14 g, 3.50 mmol) with stirring to form a white precipitate of $\text{Th}(\text{OH})_4$. The precipitate was washed with distilled H_2O (5 mL) and centrifuged for 10 m at 3000 rpm. The supernatant solution was discarded and the solid washed with distilled H_2O (5 mL) and a further 2 mL of NaOH solution (0.14 g, 3.50 mmol) was added. The resulting solution was centrifuged for a further 10 m at 4000 rpm, and the supernatant discarded. The wet solid was dissolved in a solution of HTFSI (2.25 g, 8.00 mmol, 5 mL H_2O) to form a clear solution. This solution was then heated at 80 – 90 °C in an open beaker for 5 h to produce a white, microcrystalline product which was stored under Ar (near quantitative yield) (found: C, 7.60 %; H, 0.30 %; N, 4.39 %; S, 19.91 %; Calc. for $\text{H}[\text{Th}(\text{TFSI})_5] \cdot 2\text{H}_2\text{O}$: C, 7.20 %; H, 0.30 %; N, 4.20 %; S, 19.21 %).

5.3 Thermogravimetric analysis of $\text{H}[\text{Th}(\text{TFSI})_5] \cdot 2\text{H}_2\text{O}$

Thermogravimetric analysis (TGA) of $\text{H}[\text{Th}(\text{TFSI})_5] \cdot 2\text{H}_2\text{O}$ was undertaken and the results are shown in Figure 5.3.1. The sample (16.00 mg) was heated from 25 to 900 °C at a rate of 5 °C m⁻¹. TGA analysis showed four decomposition steps at *ca.* 70, 160, 235

and 390 °C (mass loss of 0.46, 0.80, 2.77 and 9.63 mg, respectively). A final mass of 2.34 mg was recorded, attributed to the formation of ThO₂.

Using the mass of ThO₂ measured at the end of the experiment the initial mass of H[Th(TFSI)₅].2H₂O present was calculated to be 14.79 mg. The discrepancy of 1.21 mg (between the measured and calculated masses) is attributed to absorbed water from the atmosphere and corresponds to 8 water molecules per Th complex. The loss of this water corresponds to the first two decomposition steps at 70 °C and 160 °C. The decomposition steps at 235 and 390 °C are thus assigned to the loss of coordinated ligands to form ThO₂. Based on these assignments, a decomposition route is proposed and is shown in Figure 5.3.2. It should be noted that HTFSI sublimes at *ca.* 60 °C, thus the mass loss corresponding to a formula of C₂F₆NS₂O₆H₅ suggests that HTFSI is coordinated to the Th centre as opposed to co-crystallising.

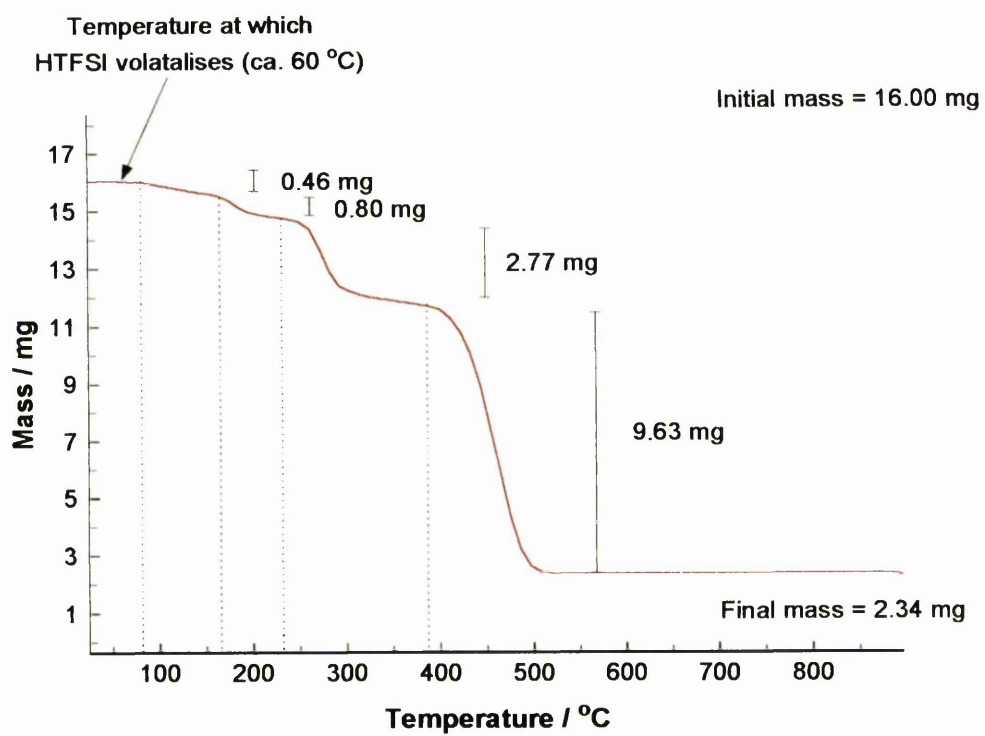


Figure 5.3.1: Thermogravimetric analysis of $\text{H}[\text{Th}(\text{TFSI})_5] \cdot 2\text{H}_2\text{O}$

Formula	Theoretical mass loss	Actual mass loss
ThC ₁₀ F ₃₀ N ₅ S ₁₀ O ₂₂ H ₅ + 8H ₂ O		
↓ 70 °C -3H ₂ O	0.48 mg	0.46 mg
ThC ₁₀ F ₃₀ N ₅ S ₁₀ O ₂₂ H ₅ + 5H ₂ O		
↓ 160 °C -5H ₂ O	0.80 mg	0.80 mg
ThC ₁₀ F ₃₀ N ₅ S ₁₀ O ₂₂ H ₅		
↓ 235 °C	2.81 mg	2.77 mg
↓ -C ₂ F ₆ NS ₂ O ₆ H ₅		
ThC ₈ F ₂₄ N ₄ S ₈ O ₁₆		
↓ 390 °C	9.64 mg	9.63 mg
↓ -C ₈ F ₂₄ N ₄ S ₈ O ₁₄		
ThO ₂		

Figure 5.3.2: Proposed thermal decomposition route for H[Th(TFSI)₅].2H₂O

5.4 Vibrational spectroscopy

Solid state ATR mid-IR and Raman spectra of H[Th(TFSI)₅].2H₂O were recorded and are shown in Figure 5.4.1. Using the vibrational spectroscopic studies on Li[TFSI] and Ln-TFSI complexes (Chapter 4), the IR and Raman bands have been assigned and are given in Table 5.4.1 Bands due to TFSI are observed in both the IR and Raman spectra. The vibrational spectra show similarities to those obtained for the Ln-TFSI complexes (Ln = La, Sm and Eu, Chapter 4), thus it is proposed that TFSI coordinates to the Th centre.

Differences in band positions are attributed to the differences in size between the Th^{4+} and Ln^{3+} centres.

In the IR and Raman spectra bands due to N-H modes have also been observed. Both elemental analysis and TGA suggest that HTFSI is present in the Th-TFSI complex, and this assignment is supported by the observation of bands due to N-H vibrational modes. Comparison of the $\delta(\text{NH})$ (IR) and $\omega(\text{NH})$ (Raman) band positions with those of HTFSI show differences in band positions (1438 cm^{-1} *cf.* 1463 cm^{-1} for $\delta(\text{NH})$ and 1450 cm^{-1} *cf.* 1332 cm^{-1} for $\omega(\text{NH})$ for $\text{H}[\text{Th}(\text{TFSI})_5] \cdot 2\text{H}_2\text{O}$ and HTFSI, respectively). Therefore, taking the TGA data into account, this is a further indication that HTFSI is coordinated to the Th centre as opposed to co-crystallising.

Bands due to water have also been detected at 3257 and 1639 cm^{-1} ($\nu(\text{H}_2\text{O})$ and $\delta(\text{OH})$, respectively). It is known from the literature that the $\nu(\text{H}_2\text{O})$ band appears in the $3550\text{--}3200\text{ cm}^{-1}$ range with $\delta(\text{OH})$ in the $1630\text{--}1600\text{ cm}^{-1}$ range,^{13,14} and the observed band positions are comparable to these ranges. Previously the $\nu(\text{H}_2\text{O})$ and $\delta(\text{OH})$ bands for coordinated water have been observed in the $3415\text{--}3460\text{ cm}^{-1}$ ($\nu(\text{H}_2\text{O})$) and $1635\text{--}1640\text{ cm}^{-1}$ ($\delta(\text{OH})$) ranges for $\text{A}_2[\text{Th}(\text{O}_2)\text{F}_2(\text{OH})_2] \cdot n\text{H}_2\text{O}$ (where $\text{A} = \text{NH}_4$, $n = 3$; Na or K , $n = 1$) and $[\text{Th}(\text{O}_2)_3\text{L}(\text{H}_2\text{O})_4] \cdot 5\text{H}_2\text{O}$ ($\text{L} = \text{C}_2\text{O}_4$ or SO_4).¹² Additionally, the $\rho(\text{Th-OH}_2)$ band has been observed at *ca.* 730 cm^{-1} in the IR spectrum.¹² However, in the IR spectra of the Th-TFSI complex, no distinct band that can be assigned to a $\rho(\text{Th-OH}_2)$ mode was observed in the $700\text{--}800\text{ cm}^{-1}$ range. The vibrational spectroscopic data thus show that

water is present in the complex, however it does not conclusively distinguish between coordinated water or waters of crystallisation.

Assignment	Li[TFSI]		[La(TFSI) ₃ (H ₂ O) ₃]		H[Th(TFSI) ₅].2H ₂ O		HTFSI ¹²	
	IR	Raman	IR	Raman	IR	Raman	IR	Raman
ν (H ₂ O)	-	-	3458	-	3257	-	-	-
δ (OH)	-	-	1631	-	1639	-	-	-
δ (NH)	-	-	-	-	1438	-	1463	-
ω (NH)	-	-	-	-	-	1450	-	1332
$\nu_a^{i.p./o.p.}$ (SO ₂)	1323	1318	1312	1316	1334	1331	1442	1436
	1307				1324	1318		1427
					1314			
ν_s (CF ₃)	1242	1247	1235?	1243	1239?	1237	1301	1250
							1241	
ν_a (CF ₃)	1195	-	1219	-	1226?	-	1225	1220
			1196		1196		1200	1208
$\nu_s^{o.p.}$ (SO ₂)	1138	-	1138	-	1133	-	1140	1134
			1126		1115			
			1105					
$\nu_s^{i.p.}$ (SO ₂)	-	1131	-	1146	-	1152	-	-
						1137?		
ν_a (SNS)	1062	-	1051	-	1054	-	859	830
ν (CS)	810?	-	806?	-	797	803?	-	-
ν_s (SNS)	773?		773	-	771	-	-	-
δ_s (CF ₃)	746	747	750	755	741	747	778	765
δ (SNS)	ca. 665	-	662	-	651	658?	647	634
			650		639			
$\delta^{o.p./i.p.}$ (SO ₂)	606	593?	597	-	581	588	615	583
δ_a (CF ₃)	569		573	575	560	575	570	570
	510						503	
δ_s (SO ₂)	554?	552?	-	554	554?	554	-	555
γ (NH)	-	-	-	-	459?	514?	460	526
ρ (SO ₂)	-	330	-	332	-	334	-	-
		310		310		311?		
ρ (CF ₃)	-	276	-	-	-	-	-	-
ν (LnO)	-	-	-	297?	-	-	-	-
ν (ThO)	-	-	-	-	-	286	-	-

Table 5.4.1: Solid state ATR mid-IR and Raman bands of H[Th(TFSI)₅].2H₂O.

IR/Raman bands of Li[TFSI], HTFSI and [La(TFSI)₃(H₂O)₃] crystals shown for

comparison. ν , stretching; δ , bending; ω , wagging; τ , torsion; ρ , rocking; ? =

tentative assignment

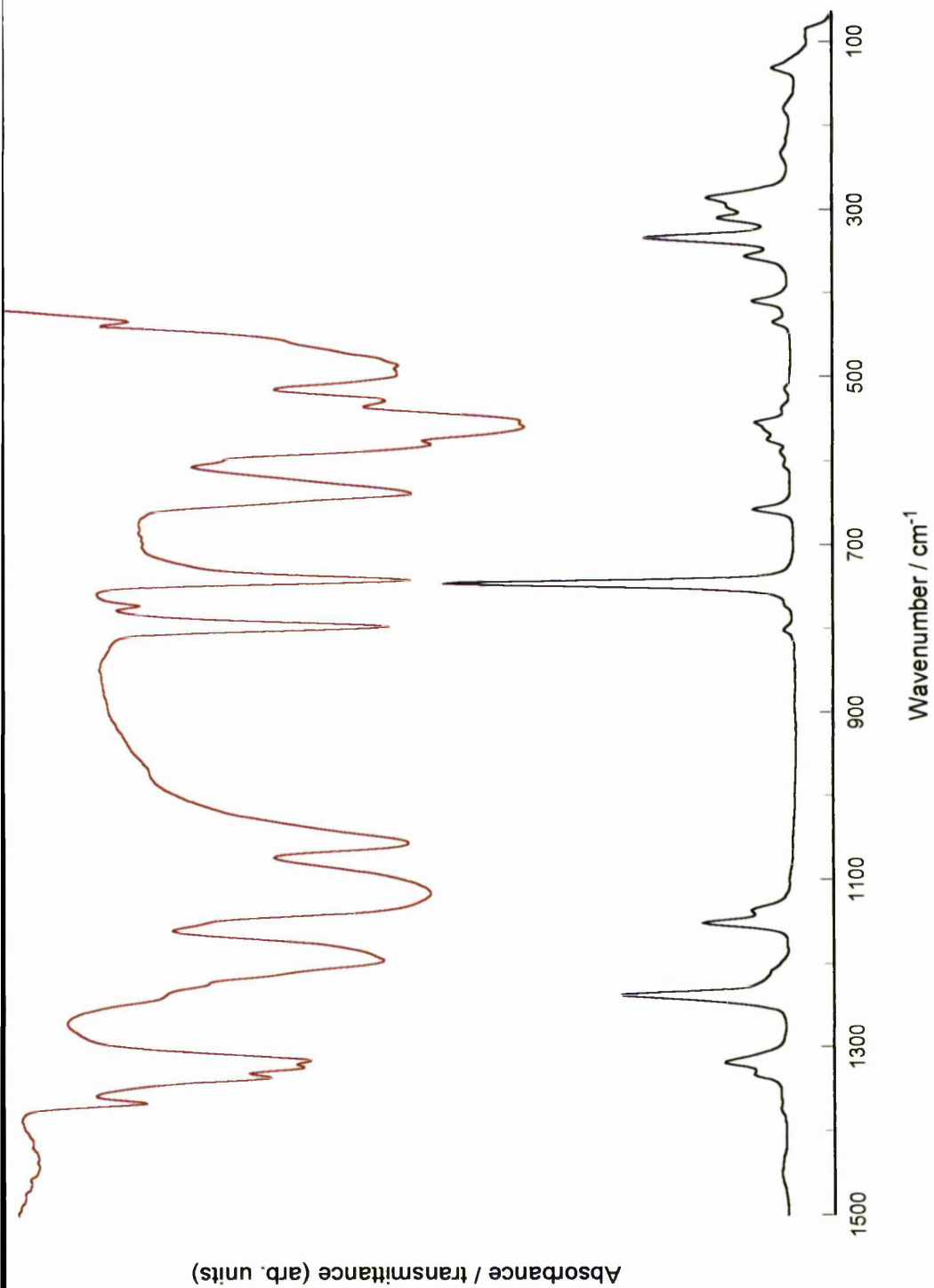


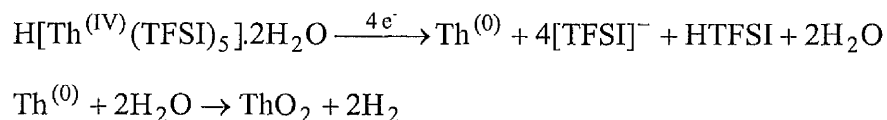
Figure 5.4.1: Solid state ATR mid-IR and Raman spectra of $\text{H}[\text{Th}(\text{TFSD})_5] \cdot 2\text{H}_2\text{O}$

5.5 Electrochemistry

$\text{H}[\text{Th}(\text{TFSI})_5] \cdot 2\text{H}_2\text{O}$ (0.21 mmol) was dissolved in $[\text{Me}_3\text{N}^n\text{Bu}][\text{TFSI}]$ (4 mL) and cyclic voltammograms were recorded and are shown in Figure 5.5.1. A typical 3 electrode cell was used with a glassy carbon working electrode (2 mm dia.), a large surface area platinum gauze counter electrode and a Ag wire quasi-reference electrode (see Chapter 2). All measurements were recorded at 25 °C inside a Faraday cage under an Ar atmosphere to minimise electrochemical noise. The solution was purged with Ar for at least 30 min prior to measurements and for 30 s between scans. The solution was kept under a blanket of Ar at all times. All potentials quoted are relative to a Ag wire quasi-reference electrode.

Cyclic voltammograms of $\text{H}[\text{Th}(\text{TFSI})_5] \cdot 2\text{H}_2\text{O}$ in $[\text{Me}_3\text{N}^n\text{Bu}][\text{TFSI}]$ showed one cathodic wave at *ca.* -2.15 V, and one broad anodic wave at -1.88 V. Based on the known electrochemical behaviour of Th in molten salts these waves could be due to either the Th(IV)/Th(0) or Th(IV)/Th(II) processes. The addition of ferrocene (0.24 mmol, $E_{1/2} = 0.14$ V) as an internal standard confirmed the former process. Firstly the cathodic peak position ($E_{p/c} = -2.29$ V *vs.* Fc/Fc^+) is comparable to that of the standard reduction potential of the Th(IV)/Th(0) process ($E^0 = -2.299$ V *vs.* Fc^+/Fc , -1.899 V *vs.* SHE).¹ Secondly, comparison of the peak area for the ferrocene reduction and the Th reduction peak showed a ratio of 1:4, which suggest that the Th is reduced in one step with a four electron transfer as previously observed in DMSO and in molten LiCl-KCl eutectic.²⁻⁵

The waveforms for the reduction of $\text{H}[\text{Th}(\text{TFSI})_5] \cdot 2\text{H}_2\text{O}$ share features in common with those of $[\text{Ln}(\text{TFSI})_3(\text{H}_2\text{O})_3]$, *i.e.* a well defined reduction peak and a broad, shallow oxidation peak (see Chapter 4). In the case of the lanthanide electrochemistry this was assigned to the formation of an oxide layer due to the presence of moisture in the system (Chapter 4). The waveforms for the oxidation/reduction processes are consistent with those expected for the deposition of an insoluble product on the electrode surface,^{15,16} suggesting a similar electrode reaction is progressing *i.e.* reduction to thorium metal on the electrode surface, followed by reaction with water to yield ThO_2 . Multiple cycles around this region showed a decrease in current intensity for the reduction peak, as would be expected for the formation of a non-conducting oxide layer (Figure 5.4.2). The following reaction mechanism is proposed to account for this behaviour:



Martinot *et al.* have previously observed the formation of ThO_2 in DMSO.⁴ In their experiment, bulk electrolysis of a solution of ThCl_4 in DMSO formed a mixture of Th metal and thorium oxide (as well a mixture of organic compounds presumably from the degradation of DMSO).

It should be noted that both TGA analysis and vibrational spectroscopy have both suggested the presence of HTFSI in the Th complex. The possible cathodic peak observed at -0.44 V in Figure 5.5.1 is therefore assigned to the H^+/H_2 reduction process.

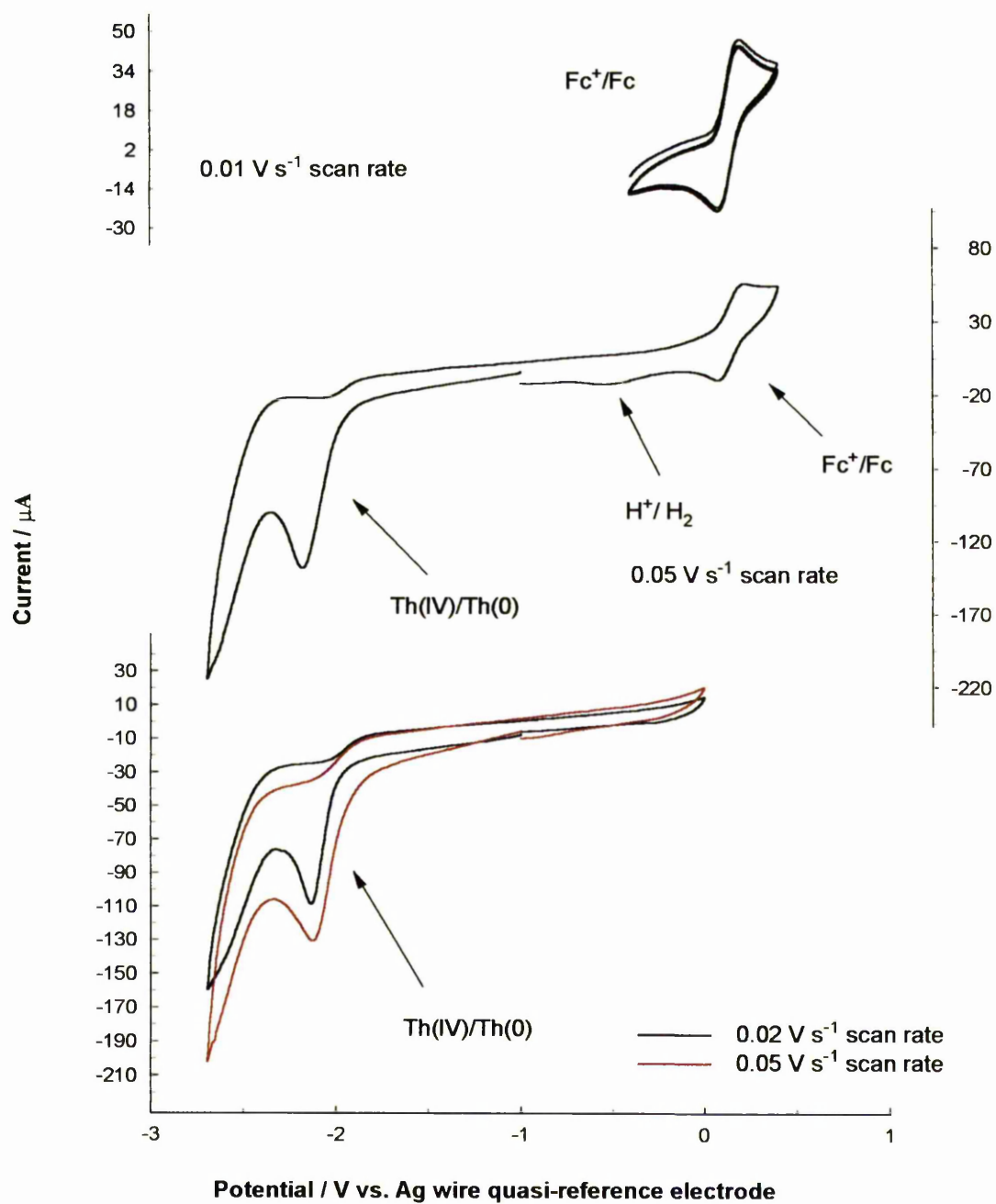


Figure 5.5.1: Cyclic voltammograms of $\text{H}[\text{Th}(\text{TFSI})_5] \cdot 2\text{H}_2\text{O}$ in $[\text{Me}_3\text{N}^n\text{Bu}][\text{TFSI}]$ at 25°C

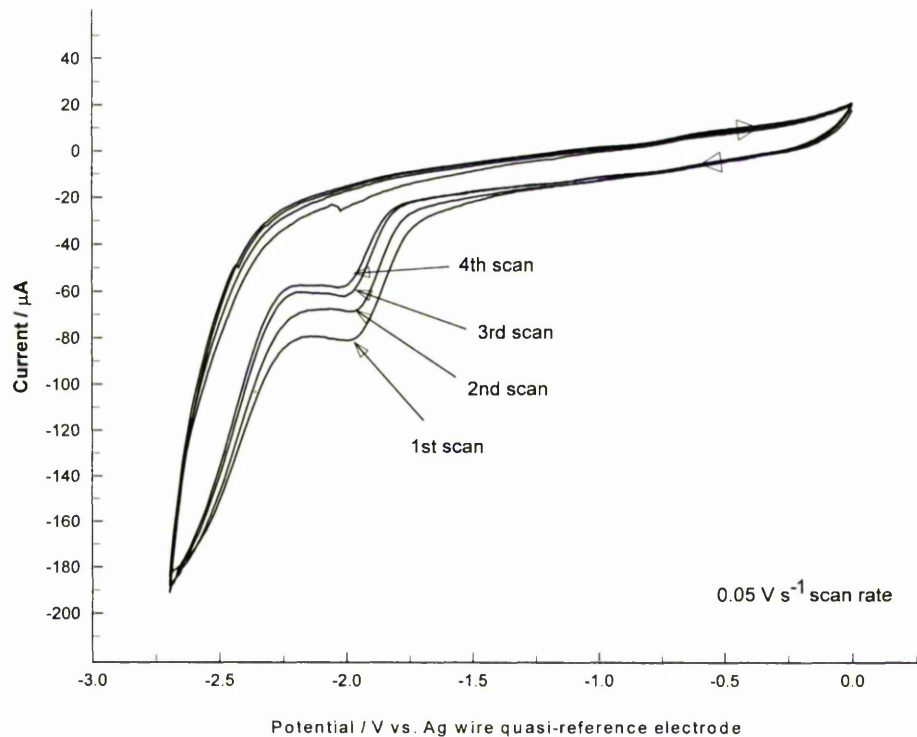


Figure 5.5.2: Effect of multiple cycles around the Th(IV)/Th(0) reduction peak.

5.6 Summary

The actinide TFSI salt, $\text{H}[\text{Th}(\text{TFSI})_5] \cdot 2\text{H}_2\text{O}$ has been synthesised and characterised by elemental analysis, thermogravimetric analysis and vibrational spectroscopy. The spectroscopic studies showed that the TFSI anion coordinated to the metal centre, however there are differences in coordination from the lanthanide salts as a result of probable coordination of HTFSI.

The electrochemistry of $\text{H}[\text{Th}(\text{TFSI})_4]_2\text{H}_2\text{O}$ was investigated in the LTIL $[\text{Me}_3\text{N}^+\text{Bu}][\text{TFSI}]$. Voltammograms show a single reduction peak which has been assigned to the $\text{Th}(\text{IV})/\text{Th}(0)$ process. No evidence for the two step reduction mechanism involving the transient $\text{Th}(\text{II})$ (or $\text{Th}(\text{III})$) species was found on the timescales of the voltammetric experiments performed. The absence of a significant oxidation peak is explained by the occurrence of secondary chemical reactions at the electrode surface leading to an oxide formation (ThO_2), as previously observed for the lanthanides (Chapter 4). Based on the electrochemical behaviour of the lanthanides in LTILs a reaction mechanism has been proposed which involves the reduction of $\text{H}[\text{Th}(\text{TFSI})_4]_2\text{H}_2\text{O}$ to a metal, followed by the subsequent chemical reaction with water present in the system to form an oxide phase.

5.7 References

1. *CRC Handbook of Chemistry and Physics*, Ed. D. R. Lide, CRC Press, Inc., USA, 1995.
2. L. Martinot, *J. Radioanal. Nucl. Chem.*, 1986, **103**, 357.
3. L. Martinot, *J. Less-Common Met.*, 1989, **147**, 73.
4. L. Martinot, C. Licour, L. Lopes, *J. Alloys Compd.*, 1995, **228**, 6.
5. G. Duyckaerts, Cl. Degueldre, *J. Electroanal. Chem.*, 1981, **119**, 347.
6. L. Astheimer, K. Schwochau, *J. Inorg. Nucl. Chem.*, 1973, **35**, 223.
7. J. R. Ferraro, L. I. Katzin, G. Gibson, *J. Am. Chem. Soc.*, 1954, **76**, 909.

8. J. J. Katz, G. T. Seaborg, L. R. Morss, *The Chemistry of the Actinide Elements*, Chapman and Hall, New York, 1986.
9. K. R. Laud, *J. Am. Ceram. Soc.*, 1971, **54**, 296.
10. J. R. Ferraro, C. Cristallini, I. Fox, *J. Inorg. Nucl. Chem.*, 1967, **29**, 139.
11. R. C. Fay, T. J. Pinnavaia, *Inorg. Chem.*, 1968, **7**, 508.
12. C. R. Bhattacharjee, M. K. Chaudhuri, *Inorg. Chim. Acta*, 1989, **160**, 147.
13. A. Saito, G. R. Choppin, *Inorg. Chem.*, 1991, **30**, 4563.
14. K. Nakamoto, *Infrared and Raman Spectra of Inorganic and Coordination Compounds, Part B, 5th Edition*, John Wiley & Sons, New York, 1997.
15. K. Aoki, N. Kato, *J. Electroanal. Chem.*, 1988, **245**, 51.
16. D. J. Schiffrin, *J. Electroanal. Chem.*, 1986, **201**, 199.

CHAPTER 6

URANIUM SPECIATION IN TFSI-BASED

IONIC LIQUIDS AND

ELECTROCHEMISTRY IN

$[\text{Me}_3\text{N}^n\text{Bu}][\text{TFSI}]$

6.1 Introduction

The LTILs comprising Group 15 based cations and TFSI would appear to have electrochemical windows with a cathodic limit sufficiently negative to observe the reduction of U(III) and Pu(III) to the zerovalent state (Chapter 3). This is experimentally supported by the observation of the Ln(III)/Ln(0), Ln(II)/Ln(0) and Th(IV)/Th(0) reductions in these melts (Chapters 4 and 5).

Both U and Pu show complex electrochemical and chemical behaviour due to the range of available oxidation states. Both can exist in the 0, +III, +IV, +V and +VI states with the latter two often present as the actinyl cation ($\{\text{AnO}_2\}^+$ and $\{\text{AnO}_2\}^{2+}$, respectively). For Th the electrochemistry is limited to the +IV and 0 oxidation states (in $[\text{Me}_3\text{N}^n\text{Bu}][\text{TFSI}]$, see Chapter 5) and so Th(IV) can be used as an electrochemical analogue for U(IV) and Pu(IV). Similarly the electrochemical behaviour of the non-radioactive lanthanides is restricted to the +III, +II and 0 oxidation states in $[\text{Me}_3\text{N}^n\text{Bu}][\text{TFSI}]$ (see Chapter 4), and Ln(III) can therefore be used as electrochemical analogues for both U(III) and Pu(III). However, neither Th or the Lns are suitable analogues for the higher oxidation states of U.

Previously Costa *et al.* have explored the electrochemistry and speciation of U in 1,3-dialkylimidazolium chloroaluminate melts,¹⁻⁴ and using a combination of electronic absorption spectroscopy and electrochemical techniques have found evidence for *ca.* 9 different species in solution. Analogous studies using Pu showed evidence for *ca.* 10

species.⁵ This complex solution speciation is accounted for by the number of accessible oxidation states available to U, and the possibility for +V and +VI actinyl chemistry, which, upon reduction, introduce oxygen into solution as O²⁻ or its protonated forms.

In a comparable study to the 1,3-dialkylimidazolium chloroaluminate melts, Costa *et al.* have investigated the electrochemistry and speciation of U in TFSI based melts, and have postulated that upon dissolution of UCl₄ in *N,N*-ethylmethylether-methylpyrrolidinium TFSI the [UCl₄(TFSI)₂]²⁻ species is formed.⁶ Rogers *et al.* have investigated the solution speciation of U in 1-octyl-3-methylimidazolium TFSI using EXAFS.⁷ Their studies indicate that, in the presence of the strongly coordinating ligand, CMPO (octyl-phenyl-*N,N*-diisobutylcarbamoylmethylphosphine oxide), TFSI does not coordinate to the {UO₂}²⁺ cation.⁷ In the course of this work it has been shown through single crystal X-ray diffraction experiments that TFSI can coordinate to an *f*-element (La) through the sulfonyl oxygens (Chapter 4). Additionally, vibrational spectroscopy has provided further evidence for TFSI coordination *via* the sulfonyl oxygens for La, Sm, Eu and Th complexes (Chapters 4 and 5).

As previously stated, the aim of this work is to demonstrate whether LTILs could be used for the separation of U and Pu from irradiated nuclear fuel (Chapter 1). Therefore, the coordination and electrochemistry of U in LTILs need to be investigated in more depth than those of Ln and Th. Based on the electrochemical and speciation studies performed by Costa *et al.*¹⁻⁴ and the number of accessible oxidation states available to U, it is hypothesised that the electrochemistry of U will be complicated in TFSI based LTILs.

Thus in an attempt to gain further insight into the electrochemical behaviour, the solution behaviour of a number of uranium complexes has been investigated using XAS techniques (as well as UV/vis/nIR, vibrational spectroscopy and single crystal X-ray diffraction). It has already been hypothesised that TFSI is a poor ligand for *f*-elements (Chapters 4 and 5), therefore in addition to studying U-TFSI complexes, a comparative study of U-Cl complexes was also performed.

6.2 Synthesis of uranium TFSI and chloride complexes

6.2.1 General considerations

All synthesis and manipulation of samples were carried out under an inert (Ar) atmosphere using standard Schlenk line techniques. The synthesised compounds readily absorbed water from the atmosphere, and were thus stored and manipulated under Ar in an inert atmosphere drybox. Samples for elemental analysis were prepared by sealing *ca.* 5-10 mg of sample in an aluminium capsule under Ar prior to measurements. However, due to a lack of inert atmosphere facilities in the microanalysis laboratory, all elemental analysis measurements were performed in air.

UCl₃, UCl₄, UO₂Cl₂.H₂O and Tl[TFSI] were synthesised by Dr V. A. Volkovich (CRR, The University of Manchester) and used as supplied. The compounds were stored and handled inside an inert atmosphere drybox to eliminate contamination by H₂O and O₂.

[Me₄N][TFSI] and [Me₃NⁿBu][TFSI] were synthesised as reported in Chapter 3.

Tri-*n*-hexyl,tetradecylphosphonium dicyanamide ([ⁿHex₃PDec][NCNCN]) and triisobutyl,*n*-hexyl phosphonium *p*-toluenesulfate ([ⁱBu₃PⁿHex][OTs]) were obtained from Cytech, Canada and used as supplied.

6.2.2 Uranium bis(trifluoromethanesulfonyl)amide – U(TFSI)₄.xH₂O

Method A: Tl[TFSI] was added to a solution of UCl₄ in deoxygenated water to form a green coloured solution and a white precipitate of TlCl. After filtration to remove the precipitate, the solvent was removed *in vacuo* to yield a very hygroscopic green solid for which the microanalysis are expected to be unreliable, (found: C, 6.29 %; H, 0.52 %; N, 3.68 %; S, 17.04 %; U, 18.36 %; Calc. for 80 % U(TFSI)₄.4H₂O and 20 % UO₂(TFSI)₂.H₂O: C, 6.51 %; H, 0.50 %; N, 3.80 %; S, 17.37 %; U, 18.93 %)

Method B: KI (0.43 g, 2.59 mmol) was added to a solution of UCl₄ (0.93 g, 2.45 mmol) in HCl (5 mol L⁻¹) and the solution stirred. After 20 min a solution of NaOH (10 mol L⁻¹) was added dropwise until an olive green precipitate of hydrated U(OH)₄ was produced. This precipitate was collected and washed with deoxygenated water under Ar and to it a solution of HTFSI (excess *ca.* 3.50 g, 12.49 mmol in 40 mL H₂O) was added and the mixture heated at 80 °C for 24 h. The resulting clear green solution was heated at 80 °C *in vacuo* to remove water and excess HTFSI. Typical yields of 70 – 80 % were recorded (Found: C 6.52 %, H, 0.00 %, N 3.73 %, S 17.87 %, U 19.75 %; calc. for 78 % U(TFSI)₄ and 22 % UO₂(TFSI)₂: C 6.79 %, H, 0.00 %, N 3.96 %, S 18.13 %, U 19.98 %)

It should be noted that the number of waters found using elemental analysis for the products from both method A and method B varied (4 for method A and 0 for method B). As both syntheses were performed in aqueous solution, it is not immediately clear as to whether the water found in the product of method A is a result of the synthetic procedure or absorption of moisture from the atmosphere during the analysis procedure.

6.2.3 Uranyl bis(trifluoromethanesulfonyl)amide hydrate – $\text{UO}_2(\text{TFSI})_2 \cdot \text{H}_2\text{O}$

A solution of HTFSI in deoxygenated water was added to UO_3 and the resultant yellow solution stirred for 3-4 h. The solvent was removed *in vacuo* to yield a yellow hygroscopic solid (found: C, 5.62 %; H, 0.29 %; N, 3.34 %; S, 15.35 %; U, 28.48 %; Calc. for $\text{UO}_2(\text{TFSI})_2 \cdot \text{H}_2\text{O}$ C, 5.66 %; H, 0.24 %; N, 3.30 %; S, 15.12 %; U, 28.07 %)

6.3 UV/vis/nIR spectroscopy of uranium compounds in the solid state and dissolved in LTILs

UV/vis/nIR spectroscopy has previously been used to determine the oxidation state of actinide ions in compounds in the solid state and in a variety of media including molten salts and LTILs,⁸⁻¹⁶ and is a standard method for determination of actinide oxidation states. Typically the uranyl ion has a U-O charge transfer band in the 350-500 nm range often with fine structure.¹³⁻¹⁶ U(IV) and U(III) both exhibit *f-f* and *f-d* transitions in the visible and nIR regions.⁸⁻¹² Major absorption peaks for uranium complexes in the solid

state and dissolved in selected LTILs are presented in Tables 6.3.1 and 6.3.2, and these bands have been used to assign oxidation states.

It should be noted that all the measurements were recorded in an Ar drybox using fibre optic cables to minimise O₂ and H₂O contamination. Thus many of the spectra are very noisy due to light interference making some assignments difficult, and in some cases no spectra were obtained due to excessive noise. In addition, the poor quality spectra inhibited attempts to obtain accurate extinction coefficients. A sample spectrum highlighting the difficulties is shown in Figure 6.3.1. However, in the solid state, diffuse reflectance UV/vis/nIR spectroscopy showed that the product assigned as UO₂(TFSI)₂.H₂O has an +VI oxidation state and also confirmed that the U(TFSI)₄.xH₂O complex is in a +IV oxidation state.

Upon dissolution in LTILs, UV/vis spectroscopy indicated that the U(IV) and U(VI) complexes remain in the +IV and +VI oxidation state. However, for UCl₃, UV/vis spectroscopy suggests that oxidation occurs *i.e.* U(III) is oxidised to U(IV).

Compound	Major bands / nm	oxidation state	Assignment reference
UCl ₃	750	III?	8
UCl ₄	410, 514, 591, 620	IV	9-12
U(TFSI) ₄ .xH ₂ O	430, 470, 620	IV	9-12
UO ₂ (TFSI) ₂ .H ₂ O	415	VI	13-16

Table 6.3.1: Major bands in the solid state diffuse reflectance UV/vis/nIR spectra for uranium TFSI and chloride complexes

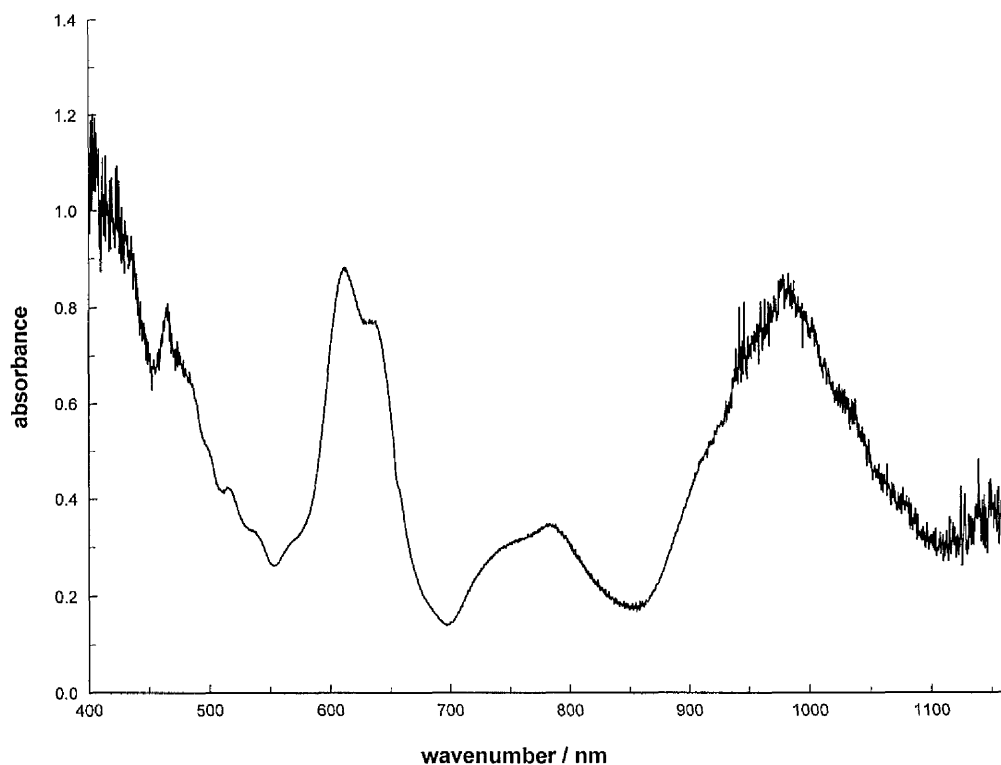


Figure 6.3.1: UV/vis/nIR spectra of U(TFSI)₄.xH₂O dissolved in [Me₃N''Bu][TFSI]

Compound	LTIL	Major bands	Oxidation State	Assignment reference
UCl ₃	[Me ₄ N][TFSI]	No spectra obtained		
	[Me ₃ N ⁿ Bu][TFSI]	No spectra obtained		
	[ⁿ Hex ₃ PDec][NCNCN]	550	III / IV*	8
	[ⁱ Bu ₃ P ⁿ Hex][OTs]	450, 550, 570, 650, 630, 750	III / IV* III / IV*	8 8
UCl ₄	[Me ₄ N][TFSI]	570, 600, 650	IV	9-12
	[Me ₃ N ⁿ Bu][TFSI]	500?, 550, 650, 800?	IV	9-12
	[ⁿ Hex ₃ PDec][NCNCN]	550, 650	IV	9-12
	[ⁱ Bu ₃ P ⁿ Hex][OTs]	570, 650, 750	IV	9-12
UO ₂ Cl ₂ .H ₂ O	[Me ₄ N][TFSI]	450	VI	13-16
	[Me ₃ N ⁿ Bu][TFSI]	No spectra obtained		
	[ⁿ Hex ₃ PDec][NCNCN]	470?	VI	13-16
	[ⁱ Bu ₃ P ⁿ Hex][OTs]	430	VI	13-16
(TFSI) ₄ .xH ₂ O	[Me ₄ N][TFSI]	630?	IV	9-12
	[Me ₃ N ⁿ Bu][TFSI]	450, 500, 600, 640, 740, 780, 980	IV	9-12
	[ⁿ Hex ₃ Pdec][NCNCN]	No spectra obtained		
	[ⁱ Bu ₃ P ⁿ Hex][OTs]	550, 650	IV	9-12
O ₂ (TFSI) ₂ .H ₂ O	[Me ₄ N][TFSI]	420	VI	13-16
	[Me ₃ N ⁿ Bu][TFSI]	No spectra obtained		
	[ⁿ Hex ₃ PDec][NCNCN]	450	VI	13-16
	[ⁱ Bu ₃ P ⁿ Hex][OTs]	420	VI	13-16

Table 6.3.2: UV/vis/nIR bands for uranium complexes dissolved in [Me₄N][TFSI] at 160 °C (room temperature solid state diffuse reflectance spectra of quenched melt), [Me₃NⁿBu][TFSI], [ⁿHex₃PDec][NCNCN] and [ⁱBu₃PⁿHex][OTs] (solution UV/vis/nIR spectra). * = tentative band assignments

6.4 Vibrational spectroscopy

Solid state IR and Raman spectra of $\text{U}(\text{TFSI})_4 \cdot x\text{H}_2\text{O}$, $\text{UO}_2(\text{TFSI})_2 \cdot \text{H}_2\text{O}$ and crystalline $[\text{UO}_2(\text{H}_2\text{O})_5][\text{TFSI}]_2$ (see Appendix 1 for single crystal X-ray diffraction data) were recorded and are shown in Figures 6.4.1, 6.4.2 and 6.4.3. Unfortunately, due to excessive absorption of radiation leading to sample decomposition for the green coloured $\text{U}(\text{TFSI})_4 \cdot x\text{H}_2\text{O}$ complex, Raman spectra for this compound could not be measured. Using the vibrational spectroscopic studies on $\text{Li}[\text{TFSI}]^{17,18}$ and Ln and Th complexes (Chapters 4 and 5), the IR/Raman bands have been assigned and are given in Table 6.4.1.

Bands attributed to TFSI are observed in the IR/Raman spectra for all three compounds. For $\text{U}(\text{TFSI})_4 \cdot x\text{H}_2\text{O}$ and $\text{UO}_2(\text{TFSI})_2 \cdot \text{H}_2\text{O}$ the band positions are comparable to those previously observed for $[\text{La}(\text{TFSI})_3(\text{H}_2\text{O})_3]$, with differences in wavenumbers attributed, in part to the smaller size of the U(IV) and $\{\text{UO}_2\}^{2+}$ cations compared to the Ln(III) cation.

Overall the spectra of $\text{U}(\text{TFSI})_4 \cdot x\text{H}_2\text{O}$ and $\text{UO}_2(\text{TFSI})_2 \cdot \text{H}_2\text{O}$ are similar suggesting similar coordination. The observation of the $\nu_a(\text{U}=\text{O})$ band in the IR spectrum of $\text{U}(\text{TFSI})_4 \cdot x\text{H}_2\text{O}$ suggests that partial oxidation of U(IV) to $\{\text{UO}_2\}^{2+}$ has occurred, which was also observed in the elemental analysis result. Comparison of the spectra of $\text{U}(\text{TFSI})_4 \cdot x\text{H}_2\text{O}$ and $\text{UO}_2(\text{TFSI})_2 \cdot \text{H}_2\text{O}$ to that obtained for crystalline $[\text{UO}_2(\text{H}_2\text{O})_5][\text{TFSI}]_2$ (where TFSI has been shown crystallographically to act as a counter ion rather than a

coordinating ligand, see Appendix 1), shows noticeable differences in band positions indicates that in $\text{U}(\text{TFSI})_4 \cdot x\text{H}_2\text{O}$ and $\text{UO}_2(\text{TFSI})_2 \cdot \text{H}_2\text{O}$, TFSI coordinates to the U centre.

The $\nu_a(\text{U}=\text{O})$ bands observed in the solid state IR spectrum of $\text{UO}_2(\text{TFSI})_2 \cdot \text{H}_2\text{O}$ and crystalline $[\text{UO}_2(\text{H}_2\text{O})_5][\text{TFSI}]_2$ are comparable to those previously reported for uncomplexed $\{\text{UO}_2\}^{2+}$ in water (968 cm^{-1} and 970 cm^{-1} , respectively compared to 962 cm^{-1}).¹⁹ In the solid state Raman spectra the $\nu_s(\text{U}=\text{O})$ band is observed at 897 cm^{-1} for $\text{UO}_2(\text{TFSI})_2 \cdot \text{H}_2\text{O}$ and is 8 cm^{-1} higher in wavenumbers than for crystalline $[\text{UO}_2(\text{H}_2\text{O})_5][\text{TFSI}]_2$. Previously this band has been observed at 870 cm^{-1} for hydrated $\{\text{UO}_2^{2+}\}$ in aqueous solution.¹⁹ The $\nu_s(\text{U}=\text{O})$ band is known to be sensitive to equatorial complexation and has been observed as high as 879 cm^{-1} for $\text{UO}_2(\text{IO}_3)_2(\text{H}_2\text{O})$ previously.²⁰ By comparison, the higher wavenumbers observed for $\text{UO}_2(\text{TFSI})_2 \cdot \text{H}_2\text{O}$ and crystalline $[\text{UO}_2(\text{H}_2\text{O})_5][\text{TFSI}]_2$ indicate that TFSI is a poor ligand for uranium compared to those previously reported in the literature. In addition, the higher wavenumber observed for $\nu_s(\text{U}=\text{O})$ coordinated by TFSI compared to that coordinated by water, indicates that water is a stronger ligand for U than TFSI (as previously observed for $[\text{La}(\text{TFSI})_3(\text{H}_2\text{O})_3]$). The vibrational spectroscopy of U complexes provides further evidence of the poor coordinating ability of TFSI to *f*-element centres. To the best of the author's knowledge, the $\nu_s(\text{U}=\text{O})$ band position at 897 cm^{-1} for $\text{UO}_2(\text{TFSI})_2 \cdot \text{H}_2\text{O}$ is the highest energy observed for this transition.

Assignment	UO ₂ (TFSI) ₂ ·H ₂ O		[UO ₂ (H ₂ O) ₅][TFSI] ₂		U(TFSI) ₄ ·xH ₂ O		[La(TFSI) ₃ (H ₂ O) ₃]		Li[TFSI]	
	IR	Raman	IR	Raman	IR	Raman	IR	Raman	IR	Raman
$\nu_a^{\text{ip/op}}(\text{SO}_2)$	1315	1319	1322	-	1313	-	1312	1316	1323/1307	1318
$\nu_s(\text{CF}_3)$	1234	1238	1259	1240	1234?	-	1235?	1243	1242	1247
$\nu_a(\text{CF}_3)$	1220? 1195	1223 -	1181	-	1194	-	1219 1196	-	-	1195
$\nu_s^{\text{op}}(\text{SO}_2)$	1132 1109	1127	1115	1130	-	-	1138/ 1126/ 1105	-	-	1138
$\nu_s^{\text{ip}}(\text{SO}_2)$	-	-	-	-	-	-	-	1146	-	1131
$\nu_a(\text{SNS})$	1039	-	1044	-	1043	-	1051	-	1062	-
$\nu_a(\text{U=O})$	968	-	970	-	979?	-	-	-	-	-
$\nu_s(\text{U=O})$	-	897	904	891	869?	-	-	-	-	-
$\nu(\text{CS})$	802	-	790	-	804	-	806?	-	810?	-
$\nu_s(\text{SNS})$	773	-	778	-	773	-	773	-	773?	-
$\delta_s(\text{CF}_3)$	744	752	745	747	746	-	750	755	746	747
$\delta(\text{SNS})$	635?	-	665?	-	636?	-	662 / 650	-	665	-

Table 6.4.1: Solid state IR and Raman bands of uranium, lanthanum and lithium TFSI salts

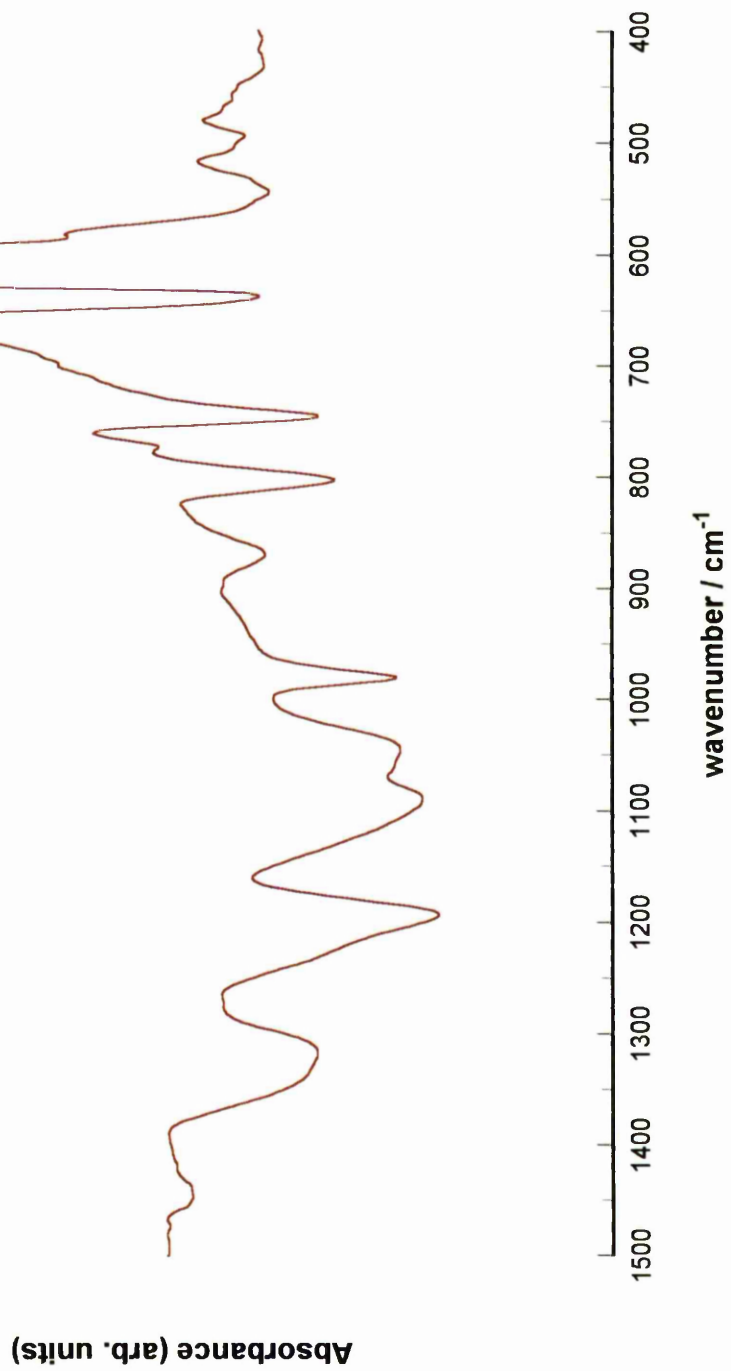


Figure 6.4.1: Solid state ATR mid-IR and far-IR spectra of $\text{U}(\text{TFSD})_4 \cdot x\text{H}_2\text{O}$

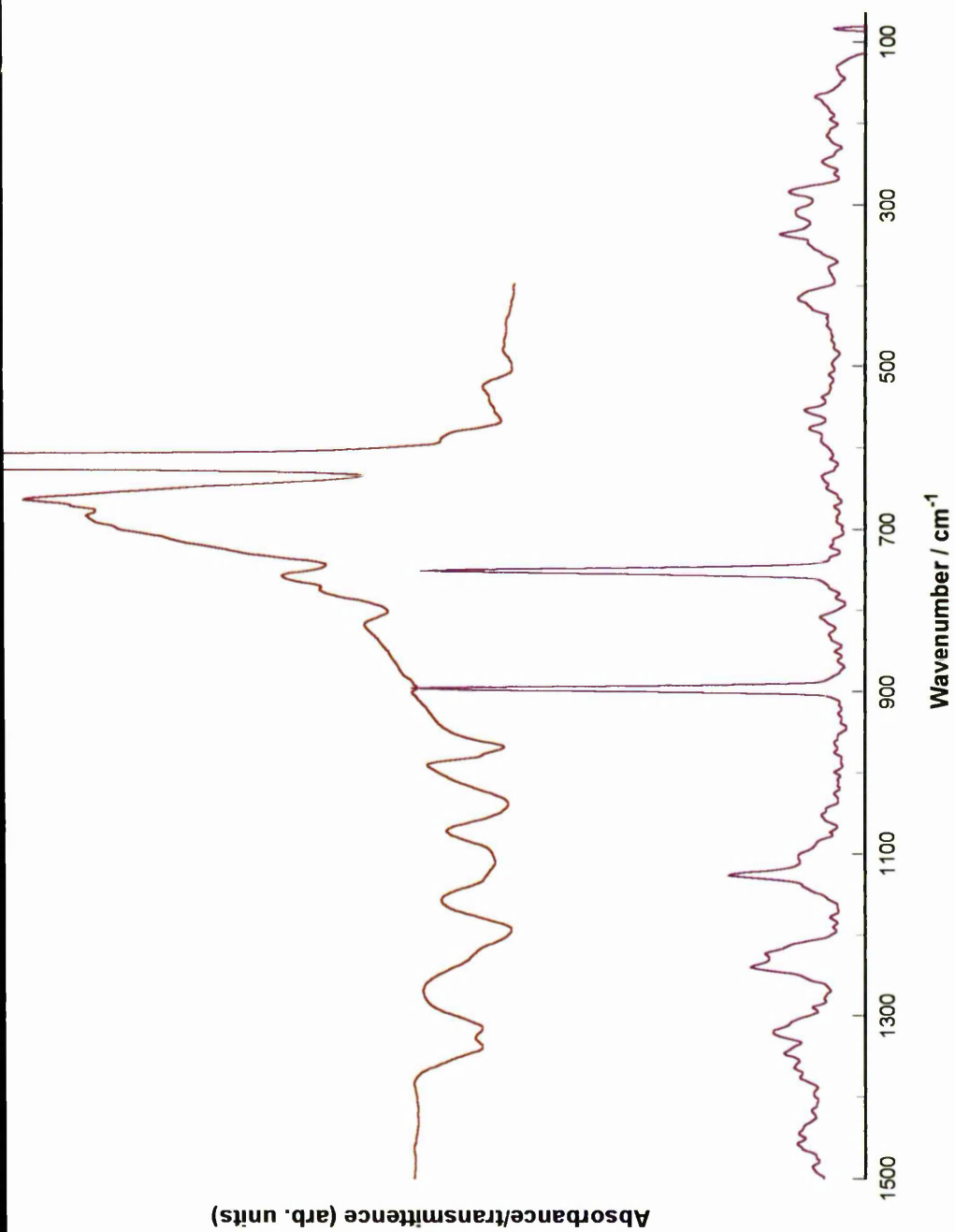


Figure 6.4.2: Solid state ATR IR (red line) and Raman spectra (purple line) of $\text{UO}_2(\text{TFSD})_2 \cdot \text{H}_2\text{O}$

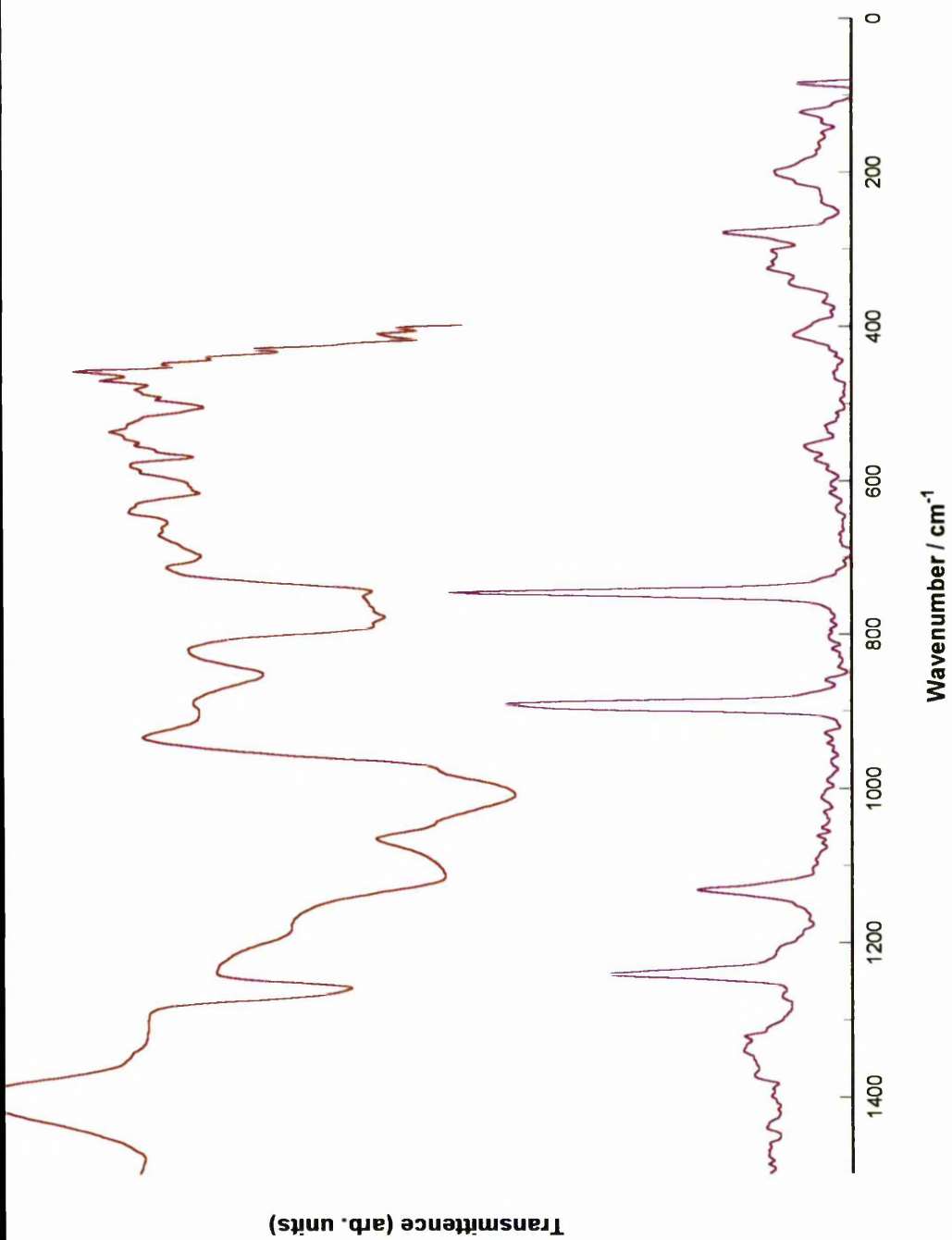


Figure 6.4.3: Solid state ATR IR (red line) and Raman spectra (purple line) of $[\text{UO}_2(\text{H}_2\text{O})_5][\text{TFSI}]_2$

6.5 X-ray absorption spectroscopy

6.5.1 Experimental method

U-L_{III} edge EXAFS and XANES spectra were recorded for uranium TFSI and chloride complexes dissolved in [Me₄N][TFSI], [Me₃NⁿBu][TFSI], [ⁿHex₃PDec][NCNCN] or [ⁱBu₃PⁿHex][OTs]. Additionally, for U(TFSI)₄.xH₂O and UO₂(TFSI)₂.H₂O measurements were also undertaken on pure solid samples supported in a BN matrix. XAS measurements were made either at the European Synchrotron Radiation Facility (ESRF) in Grenoble, France, or at the Synchrotron Radiation Source (SRS) in Daresbury, UK. Spectra were recorded in transmission mode with experimental conditions as given in Table 6.5.1.

Normalised XANES spectra were generated using EXBROOK²¹ (ESRF) or EXCALIB²¹ (SRS). To allow comparisons, the two data sets were normalised to give an edge position, defined by the maximum in the first derivative, of 17176.06 eV observed for samples of UO₂Cl₂.H₂O in both [Me₃NⁿBu][TFSI] and [Me₄N][TFSI].

EXAFS data were analysed using the EXCURV98 data analysis program.²² The goodness of fit was judged by monitoring changes in the R_{EXAFS} parameter and changes accepted only if a significant ($\geq 5\%$ decrease) was obtained. The number of parameters fitted was always lower than or equal to N_{ind} (see Chapter 2). The EXAFS results presented in this Chapter are only for U-TFSI and U-Cl complexes dissolved in [Me₃NⁿBu][TFSI], and of

U-TFSI complexes and UCl_3 in BN (the EXAFS spectra and FT fits for uranium compounds dissolved in other LTILs (Table 6.5.1) are summarised in Appendix 2).

Compound	Solvent / Support	Beamline	Scans	Normalised Edge Position / eV	Observed valency for U
UCl_3	BN	ESRF	2	17168.95	III
	$[\text{Me}_3\text{N}^w\text{Bu}][\text{TFSI}]$	SRS	1	17174.82	IV
	$[\text{Hex}_3\text{PDec}][\text{NCNCN}]$	SRS	4	17173.51	IV
	$[\text{Bu}_3\text{P}^w\text{Hex}][\text{OTs}]$	SRS	4	17173.51	IV
UCl_4	$[\text{Me}_4\text{N}][\text{TFSI}]$	SRS	4	17175.44	IV / VI
	$[\text{Me}_3\text{N}^w\text{Bu}][\text{TFSI}]$	ESRF	4	17173.99	IV
	$[\text{Hex}_3\text{PDec}][\text{NCNCN}]$	SRS	4	17174.82	IV / VI
	$[\text{Bu}_3\text{P}^w\text{Hex}][\text{OTs}]$	SRS	4	17174.19	IV
$\text{UO}_2\text{Cl}_2 \cdot \text{H}_2\text{O}$	$[\text{Me}_4\text{N}][\text{TFSI}]$	SRS	4	17176.06	VI
	$[\text{Me}_3\text{N}^w\text{Bu}][\text{TFSI}]$	ESRF	4	17176.06	VI
	$[\text{Hex}_3\text{PDec}][\text{NCNCN}]$	SRS	4	17176.68	VI
	$[\text{Bu}_3\text{P}^w\text{Hex}][\text{OTs}]$	SRS	4	17176.68	VI
$\text{U}(\text{TFSI})_4 \cdot x\text{H}_2\text{O}$	BN	ESRF	2	17174.80	IV
	$[\text{Me}_4\text{N}][\text{TFSI}]$	SRS	4	17175.44	IV / VI
	$[\text{Me}_3\text{N}^w\text{Bu}][\text{TFSI}]$	ESRF	4	17175.03	IV / VI
	$[\text{Hex}_3\text{PDec}][\text{NCNCN}]$	SRS	1	17177.31	IV / VI
	$[\text{Bu}_3\text{P}^w\text{Hex}][\text{OTs}]$	SRS	4	17176.06	IV / VI
$\text{UO}_2(\text{TFSI})_2 \cdot \text{H}_2\text{O}$	BN	ESRF	2	17175.70	VI
	$[\text{Me}_4\text{N}][\text{TFSI}]$	SRS	3	17177.31	VI
	$[\text{Me}_3\text{N}^w\text{Bu}][\text{TFSI}]$	ESRF	3	17176.06	VI
	$[\text{Hex}_3\text{PDec}][\text{NCNCN}]$	SRS	4	17177.93	VI
	$[\text{Bu}_3\text{P}^w\text{Hex}][\text{OTs}]$	SRS	4	17177.31	VI

Table 6.5.1: Experimental conditions for XAS measurements. Uranium concentrations *ca.* 0.2 mmol

6.5.2 XANES spectroscopy

The oxidation state of the uranium compounds, at the time of the XAS experiments, was determined using XANES spectroscopy (Table 6.5.1). The use of XANES spectroscopy as a valence state probe is well established, and a brief explanation is given in Chapter 2.

Comparisons of the XANES spectra for U(III), U(IV) and U(VI) compounds show a difference in energy between the oxidation states, where the U(VI) compounds have the highest absorption energy and U(III) the lowest. It has been shown previously that the absorption edge shifts to higher energies as the valence of the metal is increased,²³ and the experimental results obtained are consistent with this.

The absorption edge position of the U(VI) compounds in the XANES spectra range between 17175.70 eV to 17177.93 eV (Figure 6.5.1). The small differences in edge positions of up to 2.2 eV, may reflect differences in coordination environment around the uranyl centre. The additional band at *ca.* 17190 eV is characteristic of XANES spectra of uranyl complexes (and indeed actinyl complexes in general) and arises from multiple scattering of the linear oxo units.²⁴ The oscillations observed above 17200 eV are due to EXAFS.

For the U(IV) compounds (Figure 6.5.2) the absorption edge positions in the XANES spectra, for the most part, are lower in energy than those observed for U(VI) compounds. The edge position varies from 17173.99 eV to 17177.31 eV. For UCl₄ in [Me₄N][TFSI],

U(TFSI)₄.xH₂O in [ⁿHex₃PDec][NCNCN], [ⁱBu₃PⁿHex][OTs], [Me₃NⁿBu][TFSI] and [Me₄N][TFSI], weak features at *ca.* 17190 eV due to oxo multiple scattering are observed indicating a mixture of oxidation states, with some oxidation to U(VI).

For UCl₃ dissolved in LTILs (Figure 6.5.3), the edge positions are lower than those observed for U(VI), and as expected, no band due to oxo multiple scattering at 17190 eV (*i.e.* no {UO₂²⁺} moiety is present. The edge energies vary between 17173.51 and 17174.82 eV, and are similar in energy to those observed for U(IV) complexes in solution. UV/vis spectroscopy has indicated that upon dissolution in LTILs, UCl₃ undergoes partial oxidation to U(IV) and this is supported by the XANES data.

Interestingly the absorption edge position for pure UCl₃ in BN has a much lower energy (17168.95 eV), thus suggesting that the oxidation is a result of dissolution in the LTIL rather than oxidation of the starting material.

It should be noted that there is a lack of consistency in the literature for the absorption edge positions of uranium compounds in oxidation states III, IV and VI, as can be seen from inspection of Table 6.5.2. Nevertheless, assignment of oxidation states of uranium in the present work was guided by the data in this table and by the observation of any features deriving from multiple scattering of a *trans* dioxo grouping. These assignments are collected in Table 6.5.1, and include some in which a mixture of oxidation states are apparent from the spectra.

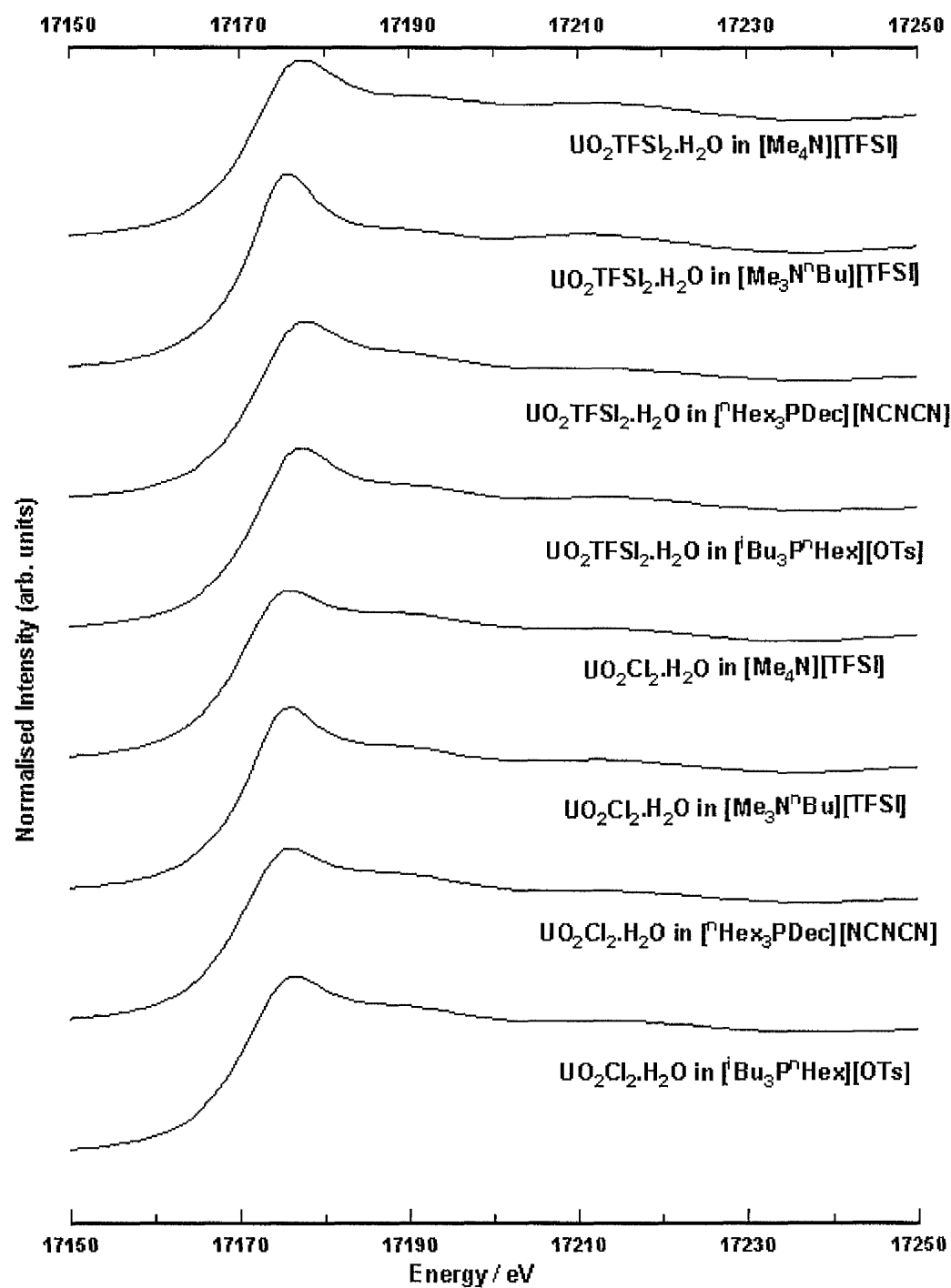


Figure 6.5.1: XANES spectra of U(VI) compounds in LTILs

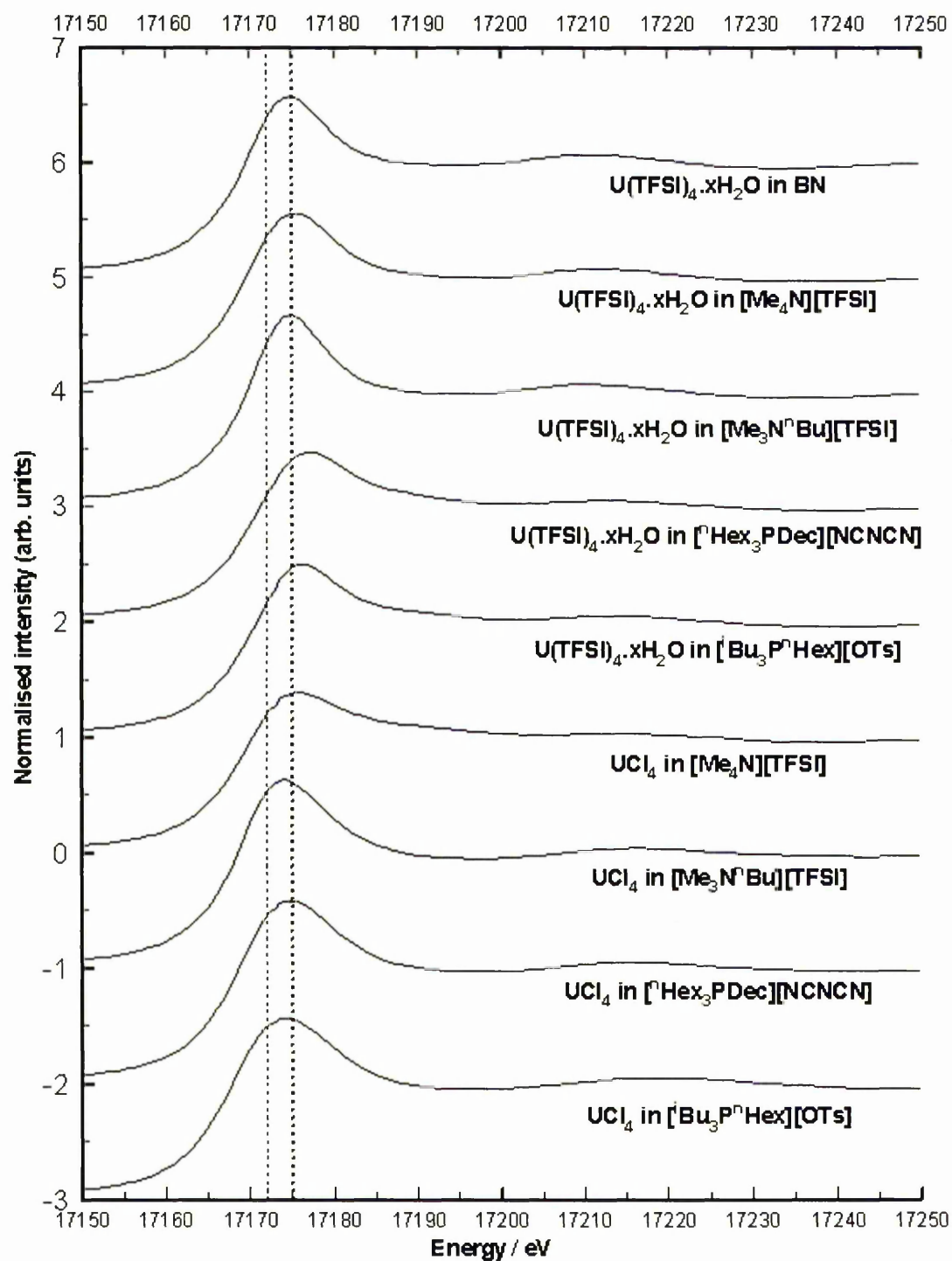


Figure 6.5.2: XANES spectra of U(IV) compounds in LTILs (dashed lines indicate previously reported²⁵⁻²⁸ U(IV) edge position region)

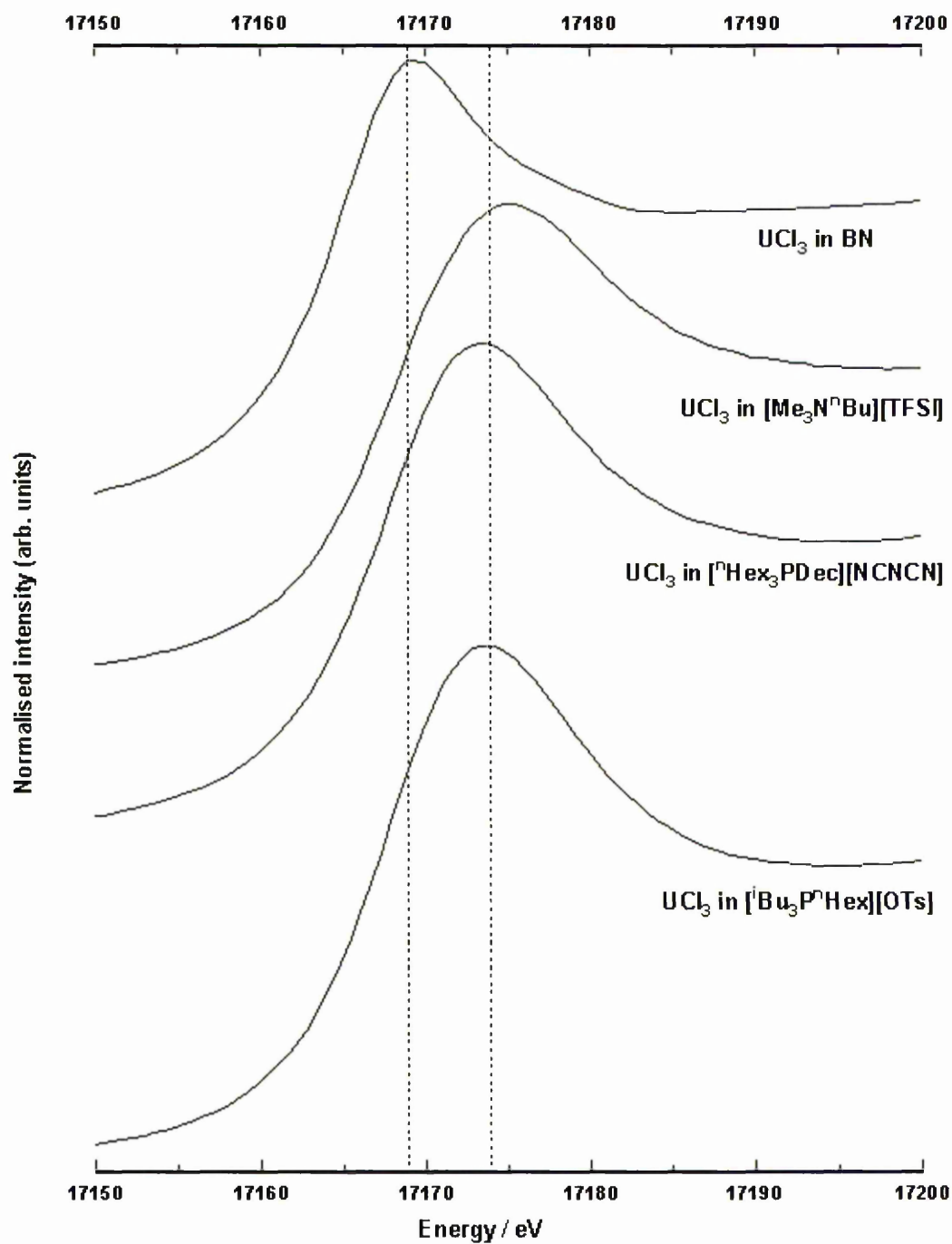


Figure 6.5.3: XANES spectra of U(III) compounds in LTILs and in BN (dashed lines indicate previously reported²⁵⁻²⁷ U(III) edge position region)

Compound	Oxidation state	Absorption edge / eV	Reference
UCl ₃	III	17173	25
UCl ₃	III	17172	26
UF ₃	III	17173	27
UBr ₃	III	17170	27
Cs ₂ LiUCl ₆	III	17172	27
UO ₂	IV	17173	28
UO ₂	IV	17177	25
UO ₂	IV	17175	26
UF ₄	IV	17175	26
UF ₄	IV	17175	27
UCl ₄	IV	17174	27
[UO ₂ (CO ₃) ₄] ^{5-†}	V	17163	29
[UO ₂ (CO ₃) ₃] ^{4-†}	VI	17166	29
UO ₂ (HPO ₄)	VI	17175	28
UO ₃	VI	17178	26
[(C ₄ N ₂ H ₁₂) ₂ (U ₂ F ₁₂).H ₂ O]	VI/IV mixture	17175	28

Table 6.5.2: Absorption edge positions of various uranium compounds reported in the literature. † Generated electrochemically in solution from UO₂Cl₂ dissolved in aqueous Na₂CO₃ (1 mol L⁻¹)

6.5.3 EXAFS of uranium compounds in BN

Coordination of the TFSI anion has previously been observed *via* the N atom for $[\text{Cu}(\text{CO})_2\text{TFSI}]^{30}$ and $[\text{Fe}(\text{CO})_2\text{CpTFSI}]$ (where $\text{Cp} = \text{C}_5\text{H}_5^-$).³¹ Additionally, coordination has been observed *via* the sulfonyl oxygen for $[\text{La}(\text{TFSI})_3(\text{H}_2\text{O})_3]$ (Chapter 4) and $[\text{Cp}_2\text{Ti}(\text{TFSI})_2]$.³¹ However, a crystallographic study of $[\text{UO}_2(\text{H}_2\text{O})_5][\text{TFSI}]_2$ shows that TFSI acts as a counter ion. Thus concomitant with the XAS measurements, the possible different coordination modes of TFSI to $\{\text{UO}_2\}^{2+}$ with bond lengths were calculated by Dr H. Steele (Department of Chemistry, The University of Manchester) as an aid for data fitting, and are shown in Table 6.5.3.

EXAFS spectra recorded for UCl_3 , $\text{U}(\text{TFSI})_4 \cdot x\text{H}_2\text{O}$ and $\text{UO}_2(\text{TFSI})_2 \cdot \text{H}_2\text{O}$ in BN, with calculated fits are shown in Figure 6.5.4. The EXAFS results and fit parameters are summarised in Table 6.5.4. It should be noted that the peaks observed below *ca.* 1.5 Å are due to noise observed during the XAS experiment.

For $\text{UO}_2(\text{TFSI})_2 \cdot \text{H}_2\text{O}$ in BN two U-O distances are observed at 1.76 Å and are assigned to the uranyl axial oxygens. Four U-O distances are also observed at 2.40 Å and are assigned to TFSI sulfonyl oxygens. Additionally U-N distances at 2.52 Å have also been observed. Assignment of this U-N interaction is supported by molecular modelling, which suggests that for TFSI chelating *via* the sulfonyl oxygens only, U-O and U-N distances should be observed at 2.39 Å and 2.58 Å, respectively. Vibrational spectroscopic studies also support this assignment of coordination mode (see Section

6.4). However, it should be noted that in the EXAFS experiment U-N and U-O scattering is very similar and crystallisation of $[\text{UO}_2(\text{H}_2\text{O})_5][\text{TFSI}]_2$ has shown that H_2O can displace TFSI. Thus, it is possible that some of the U-O or U-N interactions may arise from coordinated water.

For $\text{U}(\text{TFSI})_4 \cdot x\text{H}_2\text{O}$ in BN, U-O distances at 1.76 Å are detected indicating partial oxidation of the sample forming a $\{\text{UO}_2^{2+}\}$ species. The bond distances obtained are comparable to those previously observed crystallographically (1.69(2) Å to 1.76(2) Å)³²⁻³⁵ and from EXAFS analysis for $\text{UO}_2(\text{TFSI})_2 \cdot \text{H}_2\text{O}$ (1.76 Å) in BN. The best fit data also show shells for U-O (2.45 Å) and U-S (3.63 and 3.81 Å). The presence of the U-S interactions suggests that the TFSI anion coordinates to the uranium centre.

Crystallographically for $[\text{La}(\text{TFSI})_3(\text{H}_2\text{O})_3]$ the La-O and La-S distances are observed in the ranges 2.539 to 2.561 Å and 3.761 to 3.847 Å, respectively (see Chapter 4). The distances obtained for $\text{U}(\text{TFSI})_4$ are comparable with those for the La compound, taking into account the larger ionic radius of the Ln(III) cation. The spread in U-S distances is most probably due to the two different oxidation states of compounds in the sample. As a result of a mixture of compounds, the calculated occupancy numbers obtained do not correspond to a simple formulation.

In BN, UCl_3 shows U-Cl interactions at 2.92 Å and two U-U interactions at 4.40 and 4.71 Å. Previously, a crystallographic study of UCl_3 has shown that the U-Cl distance is 2.96 Å, with a nine coordinate U centre.³⁶ The EXAFS results show a reasonable correlation with this reported value.

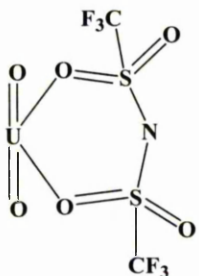
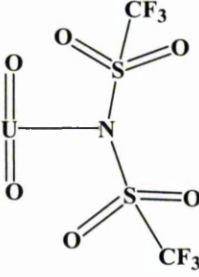
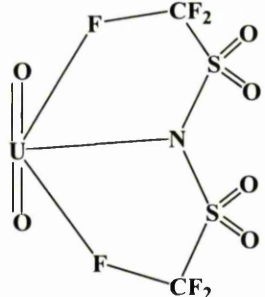
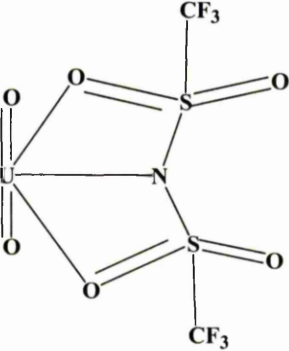
Coordination mode	U-O distance / Å	U-N distance / Å	U-S distance / Å	U-F distance / Å
	2.39	2.58	3.53	-
	2.72 – 2.8	2.60	3.31	-
	-	2.35	3.60	2.35
	2.40	2.42	3.19	-

Table 6.5.3: Calculated coordination modes of TFSI to $\{UO_2^{2+}\}$

Compound	Scatterer	Occupancy ($\pm 20\%$)	Distance / Å (± 0.02 Å)	$2\sigma^2$	R_{EXAFS}
UCl ₃	Cl	5.8	2.92	0.018	25.8
	U	2	4.40	0.014	
	U	6	4.71	0.030	
U(TFSI) ₄ .xH ₂ O	O	1.00	1.76	0.004	46.3
	O	5.00	2.45	0.015	
	S	2.00	3.63	0.011	
	S	4.00	3.81	0.020	
UO ₂ (TFSI) ₂ .H ₂ O	O	2	1.76	0.004	31.4
	O	4	2.40	0.019	
	N	2	2.52	0.013	

**Table 6.5.4: Best fit parameters to EXAFS data for solid state uranium compounds
in BN**

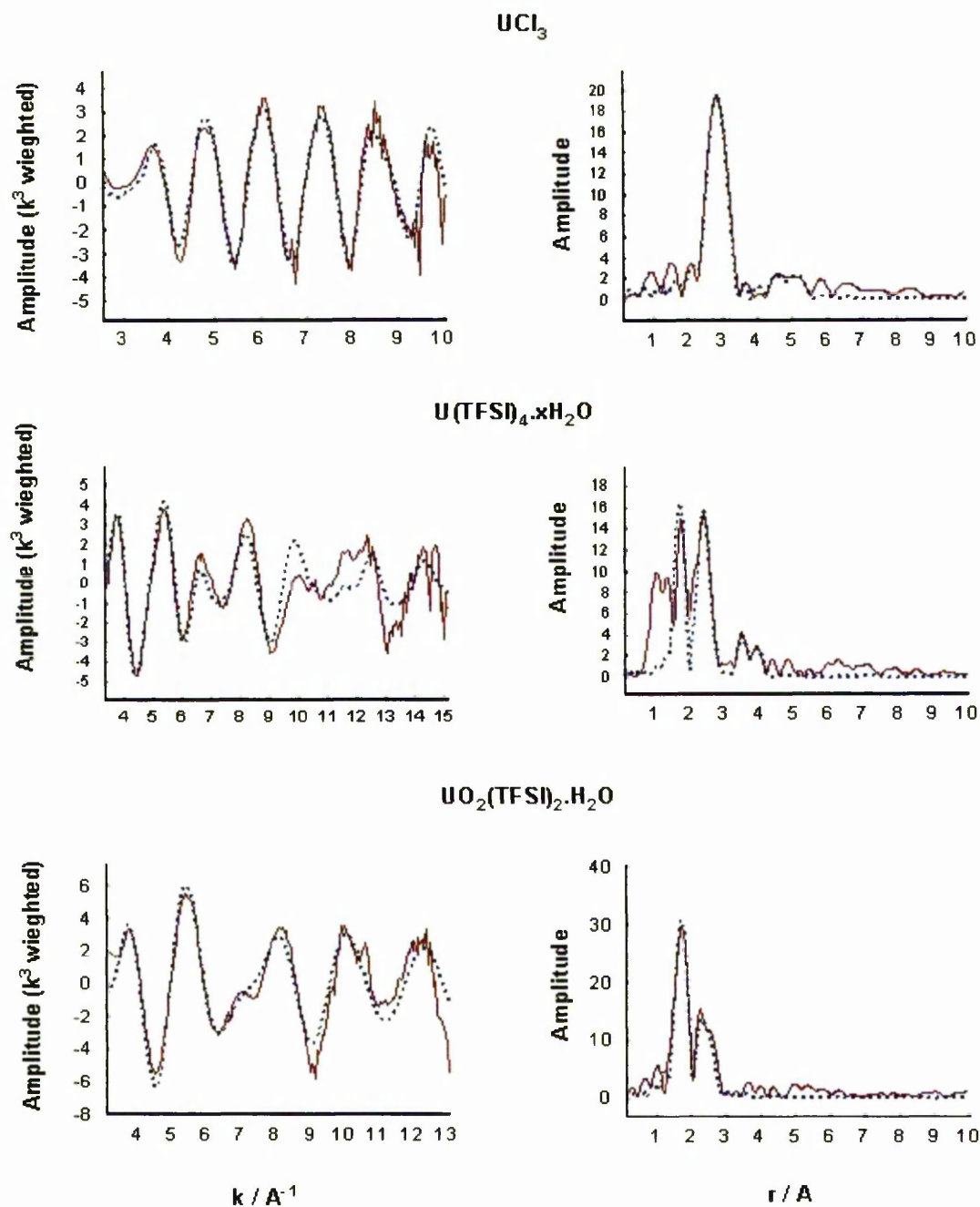


Figure 6.5.4: EXAFS (left) and their FT (right) spectra of UCl_3 , $\text{U(TFSI)}_4 \cdot x\text{H}_2\text{O}$ and $\text{UO}_2(\text{TFSI})_2 \cdot \text{H}_2\text{O}$ in BN. Solid line = experimental data, dashed line = calculated fit using the parameters in Table 6.5.4

6.5.4 EXAFS of uranium TFSI and chloride complexes in $[\text{Me}_3\text{N}^n\text{Bu}][\text{TFSI}]$

For $\text{UO}_2(\text{TFSI})_2 \cdot \text{H}_2\text{O}$ dissolved in $[\text{Me}_3\text{N}^n\text{Bu}][\text{TFSI}]$ only scattering from the first coordination sphere is observed, see Figure 6.5.6. Two U-O distances due to axial uranyl oxygens at 1.76 Å and four U-O distances at 2.43 Å give a best fit, and are comparable to those found for $\text{UO}_2(\text{TFSI})_2 \cdot \text{H}_2\text{O}$ in BN. There is no conclusive evidence for TFSI coordination due to a lack of observable back scattering from N or S atoms.

$\text{UO}_2\text{Cl}_2 \cdot \text{H}_2\text{O}$ dissolved in $[\text{Me}_3\text{N}^n\text{Bu}][\text{TFSI}]$ gives a best fit with uranyl oxygen distances at 1.78 Å, with two distinct shells of Cl at 2.71 Å and 2.88 Å. From neutron diffraction studies, U-Cl bond lengths of 2.75(2) and 2.80(2) Å have previously been observed for $\text{UO}_2\text{Cl}_2 \cdot \text{H}_2\text{O}$, where the $\{\text{UO}_2\}^{2+}$ moiety is coordinated to neighbouring $\{\text{UO}_2\}^{2+}$ centres by bridging chlorides (U-Cl distance of 2.80(2) Å).³⁷ The two distinct distances in $[\text{Me}_3\text{N}^n\text{Bu}][\text{TFSI}]$ may indicate some form of oligimerisation. The absence of any U-O interactions from TFSI in the best fit shows that TFSI does not displace Cl^- in solution. No U- O_{water} interactions are observed. Crystallographically the U- O_{water} distance has been determined to be 2.46(3) Å,³⁷ although it is possible that the broad U-Cl peak at 2.71 Å is overlapping and masking any U- O_{water} peak (see Fig 6.5.6). Alternatively, perhaps there is only Cl^- coordination in the melt.

$\text{U}(\text{TFSI})_4 \cdot x\text{H}_2\text{O}$ in $[\text{Me}_3\text{N}^n\text{Bu}][\text{TFSI}]$ shows some U-O distances in the best fit at 1.74 Å (due to uranyl oxygens) and U-O interactions at 2.45 Å assigned to coordinated TFSI. Both these U-O distances are comparable to those found for $\text{UO}_2(\text{TFSI})_2 \cdot \text{H}_2\text{O}$ in BN by

EXAFS analysis. This result combined with the XANES evidence suggests that partial oxidation of the U(IV) complex to $\{\text{UO}_2\}^{2+}$ has occurred. It should be noted that the occupancy numbers in Table 6.5.5 are the result of a mixture of oxidation states in solution.

In $[\text{Me}_3\text{N}^n\text{Bu}][\text{TFSI}]$, UCl_4 shows a best fit for U-Cl distances of 2.63 and 2.85 Å.

Additionally there is a U-O distance at 2.24 Å and U-U distances at 3.70 Å. The U-Cl distances of 2.63 and 2.85 Å (within experimental error) are comparable to the reported U-Cl distances in UCl_4 of 2.64 and 2.87 Å,^{38,39} where two U-Cl distances are observed due to Cl acting as bridging and terminal ligands, the shorter distance related to a bridging Cl.

It is known for Na_2UCl_6 that each U centre in the structure has an octahedral coordination geometry. Bendall *et al.* found that the average U-Cl bond lengths are between 2.61 Å and 2.64 Å.⁴⁰ The Cl-U-Cl bond angles for neighbouring Cl varied between 86.3 ° and 92.2 °. A similar result was obtained for Li_2UCl_6 , with bond distances between 2.57 and 2.67 Å, and bond angles for neighbouring chlorides between 88.8 ° and 92.2 °.⁴⁰ Using these compounds and UCl_6 as models,⁴¹ mathematical analysis of the two uranium centres bridged by a chlorides in the sample of UCl_4 in $[\text{Me}_3\text{N}^n\text{Bu}][\text{TFSI}]$ (U-Cl distance of 2.63 Å from EXAFS analysis, see Figure 6.5.5) indicate the theoretical U-U distance to be 3.72 Å, which is very similar to the measured distance assuming the uranium centre to be octahedrally coordinated, Cl-U-Cl angles to be 90 ° and all four chlorine atoms to be in a plane. The short range U-O interaction of 2.24 Å is assigned to a coordinated

hydroxide or water rather than coordinated TFSI. The EXAFS results of $\text{U}(\text{TFSI})_4 \cdot x\text{H}_2\text{O}$ and $\text{UO}_2(\text{TFSI})_2 \cdot \text{H}_2\text{O}$ in BN and dissolved in $[\text{Me}_3\text{N}^n\text{Bu}][\text{TFSI}]$ suggest that the coordinated $\text{U}-\text{O}_{\text{TFSI}}$ distance is in the range of 2.40 to 2.45 Å. For the related U-triflate complexes, $\text{U}-\text{O}_{\text{OTf}}$ distances of *ca.* 2.38 – 2.45 Å have been determined crystallographically,⁴² thus suggesting that the assignment may be correct. Based on these results, it is suggested that upon dissolution, UCl_4 (in $[\text{Me}_3\text{N}^n\text{Bu}][\text{TFSI}]$) forms an multinuclear cluster and a proposed structure is given in Figure 6.6.5. It should be noted that this structure is based on the available EXAFS data, and much more investigation is required before the exact structure of this multinuclear species in solution can be determined.

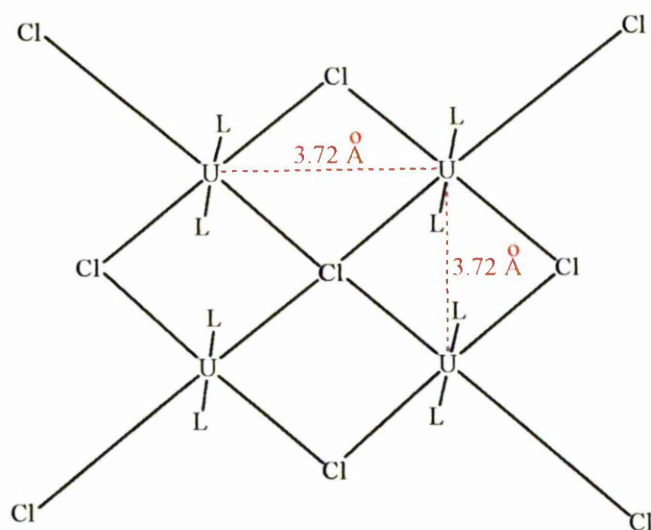


Figure 6.5.5: Proposed structure of multinuclear U species formed upon dissolution of UCl_4 in $[\text{Me}_3\text{N}^n\text{Bu}][\text{TFSI}]$ where L = coordinated water or hydroxide. U-Cl distance (non-bridging) = 2.85 Å; U-Cl distance (bridging) = 2.63 Å; U-U distance calculated using Pythagoras' theorem = 3.72 Å,

For UCl_3 only one U-Cl interaction at 2.84 Å is observed and is shorter than that observed for UCl_3 in BN (2.92 Å). XANES spectroscopy indicates that the oxidation state in this sample is a mixture of U(III) and U(IV) and the U-Cl distance is comparable to that observed crystallographically for the non-bridging Cl in UCl_4 (2.85 Å),^{38,39} suggesting that almost complete oxidation to the tetravalent state has occurred. Interestingly for this sample no evidence of a multinuclear cluster is observed even though the oxidation state of the U centre is the same as for UCl_4 . This difference in speciation may be explained by fact that there are less Cl ligands present in this sample compared to the UCl_4 sample. The lack of any U-O interactions shows that TFSI does not displace Cl, thus showing that TFSI is a poorer ligand for U than Cl.

Compound	Scatterer	Occupancy ($\pm 20\%$)	Distance / Å (± 0.02 Å)	$2\sigma^2$	R_{EXAFS}
U(TFSI) ₄ .xH ₂ O	O	0.9	1.74	0.008	25.1
	O	6	2.45	0.022	
UO ₂ (TFSI) ₂ .H ₂ O	O	2	1.76	0.004	19.8
	O	4	2.43	0.013	
UCl ₃	Cl	9	2.84	0.017	28.8
UCl ₄	O	2	2.24	0.012	29.5
	Cl	3	2.63	0.010	
	Cl	1	2.85	0.010	
	U	2	3.70	0.009	
UO ₂ Cl ₂ .H ₂ O	O	2	1.78	0.006	30.4
	Cl	2	2.71	0.004	
	Cl	1	2.88	0.009	

Table 6.5.5: Best fit parameters to EXAFS data for uranium TFSI and chloride complexes in [Me₃NⁿBu][TFSI]

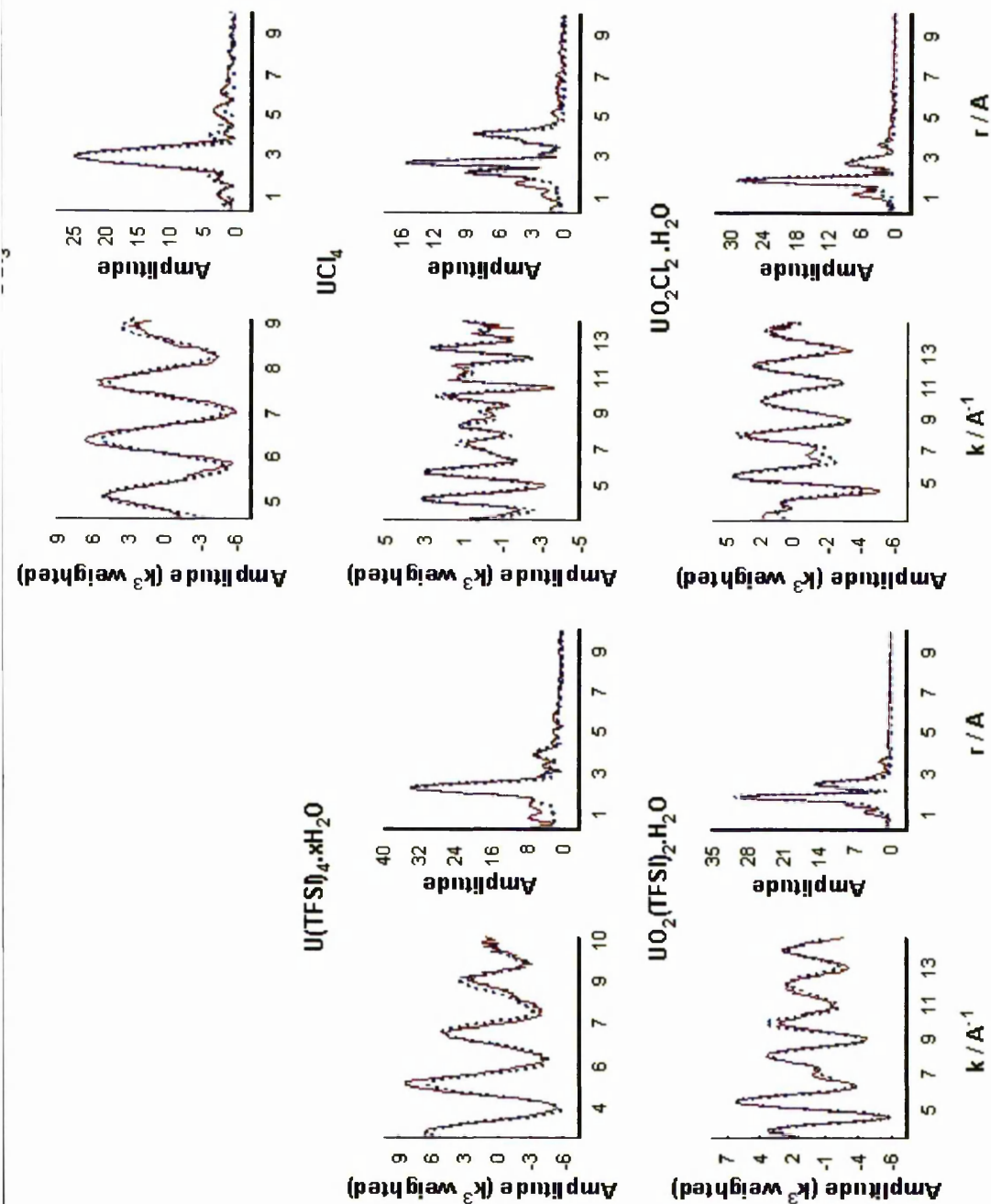


Figure 6.5.6: EXAFS (left) and FT (right) spectra of uranium TFSI and chloride complexes in $[Me_3N^+Bu][TFSI]$. Solid line = experimental data, dashed line = theoretical fit using the parameters in Table 6.5.5

6.6 Electrochemical behaviour of uranium(IV) compounds in

[Me₃N^{''}Bu][TFSI]

6.6.1 Experimental method

The electrochemical behaviour of U(TFSI)₄.xH₂O (0.14 mmol) and of UCl₄ (0.26 mmol) were investigated in [Me₃N^{''}Bu][TFSI] (3.0 mL) using cyclic voltammetry (CV) and chronoamperometry (CA). The recorded CVs are shown in Figures 6.6.1, 6.6.2 and 6.6.3. For CA measurements, solutions were heated from *ca.* 40 °C to 140 °C and allowed to equilibrate for at least 10 m. prior to measurements with the temperature measured using a thermometer. All measurements were recorded inside an inert atmosphere Ar drybox to eliminate the introduction of O₂ and additional moisture. A typical 3 electrode cell (see Chapter 2) was used for all CV and CA measurements, and was comprised of a Pt disk working electrode, a large surface area Pt gauze counter electrode and a Ag wire quasi-reference electrode (QRE). All potentials quoted are referenced to the Ag wire QRE.

6.6.2 Results and discussion

Cyclic voltammograms of U(TFSI)₄.xH₂O show a number of reduction and oxidation peaks. Considering first the peaks at more negative potentials than 0 V (Graph A, Figure 6.6.1), there are two cathodic peaks and two anodic peaks. The cathodic/anodic peaks at *ca.* -0.38 V are assigned to the U(IV)/U(III) redox processes ($E_{p/a} = -0.45$ V, $E_{p/c} = -0.3$ V), and the waves at *ca.* -0.9 V to the U(III)/U(0) process ($E_{p/a} = -0.8$ V,

$E_{p/c} = -1.0$ V). The peak shapes for the U(III)/U(0) reduction and oxidation processes are similar to those obtained for Ln (where Ln = La, Sm or Eu) and Th reductions, suggesting that a similar reduction reaction is progressing (*i.e.* formation of a metal which then forms an oxide due to chemical reaction with water in the system).

At more positive potentials than 0 V (Graph B, Figure 6.6.1), oxidation of the U(IV) to U(VI) occurs at *ca.* 0.61 V. The cathodic and anodic peaks show the beginnings of two bands. Multiple cycles around this region (purple trace), resolves these bands into two couples which have been assigned to the U(IV)/U(V) ($E_{p/a} = 0.54$ V, $E_{p/c} = 0.42$ V, $E_{1/2} = 0.48$ V) and U(V)/U(VI) processes ($E_{p/a} = 0.84$ V, $E_{p/c} = 0.78$ V, $E_{1/2} = 0.81$ V).

In Graph B (Figure 6.6.1, main CV), there is an extra unassigned process at -0.74 V. Multiple cycles around this region do not show this extra band and repeating the experiment (graph A) does not show this behaviour either. This cathodic peak may arise from electroactive species generated at the positive potentials or alternatively may be due to trace electroactive impurities in the melt. Similarly the anodic processes at 1.06 V and 1.37 V may arise from electroactive species generated at more negative potentials than 0.3 V (as multiple cycles around this region do not show these peaks) or again may be due to trace electroactive impurities present in the melt.

It was decided to investigate the voltammetry of Eu and U TFSI complexes dissolved in the same melt to observe whether both U and Eu could be reduced to the zerovalent state. Addition of an equimolar ratio of [Eu(TFSI)₃.(H₂O)₃] (1:1 Eu to U molar ratio, allowing

the solution to sit under Ar for 4 d, Figure 6.6.2) changes the shape of the CV. The peaks assigned to the U(IV)/U(V) and U(V)/U(VI) processes are less well pronounced. At negative potentials below 0 V, the U(0)/U(III) oxidation peak is much more pronounced and sharper than without added Eu. The wave shape is similar to that expected for a stripping peak⁴³ indicating that U metal has been plated onto the electrode surface rather than forming of an oxide phase.

At slow scan rates (Graph B, Figure 6.6.2) both the anodic and cathodic peaks of the U(0)/U(III) process appear to grow in intensity with multiple scans as expected for the deposition of a metal on the electrode surface. After a short period of time (*ca.* 4 h) and multiple scans the sharp stripping peak eventually decays and the CV shows a similar profile to that observed without added Eu (Graph C, Figure 6.6.2).

It seems unlikely that the plating behaviour of U is to do with the formation of an Eu/U alloy because under the same conditions the Eu(II)/Eu(0) reduction potential is more negative than that of U(III)/U(0) (-3.3 V *cf.* -1.0 V vs. Ag wire QRE, respectively in [Me₃NⁿBu][TFSI]). Therefore, it is hypothesised that the Eu complex reacts with the water liberated upon reduction of the U(IV) complex in solution thus inhibiting formation of the oxide phase. As there is only a finite quantity of Eu available at the electrode surface due to slow rate of diffusion from the bulk solution (Chapter 4), after a period of time and a number of scans the amount of water liberated exceeds the amount that can react with the Eu and thus the formation of the U oxide begins, causing the waveshapes to change to those observed for reduction of U(TFSI)₄.xH₂O without added Eu complex.

The absence of any Eu(III)/Eu(II) peaks (previously observed in the same LTIL, see Chapter 4) may be a result of the low stability of the new Eu-aqua complex formed or of peaks overlapping with the U(IV)/U(III) peaks.

This is a speculative suggestion and a lot more evidence is required before making a definite assignment for this electrochemical behaviour. However, this result does suggest that if trace water is removed from solution, then U (and presumably *f*-elements in general) can be reduced to the metallic state in [Me₃NⁿBu][TFSI]. Similar arguments about removal of water from LTILs allowing the formation of U metal electrochemically have also been proposed by Costa *et al.*⁶ Although further experiments are required, this result indicates that an LTIL-based nuclear fuels reprocessing technology based on forming U metal electrochemically may work if moisture is rigorously excluded from the system.

Cyclic voltammograms of UCl₄ in [Me₃NⁿBu][TFSI] show a different electrochemical response to that of U(TFSI)₄.xH₂O (See Figure 6.6.3). Peaks due to the U(VI)/U(V) ($E_{p/a} = 0.93$ V, $E_{p/c} = 0.67$ V, $E_{1/2} = 0.80$ V), U(V)/U(IV) ($E_{p/a} = 0.20$ V, $E_{p/c} = -0.15$ V, $E_{1/2} = 0.02$ V), U(IV)/U(III) ($E_{p/a} = -0.95$ V, $E_{p/c} = -1.19$ V, $E_{1/2} = -1.07$ V) and U(III)/U(0) ($E_{p/a} = -1.76$ V, $E_{p/c} = -2.03$ V, $E_{1/2} = -1.90$ V) are all observed. The peak positions are different to those of U(TFSI)₄.xH₂O, and this is presumably due in part to the fluxionality of the QRE (see Chapter 3) and also the different coordination environment around U. Comparisons of the differences between the observed pairs of reductions and the standard potentials⁴⁴ ((VI)/(V) and (V)/(IV) = 0.77 V vs. 0.55 V for

standard conditions; (V)/(IV) and (IV)/(III) = 1.10 V vs. 1.22 V; (IV)/(III) and (III)/(0) = 0.83 V vs. 1.18 V) show reasonable correlation and suggests that the proposed assignments are correct. The peak-peak separations are greater for the UCl_4 experiment than the $\text{U}(\text{TFSI})_4 \cdot x\text{H}_2\text{O}$ measurement and this is attributed to the coordination environment of the uranium species. EXAFS results have already indicated that upon dissolution of UCl_4 in $[\text{Me}_3\text{N}^m\text{Bu}][\text{TFSI}]$ a multinuclear species is formed.

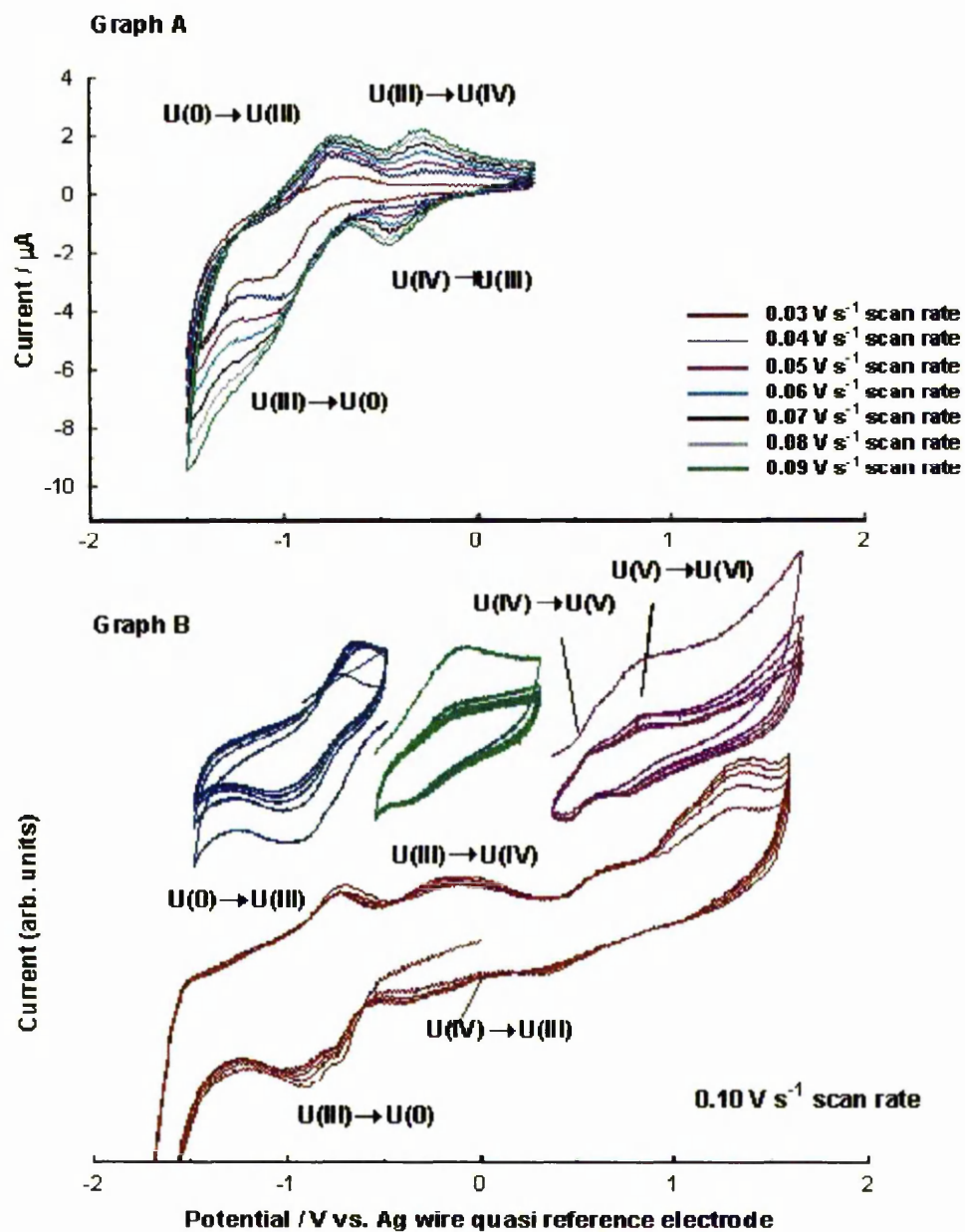


Figure 6.6.1: CV of $\text{U}(\text{TFSI})_4 \cdot x\text{H}_2\text{O}$ in $[\text{Me}_3\text{N}^r\text{Bu}][\text{TFSI}]$ at 25 °C

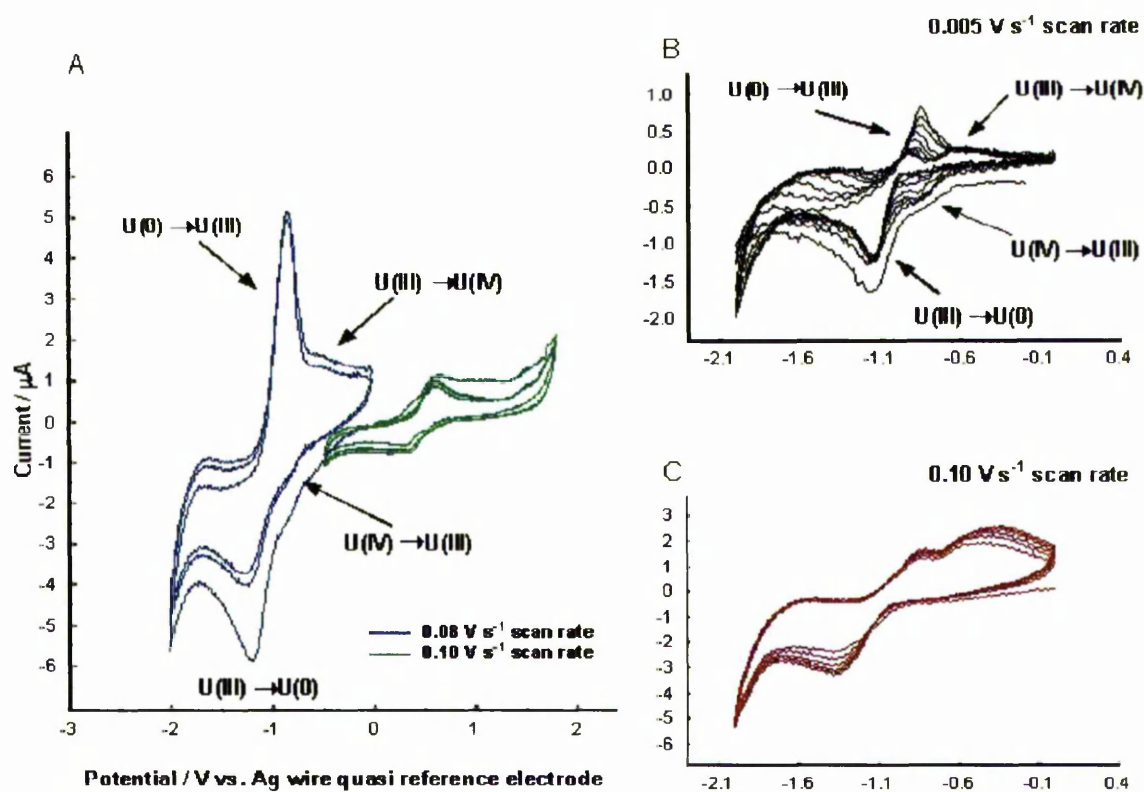


Figure 6.6.2: CV of $\text{U}(\text{TFSI})_4 \cdot x\text{H}_2\text{O}$ with added $[\text{Eu}(\text{TFSI})_3(\text{H}_2\text{O})_3]$ in $[\text{Me}_3\text{N}^r\text{Bu}][\text{TFSI}]$ at 25°C . Graph A: multiple cycles around at potentials more negative than 0 V and at potentials more positive than -0.5 V; Graph B: multiple scans at potentials more negative than -0.1 V; Graph C: multiple scans at potentials more negative than -0.1 V after 4 h.

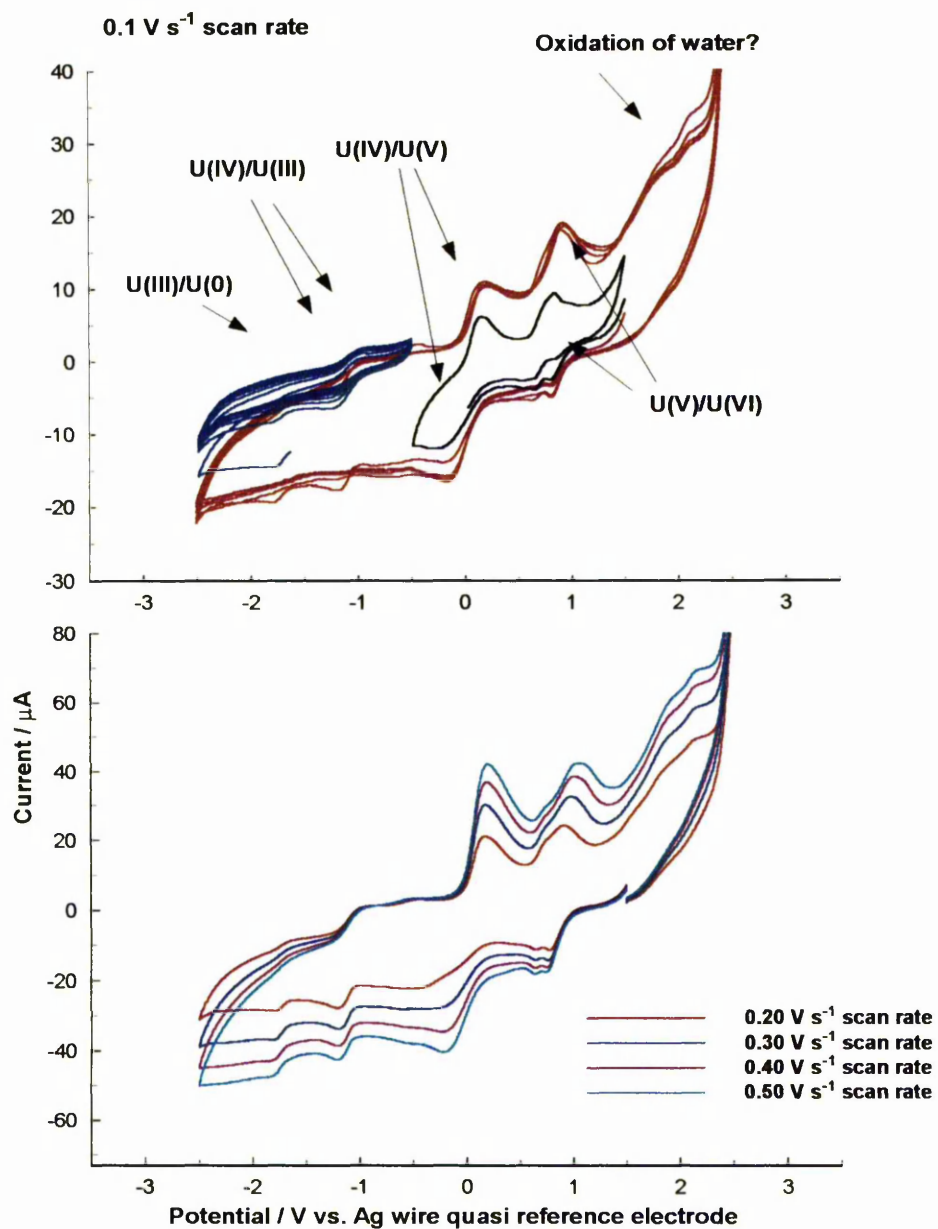


Figure 6.6.3: CV of UCl_4 in $[\text{Me}_3\text{N}^+\text{Bu}][\text{TFSI}]$ at $25\text{ }^\circ\text{C}$. Top graph shows effect of multiple cycles, bottom graph shows effect of varying scan rate

Diffusion coefficients (D) for the U(III)/U(0) reduction processes for $\text{U}(\text{TFSI})_4 \cdot x\text{H}_2\text{O}$ and UCl_4 dissolved in $[\text{Me}_3\text{N}^n\text{Bu}][\text{TFSI}]$ were measured at increasing temperature using CA and are shown in Table 6.6.1. The diffusion coefficients were calculated using the Cottrell equation (Equation 1):⁴⁵

$$i = nFAC_{\text{BULK}} \sqrt{\frac{D}{\pi t}} \quad \text{Equation 1}$$

where F = Faraday constant, A = electrode area, C_{BULK} = bulk concentration, D = diffusion coefficient and t = time and i = current.

As can be seen from Table 6.6.1, the values obtained are very low (in the region of 10^{-7} – $10^{-10} \text{ cm}^2 \text{ s}^{-1}$). The effect of temperature upon the diffusion of uranium species in $[\text{Me}_3\text{N}^n\text{Bu}][\text{TFSI}]$ was investigated, and the results are shown graphically in Figure 6.6.4. For comparison, previously reported literature values for the U(III)/U(0) reduction in the high temperature molten salt, LiCl-KCl eutectic (550 °C) are also shown.⁴⁶ The values in the LTIL are lower than those reported in high temperature molten salts. However, as the data obtained follow expected Arrhenius behaviour, an increase in temperature to *ca.* 200 °C should give similar values to those observed in LiCl-KCl eutectic (see Figure 6.6.4).

Compound	Diffusion coefficient / cm ² s ⁻¹				
U(TFSI) ₄ .xH ₂ O	1.92 × 10 ⁻⁸ (39.4 °C)	7.73 × 10 ⁻⁸ (66.6 °C)	2.31 × 10 ⁻⁷ (97.3 °C)	3.47 × 10 ⁻⁷ (125.0 °C)	4.87 × 10 ⁻⁷ (136.0 °C)
UCl ₄		1.06 × 10 ⁻⁹ (73.4 °C)	1.26 × 10 ⁻⁹ (104.0 °C)	4.03 × 10 ⁻⁹ (125.0 °C)	7.77 × 10 ⁻⁹ (136.0 °C)

**Table 6.6.1: Diffusion coefficients for the U(III)/U(0) reduction in [Me₃NⁿBu][TFSI]
measured at various temperatures (in parentheses) using CA**

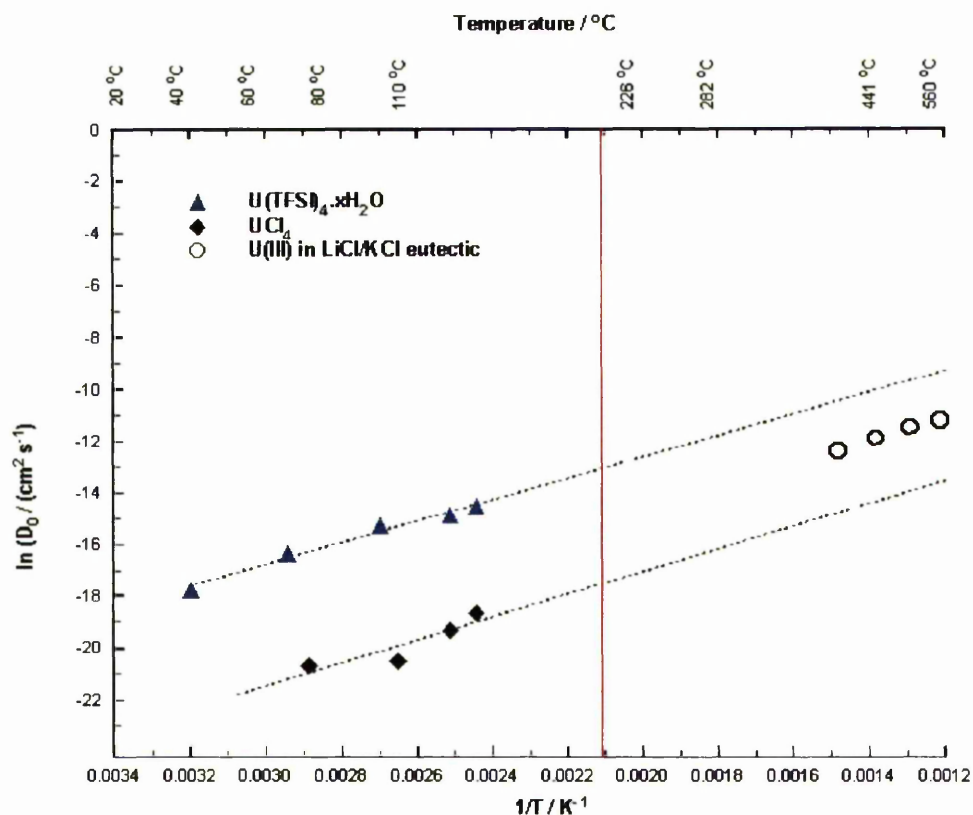


Figure 6.6.4: Arrhenius plot of $\ln D$ as a function of inverse temperature for $\text{U(III)}/\text{U(0)}$ reduction in $[\text{Me}_3\text{N}^n\text{Bu}][\text{TFSI}]$. Red line indicates 200 °C

6.7 Summary

Uranium TFSI complexes have been characterised using electronic absorption spectroscopy (in the solid state and dissolved in LTILs), vibrational spectroscopy and in the case of $[\text{UO}_2(\text{H}_2\text{O})_5][\text{TFSI}]_2$ single crystal X-ray diffraction (see Appendix 1 for crystallographic data).

The electronic absorption spectroscopy shows that in an inert atmosphere drybox, U(IV) can be stabilised in LTIL solution. In the solid state, by comparisons with spectra of $[\text{La}(\text{TFSI})_3(\text{H}_2\text{O})_3]$, vibrational spectroscopy suggests that TFSI coordinates to the U(IV) centre *via* the sulfonyl oxygens. In the case of $\text{UO}_2(\text{TFSI})_2 \cdot \text{H}_2\text{O}$, comparisons of the IR/Raman spectra with those obtained for $[\text{UO}_2(\text{H}_2\text{O})_5][\text{TFSI}]_2$ show that the TFSI anion coordinates to the $\{\text{UO}_2^{2+}\}$ centre, again *via* the sulfonyl oxygens.

The solution speciation of U in LTILs has been investigated using XAS and the effect of TFSI⁻ and Cl⁻ studied. The XANES spectroscopy shows that some U(IV) and U(III) samples were of mixed oxidation state, possibly due to oxidation of the sample during the transfer from Manchester to the various synchrotron sources prior to measurement (*ca.* 2 weeks to ESRF, and 3 h to SRS) and the lack of inert atmosphere storage facilities for radioactive samples at the synchrotron sites. In $[\text{Me}_3\text{N}^n\text{Bu}][\text{TFSI}]$, comparison of uranium Cl and TFSI compounds using EXAFS shows that the TFSI anion is a poorer ligand for U than Cl. TFSI chelates to U centres when the starting compound is a TFSI salt. Upon changing to a Cl starting material, rather than TFSI coordinating, the chlorides can act as bridging as well as terminal ligands and probably form multinuclear species in solution.

The voltammetric behaviour of U(IV) compounds in $[\text{Me}_3\text{N}^n\text{Bu}][\text{TFSI}]$ has been investigated and the reduction to the zerovalent state observed. The waveforms are suggestive of the formation of an oxide phase as observed for Ln (where Ln = La, Sm and Eu) and Th. However, experiments with added $[\text{Eu}(\text{TFSI})_3(\text{H}_2\text{O})_3]$ show waveforms

typical of plating/stripping behaviour. It is hypothesised that this is due to water present in the melt replacing TFSI in the coordination sphere of Eu^{3+} thus inhibiting oxide formation. This result suggests that if the trace amounts of water in the melt can be removed then U can be electrochemically reduced to the metallic state and thus an LTIL-based electrochemical reprocessing technology is feasible.

Diffusion coefficients for UCl_4 and $\text{U}(\text{TFSI})_4 \cdot x\text{H}_2\text{O}$ in $[\text{Me}_3\text{N}^n\text{Bu}][\text{TFSI}]$ have been measured, and although low values are observed, it is predicted that increasing the temperature up to 200 °C should give values comparable to those observed in high temperature molten salts. This is important from an engineering perspective, because the cost of designing and manufacturing a plant to operate at or below 200 °C is much cheaper than for operation above 200 °C (in this case the cost is comparable to that for molten salts).

6.8 References

1. C. J. Anderson, G. R. Choppin, D. J. Prett, D. A. Costa, W. Smith, *Radiochim. Acta*, 1999, **84**, 31.
2. T. A. Hopkins, J. M. Berg, D. A. Costa, W. H. Smith, H. J. Dewey, *Inorg. Chem.*, 2001, **40**, 1820.
3. D. A Costa, W. H. Smith, *Los Alamos yearly report*, LA-UR-99-5521, 1999.
4. W. H. Smith, D. A. Costa, *Los Alamos yearly report*, LA-UR 98-3669, 1998.

5. D. A. Costa, W. H. Smith, K. D. Abney, W. J. Oldham, *Plutonium Futures – The Science*, American Institute of Physics, 2000.
6. K. D. Abney, E. Bluhm, E. Garcia, W. H. Smith, M. Barr, W. Oldham, D. A. Costa, D. Morris, D. Tait, *Los Alamos yearly report*, LA-UR-00-5043, 2000.
7. A. E. Visser, M. P. Jensen, I. Laszak, K. L. Nash, G. R. Choppin, R. D. Rogers, *Inorg. Chem.*, 2003, **42**, 2197.
8. M. Karbowiak, J. Hanuza, J. Janczk, J. Drozdzyński, *J. Alloys and Compd.*, 1995, **225**, 338.
9. J. L. Ryan, *Inorg. Chem.*, 1964, **3**, 211.
10. S. Dai, L. M. Toth, G. D. Del Cul, D. H. Metcalf, *Inorg. Chem.*, 1995, **34**, 412.
11. J. R. Morrey, *Inorg. Chem.*, 1963, **2**, 163.
12. P. Gans, B. J. Hathaway, B. C. Smith, *Spectrochimica Acta*, 1965, **21**, 1589.
13. K. Mizuoka, S. Kim, M. Hasegawa, T. Hoshi, G. Uchiyama, Y. Ikeda, *Inorg. Chem.*, 2003, **42**, 1031.
14. V. A. Volkovich, T. R. Griffiths, D. J. Fray, R. C. Thied, *Phys. Chem. Chem. Phys.*, 2001, **3**, 5182.
15. D. L. Clark, S. D. Conradson, R. J. Donohoe, D. W. Keogh, D. E. Morris, P. D. Palmer, R. D. Rogers, C. D. Taia, *Inorg. Chem.*, 1999, **38**, 1456.
16. V. A. Volkovich, T. R. Griffiths, D. J. Fray, R. C. Thied, *Phys. Chem. Chem. Phys.*, 2000, **2**, 3871.
17. I. Rey, J. C. Lassègues, J. Grondin, L. Servant, *Electrochim. Acta*, 1998, **43**, 1505.
18. I. Rey, P. Johansson, J. Lindgren, J. C. Lassègues, J. Grondin, L. Servant, *J. Phys. Chem. A*, 1998, **102**, 3249.

19. F. Quiles, A. Burneau, *Vibr. Spec.*, 2000, **23**, 231.
20. A. C. Bean, B. L. Scott, T. E. Albrecht-Schmitt, W. Runde, *Inorg. Chem.*, 2003, **42**, 5632
21. CCLRC Daresbury Laboratory computer program.
22. N. Binsted (1998), EXCURV98: CCLRC Daresbury Laboratory computer program; N. Binsted, R. W. Strange, S. S. Hasnain, *Biochemistry*, 1992, **31**, 12117.
23. S. Bertram, G. Kaindle, J. Jove, M. Pages, J. Gal, *Phys. Rev. Lett.*, 1989, **63**, 2680.
24. E. A. Hudson, J. J. Rehr, J. J. Bucher, *Phys. Rev. B*, 1995, **52**, 13815.
25. K. Akiyama, K. Sueki, H. Haba, K. Tsukada, M. Asai, T. Yaita, Y. Nagame, K. Kikuchi, M. Katada, H. Nakahara, *J. Radioanal. Nucl. Chem.*, 2003, **255**, 155.
26. G. Kalkowski, G. Kaindle, W. D. Brewer, W. Krone, *Phys. Rev. B*, 1987, **35**, 2667.
27. Z. Hu, G. Kaindle, G. Meyer, *J. Alloys Compd.*, 1998, **274**, 38.
28. S. Allen, S. Barlow, P. S. Halasyamani, J. F. W. Mosselmans, D. O'Hare, S. M. Walker, R. I. Walton, *Inorg. Chem.*, 2000, **39**, 3791.
29. T. I. Docrat, J. F. W. Mosselmans, J. M. Charnock, M. W. Whiteley, D. Collison, F. R. Livens, C. Jones, M. J. Edmiston, *Inorg. Chem.*, 1999, **38**, 1879.
30. O.G. Polyakov, S. M. Ivanova, C. M. Gaudinski, S. M. Miller, O. P. Anderson, S. H. Strauss, *Organometallics*, 1999, **18**, 3769.
31. W. J. Oldham, D. B. Williams, *Proc. Electrochem. Soc.*, 2002, **19**, 983.

32. R. E. Berry, P. D. Smith, S. M. Harben, M. Helliwell, D. Collison, C. D. Garner, *Chem. Commun.*, 1998, 591.
33. L. Deshayes, N. Keller, M. Lance, M. Nierlich, J-D. Vigner, *Acta Cryst. C*, 1994, **C50**, 1541.
34. A. Fischer, *Z. Anorg. Allg. Chem.*, 2003, **629**, 1012.
35. J. C. Taylor, P. W. Wilson, *Acta Cryst.*, 1974, **B30**, 169.
36. W. H. Zachariasen, *Acta Cryst.*, 1948, **1**, 265.
37. J. C. Taylor, P. W. Wilson, *Acta Cryst.*, 1974, **B30**, 169.
38. J. C. Taylor, P. W. Wilson, *Acta Cryst.*, 1973, **B29**, 1942.
39. J. P. Bros, M. Guane-Escard, W. Szczepaniak, A. Bogacz, A. W. Hewat, *Acta Cryst.*, 1987, **B43**, 113.
40. P. J. Bendall, A. N. Fitch, B. E. F. Fender, *J. Appl. Cryst.*, 1983, **16**, 164.
41. J. C. Taylor, P. W. Wilson, *Acta Cryst.*, 1974, **B30**, 148.
42. J-C. Berthet, M. Nierlich, M. Ephritikine, *C. R. Chimie*, 2002, **5**, 81.
43. D. J. Schiffrin, *J. Electroanal. Chem.*, 1986, **201**, 199.
44. *CRC Handbook of Chemistry and Physics*, Ed. D. R. Lide, CRC Press, Inc., USA, 1995.
45. P. H. Rieger, *Electrochemistry*, Prentice-Hall, Inc., New Jersey, 1987.
46. Kanno M., Yamagami S., *Denki Kagaku Oyubi Kogyo Butsuri Kagaku*, 1975, **43**, 131-7.

CHAPTER 7

SYNTHESIS AND ELECTROCHEMISTRY

OF A NEPTUNIUM

BIS(TRIFLUOROMETHANESULFONYL)

AMIDE COMPLEX

7.1 Introduction

For alpha emitting isotopes of the actinides, the hazard increases proportionally as the half life decreases. Therefore, Np presents an increase in radiological hazard when compared with U (^{237}Np $t_{1/2} = 2.14 \times 10^6$ y, ^{238}U $t_{1/2} = 4.47 \times 10^9$ y), however this hazard is lower than that presented by Pu (^{239}Pu $t_{1/2} = 2.41 \times 10^4$ y).¹ It seems sensible to investigate the chemistry of Np in LTILs before considering any Pu chemistry. Additionally, Np poses a potential technological problem in the electrochemical separation of U from Pu from spent nuclear fuel due to a comparable Np(III)/Np(0) standard reduction potential. However, the high specific activity of ^{237}Np prevents the use of several physical techniques previously used to characterised the previous *f*-element complexes, including elemental and TGA analysis.

In molten salt media, the electrochemical series for the reduction of trivalent actinides to the zerovalent state follows the order $\text{U} < \text{Np} < \text{Pu}$ (-1.283 V, -1.484 V and -1.593 V vs. Ag/AgCl for the An(III)/An(0) couple in LiCl-KCl eutectic at 450 °C).² This trend is also followed in aqueous media, where the standard reduction potentials are $\text{U} = -1.798$ V, $\text{Np} = -1.856$ V and $\text{Pu} = -2.031$ V (for the An(III)/An(0) reduction).³ Based on the observation of the Ln(III)/Ln(0) and U(III)/U(0) reductions (see Chapters 4 and 6), it is hypothesised that this electrochemical series will also be followed in LTIL media, thus it is important to be able to understand the electrochemical behaviour of Np in LTIL media as this would be a major contaminant in an LTIL electrochemical separation reprocessing technology.

The electrochemistry of Np has previously been explored in basic and acidic 1-*n*-butylpyridinium-AlCl₃ LTILs by Gilbert and Schoebrechts (where acidity is defined in terms of Lewis acidity of added AlCl₃).⁴ Their studies focused on the investigation of the Np(IV)/Np(III) electrode reaction and using a combination of spectroscopy (Raman and UV/vis/nIR) and electrochemistry, they inferred that the species in solution were of the general formula [NpCl_y]^{x-}.⁴ Their results showed that the speciation *i.e.* the number of coordinated chlorides, changed depending on the acidity of the melt, and this directly influenced the rate at which the redox process took place.⁴ There have been no reports, so far, in the literature of the reduction of Np(III) to Np(0) in any LTIL media and hence not in a TFSI-based LTIL. Neither have there been any reports on the coordination of the TFSI anion to the Np centre.

It has been observed previously that the electrochemistry of U in LTILs is complicated by the number of different species and oxidation states present in solution (Chapter 6). The Np(IV) oxidation state was chosen in an attempt to minimize the influence of the Np(V) neptunyl oxo species and thus simplify the electrochemistry. It was observed that the U(TFSI)₄.xH₂O complex was hygroscopic, and by analogy it was assumed that the Np(IV) complex would also be hygroscopic, thus the attempted synthesis of a Np^(IV)-TFSI complex was attempted under an Ar atmosphere.

7.2 Synthesis of a lower oxidation state neptunium

bis(trifluoromethanesulfonyl)amide complex

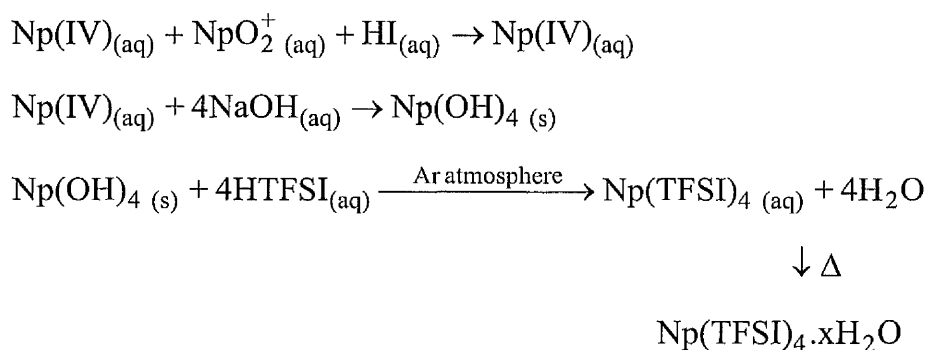
The Np stock used for this experiment (38 mmol L^{-1} Np by Gamma spectroscopy in 1 mol L^{-1} HCl) contained a mixture of Np(IV) and Np(V) (*ca.* 1:1), as determined by UV/vis/nIR spectroscopy.⁵ Reduction of the Np(V) present to Np(IV) was undertaken by the addition of HI.⁵

Addition of 2 mL HI to a solution of Np(V)/Np(IV) (1 mL, 9 mg Np) led to the formation of a red/brown solution. After addition of 2 mL H₂O and 15 m. stirring, the sample was placed under a heat lamp and evaporated to dryness. The brown coloured solid formed was then redissolved in *ca.* 2 mL H₂O and transferred to a quartz absorption spectroscopy cell and a UV/vis/nIR spectrum recorded. This procedure was then repeated until the UV/Vis/nIR spectrum showed only bands attributable to Np(IV) and no bands that could be attributed to Np(V) (*i.e.* complete reduction was achieved).

This solution was then evaporated to dryness (under a heat lamp), and the resultant brown solid dissolved in 3 mL H₂O to yield an orange solution with a fine brown suspension. The filtered solution was then mixed with NaOH solution (2 mL, 0.1 mol L^{-1}) to yield an olive green precipitate of Np(OH)₄. The suspension was then transferred to 4 small vials and H₂O added to each (3 mL) prior to centrifugation. After centrifugation the supernatant was discarded and the solid Np(OH)₄ formed was washed with H₂O and the centrifugation procedure repeated.

The resultant wet solid was then suspended in 2 mL H₂O, and transferred to a 2-necked flask under Ar. After flushing the solution with Ar for several minutes, a solution of HTFSI was added (46 mg, 0.16 mmol in 1 mL H₂O), immediately yielding an clear pale green solution. After 16 h. of stirring the solution was evaporated to dryness *in vacuo* at 80-90 °C to yield an olive green coloured, glassy, hygroscopic solid assumed to be Np(TFSI)₄.xH₂O, although analysis may suggest some oxidation to Np^(V)O₂(TFSI).xH₂O.

An overall reaction scheme for the synthesis of Np(TFSI)₄.xH₂O is shown below:



The resultant sample was then characterised by vibrational spectroscopy. The synthesis was repeated for UV/vis/nIR characterisation of the Np-TFSI complex in [Me₃NⁿBu][TFSI]. Prior to electrochemical measurements, a fresh batch of complex was synthesised and dissolved into the LTIL.

7.3 Vibrational spectroscopy of Np-TFSI complexes

Coordination of the TFSI anion to metal centres through the sulfonyl oxygens has already been postulated using vibrational spectroscopy for La^{3+} , Sm^{3+} , Eu^{3+} , Th^{4+} , U^{4+} and $\{\text{UO}_2\}^{2+}$, and observed crystallographically for $[\text{La}(\text{TFSI})_3(\text{H}_2\text{O})_3]$ and for $\text{UO}_2(\text{TFSI})_2 \cdot \text{H}_2\text{O}$ using EXAFS analysis (Chapters 4, 5 and 6). Solid state ATR mid-IR and Raman spectra for a Np(IV)-TFSI complex have been measured and are shown in Figure 7.3.1, with selected peak assignments given in Table 7.3.1. It has previously been observed that for the green coloured $\text{U}(\text{TFSI})_4 \cdot x\text{H}_2\text{O}$ complex Raman spectra could not be measured as a result of sample decomposition. However because of the less intense colouration of the Np(IV)-TFSI complex compared with that of the uranium sample, decomposition takes longer and Raman spectra could be measured (but with significant noise).

The characteristic bands of the TFSI anion have been observed in the IR spectrum of the Np(IV)-TFSI complex. Based on comparisons of these band positions with those observed for $\text{Li}[\text{TFSI}]$, crystals of $[\text{La}(\text{TFSI})_3(\text{H}_2\text{O})_3]$ and spectra of $\text{U}(\text{TFSI})_4 \cdot x\text{H}_2\text{O}$ and $\text{UO}_2(\text{TFSI})_2 \cdot \text{H}_2\text{O}$, the bands have been assigned as shown in Table 7.3.1. The IR spectrum of the Np(IV)-TFSI complex shows band positions consistent with coordinated TFSI (Figure 7.3.2). Comparison of IR spectra of crystalline $[\text{La}(\text{TFSI})_3(\text{H}_2\text{O})_3]$ and the La, Sm Eu, $\{\text{UO}_2\}^{2+}$ and U(IV) TFSI complexes with the Np(IV)-TFSI complex showed that the major band positions are comparable, with any differences in band position attributed to the differences in metal centres. Additionally, the band positions are shifted

from those observed for Li[TFSI] (Figure 7.4.2), which is known to have uncoordinated TFSI in the crystalline state.⁶ By comparison of all these spectra, with that measured for the Np(IV)-TFSI complex, it is hypothesised that TFSI is coordinated to the Np centre *via* the sulfonyl oxygens.

It has previously been shown in the vibrational spectrum for $\text{U}(\text{TFSI})_4 \cdot x\text{H}_2\text{O}$ compound that a mixture of oxidation states is present by the observation of bands assigned to the $\nu_s(\text{U}=\text{O})$ (869 cm^{-1}) and $\nu_a(\text{U}=\text{O})$ (979 cm^{-1}) modes (see Chapter 6). It is known from the literature that in the IR spectrum, the $\nu_a(\text{Np}=\text{O})$ band appears between $720 - 850\text{ cm}^{-1}$.⁷ Based on this observation, the shoulder at *ca.* 820 cm^{-1} (which is not present in the IR spectrum of Li[TFSI] and crystalline $[\text{La}(\text{TFSI})_3(\text{H}_2\text{O})_3]$) is tentatively assigned to $\nu_a(\text{Np}=\text{O})$. However, assignment of the measured IR/Raman spectra of the Np-TFSI compound to either a Np(IV) or Np(V) oxidation state TFSI complex or a mixed oxidation state complex is difficult based on the vibrational spectroscopic data.

In the Raman spectrum, the $\nu_s(\text{Np}=\text{O})$ band has previously been observed at 872 cm^{-1} for $[\text{NpO}_2(\text{IO}_3)_2\text{H}_2\text{O}]$ ⁸ and at 767 cm^{-1} for NpO_2^+ in perchlorate media.⁹ For the Np(IV)-TFSI complex no distinct band is observed within this region which can be conclusively assigned to the $\nu_s(\text{Np}=\text{O})$ mode, although, based on the previous $\{\text{UO}_2\}^{2+}$ TFSI chemistry it would be expected to come at the higher energy region.

Assignment	IR	Raman
$\nu_a^{\text{i.p./o.p.}}(\text{SO}_2)$	1319 / 1338	-
$\nu_s(\text{CF}_3)$	1240 (sh)	1243
$\nu_a(\text{CF}_3)$	1188	-
$\nu_s^{\text{o.p.}}(\text{SO}_2)$	1125	1135
$\nu_a(\text{SNS})$	1051	-
$\nu_a(\text{Np=O})$	823? (sh)	-
$\nu(\text{CS})$	793	-
$\nu_s(\text{SNS})$	767	-
$\delta_s(\text{CF}_3)$	741	745
$\delta(\text{SNS})$	667	-

Table 7.3.1: Solid state ATR mid-IR and Raman bands of synthesised Np(IV)-TFSI compound. sh = shoulder; ? = tentative assignment;

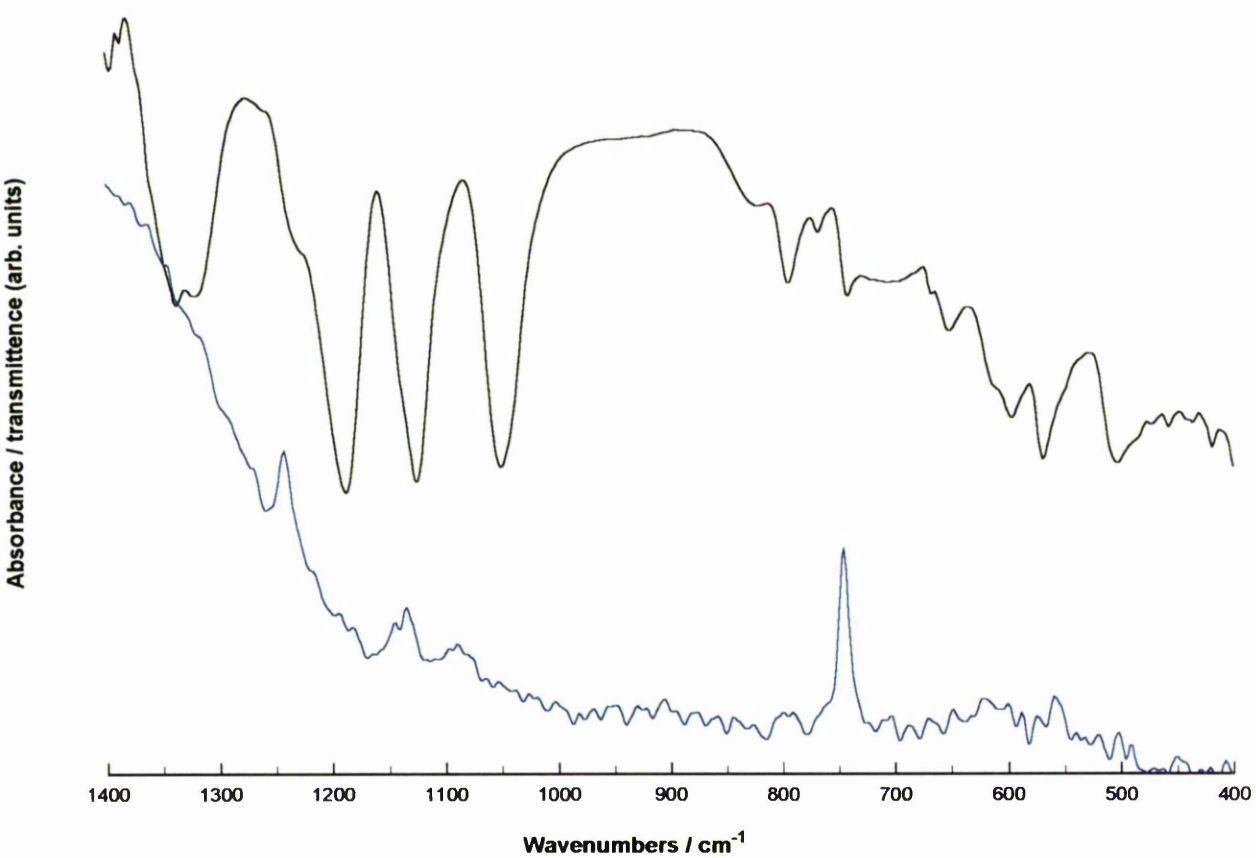


Figure 7.3.1: Solid state ATR IR and Raman spectra of Np(IV)-TFSI complex

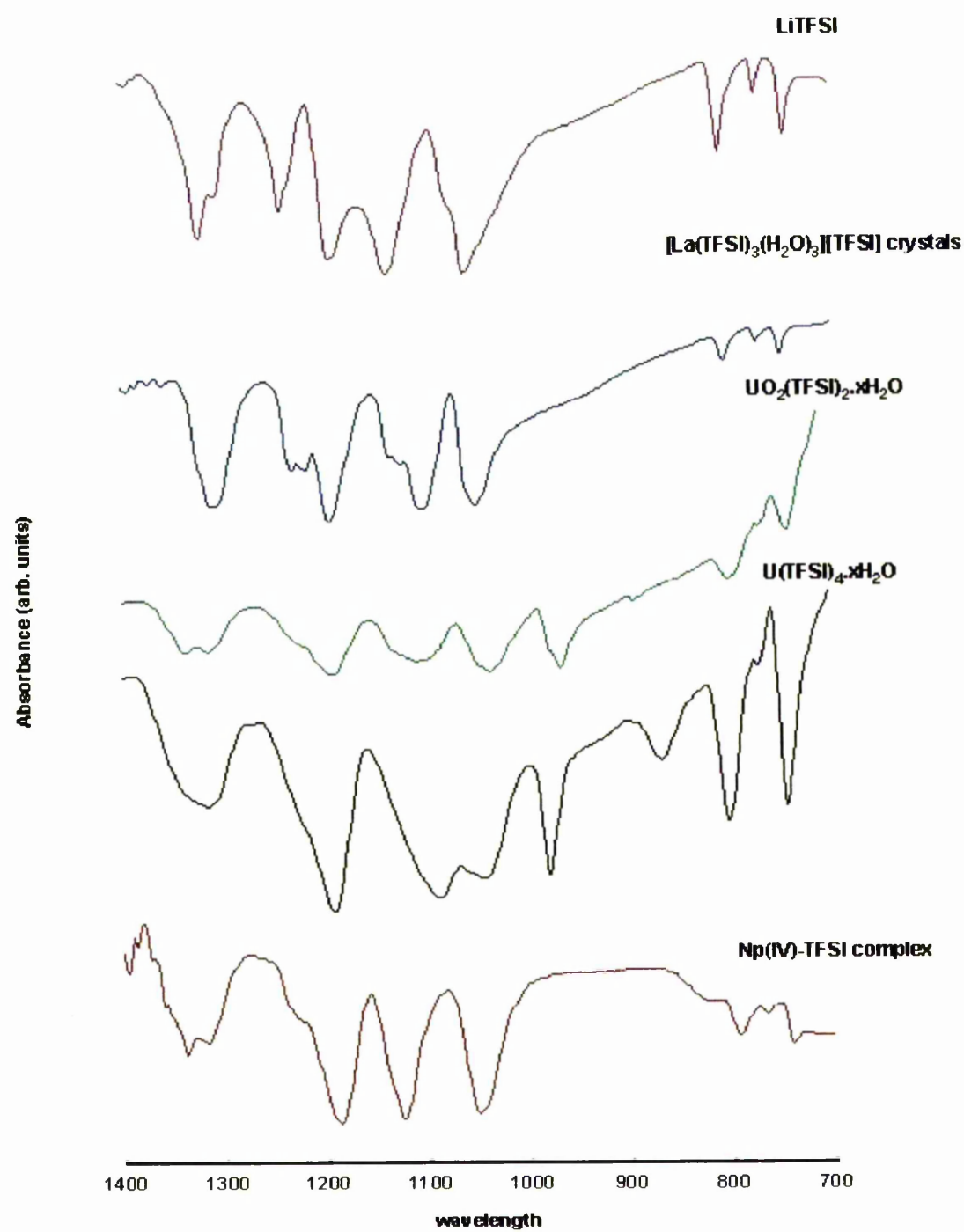


Figure 7.3.2: Comparison of the IR spectra of Np, Li, La, U(IV) and $\{UO_2\}^{2+}$ TFSI complexes

7.4 UV/vis/nIR spectroscopy of Np-TFSI complexes in solution

7.4.1 UV/vis/nIR studies of Np-TFSI complexes in aqueous solution

The mixed Np(V)/Np(IV) stock solution was converted to a Np(IV) solution by the reaction with HI. The reaction was monitored using UV/vis/nIR spectroscopy. It is known that the UV/vis/nIR spectrum of Np(IV) has major characteristic bands at *ca.* 720 and 960 nm and Np(V) has a major characteristic band at 980 nm.^{4,10-15} During the synthesis, additional HI was added to the reaction mixture until the UV/vis/nIR spectrum showed complete reduction of Np(V) to Np(IV) by the absence of a band at 980 nm. Spectrum A in Figure 7.4.1 shows the UV/vis/nIR spectrum of the Np(V)/Np(IV) stock solution, whilst spectrum B shows the complete reduction of Np(V) to Np(IV) with major bands at 960 nm and 720 nm that are attributed to *f-f* transitions of Np(IV).^{4,10-15} The origin of the high intensity band beginning at *ca.* 650 nm is unknown, but may be due to the I₂ charge transfer band arising from small quantities of I₂ in the sample formed during reduction of Np(V) using HI.¹⁶

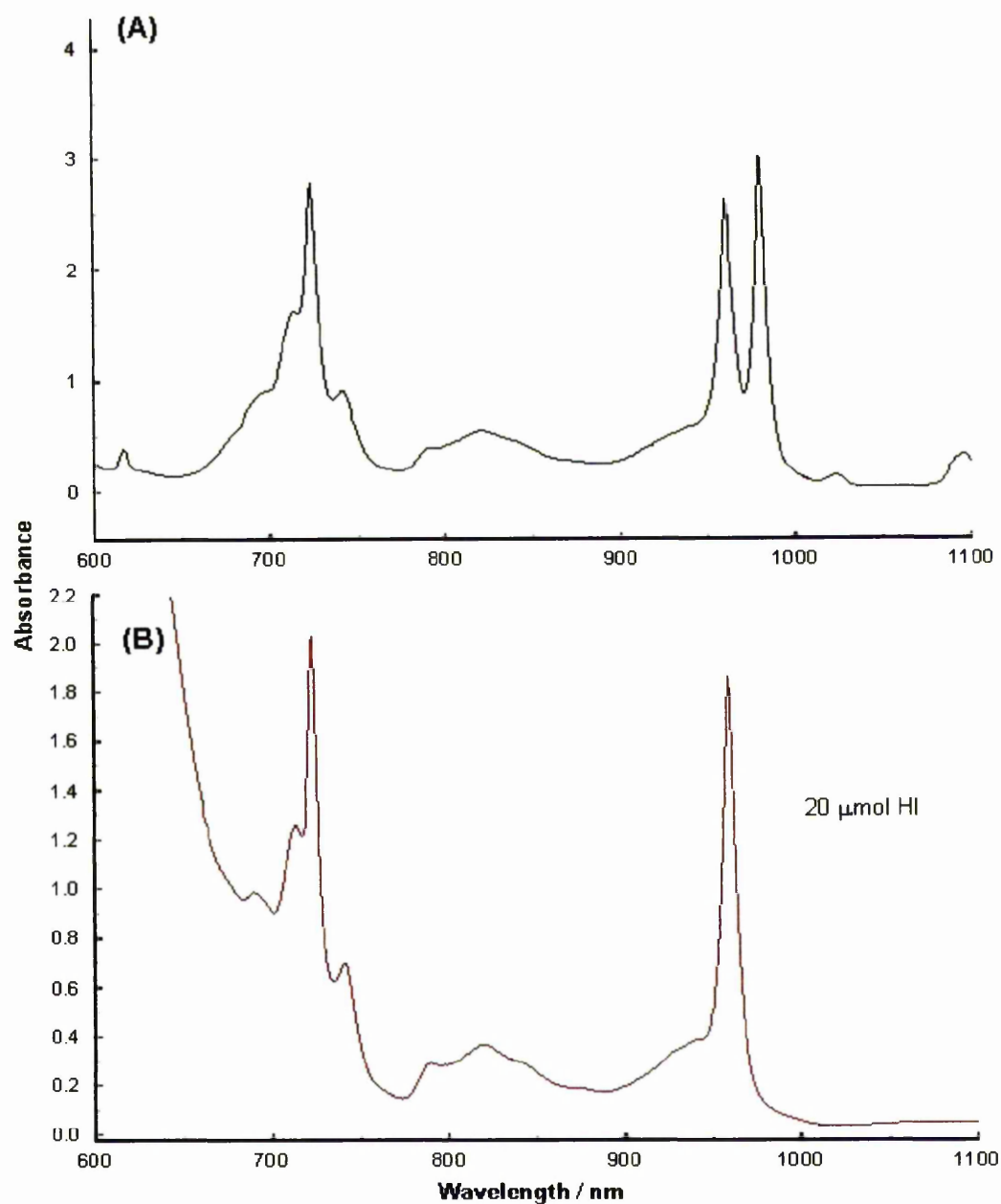


Figure 7.4.1: Reduction of Np(V) using HI monitored using solution UV/vis/nIR spectroscopy. Spectrum A, initial UV/vis/nIR spectrum of the Np(V)/Np(IV) stock solution (38 mmol L^{-1}); spectrum B, complete reduction of Np(V) to Np(IV) (19 mmol L^{-1})

7.4.2 UV/vis/nIR studies of Np-TFSI complexes in $[Me_3N^nBu][TFSI]$ solution

After repeating the synthesis (Section 7.2), a sample of Np(IV)-TFSI compound (assuming to contain 9 mg Np if 100 % yield) was dissolved in $[Me_3N^nBu][TFSI]$ under Ar and the UV/vis/nIR spectrum of this solution was measured in order to monitor the oxidation state of Np. Spectra were taken over a period from 10 m after dissolution to 14 h, and selected spectra are shown in Figure 7.4.2.

Initially, the UV/vis/nIR spectrum of the Np(IV)-TFSI complex dissolved in the LTIL (Figure 7.4.2, Spectrum A) shows bands due to $f-f$ transitions^{4,10-15} of both Np(IV) (738 nm) and Np(V) (major bands at 618, 969, 980 and *ca.* 1080 nm). Combining this data with the IR/Raman data from Section 7.3.2, it is hypothesised that initially mixed oxidation state, Np(IV)/Np(V)-TFSI complexes were synthesised with more Np(V) than Np(IV) complex present. After 280 m, the spectrum shows complete oxidation of the remaining Np(IV), with the formation of another band attributed to Np(V) as a shoulder at 998 nm.

The oxidation of Np(IV) to Np(V) is most probably due to the reaction of Np(IV) with water in the LTIL and/or associated with the complex itself. Figure 7.4.2. shows that the Np(IV)-TFSI compound is being oxidised to Np(V) by the decrease in band intensity at 738 nm (which has been assigned to Np(IV) $f-f$ transitions). After 280 m. the oxidation reaction is complete (disappearance of the band at 738 nm, Spectrum B, Figure 7.4.2) and a solution of Np(V) is formed.

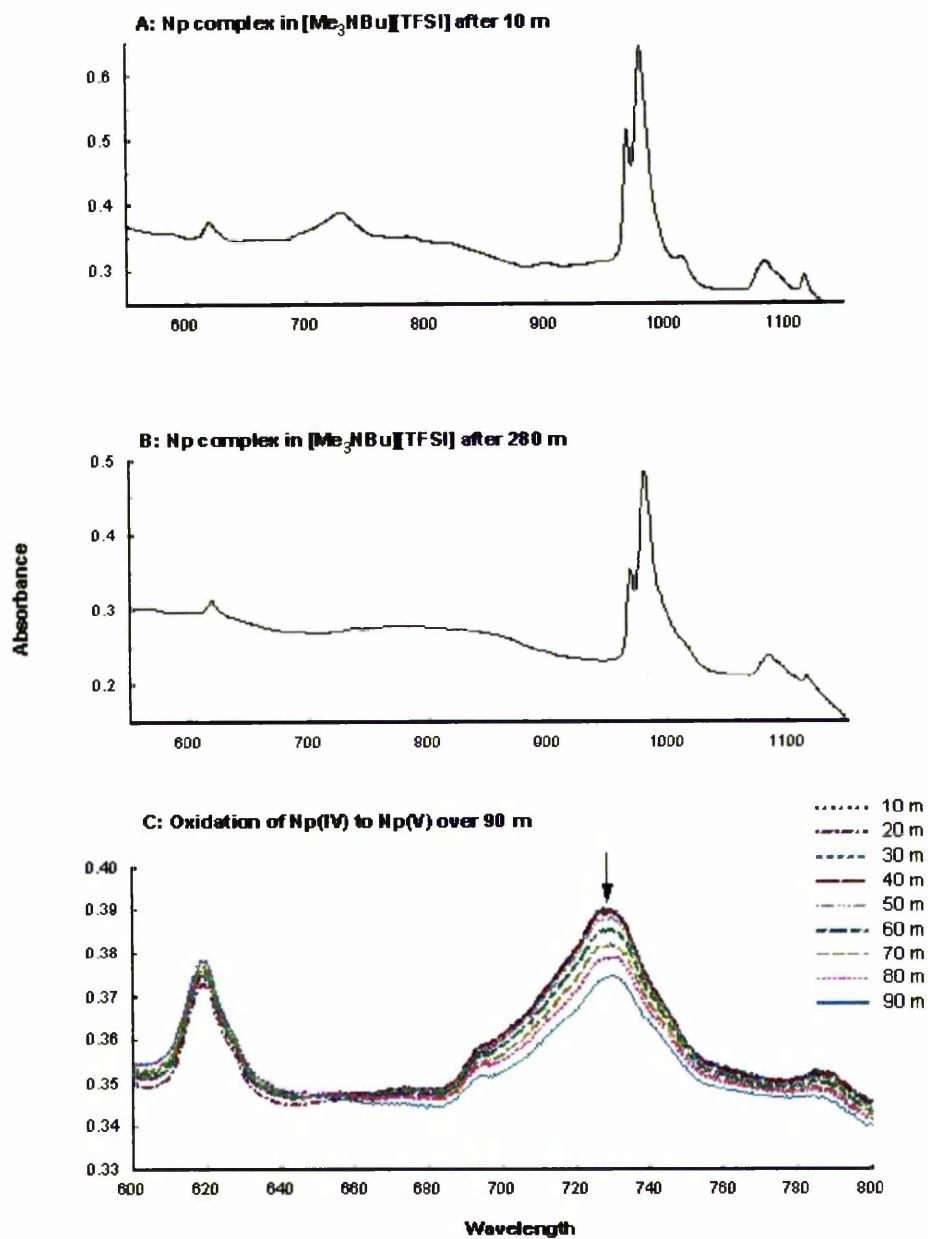


Figure 7.4.2: Oxidation of Np(IV) in $[Me_3N^+Bu][TFSI]$. Spectrum A, after 10 m. showing mixed Np(IV)/Np(V) species in solution; Spectrum B after 280 m. showing only Np(V) species present; Spectrum C, showing oxidation of Np(IV) over 90 m. as observed by the decrease in intensity of the band at 738 nm.

Pitzer and Matsika have previously assigned the Np(V) absorption spectra for NpO_2^+ with Cl^- and H_2O ligands in the equatorial plane, using a combination of experiment and theoretical calculations.^{17,18} Their results indicate that the NpO_2^+ moiety is 5 coordinate in the equatorial plane.^{17,18} Based on this study, the major f - f transitions observed in the present UV/vis/nIR have been assigned (Table 7.4.1).

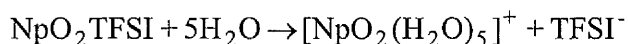
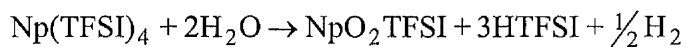
The relatively intense $^3\text{H}_{2g} \rightarrow ^3\text{I}_{2g}$ band (at 980 nm) is known to be sensitive to complexation.^{17,18} This is because the linear $\{\text{NpO}_2\}^+$ moiety has a $d_{\infty h}$ symmetry, thus the f - f transitions are symmetry forbidden.^{17,18} However, coordination of 5 equatorial ligands removes the centre of symmetry present in the linear $\{\text{NpO}_2\}^+$ moiety allowing the transition to take place.^{17,18} As a result of this, any changes in the equatorial ligands will influence the band observed in the UV/vis/nIR spectrum.

Based on this the $^3\text{H}_{2g} \rightarrow ^3\text{I}_{2g}$ bands observed at 969 and 980 nm indicate that there are more than one species in solution. The band at 980 nm is in a similar position to that observed for $[\text{NpO}_2(\text{H}_2\text{O})_5]^+$ and thus assigned to a NpO_2^+ hydrated ion in the LTIL, noting that H_2O had not been rigorously excluded in the synthetic procedures. The band at 969 nm is lower than that previously observed at 980.2 nm for $[\text{NpO}_2(\text{H}_2\text{O})_5]^+$ in water,^{11,12,15,17} suggesting a weaker coordinating equatorial ligand. It has previously been observed for $\{\text{UO}_2\}^{2+}$ coordinated to TFSI ligands, that the ν ($\text{U}=\text{O}$) band in the Raman spectrum is shifted from that observed for $[\text{UO}_2(\text{H}_2\text{O})_5]^{2+}$ (897 cm^{-1} for $\text{UO}_2(\text{TFSI})_2 \cdot \text{H}_2\text{O}$ compared to 870 cm^{-1} for $[\text{UO}_2(\text{H}_2\text{O})_5][\text{TFSI}]$, see Chapter 6) and thus the TFSI anion is

a weaker coordinating ligand than water. Based on these observations, the band at 969 nm is assigned to a $\{\text{NpO}_2\}^+-\text{TFSI}$ complex in solution.

The shoulders at 998 and 1017 nm suggest a stronger coordinating equatorial ligand than water. Sevost'yanova *et al.* have previously observed the $^3\text{H}_{2g} \rightarrow ^3\Pi_{2g}$ transition at 991 nm for NpO_2OH .¹⁹ Based on this work and the synthetic route used, it is hypothesised that these shoulders are due to small quantities of unreacted hydrated $\text{NpO}_2(\text{OH})$ and/or $\text{NpO}_2(\text{OH})_2^-$ with additional coordinated H_2O ligands in the equatorial plane.

The following reactions are proposed for the oxidation of Np(IV) to Np(V) in $[\text{Me}_3\text{N}^n\text{Bu}][\text{TFSI}]$:



Based on the UV/vis/nIR studies, it seems clear that Np(IV) cannot be stabilised by TFSI in the presence of trace water, and oxidation to Np(V) occurs (forming the neptunyl species). Further work would be required to determine whether this oxidation occurs without dissolved water in the melt, although this chemistry would be extremely challenging.

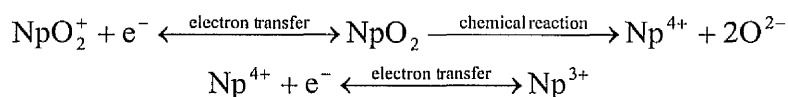
Band / nm	Transition [†]	Absorbance
568	$^3H_{2g} \rightarrow ^3\Delta_{2g}$	0.0051
618	$^3H_{2g} \rightarrow ^1\Pi_{1g}$	0.016
969	$^3H_{2g} \rightarrow ^3\Pi_{2g}$	0.10
980	$^3H_{2g} \rightarrow ^3\Pi_{2g}$	0.23
998 (sh)	$^3H_{2g} \rightarrow ^3\Pi_{2g}$	-
1017 (sh)	$^3H_{2g} \rightarrow ^3\Pi_{2g}$	-
<i>ca.</i> 1080	$^3H_{2\gamma} \rightarrow ^3\Pi_{1\gamma} + ^3\Sigma_{1\gamma}$	0.024

Table 7.4.1: Assignments for major bands observed in the UV/vis/nIR spectra of Np(V) in [Me₃N^{''}Bu][TFSI]. [†]Assigned for a d_{∞h} point symmetry of the linear {NpO₂}⁺ moiety

7.5 Electrochemistry of a $\{\text{NpO}_2\}^+$ -TFSI complex in $[\text{Me}_3\text{N}^n\text{Bu}][\text{TFSI}]$

The electrochemistry of $\{\text{NpO}_2\}^+$ (Section 7.2) has been investigated in $[\text{Me}_3\text{N}^n\text{Bu}][\text{TFSI}]$ using cyclic voltammetry (CV) and linear scan voltammetry (LSV). All measurements were performed under Ar in a Faraday cage to minimise electrochemical noise using a 3 electrode cell (Chapter 2). Solutions were purged with Ar for at least 5 m. prior to measurements. Based on the UV/vis/nIR experiments where after 280 m. complete oxidation of Np(IV) to Np(V) was observed for Np in $[\text{Me}_3\text{N}^n\text{Bu}][\text{TFSI}]$ (see Section 7.4), solutions of the Np-TFSI complex dissolved in $[\text{Me}_3\text{N}^n\text{Bu}][\text{TFSI}]$ were left overnight (*ca.* 720 m.), to allow full oxidation of the residual Np(IV) to Np(V). Cyclic and linear scan voltammograms of $\{\text{NpO}_2\}^+$ -TFSI complexes in $[\text{Me}_3\text{N}^n\text{Bu}][\text{TFSI}]$ show a number of oxidation and reduction peaks, as shown in Figures 7.5.1 and 7.5.2

The reduction peak at *ca.* 0.40 V (all potentials quoted against Ag wire quasi reference electrode) in the CV has been assigned to the Np(V) to Np(IV) reduction processes. The reduction of Np(V) to Np(IV) will involve the breaking of the neptunyl oxo bonds to form the Np^{4+} cation (which in turn can be reduced to Np^{3+}):



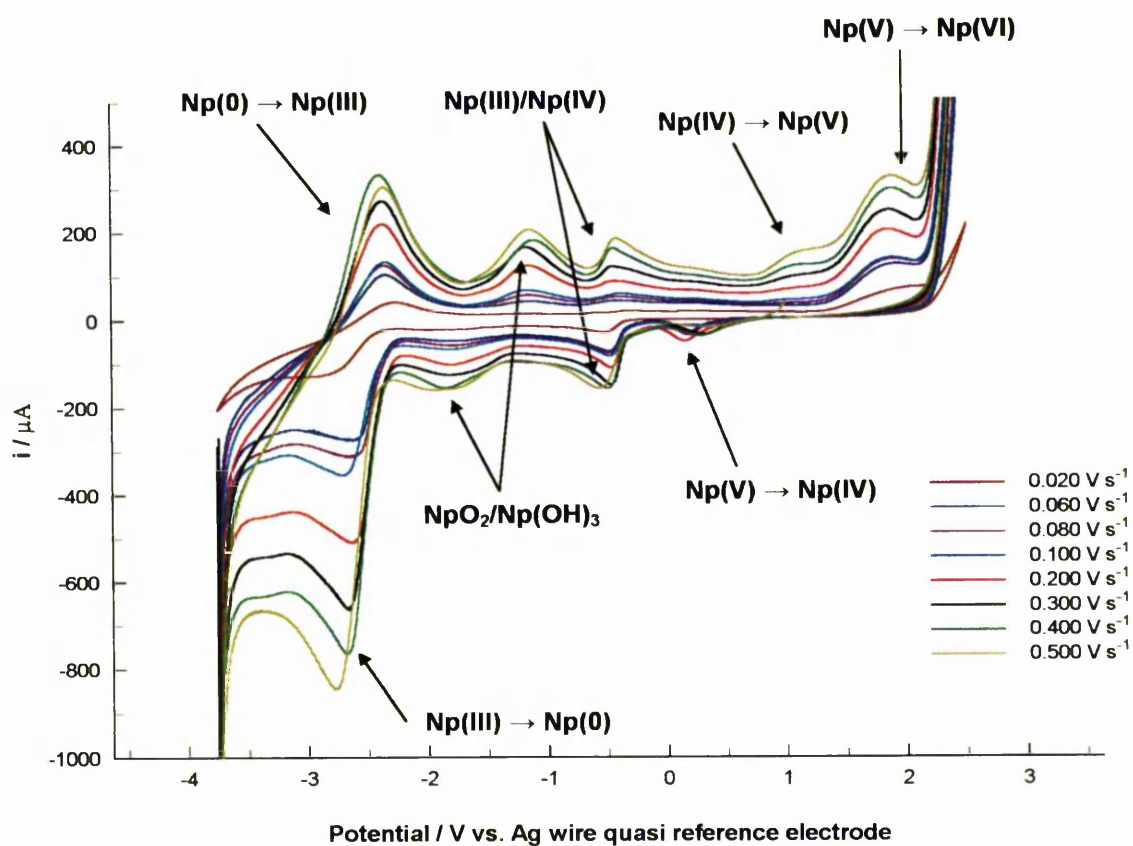


Figure 7.5.1 CV of $\{NpO_2\}^+$ in $[Me_3N^+Bu][TFSI]$ at 25 °C. CVs run after 720 m. to allow full oxidation of residual Np(IV) to Np(V)

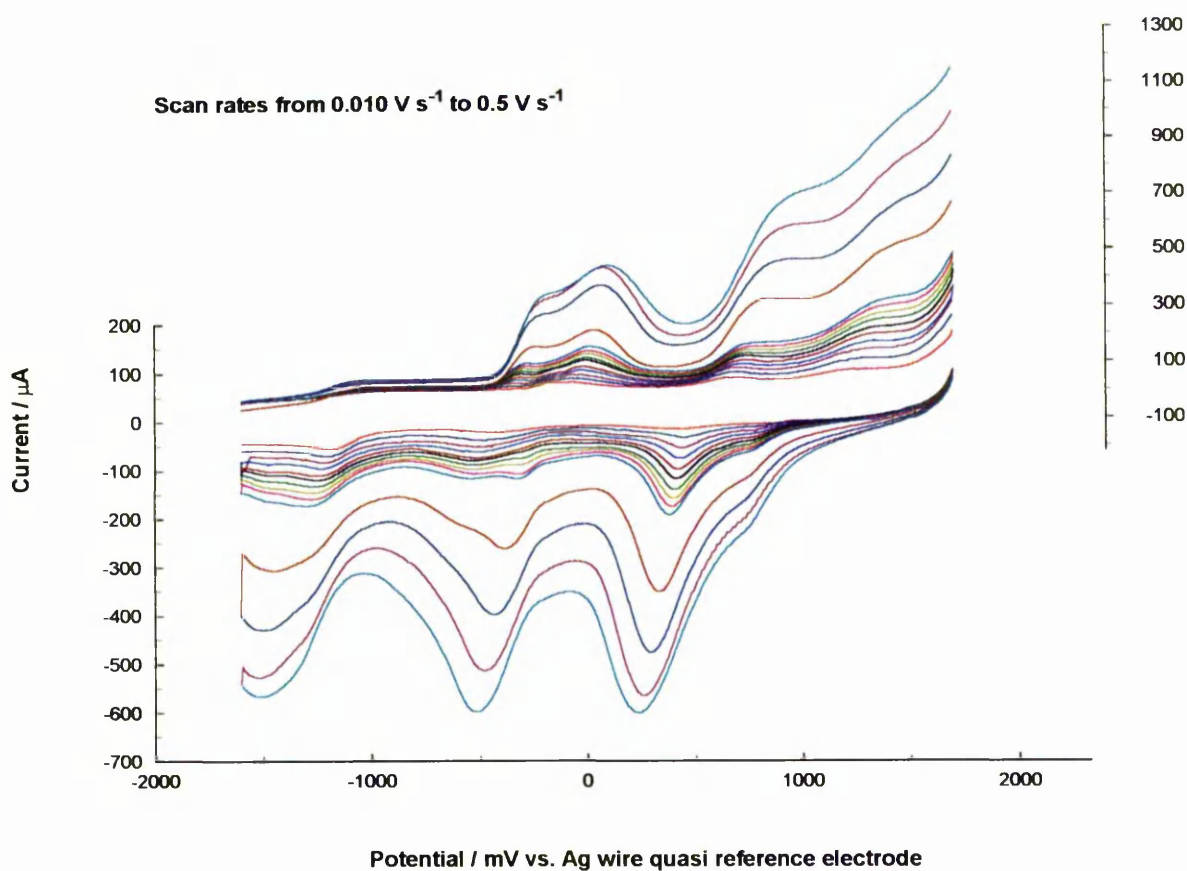


Figure 7.5.2 LSV of $\{\text{NpO}_2\}^+$ in $[\text{Me}_3\text{N}^+\text{Bu}][\text{TFSI}]$ at 25 °C. LSVs run after 720 m. to allow full oxidation of residual Np(IV) to Np(V)

The theory of this type of electrochemical ECE mechanism has previously been investigated by Shain and Nicholson.^{20,21} Costa *et al.* have applied this treatment to the similar $\{\text{UO}_2\}^{2+}/\text{U}^{4+}$ reaction in 1-ethyl-3-methylimidazolium chloroaluminate LTIL.²² Based on these studies the Shain and Nicholson treatment has been applied to the Np(V)/Np(IV) reduction. For an ECE mechanism it is known that plots of $i_p/v^{1/2}$ as a function of $\log v$ (measured from LSV) give rise to a curve, whereas for an

uncomplicated reversible electron transfer a straight line is obtained.²¹ A plot of $i_p/v^{1/2}$ vs. $\log v$ is shown in Figure 7.5.3, Graph A for the Np(V)/Np(IV) reduction peak. As can be observed from the plot, a curve is obtained suggesting that the assignment proposed for this reduction peak is correct.

From the CV, plots of $i_{p/c}$ vs. $v^{1/2}$ show two linear regions (Figure 7.5.3, Graph B) indicating two scan rate dependent processes. In theory at slow scan rates the peak current observed should be related to the reduction of NpO_2^+ to Np^{4+} , and at very fast scan rates the NpO_2^+ should be reduced to NpO_2 (*i.e.* the chemical reaction is not observed on the timescale of the experiment). The results obtained are not consistent with this mechanism as the slopes of the graph are shallower at slow scan rates and steeper at high scan rates implying that the number of electrons transferred is higher at fast scan rates (assuming the diffusion coefficient is the same for all species involved). The reason for this may be due to the peak at *ca.* 0.75 V in the LSV. It is possible that this is due to the Np(VI)/Np(V) reduction and so at fast scan rates the excess current observed is due to the Np(VI)/Np(V) reduction. In the CVs this reduction peak is not observed, but an oxidation peak at *ca.* 1.75 V (assigned to the Np(V)/Np(VI) oxidation) is observed. A plot i_p vs. $v^{1/2}$ shows a linear relationship (Figure 7.5.4) suggesting that this assignment is correct. The scatter in data points is a result of the poorly defined peak position due to the peak being at the end of the electrochemical window.

Turning to the redox couple at $E_{1/2} = -0.43$ V ($E_{p/a} = -0.35$ V, $E_{p/c} = -0.51$ V), this has been assigned to the Np(IV)/Np(III) couple. Plots of $i_{p/c}$ vs. $v^{1/2}$ (from the CV) again show

two linear regions again indicating two different scan rate dependent processes, this is not consistent with what is expected for the Np(IV)/Np(III) couple (Figure 7.5.5). The results are explained by the reduction of two Np(IV) species in solution. At slow scan rates, $\{\text{NpO}_2\}^+$ is reduced to Np^{4+} , which in turn can be reduced to Np^{3+} . However, at fast scan rates NpO_2 is formed upon reduction of $\{\text{NpO}_2\}^+$ which can then be reduced to a Np(III) species. This is observed in the linear scan voltammograms (Figure 7.5.2) where the (IV)/(III) reduction is split into 2 distinct bands at slow scan rates.

The redox processes at *ca.* -1.5 ($E_{p/a} = -1.15$ V, $E_{p/c} = -1.79$ V), has been assigned to the reduction of the NpO_2 species to Np(OH)_3 . The difference between the Np(IV)/Np(III) couple ($E_{1/2} = -0.43$ V) and the $\text{NpO}_2/\text{Np(OH)}_3$ reduction process ($E_{p/c} = -1.79$ V) is experimentally found to be 1.36 V and is comparable to the literature value of 1.11 V³ taking into consideration the different chemical environment. It should be noted that the NpO_2 reduction to Np(OH)_3 requires the chemical reaction of the NpO_2 with water. It has already been inferred from the UV/vis/nIR studies, that a quantity of water is present in the solution and so this reaction mechanism is plausible.

The Np(III)/Np(0) reduction is assigned to the redox couple at $E_{1/2} = -2.57$ V ($E_{p/a} = -2.44$ and $E_{p/c} -2.69$ V). The difference between the Np(IV)/Np(III) couples and Np(III)/Np(0) couple has been measured to be 2.07 V, which is comparable to the literature value of 2.01 V (Np(III)/Np(0) $E^0 = -1.856$ V) and plots of $i_{p/c}$ vs. $v^{1/2}$ show a linear relationship (Figure 7.5.6). Using this linear relationship the diffusion coefficient has been calculated to be $1.13 \times 10^{-8} \text{ cm}^2 \text{ s}^{-1}$ from the Randles-Sevcik equation.^{23,24} This result is directly

comparable to the diffusion coefficient measured for $\text{U}(\text{TFSI})_4 \cdot x\text{H}_2\text{O}$ in $[\text{Me}_3\text{N}^n\text{Bu}][\text{TFSI}]$ ($1.92 \times 10^{-8} \text{ cm}^2 \text{ s}^{-1}$). The diffusion coefficient measured is also comparable to that reported previously for $[\text{NpCl}_6]^{2-}$ 1-*n*-butylpyridinium- AlCl_3 LTIL (between 1.1 and $1.9 \times 10^{-7} \text{ cm}^2 \text{ s}^{-1}$ depending on acidity of melt).⁴

The $\text{Np}(\text{III})/(\text{0})$ oxidation peak at *ca.* -2.44 V is much sharper (occurs on a narrower potential range) than the corresponding oxidation peak observed for La, Sm, Eu, Th and U. This indicates a substantial amount of $\text{Np}(\text{0})$ exists at the electrode to be reoxidised, however no plating/stripping behaviour is observed. It has been hypothesised previously that the reduction of an *f*-element ion to its metallic state in $[\text{Me}_3\text{N}^n\text{Bu}][\text{TFSI}]$ is complicated by the reaction of the metal produced with water to form an oxide phase (see Chapters 4, 5 and 6). The shape of the oxidation peak may be explained in terms of the rate of reaction of formation of NpO_2 being slower than that of the other metals investigated because of the lower thermodynamic driving force ($\Delta G_{\text{formation}}$ for $\text{NpO}_2 = -979 \text{ kJ mol}^{-1}$ cf. La_2O_3 , $-1705.8 \text{ kJ mol}^{-1}$; Sm_2O_3 , $-1734.7 \text{ kJ mol}^{-1}$; Eu_2O_3 , $-1556.9 \text{ kJ mol}^{-1}$; ThO_2 , $-1169.2 \text{ kJ mol}^{-1}$; UO_2 $-1031.8 \text{ kJ mol}^{-1}$ and UO_3 , $-1145.7 \text{ kJ mol}^{-1}$).²⁵

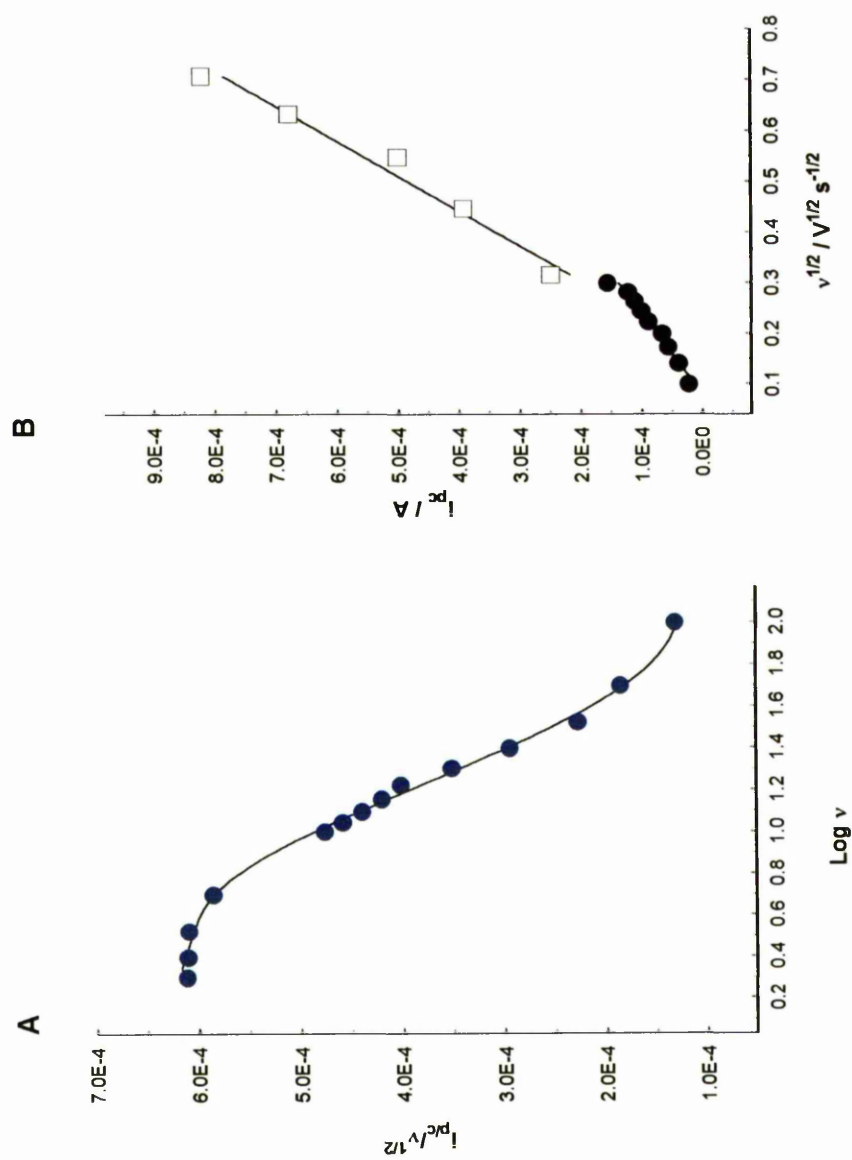


Figure 7.5.3: Shain and Nicholson treatment of the Np(V)/Np(IV) reduction observed at 0.40 V in the CV experiment shown in

Figure 7.5.1

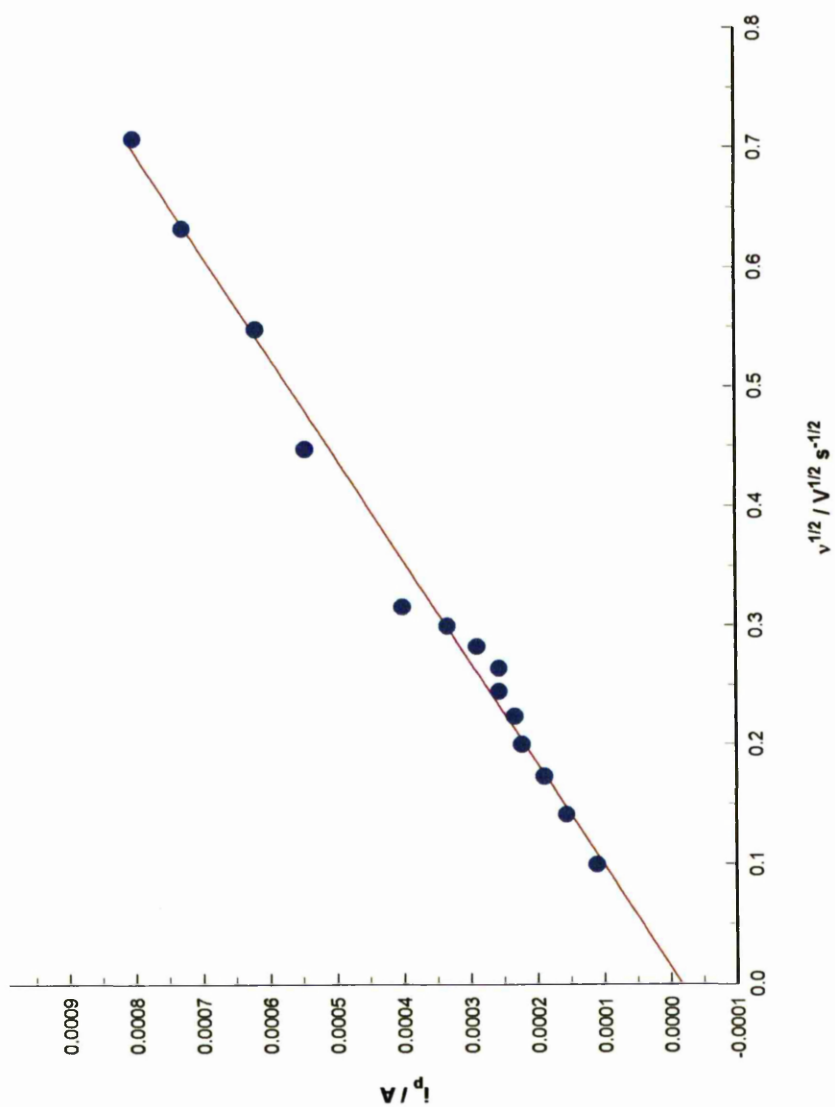


Figure 7.5.4: Randles-Sevcik plot of the oxidation of Np(V) to Np(VI) observed at 1.75 V in the CV experiment shown in

Figure 7.5.1

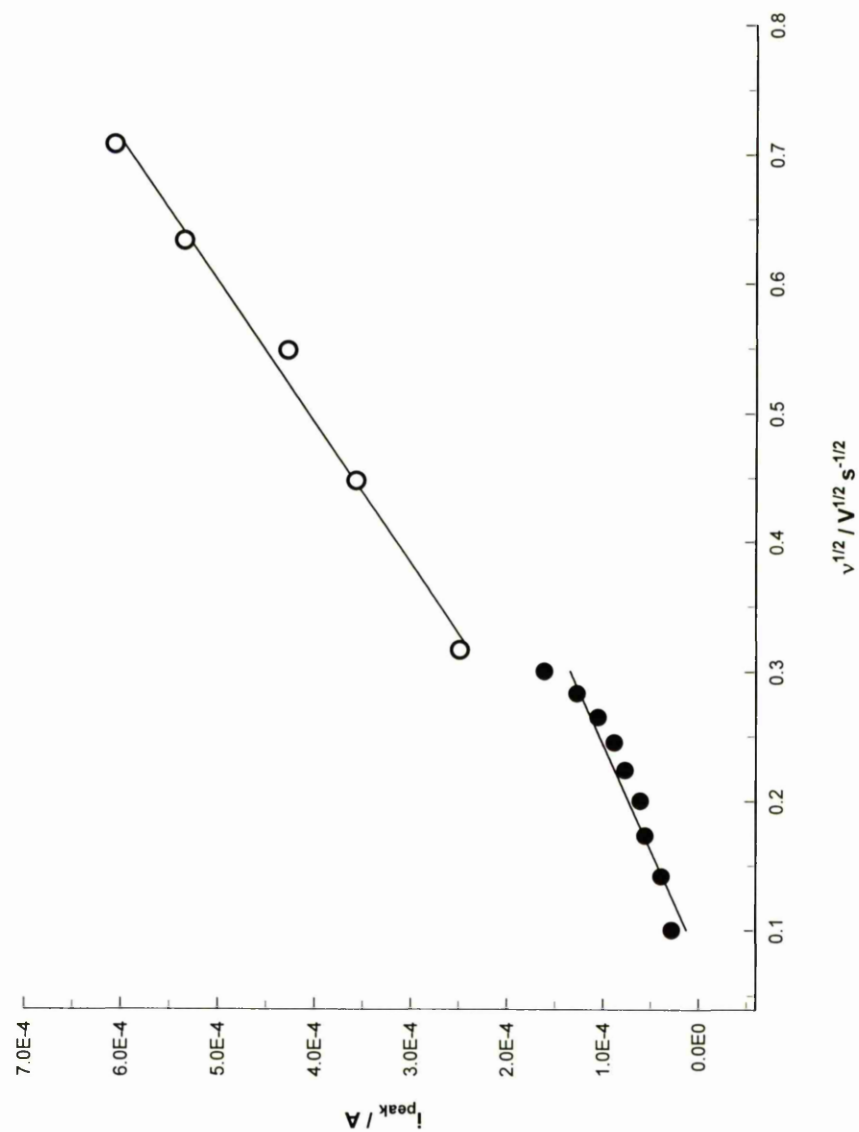


Figure 7.5.5: Randles-Sevcik plot of the reduction of Np(IV) to Np(III) observed at -0.50 V in the CV experiment shown in

Figure 7.5.1

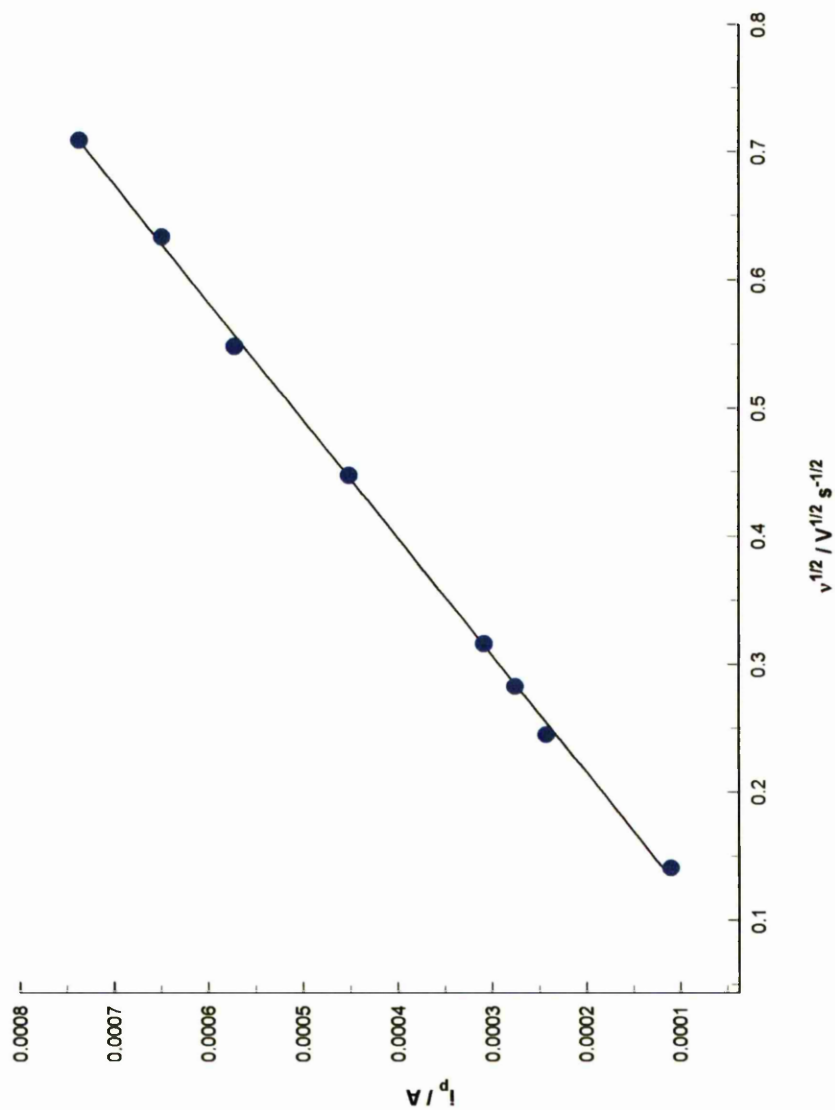


Figure 7.5.6: Randles-Sevcik plot of the reduction of Np(III) to Np(0) observed at -2.69 V in the CV experiment shown in

Figure 7.5.1

7.6 Summary

The synthesis of a Np(IV)-TFSI complex has been attempted with the coordination of the TFSI anion investigated using vibrational spectroscopy. Solid state IR/Raman data indicate that a mixture of Np oxidation states are present (IV and V) with the characteristic bands of TFSI indicating direct coordination to the Np centre(s) through the sulfonyl oxygens. The oxidation of Np(IV) to $\{\text{NpO}_2\}^+$ upon dissolution of Np-TFSI in $[\text{Me}_3\text{N}^n\text{Bu}][\text{TFSI}]$ has been studied using UV/vis/nIR spectroscopy, and it is hypothesised that this reaction occurs *via* dissolved water in $[\text{Me}_3\text{N}^n\text{Bu}][\text{TFSI}]$ (or from hydration in the Np-TFSI complex), thus showing that $[\text{Me}_3\text{N}^n\text{Bu}][\text{TFSI}]$ does not stabilise Np(IV). UV/vis/nIR spectroscopy indicates the presence of 4 different $\{\text{NpO}_2\}^+$ complexes which are postulated to be NpO_2TFSI , $(\text{NpO}_2)(\text{H}_2\text{O})^+$, $\text{NpO}_2(\text{OH})$ and $\text{NpO}_2(\text{OH})_2^-$.

The electrochemical behaviour in $[\text{Me}_3\text{N}^n\text{Bu}][\text{TFSI}]$ has been investigated and the Np(III)/Np(0) reduction observed. The electrochemical behaviour is complex and a number of different species in solution have been postulated which include the neptunyl ion, $\{\text{NpO}_2\}^+$ and $\text{Np}(\text{OH})_3$. The electrode reactions have been studied using LSV and CV, and the peaks assigned using theoretical treatments developed by Shain and Nicholson and Randles and Sevcik.

Although no plating of Np on the electrodes was observed, the reduction of Np to the metallic state and the subsequent formation of an oxide phase is consistent with the data

obtained for La, Sm, Eu, Th and U complexes in the same LTIL. The oxidation peak observed for the $\text{Np}(0) \rightarrow \text{Np}(\text{III})$ reaction is larger (shows greater current flow) than that observed for the other f -elements and it is hypothesised that this is due to the rate of formation of the oxide being slower than that of the other metals investigated. This trend is supported by literature data, which show the Gibbs free energy of formation is lower for Np oxide than it is for the other f -elements.²⁵

7.7 References

1. P. Scott, N. Kaltsoyanis, *The f Elements*, Oxford University Press, Oxford, 1999.
2. T. Inoue, Y. Sakamura, *Molten Salts From Fundamentals to Applications*, Ed. M. Guane-Escard, Kluwer Academic Publishers, The Netherlands, 2002.
3. *CRC Handbook of Chemistry and Physics*, Ed. D. R. Lide, CRC Press, Inc., USA, 1995.
4. J. P. Schoebsch, B. Gilbert, *Inorg. Chem.*, 1985, **24**, 2105.
5. J. J. Katz, G. T. Seaborg, L. R. Morss, *The Chemistry of the Actinide Elements*, Chapman and Hall, New York, 1986.
6. J. L. Nowinski, P. Lightfoot, P. G. Bruce, *J. Mater. Chem.*, 1994, **4**, 1579.
7. A. J. Gaunt, I. May, M. Helliwell, S. Richardson, *J. Am. Chem. Soc.*, 2002, **124**, 13350.
8. A. C. Bean, B. L. Scott, T. E. Albrecht-Schmitt, W. Runde, *Inorg. Chem.*, 2003, **42**, 5632.
9. B. Guillaume, G. M. Begun, R. L. Hahn, *Inorg. Chem.*, 1982, **21**, 1159.

10. A. Saito, K. Ueno, *J. Inorg. Nucl. Chem.*, 1977, **39**, 315.
11. H. A. Friedman, L. M. Toth, M. M. Osborne, *J. Inorg. Nucl. Chem.*, 1979, **41**, 1339.
12. K-W Kim, K-C Song, E-H Lee, I-K Choi, J-H Yoo, *J. Radioanal. Nucl. Chem.*, 2000, **246**, 215.
13. C. S. Burgener, J. C. Sullivan, *Inorg. Chem.*, 1970, **9**, 2604.
14. I. May, R. J. Taylor, I. S. Denniss, G. Brown, A. L. Wallwork, N. J. Hill, J. M. Rawson, R. Less, *J. Alloys and Compd.*, 1998, **275-277**, 769.
15. P. G. Hagan, J. M. Cleveland, *J. Inorg. Nucl. Chem.*, 1966, **28**, 2905.
16. N. N. Greenwood, A. Earnshaw, *Chemistry of the Elements*, Butterworth-Heinemann, Oxford, 1984.
17. S. Matsika, R. M. Pitzer, *J. Phys. Chem. A*, 2000, **104**, 11983.
18. S. Matsika, R. M. Pitzer, *J. Phys. Chem. A*, 2000, **104**, 4064.
19. E. P. Sevost'yanova, G. V. Khallurin, *Radiokhimiya*, 1976, **6**, 870.
20. R. S. Nicholson, I. Shain, *Anal. Chem.*, 1964, **36**, 706.
21. R. S. Nicholson, I. Shain, *Anal. Chem.*, 1965, **37**, 191.
22. D. A Costa, W. H. Smith, *Los Alamos yearly report*, LA-UR-99-5521, 1999.
23. A. Sevcik, *Collection Czech. Chem. Commun.*, 1948, **13**, 349.
24. J. E. B. Randles, *Trans. Faraday Soc.*, 1948, **44**, 327.
25. *Knovel Critical Tables*, Knovel, New York, 2003.

CHAPTER 8

CONCLUSIONS

8.1 Conclusions

The work presented in this thesis contains a systematic study of the chemical and electrochemical properties of a series of quaternary group 15 cation and TFSI anion based LTILs. Of all the LTILs studied one, $[\text{Me}_3\text{N}^+\text{Bu}][\text{TFSI}]$, appears to be the most suitable for actinide electrorefining. $[\text{Me}_3\text{N}^+\text{Bu}][\text{TFSI}]$ is a liquid at room temperature with high thermal and radiological stability. The wide electrochemical window (-3.2 - +2.7 V vs. Fc^+/Fc) indicates cathodic stability above the negative potential required for U(III) and Pu(III) reduction to the zerovalent state.

Three new Ln-TFSI complexes, of the general formula $[\text{Ln}(\text{TFSI})_3(\text{H}_2\text{O})_3]$ ($\text{Ln} = \text{La}$, Sm and Eu), have been synthesised, with the La(III) complex also being the first crystallographically characterised *f*-element TFSI complex. Bidentate coordination of the TFSI ligands is observed with structural evidence for the poor coordinating ability of this ligand (it appears that H_2O is more strongly coordinated to the La centre). Elemental analysis and vibrational spectroscopy have been used to confirm that isostructural complexes have been synthesised for La, Sm and Eu. The electrochemical behaviour of the Ln-TFSI complexes has been investigated in $[\text{Me}_3\text{N}^+\text{Bu}][\text{TFSI}]$, (as well as in $[\text{Me}_4\text{N}][\text{TFSI}]$ and $[\text{Me}_4\text{P}][\text{TFSI}]$ and in MeCN using $[\text{Me}_3\text{N}^+\text{Bu}][\text{TFSI}]$ as supporting electrolyte) and the reduction to the zerovalent state observed. As the Ln(III)/Ln(0) and Ln(II)/Ln(0) standard reduction potentials are more negative than those of Pu(III)/Pu(0) this result suggests that Pu may be electrochemically reduced to the zerovalent state in $[\text{Me}_3\text{N}^+\text{Bu}][\text{TFSI}]$. However, electroplating of a metal was not observed in the voltammograms, probably due to the presence of moisture in the system resulting in an immediate oxide formation on the

electrode surface. Any future studies should thus involve the elimination of moisture from the system *via* use of anhydrous Ln starting materials and perhaps a concomitant investigation into additional drying techniques for $[\text{Me}_3\text{N}^n\text{Bu}][\text{TFSI}]$.

A Th(IV)-TFSI complex, $\text{H}[\text{Th}(\text{TFSI})_5] \cdot 2\text{H}_2\text{O}$, has been synthesised and characterised using elemental analysis, TGA and vibrational spectroscopy. Vibrational spectroscopy indicates that TFSI coordinates to the Th centre *via* the sulfonyl oxygens, as previously observed for the Ln complexes. The electrochemistry in $[\text{Me}_3\text{N}^n\text{Bu}][\text{TFSI}]$ shows that Th(IV) is reduced to the zerovalent state in one step. As for the lanthanides, voltammograms did not show the electroplating of Th metal, but instead indicate that an oxide may be forming on the electrode surface. The use of low specific radioactivity of ^{232}Th , coupled with simple redox chemistry, facilitated relatively straightforward access to actinide chemistry and electrochemistry in the chosen melt system.

$\text{U}(\text{TFSI})_4 \cdot x\text{H}_2\text{O}$ and $\text{UO}_2(\text{TFSI})_2 \cdot \text{H}_2\text{O}$ have been synthesised and characterised using, elemental analysis, UV/vis/nIR, XAS (XANES and EXAFS) and vibrational spectroscopies. Solution speciation in $[\text{Me}_3\text{N}^n\text{Bu}][\text{TFSI}]$ has also been investigated using XAS (XANES and EXAFS) and UV/vis/nIR spectroscopies. Direct coordination of the TFSI ligand to both U(IV) and $\{\text{UO}_2\}^{2+}$ has been observed although the relative ease of oxidation of U(IV) to $\{\text{UO}_2\}^{2+}$ in the presence of TFSI indicates that the weakly coordinating ligand does not stabilise the lower oxidation state. The electrochemical behaviour of $\text{U}(\text{TFSI})_4 \cdot x\text{H}_2\text{O}$ and $\text{UO}_2(\text{TFSI})_2 \cdot \text{H}_2\text{O}$ in $[\text{Me}_3\text{N}^n\text{Bu}][\text{TFSI}]$ has also been investigated with reduction of U to the zerovalent state observed and all the other main U redox processes also observed. The

voltammetric results indicated that oxide formation is occurring at the electrode surface, similar to that observed in the Ln and Th cases. Interesting voltammetric $\text{U}(\text{TFSI})_4 \cdot x\text{H}_2\text{O}$ experiments undertaken in the presence of $[\text{Eu}(\text{TFSI})_3(\text{H}_2\text{O})_3]$ showed waveforms similar to that expected for the electroplating of U metal. It would appear that the Eu^{3+} ion is reacting with trace water present in the system. This result indicates that bulk deposition of U metal in $[\text{Me}_3\text{N}^n\text{Bu}][\text{TFSI}]$ may indeed be possible, highlighting the need for further investigations into the removal of trace moisture from the melt.

The high specific activity of ^{237}Np , and resultant small reaction scale, made the synthesis and characterisation of Np-TFSI complexes difficult. However, vibrational spectroscopy showed that TFSI coordinates to the Np centres in an analogous manner to that observed for Ln, Th and U. UV/vis/nIR spectroscopy showed that Np(IV) is not stabilised by TFSI and $\{\text{NpO}_2\}^+$ dominates solution speciation in $[\text{Me}_3\text{N}^n\text{Bu}][\text{TFSI}]$. Nevertheless, an electrochemical study showed that Np can be reduced to the zerovalent state in $[\text{Me}_3\text{N}^n\text{Bu}][\text{TFSI}]$, with additional redox processes also observed and assigned. The voltammetry again suggests that a Np oxide is formed on the electrode surface due to reactions with trace water in the system. However, the sharper oxidation peak for the $\text{Np}(0) \rightarrow \text{Np}(\text{III})$ reaction is consistent with thermodynamic parameters and supports the oxide formation theory, further emphasising the need to eliminate water from the system.

The observation of the $\text{Np}(\text{III})/\text{Np}(0)$ reduction in $[\text{Me}_3\text{N}^n\text{Bu}][\text{TFSI}]$ provides a strong indication that the $\text{Pu}(\text{III})/\text{Pu}(0)$ should be observable in this LTIL. In addition, the observation of the $\text{Ln}(\text{III})/\text{Ln}(0)$ and $\text{Ln}(\text{II})/\text{Ln}(0)$ reductions in this LTIL show that a

sufficient overpotential is available, therefore electroplating of U and Pu should be possible in $[\text{Me}_3\text{N}^n\text{Bu}][\text{TFSI}]$ if the oxide formation problem is solved.

In summary, a room temperature ionic liquid, $[\text{Me}_3\text{N}^n\text{Bu}][\text{TFSI}]$, with a wide enough electrochemical window to observe the U and Pu reduction to the zerovalent state has been identified. This ionic solvent probably has sufficient overpotential for the efficient electrodeposition of U and Pu. However, problems with trace moisture in the melt complicate the electrochemical behaviour of *f*-elements within this system and procedures to remove this moisture need to be in place.

To prove whether the electrochemical separation of U and Pu in LTILs can work on an industrial scale, bulk electroreduction has to be achieved. It has also been shown that the diffusion of *f*-elements within $[\text{Me}_3\text{N}^n\text{Bu}][\text{TFSI}]$ is slow, however mass transport on an industrial scale may not be dependent on diffusion, but rather on mechanical stirring. Any future studies should therefore be directed towards this natural next step towards industrialisation, as well as developing methods of U/Pu separation.

APPENDIX 1

SINGLE CRYSTAL X-RAY DIFFRACTION

STRUCTURE OF

PENTA-AQUADIOXOURANIUM(VI)

BIS {BIS(TRIFLUOROMETHANESULFONYL)

AMIDE} - $[\text{UO}_2(\text{H}_2\text{O})_5][\text{TFSI}]_2$

A1.1 Single crystal X-ray diffraction of $[\text{UO}_2(\text{H}_2\text{O})_5][\text{TFSI}]_2$

Investigations of coordination of TFSI to Ln^{3+} and Th^{4+} (Chapters 4 and 5) and $\{\text{UO}_2\}^{2+}/\text{U(IV)}$ EXAFS measurements (Chapter 6) show that TFSI is a poorly coordinating ligand for *f*-elements. All attempts to recrystallise uranium TFSI-complexes (even in dried and degassed organic solvents) failed. One such attempted recrystallisation of $\text{UO}_2(\text{TFSI})_2 \cdot \text{H}_2\text{O}$ from H_2O , yielded the pentahydrate complex with TFSI acting as a counter ion. A similar Mg complex, $[\text{Mg}(\text{H}_2\text{O})_6][\text{TFSI}]_2$,¹ has previously been observed.

$[\text{UO}_2(\text{H}_2\text{O})_5][\text{TFSI}]_2$ crystallises in the monoclinic space group $P2_1/c$. The unit cell comprises 8 molecules of which there are two distinct $[\text{UO}_2(\text{H}_2\text{O})_5]^{2+}$ cations (labelled $[\text{UO}_2(\text{H}_2\text{O})_5]^{2+}\text{-1}$ and $[\text{UO}_2(\text{H}_2\text{O})_5]^{2+}\text{-2}$) and six TFSI anions comprising four distinct TFSI anions ($[\text{TFSI}]\text{-1}$, $[\text{TFSI}]\text{-2}$, $[\text{TFSI}]\text{-3}$ and $[\text{TFSI}]\text{-4}$). Each U(VI) cation is axially coordinated to two oxygens and equatorially to five water molecules to form a seven coordinate uranium centre. Both dicationic complexes are closely associated with two TFSI anions. Crystallographic information and selected bond lengths are given in Tables A1.1 and A1.2, with the structure represented in Figure A1.1.

The U centre in the $[\text{UO}_2(\text{H}_2\text{O})_5]^{2+}\text{-1}$ cation has a pentagonal bipyramidal geometry with respect to the coordinating oxygens. The $\text{U}-\text{O}_{\text{ax}}$ (uranyl) bond lengths of 1.736(3) and 1.754(3) Å, and $\text{O}_{\text{ax}}\text{-U}-\text{O}_{\text{ax}}$ bond angle of 177.87(16) ° are within the expected range for 7-coordinate uranyl.²⁻⁵ The $\text{U}-\text{O}_{\text{w}}$ distances ranging between 2.391(3) and 2.439(4) Å for the coordinated waters are within literature values for $\{\text{UO}_2\}^{2+}\text{-O}_{\text{w}}$ bonds (2.394 – 2.447

Å for $\text{UO}_2(\text{ClO}_4)(\text{H}_2\text{O})_3$; 2.39 – 2.44 Å for $\text{UO}_2(\text{ClO}_4)(\text{H}_2\text{O})_5$; 2.397 – 2.427 Å for $\text{UO}_2(\text{ClO}_4)(\text{H}_2\text{O})_5 \cdot 2\text{H}_2\text{O}$; 2.384 – 2.42 Å for $\text{UO}_2(\text{H}_2\text{O})_5(\text{OTf})_2(18\text{crown}6)$; 2.39 – 2.47 Å for $[\{\text{UO}_2(\text{H}_2\text{O})_3\} \{\Delta\text{-V(hida)}_2\} \cdot 2\text{H}_2\text{O}]_n$.²⁻⁵ The $\text{O}_w\text{-U-O}_w$ bond angles are slightly distorted (ranging between 68.93(13) ° and 75.30(12) °) from the ideal value of 72 ° expected for a pentagonal bipyramidal geometry, due to the two hydrogen atoms on O_w22 lying in the equatorial plane (as opposed to the axial plane for all the others). As a result, O_w23 and O_w21 are pulled closer to O_w22 due to hydrogen bonding.

For the $[\text{UO}_2(\text{H}_2\text{O})_5]^{2+}\text{-}2$ cation the U-O_{ax} bond lengths of 1.740(3) and 1.757(3) Å are slightly longer than those observed in $[\text{UO}_2(\text{H}_2\text{O})_5]^{2+}\text{-}1$, but are still comparable to those previously reported in the literature. The $\text{O}_{\text{ax}}\text{-U-O}_{\text{ax}}$ bond angle of 176.43(15) ° is more accurate than for $[\text{UO}_2(\text{H}_2\text{O})_5]^{2+}\text{-}1$ (177.87(16) °). Four of the five coordinated water molecules lie in the equatorial plane, with the remaining water lying significantly out of the plane. The U-O_w bond lengths of 2.377(4) to 2.409(3) Å are comparable to the literature values as for the previous cation.

Using a least squares geometrical analysis (WinGx program),⁶ O_w29 was found to be 17.8 ° above the $\text{O}_w28\text{-O}_w27\text{-O}_w26\text{-O}_w30\text{-U}2$ plane (Figure A2.2). As there are no strongly coordinating ligands present, this is presumably due to crystal packing effects. This in turn due to electronic repulsions between $\text{O}_{\text{ax}}25$ and the out of plane water molecule causes the slight bending of the $\text{O}_{\text{ax}}\text{-U-O}_{\text{ax}}$ bond observed.

The bond lengths of the TFSI anions are , for the most part, comparable to those observed for [Me₄Sb][TFSI] in Chapter 3. The major differences between the four TFSI anions lie with the CF₃ group orientation for the [TFSI]-1 and [TFSI]-2 anions the CF₃ group adopt a *trans* orientation (with respect to the SNS plane), with C-S-S-C dihedral angles of 171.71(27) and 172.06(29) ° respectively. In the case of [TFSI]-4, the *trans* geometry is distorted and a dihedral angle of 153.57(25) ° is observed. Finally for [TFSI]-3, a *cis* CF₃ orientation with CSSC dihedral angle of 24.48(27) ° is found. For the [TFSI]-1, [TFSI]-2 and [TFSI]-3 anions the dihedral angles are comparable to those observed for [Me₄Sb][TFSI] (173.49(40) °) and those previously reported for HTFSI⁷ (174.2 °) and KTFSI⁸ (17.1 °), and are consistent with those calculated for an uncoordinated TFSI salt. The dihedral angle found for [TFSI]-4 is markedly different and has a similar value to the *transoid* geometry found in Λ-[La(TFSI)₃(H₂O)₃] (148.00(32) °, Chapter 4).

As expected, there is considerable hydrogen bonding between the waters on the uranyl centres and the O, N and S atoms of the TFSI anions with H-Z (where Z = O, N or S) distances ranging from 1.91 to 3.03 Å. For the [UO₂(H₂O)₅]²⁺-1 cation H-O_{TFSI} distances of 2.14(3) and 2.03(4) Å are found between the [TFSI]-1 and [TFSI]-2 anions. In the case of [UO₂(H₂O)₅]²⁺-2, a shorter H-O_{TFSI} distance of 1.97(2) Å is found for [TFSI]-3 and 2.00(2) for [TFSI]-4. The closer cation/anion distance and the different dihedral angle (compared to the other anions) perhaps explains the out of plane water coordinated to the second Uranyl cation.

Empirical formula	C ₄ H ₁₀ F ₁₂ N ₂ O ₁₅ S ₄ U
Formula weight	920.41
Space group	<i>P</i> 2 ₁
Crystal group	Monoclinic
<i>a</i> (Å)	23.986(3)
<i>b</i> (Å)	10.3895(11)
<i>c</i> (Å)	20.895(2)
α (deg)	90
β (deg)	114.803(2)
γ (deg)	90
<i>V</i> (Å ³)	4726.8(9)
<i>Z</i>	8
<i>T</i> (K)	100(2)
λ (Å)	0.71073
<i>D</i> _{calcd} (mg M ⁻³)	2.587
μ (mm ⁻¹)	7.383
<i>R</i> ₁ , <i>Rw</i> ² indices [<i>I</i> > 2 σ ² (<i>I</i>)]	0.0295, 0.0623
<i>R</i> ₁ , <i>Rw</i> ² (all data)	0.0367, 0.0651

Table A1.1: Crystallographic data for [UO₂(H₂O)₅][TFSI]₂

Bond lengths / Å

[UO ₂ (H ₂ O) ₅] ²⁺ -1		[UO ₂ (H ₂ O) ₅] ²⁺ -2	
U(1) – O _{ax} (17)	1.736 (3)	U(2) – O _{ax} (24)	1.740 (3)
U(1) – O _{ax} (18)	1.754 (3)	U(2) – O _{ax} (25)	1.757 (3)
U(1) – O _w (19)	2.408 (4)	U(2) – O _w (26)	2.377 (4)
U(1) – O _w (20)	2.391 (3)	U(2) – O _w (27)	2.378 (4)
U(1) – O _w (21)	2.394 (4)	U(2) – O _w (28)	2.415 (3)
U(1) – O _w (22)	2.439 (4)	U(2) – O _w (29)	2.413 (3)
U(1) – O _w (23)	2.399 (3)	U(2) – O _w (30)	2.409 (3)

[TFSI]-1		[TFSI]-3	
N(1) – S(1)	1.564 (4)	N(3) – S(5)	1.583 (4)
N(1) – S(2)	1.578 (4)	N(3) – S(6)	1.577 (4)
S(1) – O(1)	1.426 (4)	S(5) – O(9)	1.431 (3)
S(1) – O(2)	1.448 (3)	S(5) – O(10)	1.429 (4)
S(1) – C(1)	1.824 (5)	S(5) – C(5)	1.827 (5)
S(2) – O(3)	1.426 (4)	S(6) – O(11)	1.431 (3)
S(2) – O(4)	1.428 (4)	S(6) – O(12)	1.440 (3)
S(2) – C(2)	1.838 (5)	S(6) – C(6)	1.824 (5)

[TFSI]-2		[TFSI]-4	
N(2) – S(3)	1.578 (4)	N(4) – S(7)	1.581 (4)
N(2) – S(4)	1.576 (4)	N(4) – S(8)	1.586 (4)
S(3) – O(5)	1.423 (4)	S(7) – O(13)	1.420 (3)
S(3) – O(6)	1.423 (4)	S(7) – O(14)	1.424 (4)
S(3) – C(3)	1.821 (5)	S(7) – C(7)	1.842 (5)
S(4) – O(7)	1.426 (4)	S(8) – O(15)	1.428 (3)
S(4) – O(8)	1.430 (4)	S(8) – O(16)	1.432 (3)
S(4) – C(4)	1.816 (6)	S(8) – C(8)	1.848 (5)

Bond Angles / °

O _{ax} (17) – U(1) – O _{ax} (18)	177.87 (16)	N(1) – S(2) – C(2)	102.7 (2)
O(17) _{ax} – U(1) – O _w (21)	90.26 (14)	O(3) – S(2) – O(4)	118.3 (2)
O(17) _{ax} – U(1) – O _w (20)	91.03 (14)	F(1) – C(1) – F(2)	109.1 (4)
O _w (19) – U(1) – O _w (20)	72.35 (13)	F(4) – C(2) – F(5)	108.2 (4)

O _{ax} (24) – U(2) – O _{ax} (25)	176.43 (15)	S(7) – N(4) – S(8)	126.1 (3)
O _{ax} (24) – U(2) – O _w (27)	91.11 (14)	O(13) – S(7) – O(14)	119.8 (2)
O _{ax} (24) – U(2) – O _w (28)	87.57 (14)	N(4) – S(7) – C(7)	105.9 (2)
O(26) _w – U(2) – O _w (27)	75.38 (13)	O(15) – S(8) – O(16)	118.6 (2)
		N(4) – S(8) – C(8)	106.7 (2)
S(1) – N(1) – S(2)	125.2 (3)	O(15) – S(8) – O(16)	118.6 (2)
O(1) – S(1) – O(2)	117.8 (2)	F(19) – C(7) – F(20)	109.2 (4)
N(1) – S(1) – C(1)	103.7 (2)	F(23) – C(8) – F(24)	109.3 (4)
O(3) – S(2) – O(4)	118.3 (2)		

Table A1.2: Selected bond lengths and angles for [UO₂(H₂O)₅][TFSI]₂

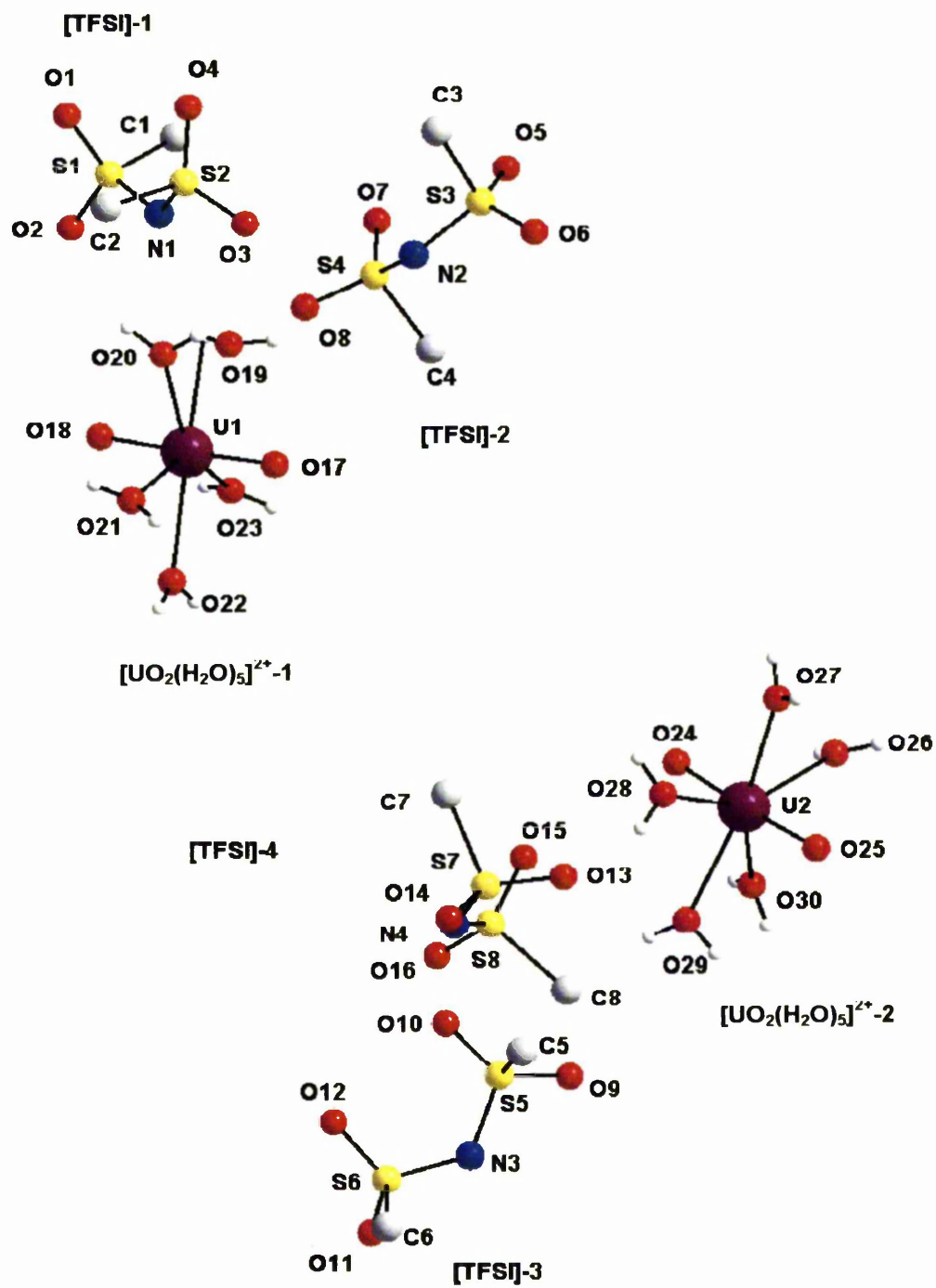


Figure A1.1: Single crystal X-ray diffraction structure of [UO₂(H₂O)₅][TFSI]₂
(F and most H atoms omitted for clarity)

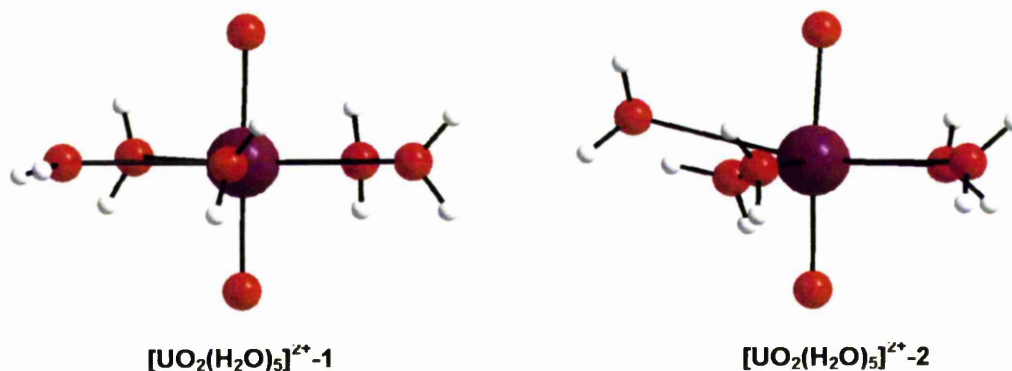


Figure A1.2: Structure of $[\text{UO}_2(\text{H}_2\text{O})_5]^{2+}-1$ (left) and $[\text{UO}_2(\text{H}_2\text{O})_5]^{2+}-2$ (right) cations showing the out of plane coordinated water observed for $[\text{UO}_2(\text{H}_2\text{O})_5]^{2+}-2$

A1.2 References

1. A. Haas, Ch. Klare, P. Betz, J. Bruckman, C. Krüger, Y. Tsay, F. Aubke, *Inorg. Chem.*, 1996, **35**, 1918.
2. J-C. Berthet, M. Nierlich, M. Ephritikine, *Angew. Chem. Int. Ed.*, 2003, **42**, 1952
3. A. Fischer, *Z. Anorg. Allg. Chem.*, 2003, **629**, 1012.
4. L. Deshayes, N. Keller, M. Lance, M. Nierlich, J-D. Vigner, *Acta Cryst. C*, 1994, **C50**, 1541.
5. R. E. Berry, P. D. Smith, S. M. Harben, M. Helliwell, D. Collison, C. D. Garner, *Chem. Commun.*, 1998, 591.
6. L. J. Farrugia, *J. Appl. Cryst.*, 1999, **32**, 837.

7. Z. Žák, A. Růžicka, Ch. Michot, *Z. Kristallogr.*, 1998, **213**, 217.
8. Z. Žák, A. Růžicka, Ch. Michot, *Z. Kristallogr.*, 1998, **213**, 217.

APPENDIX 2

ADDITIONAL X-RAY ABSORPTION SPECTROSCOPY MEASUREMENTS

**A2.1 U L_{III} edge EXAFS of uranium TFSI and chloride complexes
dissolved in [Me₄N][TFSI]**

Compound	Scatterer	Occupancy (± 20 %)	Distance / Å (± 0.02 Å)	2σ ²	R _{EXAFS}
U(TFSI) ₄ .xH ₂ O	O	1.05	1.75	0.008	37.6
	O	4.32	2.43	0.018	
	S	0.85	3.78	0.007	
	U	2.53	3.83	0.018	
UO ₂ (TFSI) ₂ .H ₂ O	O	2	1.74	0.004	29.1
	O	4	2.40	0.012	
	N	2	2.91	0.015	
UCl ₄	O	1.45	1.75	0.008	31.5
	Cl	2.62	2.54	0.014	
	Cl	2.00	2.77	0.007	
UO ₂ Cl ₂ .H ₂ O	O	2	1.77	0.005	29.3
	Cl	4	2.80	0.020	

**Table A2.1: Best fit parameters to EXAFS data for uranium TFSI and chloride
complexes in [Me₄N][TFSI]**

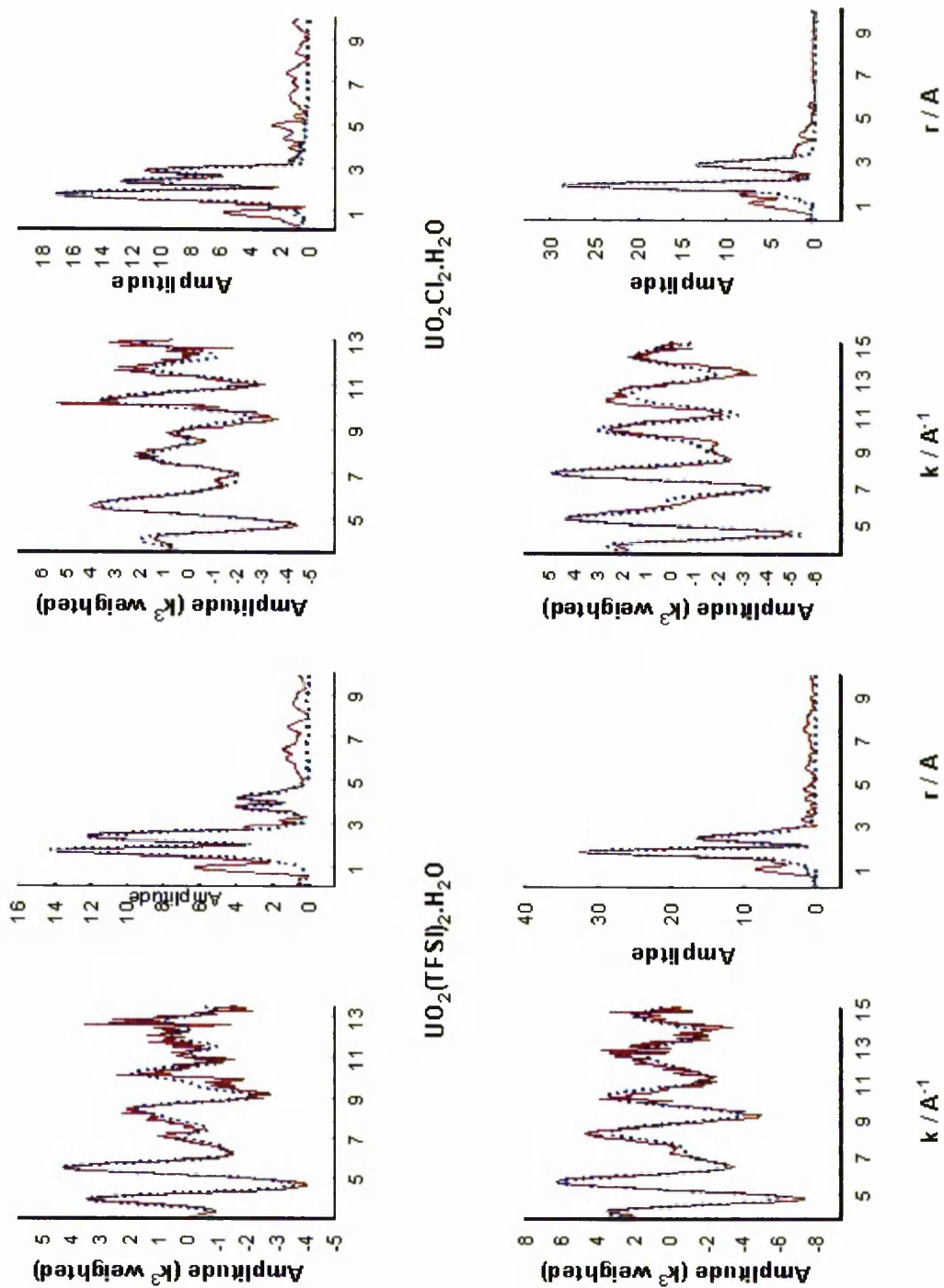


Figure A2.1: EXAFS (left) and FT (right) spectra of uranium TFSI and chloride complexes in $[\text{Me}_4\text{N}][\text{TFSI}]$. Solid line = experimental data, dashed line = theoretical fit

**A2.2 U L_{III} edge EXAFS of uranium TFSI and chloride complexes
dissolved in [ⁿHex₃PDec][NCNCN]**

Compound	Scatterer	Occupancy (± 20 %)	Distance / Å (± 0.02 Å)	2σ ²	R _{EXAFS}
U(TFSI) ₄ .xH ₂ O	O	2	1.82	0.017	35.0
	O	4	2.44	0.030	
UO ₂ (TFSI) ₂ .H ₂ O	O	2	1.79	0.004	24.8
	N	3	2.47	0.022	
	O	2	2.93	0.018	
UCl ₃	Cl	2	2.19	0.031	59.18
	N	2	3.20	0.010	
UCl ₄	O	0.40	1.72	0.007	28.2
	N	2.00	2.23	0.009	
	Cl	3.60	2.66	0.018	
	P	2.00	4.39	0.011	
UO ₂ Cl ₂ .H ₂ O	O	2	1.79	0.004	21.2
	N	2	2.44	0.031	
	Cl	2	2.69	0.007	

**Table A2.2: Best fit parameters to EXAFS data for uranium TFSI and chloride
complexes in [ⁿHex₃PDec][NCNCN]**

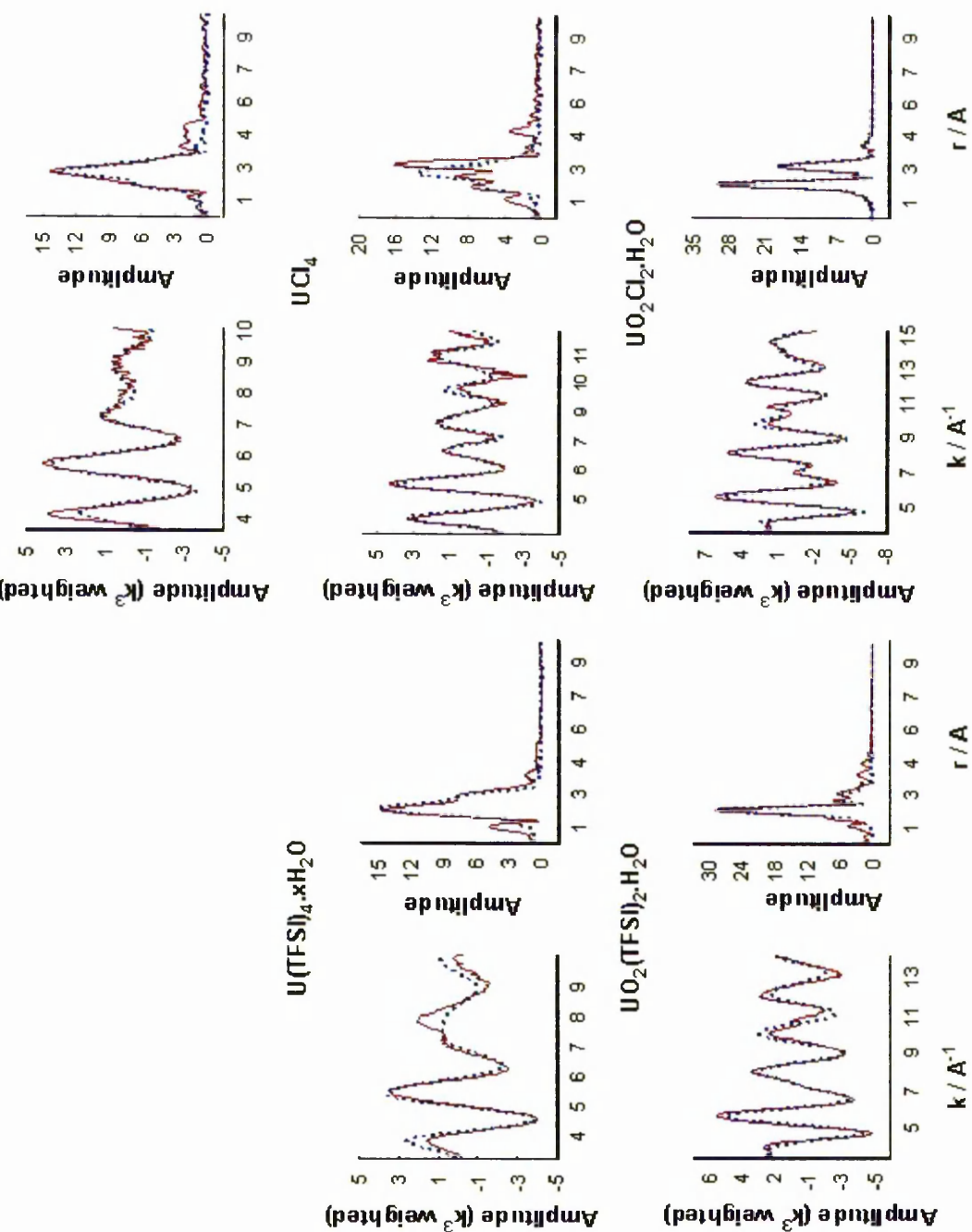


Figure A2.2: EXAFS (left) and FT (right) spectra of uranium TFSI and chloride complexes in $[^{238}\text{Hex}_3\text{PDec}][\text{NCN}(\text{CN})]$. Solid

line = experimental data, dashed line = theoretical fit

A2.3 U L_{III} edge EXAFS of uranium TFSI and chloride complexes

dissolved in [i Bu₃P''Hex][OTs] (where OTs = *p*-toluenesulfonate)

Compound	Scatterer	Occupancy ($\pm 20\%$)	Distance / Å (± 0.02 Å)	$2\sigma^2$	R _{EXAFS}
U(TFSI) ₄ .xH ₂ O	O	2	1.78	0.010	30.2
	O	2	2.31	0.011	
	S	2	2.69	0.011	
	P	1	3.86	0.007	
UO ₂ (TFSI) ₂ .H ₂ O	O	2	1.77	0.004	24.8
	O	4	2.35	0.018	
	O	2	2.93	0.015	
	S	1	3.87	0.005	
UCl ₃	O	2	2.26	0.003	29.5
	Cl	4	2.63	0.017	
	S	2	3.84	0.011	
UCl ₄	O	2	2.26	0.006	29.2
	Cl	4	2.63	0.010	
	S	2	3.84	0.011	
UO ₂ Cl ₂ .H ₂ O	O	2	1.78	0.005	24.4
	O	2	2.31	0.011	
	Cl	2	2.67	0.009	
	S	2	3.46	0.004	

Table A2.3: Best fit parameters to EXAFS data for uranium TFSI and chloride complexes in [i Bu₃P''Hex][OTs]

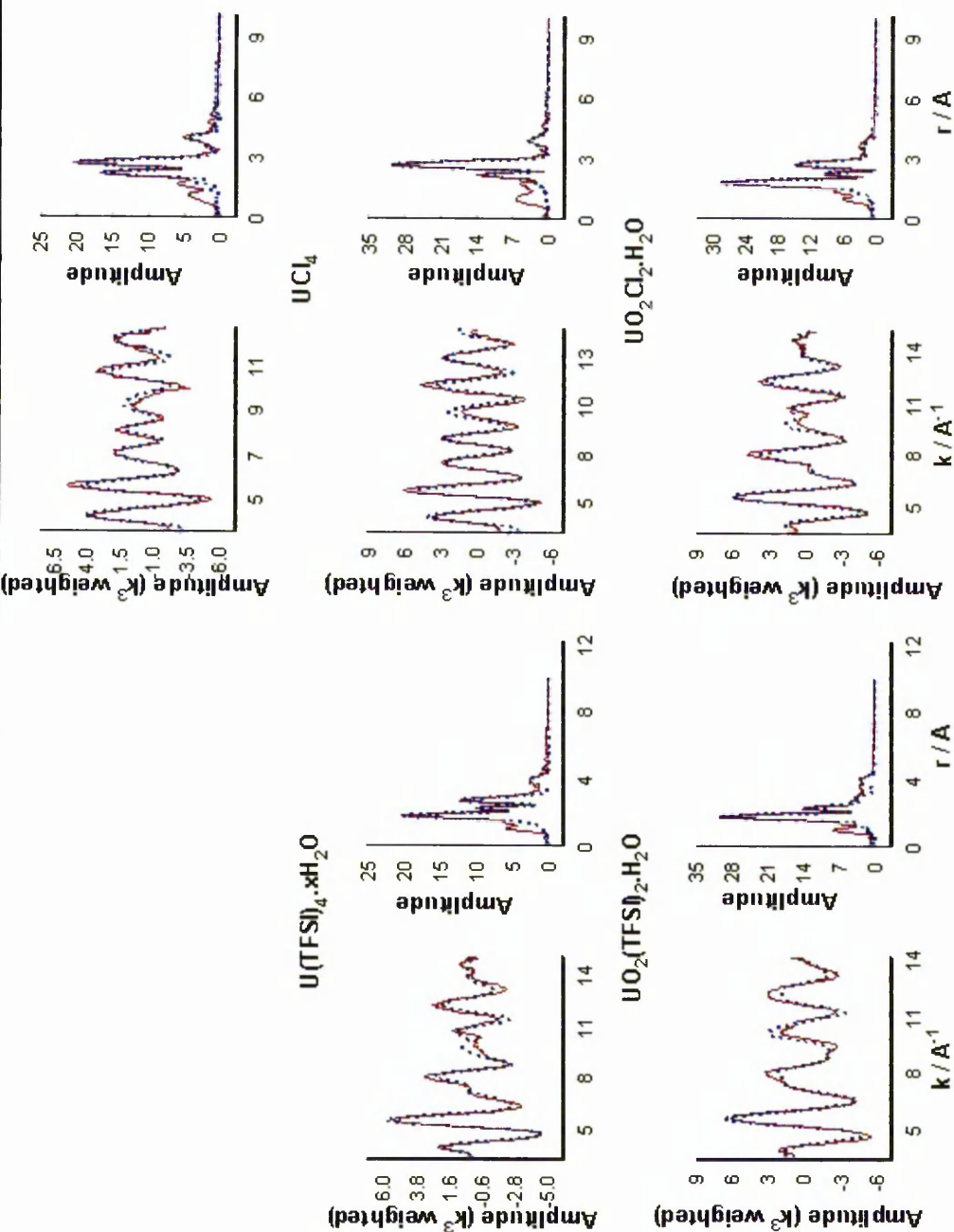


Figure A2.3: EXAFS (left) and FT (right) spectra of uranium TFSI and chloride complexes in $[\text{Bu}_3\text{P}^n\text{Hex}][\text{OTs}]$. Solid line = experimental data, dashed line = theoretical fit

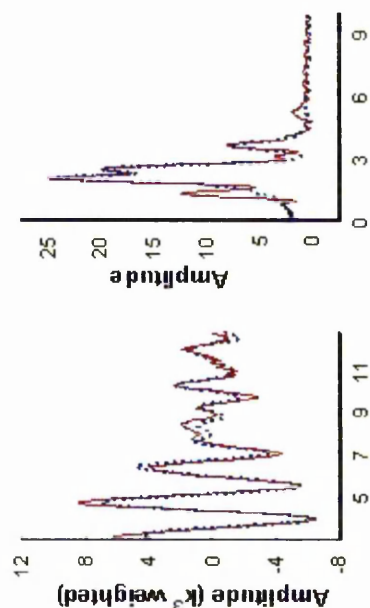
A2.4 Zr K edge EXAFS of ZrCl₄ dissolved in quaternary alkyl group 15 cation and TFSI anion based LTILs

Solid state Zr K edge EXAFS spectra of ZrCl₄ dissolved in [Me₄N][TFSI], [Me₄As][TFSI] and [Me₄Sb][TFSI] at 160 °C (quenched samples) and solution spectra in molten [Me₃NⁿBu][TFSI] at 25 °C were measured at the Synchrotron Radiation Source (SRS) in Daresbury, UK, and recorded in transmission mode. Samples of ZrCl₄ dissolved in [Me₄N][TFSI], [Me₄As][TFSI] and [Me₄Sb][TFSI] were recorded in the solid state using quenched samples, whilst ZrCl₄ in [Me₃NⁿBu][TFSI] was recorded in the liquid state. Best fit parameter to the EXAFS data is given in Table A2.4 and EXAFS spectra and their FT fits are shown in Figure A2.4.

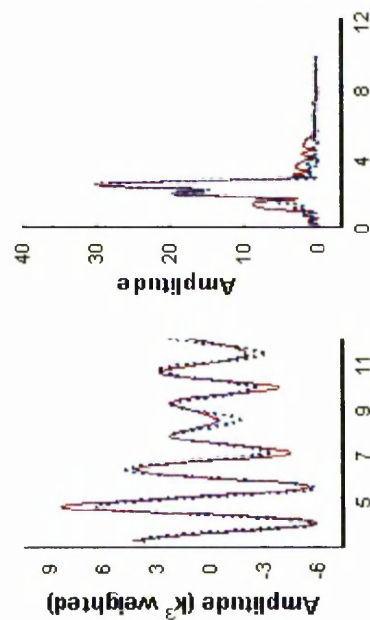
LTIL	Scatterer	Occupancy ($\pm 20\%$)	Distance / \AA ($\pm 0.02 \text{ \AA}$)	$2\sigma^2$	R_{EXAFS}
[Me ₄ N][TFSI]	Cl	3	2.47	0.011	23.0
	O	2	2.11	0.006	
[Me ₃ N ⁿ Bu][TFSI]	Cl	2	2.47	0.011	21.7
	O	4	2.16	0.011	
	Zr	0.5	3.55	0.004	
[Me ₄ As][TFSI]	Cl	2	2.48	0.012	25.3
	O	4	2.14	0.014	
	As	2	3.57	0.016	
[Me ₄ Sb][TFSI]	Cl	1	2.49	0.010	21.2
	O	6	2.17	0.014	
	Sb	1	3.48	0.006	

Table A2.4: Best fit parameters to EXAFS data for ZrCl₄ dissolved in quaternary alkyl group 15 and TFSI anion based LTILs

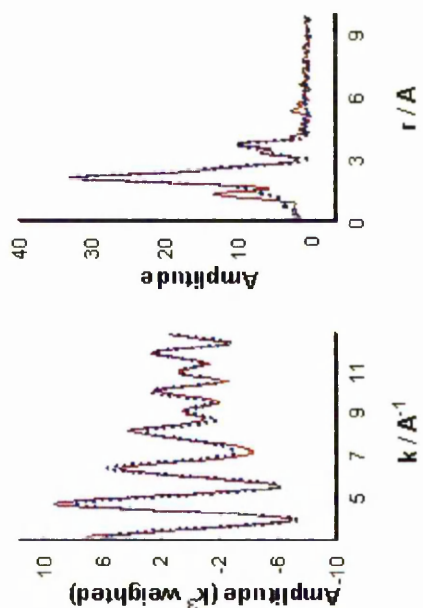
ZrCl₄ in [Me₄As][TFSI]



ZrCl₄ in [Me₄N][TFSI]



ZrCl₄ in [Me₄Sb][TFSI]



ZrCl₄ in [Me₃N⁺Bu][TFSI]

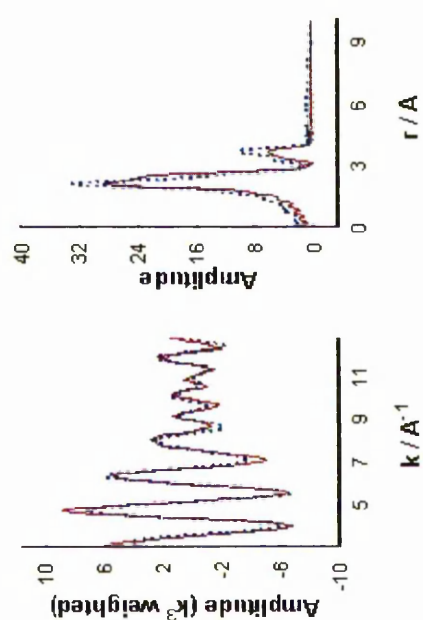


Figure A2.4: EXAFS (left) and FT (right) spectra of ZrCl₄ dissolved in quaternary alkyl group 15 and TFSI anion based

LTHLs. Solid line = experimental data, dashed line = theoretical fit